HAL
open science

Bio-sensing 2.0 : Electrical and optical measurement tools Towards a research platform for investigating bio-surface interactions

Patrik Aspermair

To cite this version:

Patrik Aspermair. Bio-sensing 2.0 : Electrical and optical measurement tools Towards a research platform for investigating bio-surface interactions. Micro and nanotechnologies/Microelectronics. Université de Lille; Universität für Bodenkultur (Vienne), 2019. English. NNT : 2019LILUI118 . tel-03626169

HAL Id: tel-03626169

https://theses.hal.science/tel-03626169v1

Submitted on 31 Mar 2022

HAL is a multi-disciplinary open access archive for the deposit and dissemination of scientific research documents, whether they are published or not. The documents may come from teaching and research institutions in France or abroad, or from public or private research centers.

L'archive ouverte pluridisciplinaire **HAL**, est destinée au dépôt et à la diffusion de documents scientifiques de niveau recherche, publiés ou non, émanant des établissements d'enseignement et de recherche français ou étrangers, des laboratoires publics ou privés.

University of Natural Resources and Life Sciences, Vienna

No Etudiant: 11610069
Enrollment number: 00930606

Thèse de Doctorat en Univerité Lille

Ecole doctorale Sciences Pour l'Ingenieur (EDSPI)

Micro et Nanotechnologies, Acoustique et Télécommunications

Présentée et soutenue publiquement par

Patrik Aspermair

intitulé

Bio-sensing 2.0 – Outils de mesure électriques et optiques pour le développement d'une plateforme d'investigation pour les interactions de bio-surface

le 17 décembre 2019

Membres du jury

Examinateurs:	Vincent BOUCHIAT José Luis TOCA-HERRERA
Directeurs de thèse:	Sabine Szunerits Wolfgang Knoll

cotutelle de thèse en
Université Lille, Lille, France et
University of Natural Resources and Life Sciences, Vienna, Austria
December 2019

Copyright 2019, Patrik Aspermair

Université de Lille
iemn
AIT AUSTRIAN INSTITUTE OF TECHNOLOGY TOMORROW TODAY
CEST
BOKU
University of Natural Resources and Life Sciences, Vienna
No Etudiant: 11610069
Enrollment number: 00930606

Doctorate Thesis at University of Lille

Doctoral School of Engineering Science (EDSPI)

Micro et Nanotechnologies, Acoustique et Télécommunications

presented by

Patrik Aspermair

entitled

Bio-sensing 2.0 – Electrical and optical measurement tools Towards a research platform for investigating bio-surface interactions

presented on December, 17th 2019

Jury composed of

Examiners:	Vincent BOUCHIAT José Luis TOCA-HERRERA
Director of Thesis:	Sabine Szunerits Wolfgang Knoll

co-tutorial PhD thesis at
University of Lille, Lille, France
University of Natural Resources and Life Sciences, Vienna, Austria
December 2019

Copyright 2019, Patrik Aspermair

Patrik Aspermair

Bio-sensing 2.0 – Electrical and optical measurement tools Towards a research platform for investigating bio-surface interactions

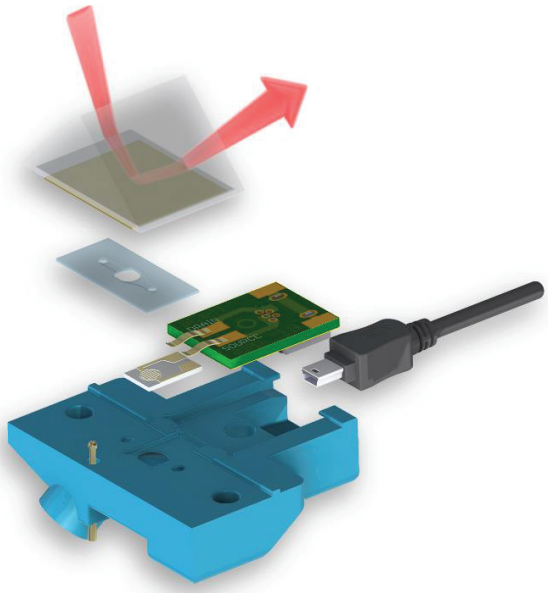

WHAT I CANNOT CREATE, I DO NOT UNDERSTAND

Richard Feynman

Eidesstaatliche Erklärung

Ich erkläre eidesstattlich, dass ich die Arbeit selbständig angefertigt, keine anderen als die angegebenen Hilfsmittel benutzt und alle aus ungedruckten Quellen, gedruckter Literatur oder aus dem Internet im Wortlaut oder im wesentlichen Inhalt übernommenen Formulierungen und Konzepte gemäß den Richtlinien wissenschaftlicher Arbeiten zitiert, durch Fußnoten gekennzeichnet bzw. mit genauer Quellenangabe kenntlich gemacht habe.

Patrik Aspermair

Abstract

The race in biomedical diagnostics between optical detection principles and electrical concepts is not decided yet. Both approaches continue to offer solutions for fast, multiplexed, simple and cheap detection of biological relevant molecules. However, if it comes to the detection of small analytes and/or if the achievable analyte binding density at the transducer surface is low, label-free optical detection schemes have a problem because the change in the optical interfacial architecture induced by the mere binding of the analyte may be simply too minute to be detected. In this work, an innovative and versatile sensing platform, combining an electrical and optical read-out device to compare the different signal behaviors during a biological binding event in real time was developed. It is based in coupling the read out of a graphene-based field-effect transistor (gFET) with that of surface plasmon resonance (SPR). Various binding events including biotin/neutravidin, PNA/DNA and ssRNA/ssDNA aptamers for protein detection were investigated and the results discussed.

Biography of Patrik Aspermair

Patrik Aspermair started his career as electrical engineer in 2006 at the company KEBA in Linz, where he was part of the electrical development team for self-service machines. His competence in problem solving and creative approaches during three years of employment evolved and was very helpful to create various products such as ATMs, lottery terminals and self-service mail pick up stations.

The quest for knowledge and his appetite for research grew meanwhile and so he decided in 2009 to start a bachelor degree in biomedical engineering at the Technical University in Graz, which he continued in a master degree. After an Erasmus semester in Istanbul and a master thesis at the Austrian Institute of Technology (AIT) in Vienna, he defended his graduate studies in 2016.

Right at this time, Patrik moved to France to start a joined PhD program, a so-called co-tutelle de thèse between the University of Lille, France and the Natural Resources and Life Science University in Vienna, Austria. The first period of his PhD degree was in an unknown environment, in a country with a foreign language, but he accepted the challenge and contributed in the laboratory of Sabine Szunerits. He was able to establish new measurement set-ups for fellow students with his electrical engineering knowledge and learned new methods for surface modifications in return.

In the summer of 2017, he returned from his excursion back to Vienna and continued the research in the new facility at the University and Research Center in Tulln, as an employee of CEST in the lab of Wolfgang Knoll to finish his PhD thesis.

Acknowledgments

This work was conducted at two different research institutes as part of a co-tutelle/joint-study program: at IEMN in Lille, France, Institut d'électronique de microélectronique et de nanotechnologie and at CEST in Tull, Austria, Center of Elechtrochemical Surface Technology.

The financial support by the European “PANG project IEMN-UMR CNRS 8520” and the FFG/COMET project are highly appreciated.

I would like to thank the unbelievable BST group, my supervisors Sabine Szunerits, Wolfgang Knoll and the many research groups I met throughout my journey to the PhD degree.

I would like to thank especially my family, my mother Herta, my father Manfred and my brother Manfred, who supported me in any possible way to achieve this distant goal of a PhD degree and who always believed in me. Through good and bad times on my side was always my faithful companion Minou LeChat, who gave me power whenever I was weak and desperate.

Colleagues and fellow students turned into friends and became an important part of my life. Special thanks to all of you:

Sebastián Alberti, Jakob Andersson, Simone Auer, Alexandre Barras, Teresa Berninger, Johannes Bintinger, Christina Bliem, Anıl Bozdogan, Milica Budimir, Li Chengnan, Yannick Coffinier, Federica Curti, Agathe Deveraux, Chiara D'Onofrio, Jakub Dostalek, Filippo Fedi, Gonzalo Fenoy, Nicolas Ferrer-Sanchez, Simone Fortunati, Stefan Fossati, Philipp Fruhmann, Nathan Garner, Frank Andreas Geiß, Isabella Gruber, Astrid Hafner, Simone Hageneder, Ioana Silvia Hosu, Roxana Jijie, Vanessa Jungbluth, Daria Kotlarek, Mark Patrick Kreuzer, Alexandra Krissalis, Katarina Kumpf, Bernadette Lechner, Houcem Maaoui, Lisa Mayerhuber, Vladyslav Mishyn, Richard Mócsa, Yavuz Oz, Paolo Pelosi, Esteban Piccinini, Nestor Quilis, Ulrich Ramach, Ciril Reiner-Rozman, Anne Schuchanegg, Santosh Singh, Jiajun Tan, Priyamvada Venugopalan and Zhu Jiao.

Your real friends are there for you in hard times, even if you have not seen them for years or if distance separates you. I am blessed to have many of them. To whom it may concern, this is for you: Thank you.

Contents

1. CHAPTER: INTRODUCTION 1

Biosensors *2*
Aptamers 4
Apta-Sensors for Water Pollution monitoring 4
Surface plasmon resonance for biosensing 6
Graphene as Biosensor 8
Functionalization of graphene 10
Non-specific binding events 11
Development of anti-fouling coatings 11
Monitoring binding events/dissociation reactions by gFETs and SPR 13
Correlation with electrochemical and optical transduction 14
Project Goals *17*
gFET sensor performance and stability 18
Combination of gFET and SPR 18
Evaluate surface functionalization methods 19
Creation of a software tool 20
2. CHAPTER: FABRICATION OF GRAPHENE FETS AND GOLD SLIDES 23

Materials and Methods *23*
Devices and Materials 23
Software 24
Chemicals list 25
Graphene source 26
Preparation of the surface 27
Fabrication of CVD graphene FET 28
Fabrication of reduced graphene oxide FET 30
Optimize graphene oxide concentration 31
GO reduction measurement setup 32
Fabrication of gold slides for SPR 33
Preparation of buffer solutions 33
Gate Capacitance C_i: 34
Mobility calculation 34
Results of gFET fabrication *37*
Scanning electron microscope images of graphene 37
Real-time reduction measurements 39
Raman spectra of rGO and CVD graphene 40
AFM measurements of graphene 41
Graphene oxide concentration determination 42
Nanodrop OD measurements 42
SEM image evaluation 43
I_DV_G measurements for pH sensing 46
Comparison CVD graphene and rGO 49
Measurement of gate capacitance C_i: 50
Mobility comparison of rGO and CVD: 51
Discussion *53*
Manuscript #1: 54

3. CHAPTER: SURFACE MODIFICATIONS 65

Materials and Methods *65*
Graphene modification with pyrene-carboxylic acid 65
Gold slide DTSP 67
Gold slide biotinylation 67
Immobilization of amine-terminated capture probe 68
Immobilization of Streptavidin modified molecules 69
Blocking agents 69
SPR for blocking performance 71
Nanobeads immobilization 71
Differential pulse voltammetry for surface investigation 72
Graphene modification with diazonium treatment 74
Results of surface modification *77*
SPR experiment for blocking agents 77
XPS Aptamer surface coverage 78
Nanobeads SEM images 79
Differential pulse voltammetry enzyme readout 81
Performance of diazonium treated gFET 84
I_DV_G curves and mobility 85
Discussion *87*
Manuscript #2: 88
4. CHAPTER: GFET/SPR MEASUREMENT TOOL 101

Materials and Methods *101*
Source measure unit 101
Software: gFET measurement utility 103
Flow cell 1: micro fluidic design 104
Flow cell 2: gFET/SPR 105
Gasket for µCell 108
PDMS gasket fabrication 108
Tube connection to the gFET/SPR flow cells 109
Fabrication of printed circuit boards 109
Results of gFET/SPR design *111*
Measurement set-up for the gFET and gFET/SPR 111
Assembly of gFET/SPR cells: 115
Discussion *117*
5. CHAPTER: MEASUREMENTS WITH GFET AND SPR 119

Materials and Methods *119*
Human Papilloma Virus protein 119
Layer by Layer assembly 120
Biotinylated gold surface 120
Results of gFET/SPR measurements *123*
Human papilloma virus protein detection 123
Titration of different pH solutions in gFET/SPR setup 125
Layer by layer measurements 126
Biotin – Streptavidin interaction 129
Biotin – Neutravidin interaction 130
Human Papilloma Virus I_DV_G analysis 131
Discussion *133*
Manuscript #3: 134
6. CHAPTER: CONCLUSION 141

Outlook 142

1. Chapter:

Introduction

Since modern medicine arose, it has been of great interest to detect the variety of diseases and its cause in nutrition and environment. Part of these investigations aim to identify bio-molecules, such as bacteria, viruses, proteins, hormones, toxins, DNA strains and heavy metals. Diagnostical tools were established over the past decades to monitor the concentrations of bio-markers in human samples, e.g. blood, urine and salvia or bio-active substances in food and the environment. Mostly aqueous solution-based samples are investigated with electrochemical (cyclic voltammetry, differential pulse voltammetry etc.), electrical (impedance spectroscopy, resistivity measurements, field-effect transistors, etc.) and optical (UV/Vis absorption, fluorescence, surface plasmon spectroscopy, etc.) measurement techniques to obtain the concentration of the bio-molecules. These approaches continue to offer solutions for fast, multiplexed, simple and cheap detection of bio-molecules, oligonucleotides, PCR amplicons, genomic DNA (fragments), etc. [1–3]

However, if it comes to the detection of small analytes and/or if the achievable analyte binding density at the transducer surface is low, label-free optical detection schemes have a problem because the change in the optical interfacial architecture induced by the mere binding of the analyte may be simply too minute to be detected – a classical challenge even in commercial instruments like the Biacore™ SPR setups. [4]

Biosensors

Label-free electronic biosensors have attracted increasing attention in recent years [5–9] due to their potential for implementation in compact and cost-efficient analytical devices that rival in performance with state-of-the-art approaches such as high-performance liquid chromatography (HPLC), [10,11] gas chromatography-mass spectrometry (GC-MS),[12] and liquid chromatography-tandem mass spectrometry (LC-MS/MS). [13–15] Biosensors are analytical devices that typically consist of three main components: (i) a biological recognition element that binds to the target molecule, (ii) a signaling component that converts the biological recognition into physically detectable signals (e.g. electrochemical or optical transducers) and (iii) an electronic system for signal amplification/processing and user-friendly data read-out, shown in Figure 1. [16] Electrolyte gated field-effect transistors (EG-FETs) are a particularly promising class of candidates for point-of-care monitoring as they allow operation in biologically relevant media at very low voltages (<0.5 V). [9,17] In EG-FETs, an electrolyte, typically a water-based ion solution, is used as the dielectric and separates the semiconductor from the gate electrode. The current between the source and drain electrodes is then modulated by the gate potential and due to the high capacitance resulting from the formation of the Helmholtz double layer at the gate and semiconductor interfaces, the devices can be operated in the sub-volt regime. [18,19] However, despite dramatic progress in the field and even demonstrating label-free single molecule detection, [15] no commercial EG-FET biosensor has entered the market yet. Arguably, this can be attributed, at least partially, still to a lack of understanding the fundamental principles of surface-based bio-interactions in these systems as well as issues associated with low reproducibility, unspecific binding, sensor drift and batch to batch variations which have hindered large scale deployment of this emerging class of biosensors.

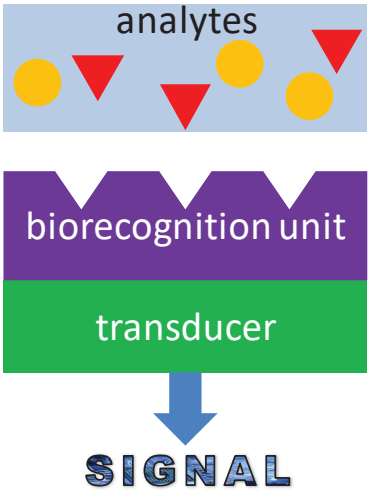

Figure 1: Schematic principle of a biosensor, converting a biological binding event to a physically measurable dimension

Target induced conformational changes of recognition units, shown in Figure 2 are widely considered as main cause for signal transduction but depending on the functionalization site of the target-specific receptors (e.g. on the channel or on the electrodes), different measurement principles are discussed in literature. In the case of biorecognition immobilization on the channel, signal transduction is based on electrostatic gating effects [20–22] which in turn lead to a rearrangement of charge distribution and thus a change in the overall electronic read-out.

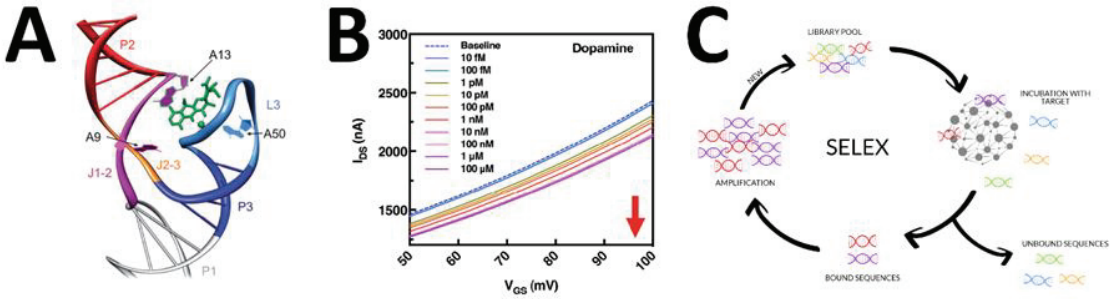

Figure 2: The schematic illustrations of an aptamer with its ligand is shown in (A). [23] Figure (B) shows the target-binding induced changes of the transfer characteristic on the electrical sensor readout. [24] The aptamer selection, purification and amplification process are schematically shown in (C). (from igem.org).

Conformational changes can also be measured in the case of gate-electrode functionalization, in which case the transduction is governed by the small capacitance variations due to receptor-ligand interactions. [6,25] However, these findings and resulting conclusions are based on electronic measurements using EG-FET devices with unknown receptor surface concentrations (or estimated using ex-situ XPS measurements) under static conditions. [15,26] Real-time dynamic measurements [27,28] that could correlate the sensor response directly to the amount of immobilized receptor units as well as monitoring the degree of conformational changes on surfaces in-situ are not available, thus preventing us to get the full picture of (bio-) adsorption processes on surfaces and developing a better understanding of the fundamental principles of EG-FET based biosensors.

Aptamers

Recognition molecules (receptors) are the cornerstone of any biosensor as their binding affinity and specificity determine the sensor performance. Most commonly, antibodies have been used in biosensor development since they can selectively bind a wide range of analytes and are commercially available for many analytes. [29] However, antibodies suffer from drawbacks such as high production cost and strong batch-to-batch variation. For this reason, aptamers have been proposed as promising alternative recognition elements for biosensor platforms ("Apta-sensors"). [22,26,30,31]

Aptamers are synthetic oligonucleotides (single-stranded DNA or RNA with a length between 25 and 70 nucleotides), capable of forming highly organized, three-dimensional structures that bind target molecules with high affinity and specificity (equal or even superior to monoclonal antibodies, shown in Figure 2 (A). [32] Aptamers are generated in vitro by an iterative selection process, known as Systematic Evolution of Ligands by EXponential enrichment (SELEX),[33,34] which allows to isolate aptamers against virtually any molecule of choice, Figure 2 (C). Once identified, aptamers can be produced in large amounts via chemical synthesis at relative low costs with little batch-to-batch variation. The chemical synthesis also allows the introduction of functional groups for site-specific immobilization of the aptamer to surfaces, which is a key factor to maximize sensor performance. [26,35] Also, aptamers have longer shelf lives, better chemical stability and are smaller than antibodies (aptamer ~5-15 kDa, antibody ~150 kDa) allowing higher surface coverage on the sensor surface, leading to better performance with limits of detection at sub pM concentrations. [26] Despite these advantages, the application of Apta-sensors is still in an early stage. A major barrier in this respect is the lack of well characterized aptamer candidates that are optimized for sensor architectures.

Apta-Sensors for Water Pollution monitoring

Water is a crucial resource used for various purposes such as drinking, recreation, irrigation, aquaculture and industrial applications. Shortcomings in water quality affect

public and environmental health on a global scale. [36] The two main types of contamination are fecal pollution on the one hand and introduction of hazardous chemicals on the other hand.

Among chemical contaminants the group of antimicrobial substances have become a growing concern. In many regions of the world the presence of antibiotics in environmental waters are contributing to the proliferation of antimicrobial resistance in bacteria. [37] Organic water contaminants are traditionally detected by high-resolution chromatographic methods in combination with mass spectrometry. For some of them immunological methods have also found application, but unfortunately many of the emerging contaminants are found at very low concentrations in environmental waters. Another global threat to water quality is fecal pollution. Fecal material may contain intestinal pathogens in significant numbers which frequently cause severe outbreaks or contribute to the background rate of endemic disease. [38] Determination of fecal pollution still relies on the selective growth of fecal indicator bacteria such as Escherichia coli (E. coli) and intestinal enterococci using standardized microbiological methods [39] with analysis time from sampling to results of at least 18 hours. Therefore, alternative methods based on molecular diagnostics, enzymatic activity measurements or direct cell detection have been proposed to allow a more rapid detection directly at the water resource. [40]

For this purpose, numerous aptamers have been reported in the last decade for various antibiotic classes, including tetracyclines, β-lactams, aminoglycosides, anthracyclines, chloramphenicol, (Fluoro)quinolones and sulfonamide (recently reviewed by Mehlhorn et al.). [14] Likewise, the number of published aptamers that bind to whole bacterial cells has steadily grown, ranging from standard fecal indicator bacteria, such as E. coli to clinically relevant pathogens, such as Staphylococcus aureus, Listeria spp., or Salmonella spp. [41–43]

Most of these aptamers have been characterized simply based on secondary structure prediction and single binding assays to determine the equilibrium dissociation constants (K_d) of aptamers free in-solution. However, detailed information on binding affinities when immobilized on solid-surfaces [22] or other analytical metrics (selectivity, specificity) are scarce. [44]

Moreover, sequence refinements and optimizations to improve the detection abilities of the reported aptamers are lacking. This is mostly because the aptamer selection process (SELEX) is very expensive, time-consuming and the success rate for obtaining aptamers is low (<30%). [45] As a result, often either poorly characterized full-length aptamer sequences are integrated into sensor platforms or the same aptamer is used for multiple proof-of-concept Apta-sensors. [44,46] This lack of functional validation and sequence optimization make many of the reported aptamers unreliable or inefficient biorecognition elements, selling short the role that Apta-sensor could play in future environmental monitoring.

Surface plasmon resonance for biosensing

Since the reports of the propagation of electromagnetic waves along a surface in the year 1907, [47] interest arose on the so-called evanescent waves at the boundary of interfaces. The investigations of thin metallic foils and the plasma losses corresponding to the fast electrons within the metal, lead to a deeper understanding of phenomena occurring on the surface - the term surface plasmons was born. [48] The fundamental properties of the oscillating surface plasmons, such as dispersion, extension and the propagation length of the electromagnetic fields were discussed in detail and mathematically described. The first models to evaluate the dispersion properties were on Ag/air interfaces and follow eq 1:

$$k_x = \frac{\omega}{c}\left(\frac{\varepsilon_1\varepsilon_2}{\varepsilon_1+\varepsilon_2}\right)^{1/2} \qquad \text{eq 1}$$

with the resulting dispersion k_x, by photons coupled to the dielectric interface, defined by the dielectric constants ε_1 and ε_2 of silver and air. [49] The exploitation of the photon conversion to a decaying evanescent field was exploited by Kretschman *et al.* by the incidence of a polarized monochromatic light source to a metallic surface under a certain angle. [50] The collective charge oscillations at an interface between metal and dielectric, [49] lead to a surface plasmon resonance (SPR) at an angle θ, being the resonance angle. At this angle, most of the photons are converted to an electromagnetic, decaying field on the surface, strongly dependent to the dielectric constants ε_1 and ε_2. The arrangement of an incident light to a thin metal film on a glass prism, exciting the plasmons

at the surface is since then called the Kretschmann configuration, one of the most commonly used SPR arrangements. Figure 3 shows the schematic assembly of prims, light source, detector and the plasmon resonance surface (A), whereas in (B) an example of an angular scan is shown, at two different refractive indices n_c and $n_c + \Delta n$. [51]

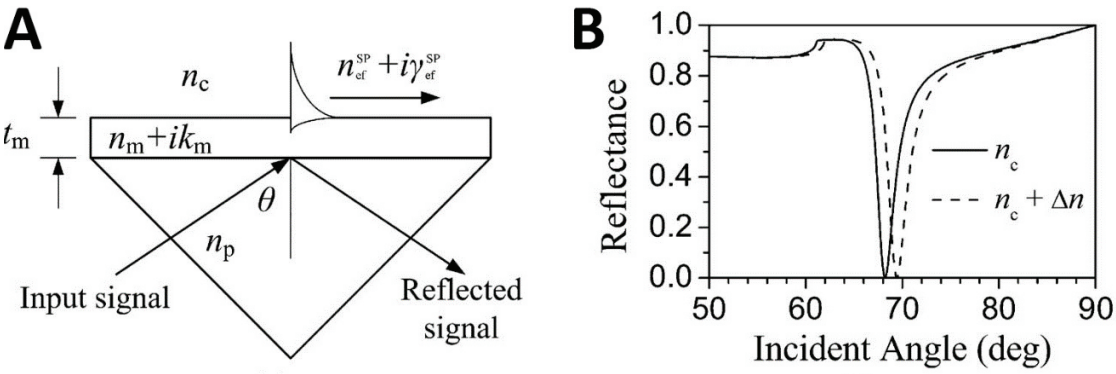

Figure 3: The schematic Kretschmann configuration is shown in (A) with the incident light, illustrated as input signal and the reflected light beam at an angle ϑ. The decay of the electromagnetic field is indicated on top of the thin metallic film with the thickness t_m. The reflected angle ϑ dependent magnitudes at different refractive indices n are shown in (B). [51]

Due to the variation of the refractive index n by Δn the resonance angle, represented by the minimum of the reflectance, for the creation of surface plasmons changes. Under the resonance condition, the emitted photons are converted to plasmons at the surface, hence missing in the reflected signal. The changes in refractive index can be caused by different solvent on the surface, happening when exposed to different bulk solutions or when molecules adhere on the interface. The adsorption of molecules to the SPR surface can be caused by non-specific interaction or by label-free specific molecule-molecule interactions with previously immobilized capture probes. Since the establishment of the Kretschmann configuration, the interface of the metallic and dielectric material, was investigated with very sensitive optical SPR devices. In the early 1980's and 1990's, the challenges of surface plasmon resonance for bio-sensing were addressed and discussed and paved the way for analysis [52] and rapid detection of chemical and biological species. [53]

Due to the well-defined surface architecture and continuous improvement of the measurement technique, quantitative analysis can be achieved and makes SPR measurements a reliable instrument for biological binding events. [54]

In some cases the use of labelling techniques employing fluorescent chromophores [55], quantum dots, Au Nanoparticles, or magnetic beads may help; however, in many cases the labelling of the analyte is not an option or undesirable, or the (small) size of the analyte molecule simply prevents the attachment of a suitable label, e.g., for odorants, or food pathogens like Mycotoxins. [3]

Here, the use of electrochemical and electronic detection principles, based, e.g., on the use of transistor devices offer an attractive alternative, especially if the analyte is charged as, e.g. DNA oligonucleotides no matter how short they are. This has been demonstrated convincingly in many examples reported in the literature by the use of organic field-effect transistors, short OFET. [56–60]

A drawback of the OFET detection of hybridization reactions, monitored on-line in a flow cell with buffer, is the requirement of a protective layer that shields the organic semiconducting material against the in-diffusion of ions from the buffer solution. These would otherwise destructively interfere with the electronic performance of the transistor. The drain-source current I_{DS} will be modified not only by the gating charges on the surface and/or bulk solution, but also by the accumulation within the organic semiconductor. As a result, an unprotected sensor in physiological buffer solution will be instable and will underly an unpredictable drift. [61]

With the introduction of graphene as the semiconducting material used for the fabrication of the channel of a transistor [62] this has significantly changed: the assembly and use of electronic sensors based on reduced graphene oxide (rGO) as the channel material are by far easier. [63] These devices can operate in aqueous buffer solutions even without any protective coating because the intrinsic high conductivity of graphene guarantees that most of the current from the source to the drain electrode flows through the graphene layer and is there modified by the analyte binding as the transduction mechanism, even if the conductive buffer solution at physiological ionic strength generates a short-cut to some extent between the source and drain electrodes. [64] This will reduce the fabrication costs of the transistors for commercial use significantly. The schematic transistor architectures for bio-sensing are shown in Figure 4. Both versions consist of a graphene channel between

the drain and source electrode, but configuration (A) has a liquid gate electrode silver wire, coated with chloride, while in device (B) the gate electrode is beneath an insulating Al_2O_3 layer to form a so-called back-gated device. The difference between the two architectures is the fact, that only the gate electrode of (A) is exposed to the liquid ion channel, therefore to the analyte.

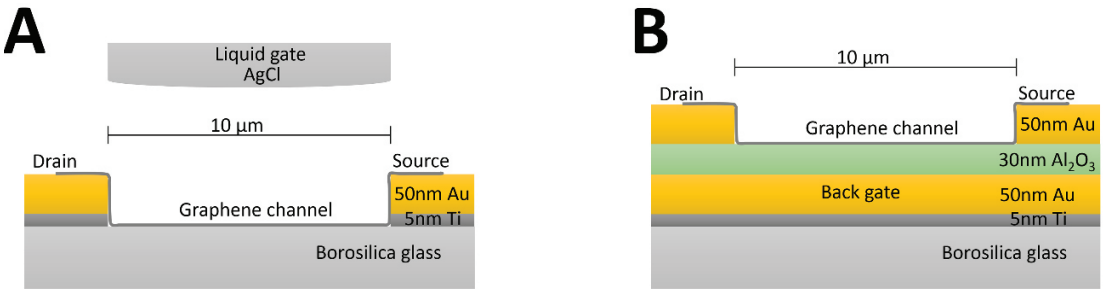

Figure 4: The two common architectures of graphene field-effect transistors for bio-sensing are shown. (A) represents the liquid-gated graphene FET and (B) the back-gated graphene FET. Only the channel architecture (A) is exposed to the ionic liquid, hence the analyte in solution. Therefore, the solution itself experiences the applied voltage and field-effect and electrical double layer form on both sides, the gate electrode and the drain-source channel.

Diagnostics with graphene FETs (gFET for short) is the youngest approach in general biosensing and for DNA detection, in particular. [65] However, the cheap fabrication of graphene transistors and their ease of operation, including the potential for multiplexing and high integration into arrays, together with the simple data handling by the electronic read-out promises to offer a versatile, label-free detection scheme for all kinds of analytes.

Based on the MOSFET theory, [66] one can derive an equation for the drain-source current, I_{DS}, as a function of the applied drain-source voltage V_{DS}, shown in eq 2:

$$I_D = \mu\ C_{ox} \frac{W}{L} (V_G - V_{th})\ V_D \qquad \text{eq 2}$$

with μ being the carrier mobility, W and L the channel width and length, V_G and V_{th} being the gate and threshold voltage, respectively. For the oxide layer capacitance (C_{ox}) of a MOSFET, here we need to consider the capacitance of the ionic liquid-graphene interface, in particular, the solid-solution interfacial capacitance, C_{el}, which can be expressed as $1/C_{el} = 1/C_H + 1/C_{diff}$, with C_H being the Helmholtz double layer capacitance and C_{diff} the diffuse double layer capacitance, [67] causing an ion concentration dependency.

Functionalization of graphene

In previous projects on smell sensing the concept of pyrene-based immobilization of receptors, such as odorant binding proteins to the graphene surface of the FETs was reported. [68] The EDC-NHS coupling chemistry for the stable attachment of the receptor molecules is shown in Figure 5.

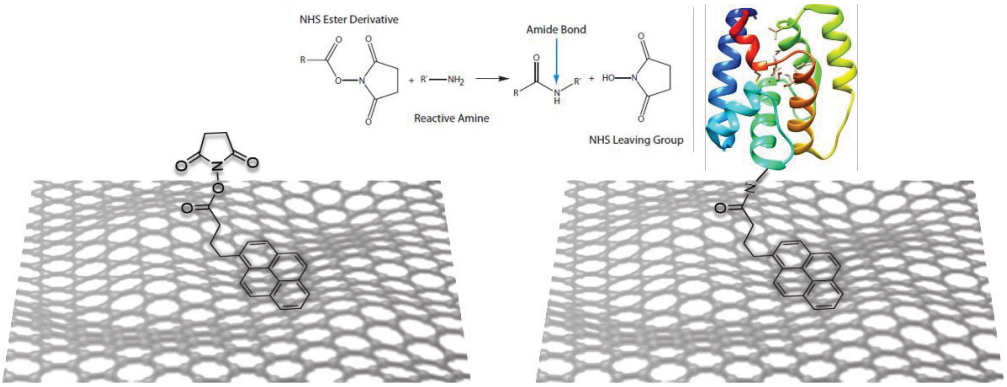

Figure 5: Immobilization strategy used to covalently couple proteins to graphene via a pyrene derivative with an NHS activated ester group that couples spontaneously to the lysine groups of the odorant binding protein. [68]

The same technique can be used for the immobilization of DNA- or PNA capture probe single strands end-functionalized by amine-groups. PNAs might be preferable because they are the charge-neutral equivalent of DNA, allowing for the DNA analytes from solution to hybridize to the surface-immobilized capture probe layer by forming hybrid PNA/DNA double strands just as well (if not better) as DNA/DNA hybrids. However, for electronic or electro-chemical sensing that concept offers the advantage that the off state of the device is neutral; hence, the sensor device experiences upon binding of a (charged) target strand a maximum change in charge density at its surface.

Whichever immobilization strategy will be employed, an important characterization step concerns the receptor layer density at the sensor surface. [69]{Citation} It determines on the one hand side the signal strength; however, on the other hand the optimum density for the best device performance might be reached at a density much lower than the maximum coverage. E.g., the hybridization event between DNA strands from solution to the capture probe brush layer at the FET surface might be self-blocking if too dense.

Non-specific binding events

A new challenge that should be mentioned here in the context of electronic/electrochemical detection concepts is the control and eventual minimization of non-specific binding events of bio-components from real-world analyte solutions (peptides, proteins, DNA, lipids, saccharides, exosomes, membrane fragments etc. from body liquids like plasma, blood, saliva, urine or food samples, waste water, etc.). These would interfere with the signal that originates from the specific recognition and binding of the analyte of interest to the receptor that is specifically immobilized at the transducer surface (receptor molecule, antibodies, capture probe oligonucleotides, etc.). In the case of optical transduction principles, it is generally assumed that the problem is solved by the coating of the sensor surface by a so-called "anti-fouling" layer that prevents the unwanted adsorption of any of the bio-molecules other than the analyte of interest to the transducer surface. Ions are generally not considered because any change in ionic strength or composition at or near the sensor surface does not translate into a measurable (refractive index) change that could interfere with the optical detection signal.

This is fundamentally different for electronic read-out concepts because any (unwanted) change in the ionic milieu of the analyte solution in contact with the electrode of the sensor device that happens within the electrical double layer will interfere with the signal of interest and, hence, needs special attention [65].

Development of anti-fouling coatings

Typically, the control and minimization of the non-specific binding (NSB) of biomolecules other than the analyte of interest from real world samples is typically more difficult and challenging than designing a receptor for the specific interaction with the desired analyte. As a consequence, the whole biosensor community has spent a significant amount of resources to solve this problem by clever chemistries that reduce NSB at the transducer surface. [70]

Different strategies, i.e. the coating of the device by the self-assembly monolayer of suitable, pyrene-functionalized polymer chains and blocking remaining binding sites

with Bovine serum albumin (BSA) as known from ELISA kits can be exploited.[71] A few essential features of polymer brushes relevant for their use as anti-fouling coatings are schematically depicted in Figure 6. The concept of an entropic surface spring is a possible way for anti-fouling coating strategies, by using pyrene-derivatized polyethylene glycol (PEG) or zwitterionic betaine. [72]

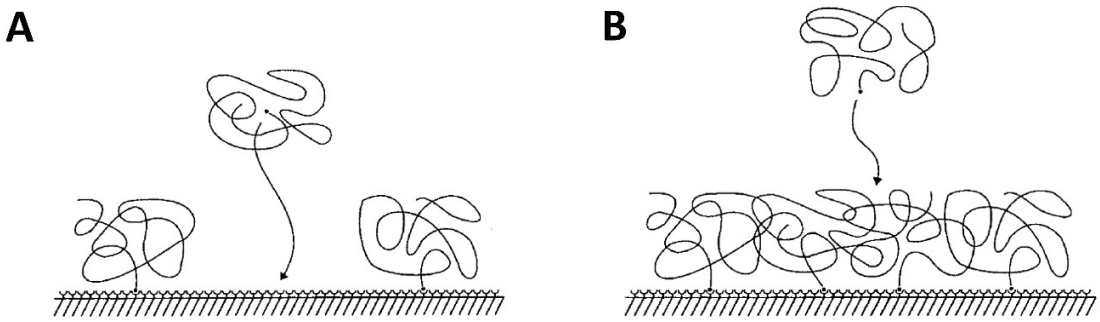

Figure 6: At sub-monolayer coverage (A) free transducer surface invites (bio-) molecules to adsorb. Upon forming a closed monolayer (right panel), the entropic penalty for an additional molecule trying to adsorb leads to the anti-fouling property of the coating. A balance of bio-recognition elements and blocking molecules is required for a selective bio-sensor. [73]

Surface plasmon resonance (SPR) can be used to test the function of these passivation layers. The functionalization of standard Au coated slides as well as slides with and additional CVD graphene layer are suitable for these optical characterization techniques. However, in addition they simulate, physically and chemically, the surface of a graphene field-effect transistor.

As mentioned before, many of the strategies described in the literature for the preparation of anti-fouling coatings are optimized to reduce NSB for optical transduction platforms. [74] Any form of electrical sensing, either electrochemically, electrically or by electronic devices, face different and additional challenges in that other than in the optical case it is not only about controlling (preventing) the adsorption of (large) proteins to the transducer surface, it is about the influence of ions, charges that non-specifically modify the double layer potential at the surface of the electrode, resulting in a response of the sensor that has nothing to do with the analyte of interest.

This provides a general understanding of what “passivation” of an electrical/ electrochemical/electronic transducer means as compared for an optical sensor, the former being extremely sensitive to the presence of charges, like protons and other ions, while an

optical transducer barely responds to the presence of interfacial ions and only monitors the non-specific adsorption of proteins or other biopolymers.

Monitoring binding events/dissociation reactions by gFETs and SPR

A more fundamental understanding of the actual signal generation mechanism of a gFET biosensor that monitors a binding event between a receptor, immobilized at its gate or channel surface and a bio-analyte molecule approaching from solution and binding at some "site" of the receptor can be given by example data.

Experiments were previously reported, making use of graphene FET devices for the detection of food pathogens, monitoring the binding of a test protein, bovine serum albumin (BSA), to the surface immobilized receptor, the anti BSA-antibodies, [64] shown in Figure 7 (A).

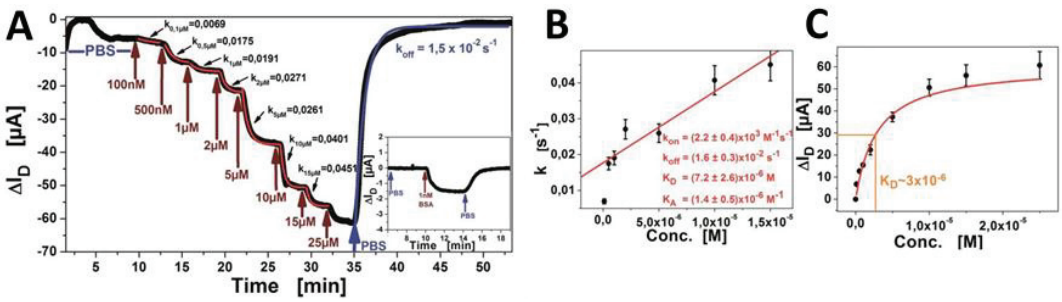

Figure 7: Global analysis of the binding of BSA from solution to an antiBSA-AB functionalized gFET sensor; (a) shows the original data measured after injecting BSA solutions of different concentrations, as indicated by the red arrows, and after rinsing pure PBS buffer though the flow cell (blue arrow); the inset shows the current race after injecting an analyte solution of only 100 nM concentration; (b) Analysis of the rate constants, resulting in kon and koff values for the binding process; (c) Langmuir isotherm of the equilibrium coverage currents, ΔI_{DS}, as a function of the bulk concentration. The figure was taken from Reiner-Rozman et al. 2015. [64]

As one can see, the global analysis, i.e., the combination mode of kinetic Figure 7 (B) and titration experiments Figure 7 (C) allows for the determination of the rate constants of association, k_{on}, as well as for the dissociation process, k_{off}. Both, the kinetic data as well as the titration experiment, i.e., surface coverage versus bulk concentration lead to similar

values for the affinity constant for the reaction, $K_A = 2x10^{-6}\ M^{-1}$, pointing to a Langmuir model describing a fully reversible process. This model as well as the kinetic and equilibrium parameters were very close to the values found by studies with the OFET [75] and by optical techniques. [76] However, assuming that the model and that this affinity constant are correct, indeed, the measurement at 100nM bulk concentration shown in the inset of Figure 7 (A) is remarkable: at this bulk concentration the expected coverage is only 1/1000 of a fully covered antibody layer, yet the change in the source-drain current is clearly seen with an excellent S/N ratio. The combination of the electrical and optical measurement device can yield to a better understanding of the correlation of details of the interfacial architecture, the ongoing processes, and the resulting response of the electric device.

Correlation with electrochemical and optical transduction

Due to the fact, that specific as well as non-specific binding events contribute to the signal generation in biosensors, it can be observed, that different transducing mechanisms, such as electrochemical and optical respond to different interfacial events. Figure 8 exemplifies schematically some of the scenarios in DNA sensing that were investigated in earlier optical studies by SPFS and in parallel by various electrochemical techniques, ranging from cyclic voltammetry, square wave voltammetry and differential pulse voltammetry analysis. [77]

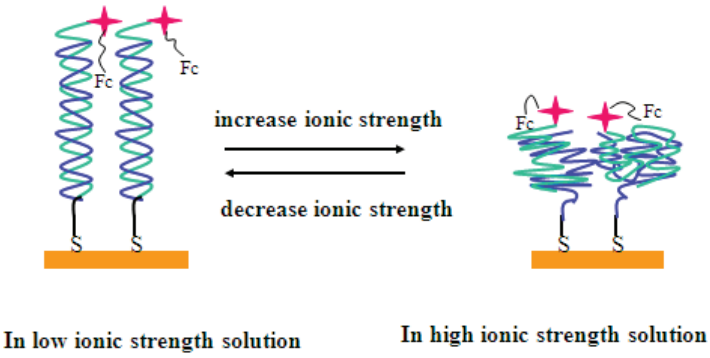

Figure 8: Structural changes for a surface-immobilized DNA double strand upon changing the ionic strength of the surrounding buffer solution. The collapsing DNA strand results in

a quenched optical signal, while the electrochemical active species ferrocene is not influenced, resulting in a constant readout. [77]

Some of the observed effects were related to the (supra-) molecular details of the interfacial architectures, like the length of the capture and target strands, respectively, the packing density of the functional layer, or the intrinsic stiffness of the single-stranded capture and the double-stranded hybrid. Other factors were directly related to the sensing event: in the case of DNA analytes, the recognition and hybridization leads to a significant change in the charge density at the transducer surface. At high capture probe layer density and/or at high coverage this leads to a significant deviation from a simple Langmuir model which is based on the assumption, that all individual binding events are independent from each other and, hence, are also independent from the coverage of the sensor surface. These deviations can have a huge impact on the quantitative evaluation of the measured data. [78] And finally, the ionic buffer solution itself influences the measured signal, e.g., the ionic strength modulates the degree of charge repulsion along the single strand and, hence, the degree of stretching, it might influence via counter ion condensation, and influences the repulsion between probe and target strand.

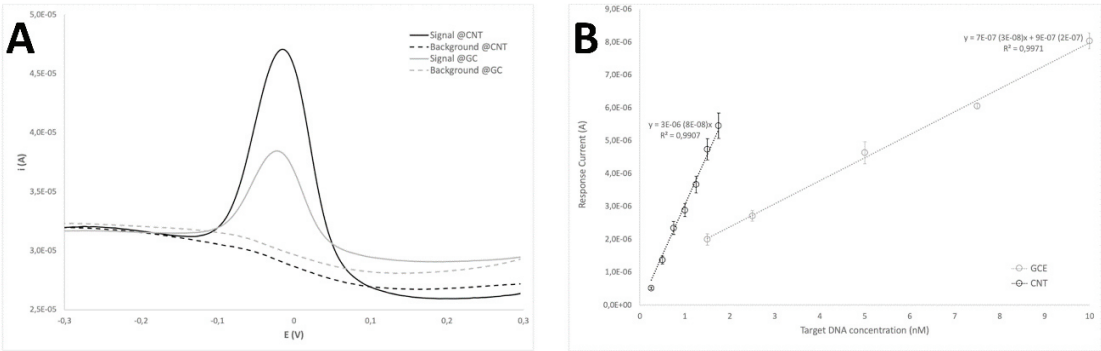

Figure 9: The readout of differential pulse voltammetry (DPV) on two different surfaces is shown in (A). Once the capture probe PNA was immobilized on SWCNT (higher signal) and on glassy carbon electrodes. (B) illustrates the different sensitivities of the surface architecture. The limit of detection (LOT) as well as the dynamic range vary between the two different, but yet carbon based systems. [79]

The comparison with electrochemical techniques, in particular, differential pulse voltammetry, might be particularly enlightening because some of these techniques have reached an impressive level of performance, e.g., in terms of sensitivity. This is shown in Figure 9 which demonstrates the high sensitivity of the differential pulse voltammetry

recordings, taken after surface hybridization reactions between a surface immobilized PNA capture probe layer and the fully complementary charged target binding from solution. Admittedly, though, this is not in real time, hence no kinetic data are obtained, and it required a label, an enzyme at a secondary binding to the target DNA. [79] This represents once more, that small variations in the surface architecture and read-out method lead to different results, although the molecular binding sites are unchanged.

Project Goals

The goal is to develop a label-free detection method for in-situ, real-time and simultaneous electrical and optical read-out of

- Polymer layer-by-layer deposition to compare the systems
- Surface functionalization to obtain the surface coverage
- Aptamer – ligand interactions.

The proposed electronic read-out platform will be based on graphene-field effect transistors, functionalized by capture probes, such as oligonucleotide single strands and aptamer-receptors with the potential for fabrication and commercialization of cheap disposable sensor chips to be used in medical applications, for environmental monitoring and for food and feed quality assessment.

Graphene FETs will be fabricated and optimized, based on previous reported reduced graphene oxide deposition methods. [80] Furthermore, Chemical Vapor Deposition (CVD), [81] will be tested as an alternative for the wet chemical strategy, aiming at higher yields in transistor fabrication and better reproducibility of the devices. The electrical properties of the graphene FETs will be tested by recording the transfer characteristics, the I_DV_G curves, of the semiconducting devise in order to characterize these chips

The focus of this work will be on the use of aptamers, for the detection of analytes and proteins. [82–87] This is a particular promising approach for FET bio-analyte detection because there are several examples in the literature that describe a significant change in the spatial organization of an aptamer upon ligand binding[88] which lead to a massive change in the charge distribution at the surface of the transistor that can be easily detected through the resulting change in the surface double layer potential and its influence on the drain-source current I_{DS}. [64]

gFET sensor performance and stability

A cornerstone of the development of a sensor is its stability and the control of the fabrication process. Herein, the fabrication of the gFET in a most controlled manner will be discussed and the production procedure adapted to hand it over to future researcher who want to utilize the graphene FET in their projects, without limitations.

Combination of gFET and SPR

A bi-modal system for the simultaneous real-time detection of label-free analytes is the aim of this work. The main concept of such a combination is using one flow cell for the analyte injection, consisting of two sensor platforms. While the optical SPR sensor platform consists of modified gold surface, that exhibits an evanescent field on the interface to the probing solution, the electrical FET setup requires a drain-source channel and a gate electrode, whereas the later can be utilized of the SPR surface itself. Therefore, a combined system of electrical and optical read-out can use the same functionalized surface, underlying different transduction mechanisms. As reported, the SPR signal is modulated by the mass uptake on the vicinity of the sensor interface. Local refractive index changes lead to the shift of resonance angle, traceable with photodetectors.

A FET on the other hand, requires changes in the local electrical field, either on the gate electrode or on the drain-source channel. The two separated concepts are shown in Figure 10 (A), where a gold slide is schematically functionalized for SPR measurements and the drain-source channel for the FET read-out. Both substrates are illustrated as graphene substrates, which ultimately leads to a direct comparison of the performance of both transducers and help to understand the functionality of binding events.

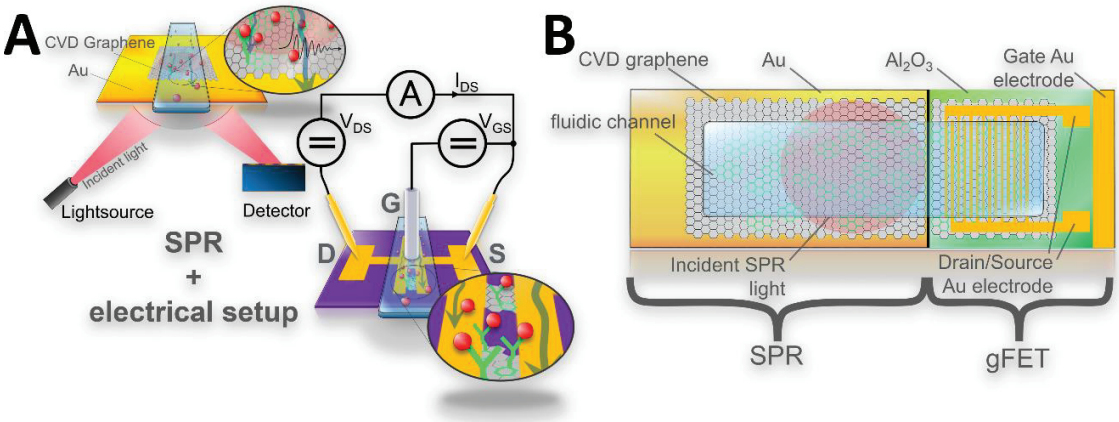

Figure 10: The different measurement systems of SPR and gFET comprise of a similar surface architecture: both have graphene, or rGO as surface layer for bio-functionalization (A). The well understood SPR system can be used compare to the novel architecture of the graphene FET. (B) illustrates one approach to combine the two devices within one flow cell.

Evaluate surface functionalization methods

Beside the combination and the investigation of already established surface modification, other approaches of bio-functionalization will be investigated and reported. The different surface architectures will be Au, Au/CVD graphene and Au/rGO. Beside the immobilization of selective molecules, such as antibodies or aptamers, the blocking of non-specific binding to the surfaces will be investigated and strategies for blocking will be developed. With the same substrate for optical and electrical read-out, graphene, direct comparison is possible and conclusions can be drawn from difference in response. Figure 11 illustrates the functionalization of the drain-source channel of a gFET and the graphene coated gold slide for SPR.

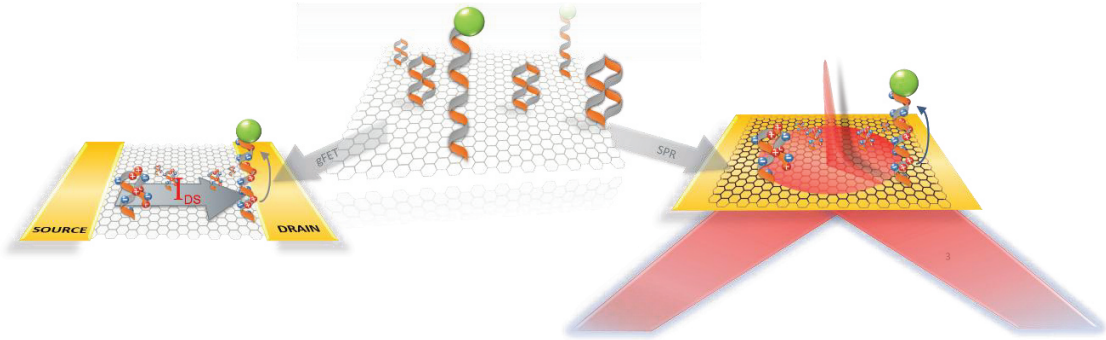

Figure 11: Graphene can be used on the gFET and SPR interfaces. The drain-source current of the FET is modulated upon the specific binding of analytes, inducing changes in the electrical double layer of the sensing area. Using the same sensor substrate graphene both devices yields in an observation tool to verify the electrical with the optical read-out.

Creation of a software tool

The control and record of all measurement during the sensing procedure is an essential component towards a reliable sensor platform. Herein will be the simultaneous recording of multiplexed gFET sensor and/or the combination of gFET and SPR in one software tool demonstrated. This enables the usage of the novel sensor platform for future research groups without a deeper understanding for the required amplification mechanisms of the hardware. The tool requires a well defined graphical user interface (GUI) and plug-and-play properties for a stan-alone device.

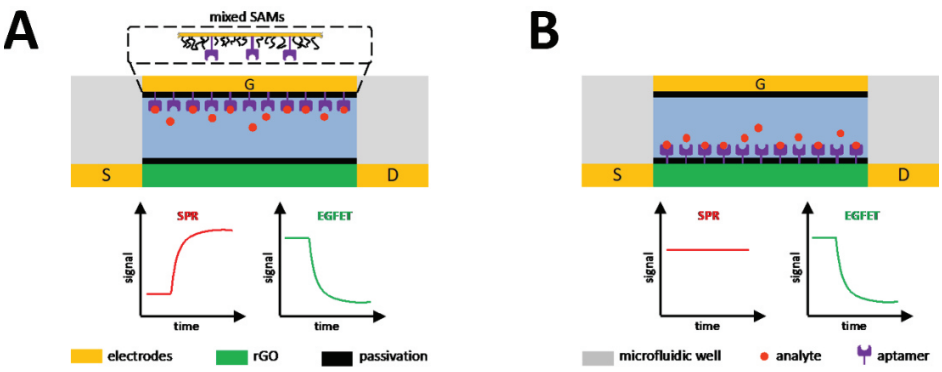

Figure 12: The concept of the combined FET/SPR is schematically illustrated here, where the gate electrode and SPR interface can be functionalized with bio-recognition elements (A), leading to a modulation of both, the SPR and FET signal. In contrary, if functionalizing

only the drain-source channel, the read-out of the SPR signal remains constant, while the FET signal represents the specific binding of analytes

Additionally, a combination of the gFET with SPR, utilizing the SPR slide as gate electrode empowers the exact same surface area for direct comparative measurements, Figure 12 (A). The targeted surface functionalization of either the gate or the drain-source substrate leads to a tunable SPR read-out: in the case of drain-source binding events, the SPR signal remains constant, unless bulk solution changes occur, shown in Figure 12 (B).

2. Chapter:

Fabrication of graphene FETs and gold slides

This chapter shows and fabrication and testing of graphene field-effect transistors, short gFETs. The focus is on the optimization of the processes and standardization to obtain reproducible results when the gFET is used as bio-sensor. Key roles play the graphene substrate, the reduction method and the way it is deposited on the electrode array. Furthermore, the deposition of gold on glass slides is shown, since this work covers the comparison of electrical bio-sensors with the optical SPR technique.

Materials and Methods

In this section, all materials, devices and methods are listed for the production of field-effect transistors with graphene as channel material on glass chips and silicon substrates. The listed materials and chemicals will be used in the following chapters and will not be listed again.

Devices and Materials

- Evaporator FL400 Auto 306 (HHV Ltd.)
- Molybdenum evaporation boats (HHV Ltd)
- 1/16” tube end fittings F 702-38 (Bola)
- 1/16” gripper fittings 002310 (Kinesis)
- 1/16” PTFE tubes 58702 (Sigma Aldrich)
- Peristaltic pump IPC 8 (ISMATEC)
- Valve switch MXX, 10-port (Rheodyne)
- Optical microscope HR800 (Horiba)

- Multimeter 87V True RMS (Fluke)
- SMU 4200 SCS (Keithley)
- SMU 2612B (Keithley)
- SMU U2722A (Keysight)
- µAutolab III (Metrohm)
- SPR device Indicator-G (Sensia)
- Ag wire, diameter 1mm
- Flow cell base ED-AIO-CELL (Micrux)
- Flow cell lid FC-PMMA-3,5 (Micrux)
- Interdigitated electrodes, 10µm channel ED-IDE1-Au w/o SU-8 (Micrux)
- SPE 110SWCNT (Dropsens)
- Monolayer CVD graphene 4 x 12 mm on Cu (Graphenea Inc.)
- Graphene oxide, modified hummers method, (University of Bayreuth)
- Microscope slides H869.1, 76 x 26 x1 mm (Carl Roth GmbH)
- Kapton Tape, (3M)
- Parafilm, (Sigma Aldrich)
- Sonicator ELMSA S180H (Elmasonic)
- Ultimaker S5 (Ultimaker B.V.)
- PVA filament (Ultimaker B.V.)
- PLA filament (Ultimaker B.V.)
- Plasma etching device 5bis (Oxford Instruments)
- Hotplate Sawatec 300 (Sawatech AG)
- UV Lamp 500W
- Raman Spectrometer LabRAM HR, confocal, 515 nm (Horiba)
- NanoDrop 2000 (Thermo Fisher)

Software

- Lua Script editor (individual software)
- Origin Lab 8.5 (OriginLab corporation)

- Sm Stream Basic (Olympus)
- Smart SEM V05 (Zeiss)
- Nova 2.1 (Metrohm)
- Cura 3.6 (Ultimaker B.V.)
- Labview™ 2016, (National instruments)
- gFET measurement utility (self made)
- SPR wasplas (Univ. Mainz)
- LabSpec (Horiba)
- Image J (NIH)

Chemicals list

- Hydrazine monohydrate, reagent grade, 98% (Sigma Aldrich)
- (3-Aminopropyl)triethoxysilane, 97% (Sigma Aldrich)
- Triethoxyphenylsilane, deposition grade, ≥ 98% (Sigma Aldrich)
- 1-Pyrenebutyric acid N-hydroxysuccinimid ester, 95% (Sigma Aldrich)
- 1-Pyrenecarboxylic acid, 97% (Sigma Aldrich)
- Streptavidin−Alkaline Phosphatase from Streptomyces avidinii (Simga Aldich)
- Tetrabutylammonium fluoride (TBAF)
- Ferrocenemethanol
- Copper(II) sulfate ($CuSO_4$)
- L-ascorbic acid
- EDTA
- N-butylhexafluorophosphate (NBu_4PF_6)
- 4-((triisopropylsilyl)ethylenyl)benzenediazonium tetrafluoroborate (TIPS-Eth-ArN_2^+)
- Hellmanex™ III (Sigma Aldrich)
- DMF (Sigma Aldrich)
- THF (Sigma Aldrich)
- DMSO (Sigma Aldrich)

- DCM (Sigma Aldrich)
- Slygard 184 PDMS (Sigma Aldrich)
- DTSP (Sigma Aldrich)
- H_2O_2 30% (Sigma Aldrich)
- NH_4OH 30% (Sigma Aldrich)
- Isopropanol (Sigma Aldrich)
- Ethanol, analytical grade (Sigma Aldrich)
- Poly(ethylene glycol) bis(3-aminopropyl) terminated (Sigma Aldrich)
- Biotinylated Alkane-PEG, SPT-0012D (Sensopath)
- DithiolalkanearomaticPEG3-OH, SPT-0013 (Sensopath)

Graphene source

Two different strategies for the production of gFETs are shown in this section. The difference between these methods is the source of graphene:

- Reduced graphene oxide
- Chemical vapor deposition graphene

The cleanest way to create a gFET is using the pure chemical vapor deposited graphene, short CVD graphene, which grew under high temperatures from a carbon source gas, e.g. ethane or methane, on copper. The second approach is a bulky, but fast and cheap approach of producing gFETs, using a water-soluble graphene oxide, deposited on the substrate and further reduced to reduced graphene oxide, short rGO. The here evaluated source for CVD graphene is the monolayer graphene on 12 mm Cu-disks from Graphenea Inc., shown in Figure 13 (A). The source of graphene oxide is the University of Bayreuth, depicted as four different dilutions in Figure 13 (B). [89]

Figure 13: (A) CVD graphene from Graphenea Inc. on copper discs with 12 mm diameter. (B) Synthesized graphene oxide from the University of Bayreuth, Germany. The GO solution was produced from graphite flakes with the modified Hummers [89]method.

Both graphene substrates are deposited on electrochemical sensor chips, commercially available from Micrux Technologies. The layout of the sensor chip consists of two interdigitated electrodes, which will be used as drain and source electrodes of the gFET. The size of the electrodes is 10 µm with a distance of 10 µm and 90 pairs in a 3.5 mm circular arrangement The deposition methods of CVD graphene and graphene oxide are shown in Figure 14 and Figure 16. Furthermore, the reduction of rGO is shown in the illustration to obtain a semiconducting material in the drain-source channel. Before either CVD graphene or rGO can be deposited on the surface, each chip has to be cleaned and covered with a self-assembly monolayer (SAM).

Preparation of the surface

a. RCA clean: SC-1 (organic + particle cleaning)

Microelectrodes (ED-IDE1-Au w/o SU8) from Micrux Technologies are cleaned by submerging in a glass beaker with 5 parts deionized water, 1 part ammonia solution (30% NH_4OH) and 1 part hydrogen peroxide (30% H_2O_2) (e.g. 50mL dH_2O + 10mL NH_4OH + 10mL NH_4OH). The glass beaker is heated to 80 °C in a water bath on the heating plate. During 15 min, all organic residues are removed from the gold and glass surface. Each chip will be then taken with a tweezer, rinsed thoroughly with dH_2O, then with absolute EtOH and blow dried with compressed air and put into a plastic Petri dishes.

b. Self-assembly monolayer deposition

For the attachment of graphene oxide and CVD graphene, the surface of the microelectrodes is being functionalized with (3-Amino-propyl)triethoxysilane (APTES) for GO or Triethoxyphenylsilane (TEPS) for CVD graphene. For this, a 2 % APTES or TEPS solution is prepared in absolute EtOH (15 mL EtOH, 0.3 mL APTES/TEPS), handling the bottles under argon to avoid exposure to oxygen. It is necessary to work in plastic dishes, because the silane attaches to glassware. The solution is poured over the chips in the plastic Petri dish and incubated in ambient conditions for 1 hour to allow the formation of a self-assembled monolayer (SAM). Subsequently, the electrodes are rinsed with absolute EtOH to remove surplus silane. It is important to not point the jet of the washing EtOH directly onto the sensing area and carefully blow dry with compressed air. All chips are placed in a glass petri dish to withstand 120 °C.

c. Annealing of the silane SAM

The glass petri dish with all chips is placed in an oven at ambient pressure and 120 °C for 2 hours, to anneal the APTES or TEPS respectively on the surface. There is no rinsing or cleaning before the deposition of GO or CVD graphene.

The interdigitated electrodes are coated with a linker for either GO or CVD graphene and the deposition is followed immediately.

Fabrication of CVD graphene FET

After the glass substrate with interdigitated electrodes is prepared with a triethoxyphenylsilane SAM, the CVD graphene can be deposited to connect the drain and source electrode for a gFET. The schematic of the wet-transfer process, starting CVD graphene on a thin copper foil, is shown in Figure 14.

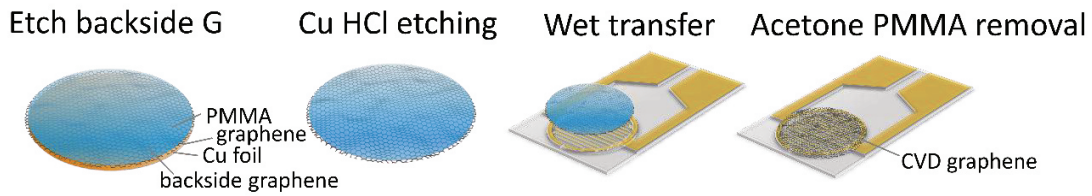

Figure 14: The process of deposition of CVD graphene on a glass substrate with interdigitated electrodes. First the backside of the copper disc is plasma etched to remove residual graphene, then the copper foil is etched in a diluted hydrochloride solution. The remaining graphene, supported by a PMMA layer is transferred to the chip and annealed for 30 min at 90 °C. The PMMA is removed in the final step.

CVD graphene deposition steps:

1. O2 plasma etching (back of the sample)

   50 W/100mT/25sccm/1 min

2. Etching of Cu foil

   Cu foil floating in a solution of HCl 2 ml /H_2O_2 2 ml and /H_2O 250 ml for two days

3. Transfer onto the host glass substrate
   - Transfer the floating PMMA/graphene to clean dH_2O water two times.
   - Place the sample under the floating PMMA/graphene
   - Lift the sample and contact the PMMA/graphene from below on one edge
   - Remove under gentle nitrogen flow the residual dH_2O
4. Annealing of CVD graphene to substrate
   - Start Sawatec 300, hot plate
   - Run annealing program as shown in Figure 15

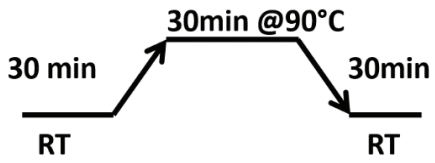

Figure 15: Annealing step after the deposition of the CVD graphene.

5. Remove PMMA protective layer
   - UV exposure (power 500Watts, lamp current 25 V) for 30 min
   - Immerse the chip in acetone for 30 min at 30 °C
   - Remove chip under continuous rinsing with acetone to avoid contamination

- rinse the substrate with isopropanol thoroughly.
- Gently dry under nitrogen flow

The CVD graphene is now deposited on the electrodes and ready for electrical characterization or bio-functionalization.

Fabrication of reduced graphene oxide FET

Subsequently to the cleaning and silanization of the surface with APTES, the graphene oxide is drop casted onto the interdigitated electrodes. The deposition of graphene oxide and the reduction process is shown in Figure 16.

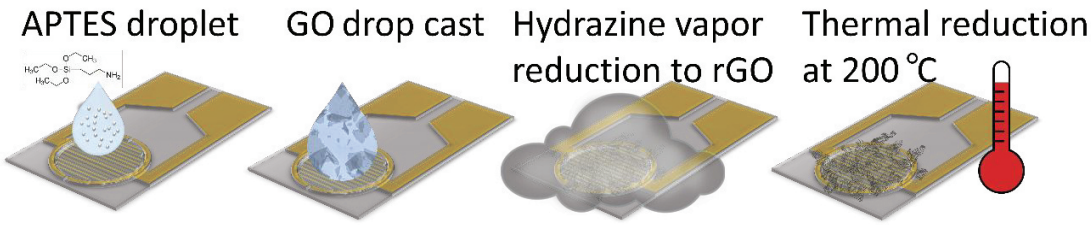

Figure 16: The deposition of graphene oxide starts with a self-assembly monolayer of APTES. Subsequently, the graphene oxide in a diluted dH_2O is drop casted onto the substrate. After a rinsing and baking step for one hour at 120 °C, the GO is reduced to rGO in hydrazine vapor for 4 hours. A thermal reduction afterwards increases the stability of the rGO gFET.

a. Preperation of GO solutions

The graphene oxide used for the deposition on the interdigitated electrodes was the GO from the University of Bayreuth. [89] The concentration of the GO solution is 4.28 mg/mL according to concentration measurements of the produced solution from Bayreuth 2017. Four different dilutions were prepared to determine the best GO solution concentration: 50 µg/mL, 25 µg/mL, 12.5 µg/mL and 6.25 µg/mL in dH_2O. After the measurements with the produced gFETs, Chapter 2: Graphene oxide concentration determination ,the optimized concentration of 12.5 µg/mL was used to produce gFETs.

b. GO drop casting

The GO suspensions are applied by a drop cast method onto the chips. For this, a drop of 15 µL of GO suspension is pipetted onto the interdigitated electrodes of the chips,

allowing the GO flakes to attach to the APTES layer for 2 hours precisely. The time is very crucial to form a uniform layer on the sensing area. Subsequently, the surplus GO suspension is rinsed off with dH_2O, not directing the jet onto the array area and carefully blow-dried with compressed air.

Reduction of graphene oxide

a. Hydrazine reduction

All GO-modified chips are placed in the center of a glass Petri dish for chemical reduction. Because of the carcinogenic properties of hydrazine, it is important to work under the fume hood at all time and treat the waste with special care. 1 mL of hydrazine is pipetted into the corners of the glass dish, while the chips are all placed in the center. Immediately, the lid is sealed air-tight with Kapton tape right afterwards and the dish is placed in the oven inside the fume hood at 80°C for 4 hours.

After reduction, the petri dish remains in the fume hood without lid for 1 hour to evaporate the remaining hydrazine before rinsing each chip with dH_2O and subsequently with isopropanol to remove hydrazine residues. Gently blow-dry and store the chips in a desiccator or directly perform the thermal reduction.

b. Thermal reduction

For thermal reduction, chips are placed in a pre-heated oven at 200 °C under vacuum for 2 hours. This leads to a more stable and reliable electrical chip performance. The chips are taken out of the oven after 2 hours and cooled down to room temperature. The resistance of the chips is measured with a Fluke multimeter immediately after reduction. The chips are stored in a desiccator at vacuum until further functionalization and measurement.

Optimize graphene oxide concentration

The graphene oxide concentration of 4.28 mg/mL in dH_2O is too high for the deposition of monolayer graphene on the surface, therefore it needs to be diluted. To optimize the properties of the rGO field-effect transistors, different GO solutions were

prepared and deposited on the substrate, according to the protocol in Chapter 2: GO drop casting. The criteria for a good field-effect transistor for bio-sensing are manifold:

- Flakes need to connect the drain-source electrodes
- Presence of semiconductive properties (transfer characteristic)
- Single- or few-layered graphene deposition
- High mobility of the finally produced gFET
- Linear dependency to environment changes (pH, ionic strength)
- Low ohmic resistance to avoid gate leakage current

Four different concentrations were drop casted on the gFET and judged according to these criteria.

GO reduction measurement setup

The reduction of the insulating material graphene oxide to the semiconductive rGO is a crucial component in the fabrication of rGO gFETs from GO as base material. The connection of the drain and source electrode with rGO flakes only leads to a semiconducting material, suitable for bio-sensing, because the unreduced GO itself can't be used for electrical measurements. The reduction of GO was carried out in two steps: The first hydrazine vapor reduction [80] and subsequently thermal reduction [90]. Both fabrication steps are explained in detail in Chapter 1: GO drop casting.

The change of conductivity as indicator for the success of the reduction was measured in real-time during the reduction. For that purpose, a measurement set-up was created with a source measure unit (SMU). Two wires were soldered to the two electrodes of the interdigitated Micrux chip and a constant voltage of 10mV was applied by the SMU. The drain-source current I_{DS} was measured throughout the entire reduction procedure and should increase in case of a reduction of the graphene oxide. The measurement was carried out during the hydrazine vapor reduction and thermal reduction. The conductance of the rGO is calculated with eq 3 $G_{DS} = \frac{I_{DS}}{U_{DS}}$ eq 3conductance, which is the reciprocal of Ohm's law

$$G_{DS} = \frac{I_{DS}}{U_{DS}} \quad \text{eq 3}$$

where G_{DS} is the calculated drain-source conductance, in S or 1/Ω, I_{DS} the measured drain-source current, in A and U_{DS} the applied drain-source voltage in V.

Fabrication of gold slides for SPR

Gold coated glass slides for SPR measurements were prepared in house. Microscope slides H869.1 from Carl Roth GmbH with dimensions 76 x 26 x 1 mm were used as base material for the optical measurement experiments. The slides were cut in 20 x 26 mm pieces with a ruler and a diamond cutter to make them suitable for the prism in the SPR device. The slides were immersed in a 2% Hellmanex™ III solution and sonicated for 15 minutes. Subsequently, the slides were immersed in dH_2O and after in analytical grade ethanol. each time sonicated for 15 minutes. The evaporator Auto306 Lab Coater from HVV Ltd. was used to coat the slides with 2 nm chromium as an adhesion layer and subsequently with a 50 nm gold layer, which is suitable for the excitement of plasmons on the surface, necessary to perform SPR experiments.

Preparation of buffer solutions

<u>Measurement buffer PBS:</u>

PBS 1x: 1 Phosphate buffered saline tablet dissolved in 200 mL dH_2O

PBS 0.1x: 1 Phosphate buffered saline tablet dissolved in 2000 mL dH_2O

<u>Activation Buffer:</u>

MES buffer: 0.1 M MES (pH adjusted to 5 with NaOH)

<u>Immobilization buffer (CB):</u>

Carbonate buffer: 0.1 M $NaHCO_3$, 0.1% w/v SDS (pH adjusted to 9 with NaOH)

<u>Hybridization buffer</u>

0.3 M NaCl, 0.02 M Na2HPO4, 0.1 mM EDTA (pH adjusted to 7.4 with HCl)

<u>Tris buffered saline (TBS):</u>

0.1 M Trizma® base, 0.02 M MgCl2 (pH adjusted to 7.4 with HCl)

TBS-T: To obtain a TBS washing buffer, 0.05% of Tween 20 were added

Reading buffer" (RB):

0.1 M Trizma® base, 0.02 M MgCl2 (pH adjusted to 9.8 with HCl)

Gate Capacitance C_i:

There are a few parameters describing the performance of a gFET, determining the output performance as sensor. While the length L and the width W are given dimensions of the FET layout and V_{DS} is the driving voltage applied to the drain-source channel, the gate capacitance C_i needs to be determined to further characterize the gFET and to calculate the mobility (Chapter 2: Mobility calculation). Cyclic voltammetry (CV) was used to obtain the gate capacitance C_i in a liquid gated FET system. A flow cell was assembled with a chloride-coated gate electrode (Chapter 4: Flow cell 1: micro fluidic design) and the graphene coated IDE1 chip from Micrux. The current was measured during a voltage sweep in a two-electrode configuration, with the gate electrode as WE and both electrodes of the IDE1 chip connected to CE and RE. CV scans at different scan rates were performed, and the resulting currents at each scan were used to determine the gate electrode capacitance. The linear fit of the slope of the plotted currents (Ampere) versus scan rates (Volts/sec) results in the gate capacitance C_i, according to the definition of current in Ampere (A) and the capacitance in Faraday (F), derived for the equations of the units:

$$Ampere: A = \frac{Q}{s} \qquad \text{eq 4}$$

$$Faraday: F = \frac{Q}{V} \qquad \text{eq 5}$$

$$slope_{CVscans} = \frac{A}{V/s} = \frac{Q/s}{V/s} = \frac{Q}{V} = F \qquad \text{eq 6}$$

When replacing the ampere in eq 6 by eq 4, it can be shown, that the slope corresponds to the capacitance of the system. The value for Ci is important for the further calculation of the mobility μ of graphene.

Mobility calculation

The reported ambipolar properties of reduced graphene oxide and CVD graphene can be observed in the transfer characteristic of a graphene-based FET. [91] To evaluate and

compare the resulting data with other graphene sources and fabrication methods, an intrinsic parameter, the mobility of the material can be calculated. Graphene has remarkable electron and hole mobilities at room temperature and this parameter can be calculated for different architecture of the graphene field-effect transistors and the applied drain-source voltage V_{DS}, using eq 7:

$$\mu_{eff} = m_{lin} \cdot \frac{L}{W \cdot V_{DS} \cdot C_i} \qquad \text{eq 7}$$

where m_{lin} is the slope from the linear fit (change of I_{DS} per V_G), L and W the channel length and width, respectively, V_{DS} the applied drain-source voltage and C_i the gate capacitance. [92] The mobility μ_{eff} represents the hole mobility of the substrate on the negative slope (left), while the electron mobility can be determined from the positive slope of the graphene FET I_DV_G curve. This ambipolar behavior cannot be found in classical metal-oxide FETs (MOSFETs) and gives graphene a unique property as a device with a zero-bandgap architecture. The herein reported FET architecture has a channel length L of 10 µm (drain-source distance), a width W of 490 mm (accumulation of all opposite drain and source electrodes) and a measured gate capacitance C_i of 3.3 µF. The linear fit was obtained from the p- and n-type regimes of the I_DV_G curve, giving the value for m_{lin}.

Results of gFET fabrication

All measurements for the fabrication and optimization of the graphene FET with CVD graphene and reduced graphene oxide are shown in this chapter. The characterization of the gFET was done electrically with I_DV_G curves, $I_D(t)$ measurement to observe the baseline drift, SEM, RAMAN and AFM experiments. The optical density (OD) of different GO solutions were measured with an OD-meter and the results of the image processing software to determine the rGO surface coverage is shown here.

Scanning electron microscope images of graphene

SEM images were recorded to determine the nanostructure of graphene flakes, verify the coverage of the drain-source channel with graphene and to observe the covered sensing area. Figure 17 shows the drain-source channels covered with CVD graphene. In Figure 18, the rGO flakes forming the sensor channels are shown. The SEM images of a gFET after 16 hours of hydrazine reduction are shown in Figure 19, where defects in the rGO substrate can be observed. A possible reason for the defects is the extensive reduction time in hydrazine vapor. This observation leads to an investigation of the minimum reduction time for the here used graphene oxide. Chapter 2: Real-time reduction measurements illustrates the conductivity increase of rGO in real time, indicating the minimum reduction time required to obtain a working gFET device.

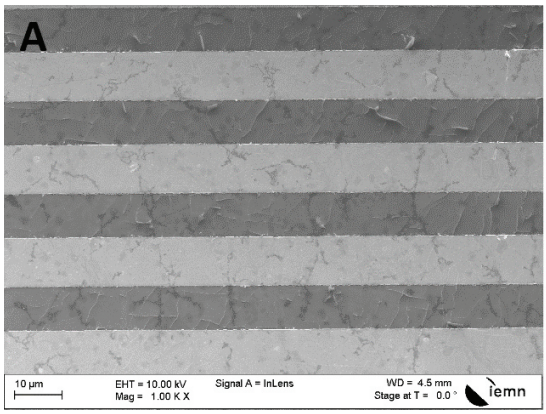

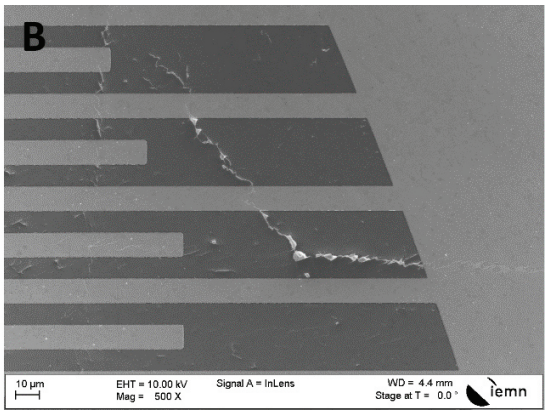

Figure 17: SEM images of CVD graphene on interdigitated electrodes. (A): full coverage of drain-source channel at magnification of 1,000x. (B): crack in CVD graphene at edge of electrode array, magnification 500x

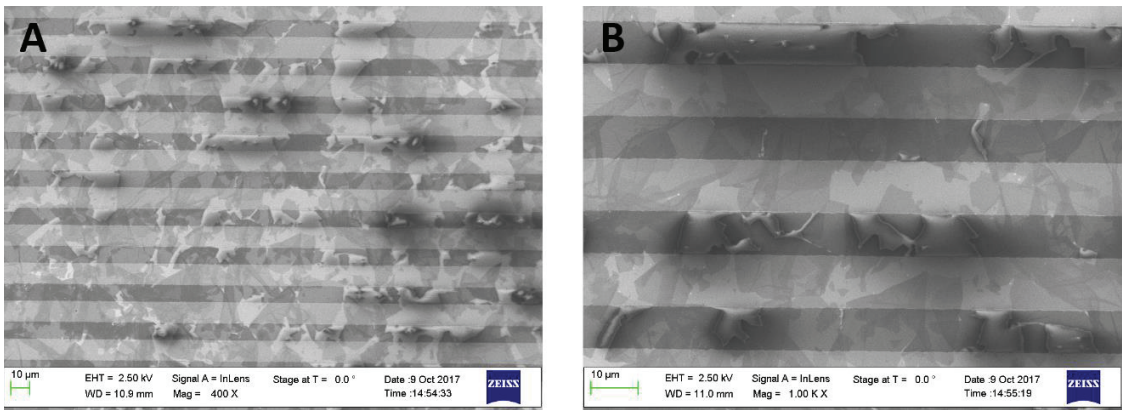

Figure 18: SEM images of reduced graphene oxide after 4 hours of reduction. (A): spread coverage of interdigitated electrodes, magnification 400x. (B): visible double layers of rGO flakes when they overlap, magnification 1,000x

The SEM images in Figure 17 and Figure 18 allow a comparison of CVD graphene and rGO. Both graphene sources with the herein reported deposition methods are forming a conductive drain-source channel, but exhibit significant morphological differences. The deposited CVD graphene consists of a uniform graphene sheet, only interrupted by minor cracks on the surface. The rGO consists of flakes in a dimension between 3 and 30 µm due to the exfoliation process of the GO. The concentrations or rGO flakes needs to be above the percolation threshold to guarantee a drain-source connection.

The rGO images were taken after the reduction of 4 hours in hydrazine vapor. After the reduction in hydrazine vapor for more than 16 hours, the graphene sheets suffered from damages in the rGO lattice, leading to the formation of holes in the rGO flakes, shown in Figure 19.

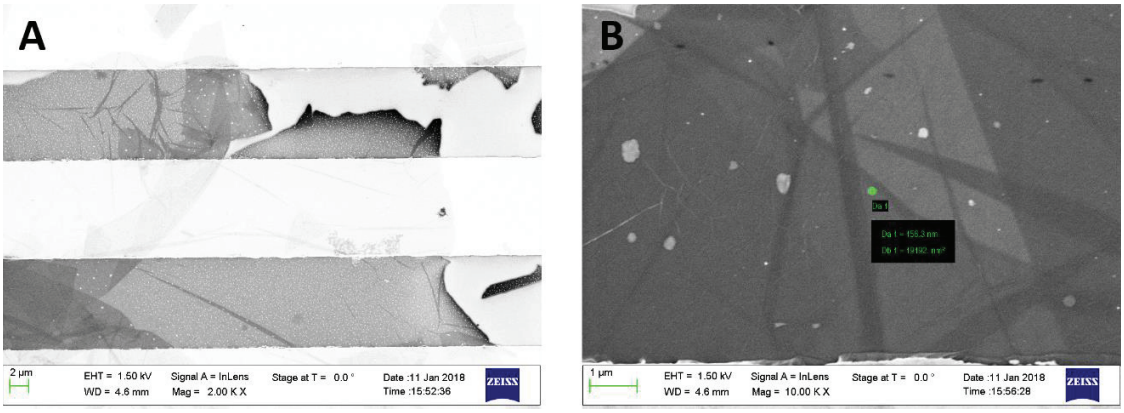

Figure 19: SEM images of defects in reduced graphene oxide after reduction for more than 12 hours. Defect size approximately 100 nm to 200 nm. A: rGO flakes covering the interdigitated electrodes, magnification 2,000x. B: defect holes in rGO flakes, magnification 10,000x

Real-time reduction measurements

The measured drain-source current I_{DS} was logged during the reduction of graphene oxide. The resulting increase of conductance is shown in Figure 20. The hydrazine vapor reduction and thermal reduction are recorded subsequently on the same chip and the increasing conductivity indicates a successful GO reduction. The hydrazine vapor reduces the GO within the first hour to approximately 75% of the final conductance. After 3 hours, the reduction reaches its peak and the conductance decreases slightly afterwards. This is either caused by the decrease of hydrazine in the vapor chamber or the formation of damages in the rGO. After 4 hours, the chip reaches a plateau of conductance and after 8 hours the chip was removed from the hydrazine vapor reduction oven.

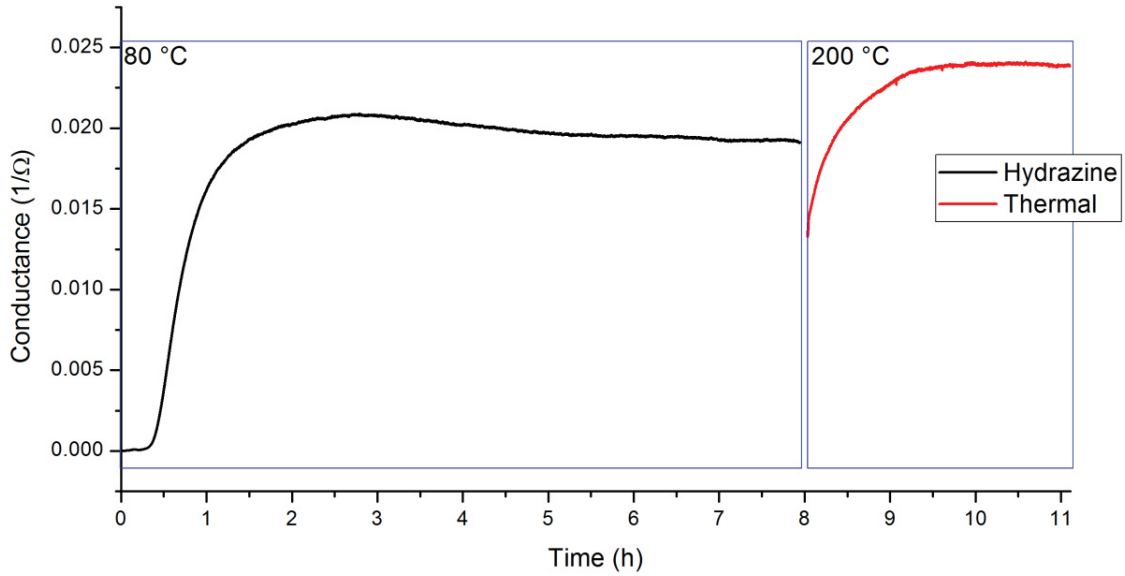

Figure 20: The reduction of graphene oxide measured in real time. The conductance increases during the reduction process, indicating the successful reduction to rGO. First, the graphene oxide on the interdigitated electrodes was reduced for 8 hours in hydrazine vapor at 80 °C, subsequently the same chip was thermally reduced at 200 °C under vacuum for 3 hours to obtain the minimum reduction time.

Due to the decrease of temperature and the absence of hydrazine, the conductance dropped between significantly before the thermal reduction, but during the thermal reduction, the conductance increased again and remained at this level. The hydrazine and thermal reduction sequence is important. Experiments with the inversed order lead to a dramatically lower outcome conductance and were therefore not further investigated.

Raman spectra of rGO and CVD graphene

The results of Raman spectroscopy of the produced CVD graphene and rGO FETs are shown in Figure 21. The CVD graphene shows a distinct 2D peak that determines a pristine and single layer graphene [93]. The background measurement was performed on the bare electrode substrate. It is only possible to observe a reduction of graphene oxide in a comparative study. The graphene oxide was measured after deposition on the interdigitated electrodes and again after the reduction with hydrazine. The ratio of D and G bands unveil the successful reduction when the ratios are compared. This is in agreement with previous reports of the rGO FET fabrication. [64]

GO: $D/G_{GO} = 0.99$

rGO: $D/G_{rGO} = 0.85$

CVD: $2D/G_{CVD} = 2.23$

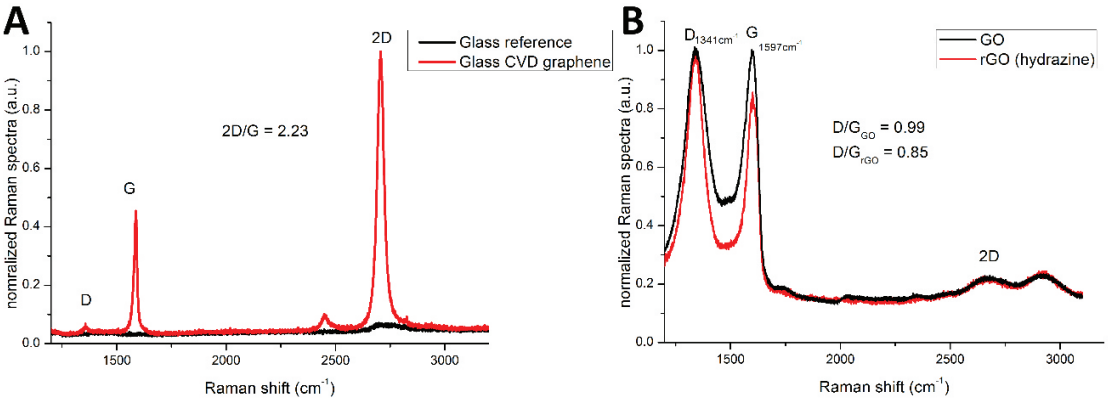

Figure 21: The Raman spectra of CVD graphene and reduced graphene oxide, recorded with a Raman spectrometer and a laser wavelength of 515 nm. A: The CVD graphene after deposition on the electrode surface shows a strong 2D band, representing a monolayer graphene. B: The reduction of graphene leads to a decrease of the G band, observable in the comparison with the graphene oxide.

AFM measurements of graphene

For topographical information of the reduced graphene oxide, Kelvin probe force–microscope, short KFM and atomic force microscope images were recorded at the Technical University of Vienna by Patrick Mesquida. The images in Figure 22 show the KFM and AFM representations of the rGO surface and the electrodes. The KFM image (A) gives information about the work function of the material and it can be observed, that the rGO is homogeneously reduced, while the black spot in the middle indicates the uncovered, non-conductive glass substrate. The AFM image (B) measures the height profile of the surface and indicates, that the graphene sheets are approximately two to three layers thick. [94]

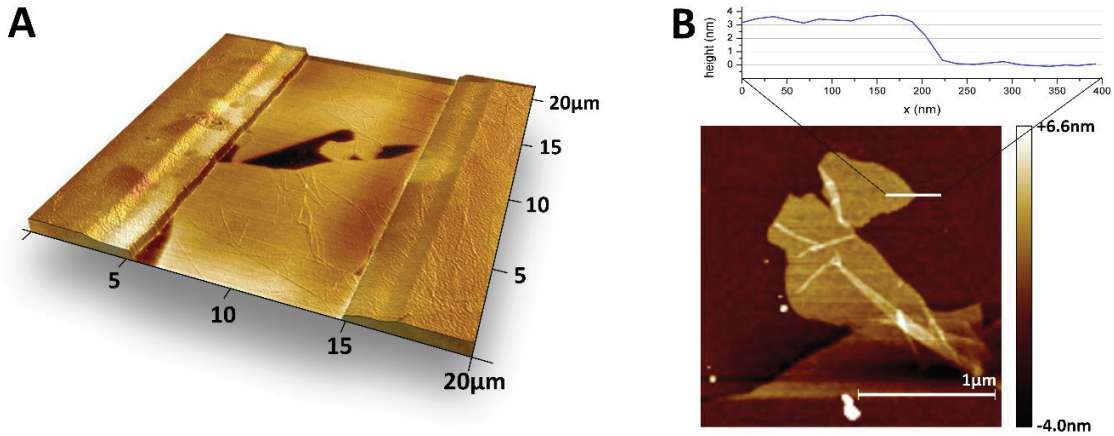

Figure 22: Topographical images of the reduced graphene oxide surface. A: KFM image of the interdigitated electrodes covered with rGO. The KFM image is a representation of the work function of the surface and shows that the rGO flakes are homogeneously reduced. The black spot in the middle is the uncovered glass slide. B: precise AFM images show the height of the graphene sheets and the recorded profile of one flake leads to the assumption, that the flakes consist of about two to three layers of graphene. [94]

Graphene oxide concentration determination

The results of the graphene coverage evaluation between the drain-source coverage is based on two important parameters: knowing the concentration of the graphene oxide solution beforehand and SEM imaging after the deposition. This is a controlling loop and can cause iterative adjustments to obtain little chip to chip and batch to batch variations. The concentration with the best sensor performance has to be evaluated and will be used for the gFET production afterwards.

Nanodrop OD measurements

For a reproducible gFET production with reduced graphene oxide, it was necessary to measure the dilution from the stock solution with an optical density measurement tool. The NanoDrop 2000 OD is capable of measuring the absorbance from 250 nm to 700 nm. The spectrum of four different GO concentrations is shown in Figure 23 (A). At the wavelength 298 nm, the GO absorbance has its maximum and the peak can be used to determine, if the created dilution contains the necessary concentration for the gFET

fabrication. From the absorbance at 298 nm, a fitting curve was calculated and is shown in Figure 23 (B). The fitted curve follows a linear function, written in eq 8:

$$c = \frac{Absorbance + 0.00396\ \mu g/ml}{0.01949} \qquad \text{eq 8}$$

where c is the concentration of GO in µg/mL. The measured value of the absorbance from the NanoDrop 2000 can be filled into the equation to calculate the concentration of the prepared GO solution in dH_2O. The desired concentration can be adjusted according to the result of the calculation.

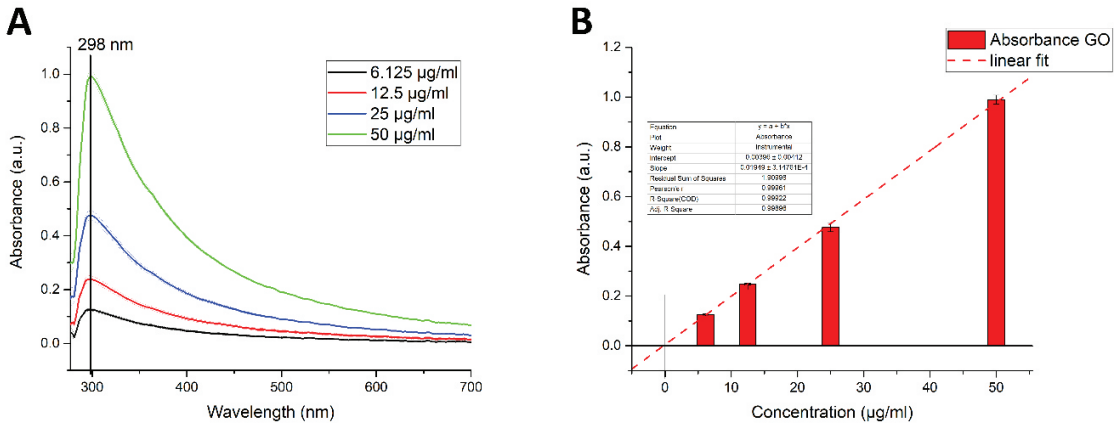

Figure 23: The NanoDrop 2000 measures the absorbance of solutions. It is used to determine the graphene oxide concentration in dH_2O. A: Spectra of four different GO concentrations with a maximum absorbance peak at 298 nm. B: Linear fit of measured GO absorbance. The linear equation can be used to determine the GO concentration of any given dilution.

SEM image evaluation

Scanning electron microscope images were recorded to obtain the dispersion of rGO flakes on the interdigitated electrodes after the reduction. Four different GO concentrations were prepared and drop casted onto the electrodes, described in Chapter 2: Fabrication of reduced graphene oxide FET. The SEM images of the four different dilutions casted on the chips are shown in Figure 24.

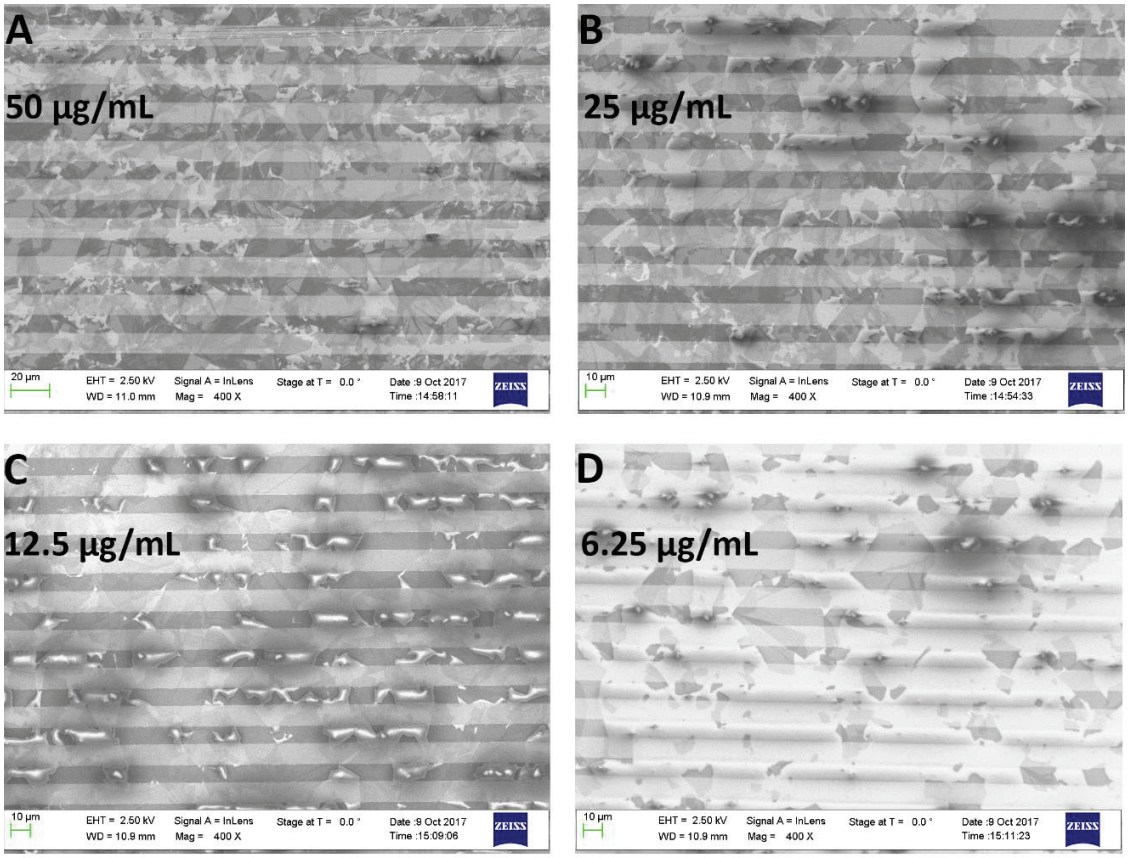

Figure 24: The SEM images of the interdigitated electrodes with different surface coverages at four different concentrations of GO solutions. All SEM images have a magnification of 400x and show the density of rGO flakes. A and B: densely packed rGO flakes. C: rGO flakes connect the drain and source electrodes, but minor overlap of different GO sheets. D: The rGO concentration is very low and connects the electrodes partially.

The SEM images show, that the rGO covers almost the entire surface at GO concentrations of 50 µg/mL and 25 µg/mL. There are many overlapping sheets leading to a multilayer formation. The dilution of 12.5 µg/mL covers the drain-source channel but has little overlapped sheets. Dilution 6.25 µg/mL is loosely packed on the surface, leading to a poor connection between the 10 µm distant electrodes.

The software tool Image J form NIH was used to determine the coverage of rGO in the gap between the electrodes. Figure 25 shows the evaluation of the SEM image with the analysis function of the software. The threshold in the grayscale values was used to distinguish between the uncovered glass slide, a single graphene sheet and more-layered graphene sheets.

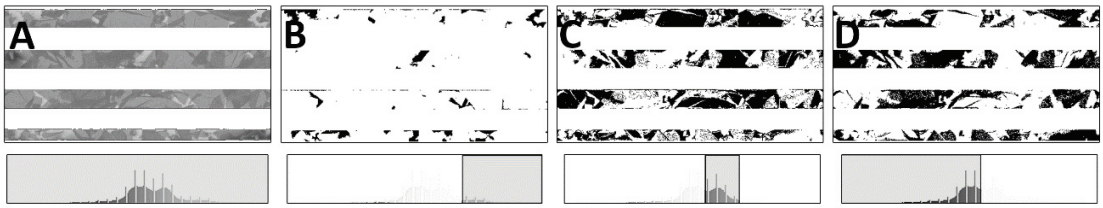

Figure 25: The images represent the graphical analysis to determine the coverage of rGO on the gFET surface with a drop casted GO concentration of 50 µg/mL. (A): section of SEM image with grayscale histogram below, 400x magnification. (B): The grayscale was adjusted to determine the uncovered glass slide. (C): Single layer graphene sheets. (D): represents the double layered graphene sheets.

The drain-source channel was evaluated with the graphics tool ImageJ and it leads to the coverage as shown in Figure 26.

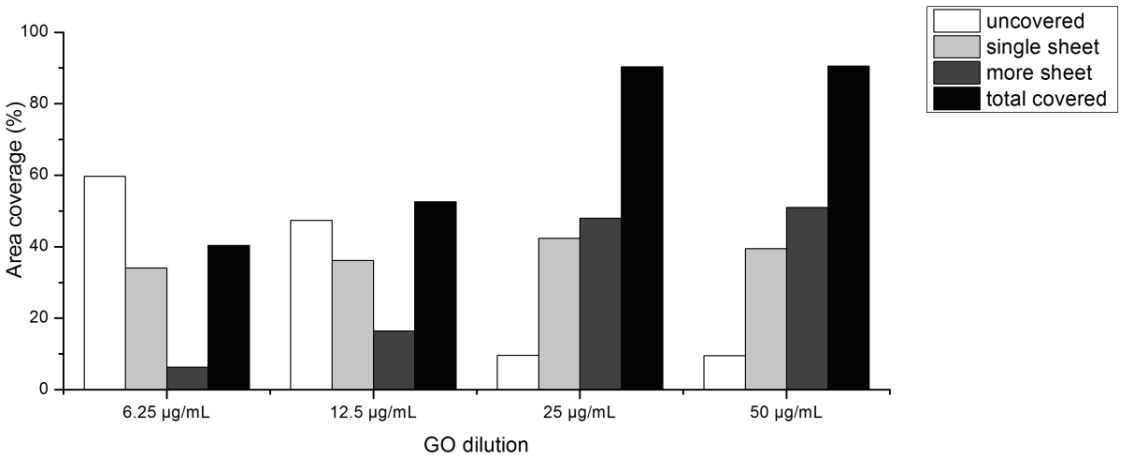

Figure 26: The channel between drain and source electrode was evaluated with the graphical software tool Image J to determine the rGO coverage. Different GO concentrations were deposited on the gFET to determine the best properties for bio-sensing. It can be seen, that the concentration of 50 µg/mL and 25 µg/mL cover more than 90% of the channel surface, but this leads to more than 50% of double layered graphene sheets. At 25 µg/mL, around 50% of the channel are covered and the single layer graphene sheets exceed the double layered. At a low GO concentration of 6.25 µg/mL, only 40% of the channel are covered by graphene sheets.

The outcome of the image analysis leads to a surprising observation: the concentration of single graphene sheets is not decreasing as fast as the multi layered rGO at low concentrations like 12.5 µg/mL and 6.25 µg/mL. The critical GO concentration is at about 6.25 µg/mL and lower, so this cannot be reduced further, otherwise the drain-source electrodes are no longer connected. Electrical measurements need to be carried out to evaluate the different surface coverages for their performance.

I_DV_G measurements for pH sensing

The graphical analysis indicates the best GO concentration for a sufficient surface coverage. To evaluate the electrical properties of the fabricated gFET, the transfer characteristic, or I_DV_G curve, can be measured. Figure 27 shows the semiconducting properties of the different GO dilutions. The subject of investigation were gFETs with different GO concentrations after hydrazine vapor reduction at 80 °C. After the first round of measurements, the same chips were further thermally reduced in vacuum at 200 °C.

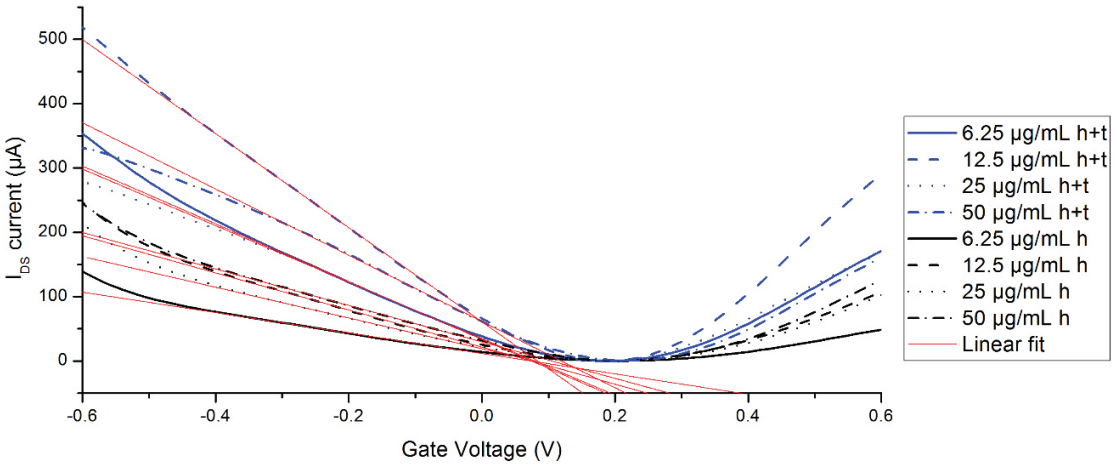

Figure 27: The figure represents the I_DV_G curves of different deposited graphene oxide concentrations. The black curves were measured after the reduction in hydrazine vapor at 80 °C at ambient pressure. The blue curves were measured on the same gFET after an additional thermal reduction at 200 °C in a vacuum oven. The red lines are linear fits in the p-doped branch of the gFET. There is a significant increase for all slopes after thermal reduction. The gFET with a deposited GO concentration of 12.5 µg/mL shows the highest mobility.

It can be observed, that the gFET with GO concentration 12.5 µg/mL has the steepest slope (I_{DS}/V_{GS}-ratio) after hydrazine vapor and thermal reduction, shown in Figure 28. The figure represents the slopes of each GO concentration at different degrees of reduction. The slope increases for each gFET from before and after thermal reduction is indicated on top of each bar diagram as a factor. It can be observed, that the thermal reduction leads to the highest increase in slope for low GO concentrations, but the sweet spot for GO coverage is at a concentration of 25 µg/mL with the steepest total slope.

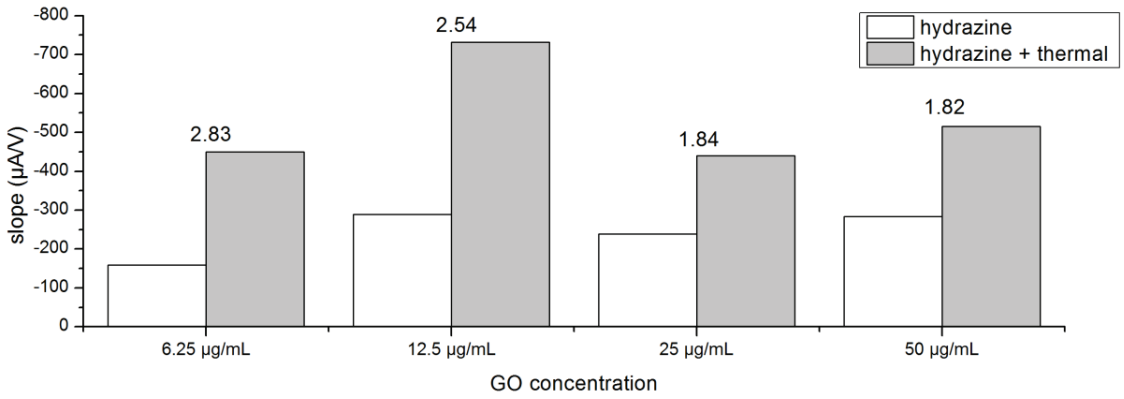

Figure 28: Evaluation of the slope of each gFET after hydrazine vapor and after subsequent thermal reduction. The steepest slope with around 750 µA/V was obtained for a GO concentration of 12.54 µg/mL after thermal reduction, while the 6.25 µg/mL chips exhibit the highest increase after thermal reduction, by a factor of 2.83.

The transfer characteristic of all four GO concentrations were also measured under different pH values of the ionic solution. The pH ranges from pH 3 to pH 9 and the I_DV_G curves were measured after hydrazine vapor reduction and again after an additional thermal reduction, shown in Figure 29. All chips show an increased slope after the thermal reduction. The Dirac point shifts to a more positive voltage for all measurements with increasing pH values. The plotted I_DV_G curves are represented as the delta of the drain-source current I_{DS}, to compare them among each other.

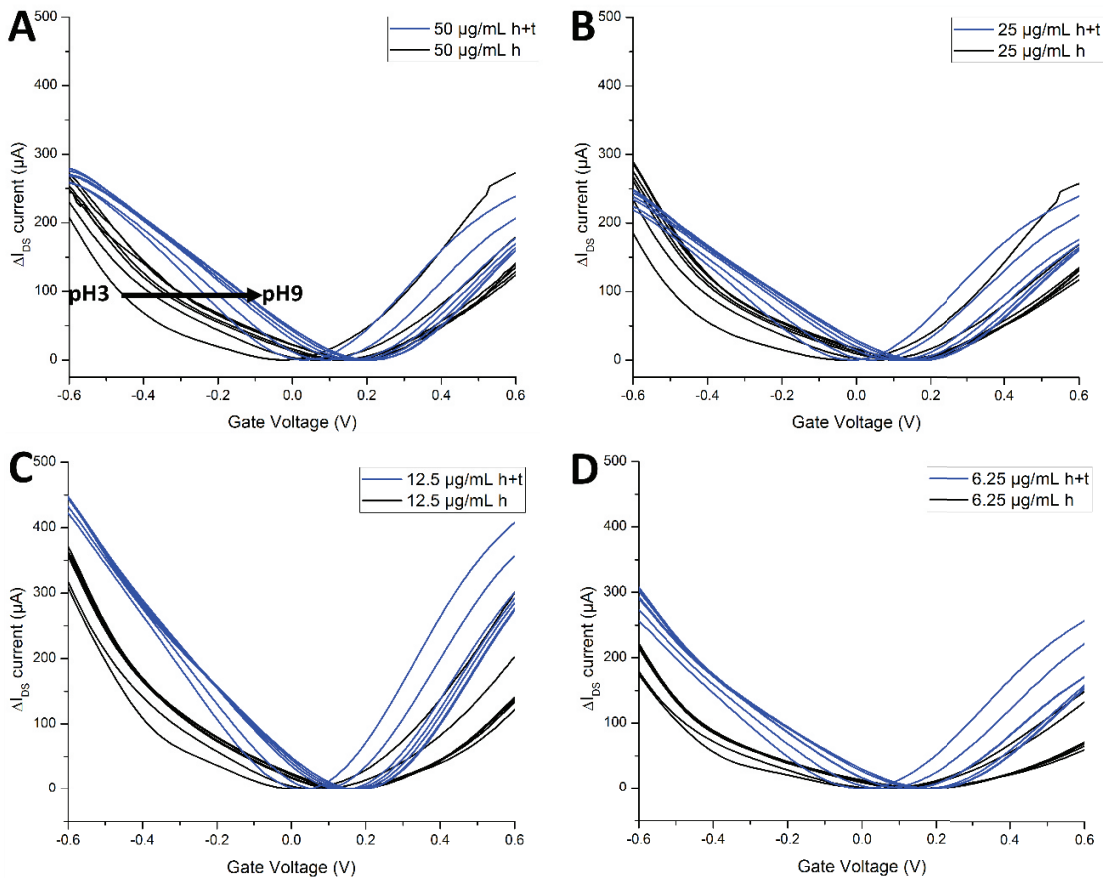

Figure 29: The four I_DV_G curve plots show the pH dependencies of four gFETs with different GO concentrations. Black lines are gFETs after the hydrazine vapor reduction. Blue lines show the transfer characteristics after an additional thermal reduction. With increasing pH values of the ionic solutions, the curves shift to the right. It can be observed, that the chip C with 12.5 µg/mL has the steepest slope throughout the entire pH range. All chips have an increased slope after the thermal reduction.

The I_DV_G curves of different GO concentrations show a linear characteristic curve after hydrazine vapor reduction and subsequent thermal reduction. The slope changes with the surface coverage between the drain-source channel. Figure 30 shows the Dirac point shift at different pH values and the baseline drift of different rGO surface coverages.

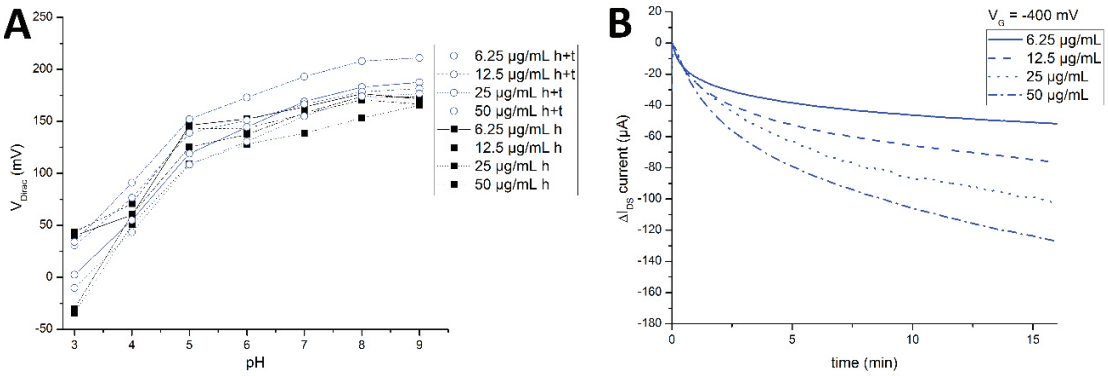

Figure 30: Plot A shows the Dirac point at different pH values of all four chips before and after thermal reduction. The Dirac point shift is slightly shifted towards a positive voltage after thermal reduction. Plot B shows the baseline drift of the gFETs with different graphene surface coverages. It occurs that a higher rGO coverage leads to a stronger baseline drift. The 50 µg/mL chip drifts within 30 min about 120 µA, while the chip with 6.25 µg/mL changes only for 40 µA.

It can be observed, that the four chips are very similar for the Dirac point shift before and after thermal reduction, although the signal is more stable. Interestingly, the gFETs with the lowest surface coverage lead to a smaller baseline drift, which can be attributed to a smaller surface, area exposed to the Figure 30 ionic solution, shown in .

Comparison CVD graphene and rGO

The fabrication of gFETs with different graphene substrates was shown in Chapter 2: Fabrication of CVD graphene FET and Chapter 2: Fabrication of reduced graphene oxide FET. The morphology was investigated in Chapter 2: Scanning electron microscope images of graphene and the purity in Chapter 2: Raman spectra of rGO and CVD graphene. It is crucial to investigate the electrical characteristics of the graphene substrates. The transfer characteristic and baseline drift over time are parameters influencing the quality of the bio-sensing performance. The comparison of gFET with CVD graphene and rGO is shown in Figure 31.

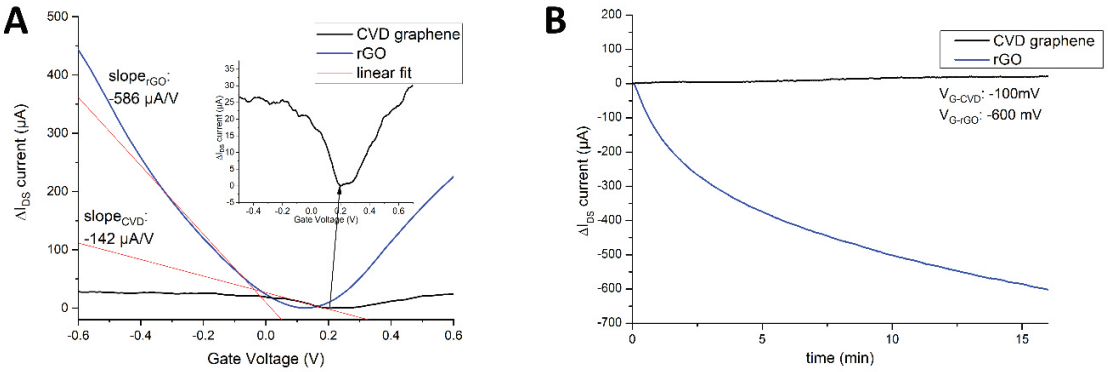

Figure 31: Plot A shows the comparison of the transfer characteristic of to different fabricated gFETs. Blue is rGO and black CVD graphene as drain-source channel substrate. The insert is a close-up to the CVD graphene I_DV_G curve. Plot B illustrates the baseline drift of the rGO FET (blue) and the CVD graphene FET (black) at an applied gate voltage of -600 mV. The CVD graphene FET has only 30% responsiveness compared to the rGO FET, but a very stable baseline.

Measurement of gate capacitance C_i:

The capacitance was obtained from cyclic voltammetry experiments, shown in Figure 32 (A). At scan rates of 10 mV/s, 20 mV/s, 40 mV/s and 80 mV/s the current was measured and the resulting values at 230 mV are plotted in Figure 32 (B).

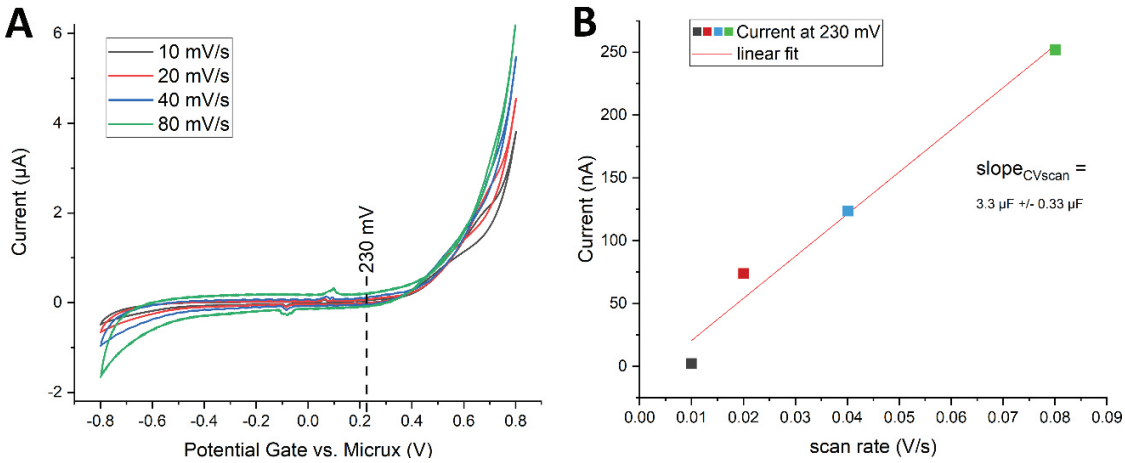

Figure 32: Cyclic voltammetry measurements at different scan rates are shown to obtain the capacitance of the Micrux cell with an AgCl wire gate electrode (A). The current at 230 mV is plotted versus the scan rate in (B) and a linear fit results in the capacitance of the system: 3.3 µF.

The evaluated slope equals the gate capacitance C_i and is 3.3 µF with 10% deviation, which is in good agreement with literature Randin *et al.* for basal plane electrodes. [95]

Mobility comparison of rGO and CVD:

The mobilities of the herein produced graphene FETs were calculated with the known parameters for the channel length L, the width W, the measured gate capacitance C_i and the applied drain-source voltage V_{DS}. The linear fit of the slopes, negative and positive to the Dirac point, allow the calculation of the mobility µ of the fabricated graphene field-effect transistor. The linear fits of rGO and CVD graphene FETs are shown in Figure 31 and the values are used to calculate the mobility with eq 7:

$$\mu_{rGO} = 725\ {}^{cm^2}/_{Vs}\ +/-10\%$$

$$\mu_{CVD} = 176\ {}^{cm^2}/_{Vs}\ +/-10\%$$

The values are low, compared to previous reports (5000 cm^2/Vs[96] to 200,000cm^2/Vs[97]), while others report low mobilities of 1cm2/Vs [98] in literature, but the absolute changes in current are by three orders higher than other reports. While usually low µA are recorded in order to measure the changes in the current, the here reported gFETs exhibit currents up to mA, improving the signal to noise ratio due to lower amplifier requirements.

Discussion

Intuitively, a higher surface coverage would lead to stepper slope, but in contrary, the slope of the gFET is steepest for the lower concentration of 12.5 µg/mL, shown in Figure 27. It can be observed, that low GO surface coverage can be better addressed by the thermal reduction, leading to a slope increase by a factor of 2.8, while high surface coverage can only increase by 1.8 times. The sweet spot for surface coverage is at about 12.5 µg/mL for 2 hours, leading to the steepest slope after the hydrazine vapor reduction and can increase by a factor of 2.5 to more about 750 µA/V. A possible explanation can be found in the surface coverage study, shown in Figure 26. A higher single layer graphene sheet coverage can be better reduced by vacuum at 200 °C, leading to a higher slope. Furthermore, the linearity of the transfer characteristic over the gate voltage range of several 100 mV increases dramatically. A steep slope represents the sensitivity of the gFET. When using the gFET as bio-sensor, it is important to set the working point, the gate voltage, in the linear regime of the I_DV_G curve and to have a big change of drain-source current I_{DS}, when the gate voltage changes due to binding events. The produced gFET have a Dirac point between 100 mV and 200 mV and the center of the linear regime can be found at -200 mV to -300 mV, perfect for bio-sensing applications where low voltage is necessary to avoid electrochemical effects. For the here fabricated and stable gFETs a mobility of 725 cm^2/Vs can be reported, leading to a fairly good performance according to the size and facile deposition method. The advantage of the sensor architecture is the cheap fabrication on a commercially available chip and the high readout current, exceeding 1 mA, so amplifiers can handle the data acquisition without special anti-noise circuits. The gFET fabrication procedure, characterization and application are discussed in detail in the publication, with the contribution of this work. [99]

Manuscript #1:

Before proceeding, the publication summarizing the design and implementation of OFET and graphene FET devices for electronic bio-sensing is attached, herein referred as Kotlowski *et al.* 2018. [99]

Kotlowski, C., Aspermair, P., Khan, H.U., Reiner-Rozman, C., Breu, J., Szunerits, S., Kim, J.J., Bao, Z., Kleber, C., Pelosi, P. and Knoll, W., 2018. **Electronic biosensing with flexible organic transistor devices.** *Flexible and Printed Electronics, 3(3)*, p.034003. https://doi.org/10.1088/2058-8585/aad433

IOP Publishing Flex. Print. Electron. 3 (2018) 034003 https://doi.org/10.1088/2058-8585/aad433

Flexible and Printed Electronics

OPEN ACCESS

RECEIVED
4 May 2018

REVISED
19 June 2018

ACCEPTED FOR PUBLICATION
18 July 2018

PUBLISHED
7 September 2018

Original content from this work may be used under the terms of the Creative Commons Attribution 3.0 licence.

Any further distribution of this work must maintain attribution to the author(s) and the title of the work, journal citation and DOI.

PAPER

Electronic biosensing with flexible organic transistor devices

Caroline Kotlowski[1,2], Patrik Aspermair[1,2,3], Hadayat Ullah Khan[4], Ciril Reiner-Rozman[1,2], Josef Breu[5], Sabine Szunerits[3], Jang-Joo Kim[6], Zhenan Bao[7], Christoph Kleber[1], Paolo Pelosi[2] and Wolfgang Knoll[1,2]

[1] Center for Electrochemical Surface Technology (CEST), Wiener Neustadt, Austria
[2] AIT Austrian Institute of Technology, Tulln, Austria
[3] Université de Lille, France
[4] Fingerprint Cards AB, Kungsgatan 20, 41119 Goteborg, Sweden
[5] Inorganic Chemistry I, University of Bayreuth, Bayreuth, Germany
[6] Department of Materials Science and Engineering, Seoul National University, Seoul, Republic of Korea
[7] Department of Chemical Engineering, Stanford University, CA, United States of America

E-mail: wolfgang.knoll@ait.ac.at

Keywords: electronic biosensing, immunosensing, antigen–antibody interaction, OFET, rGO–FET, biomimetic smell sensing

Abstract

In this short review, we summarize the design and implementation of organic semiconducting materials-based field-effect transistors (OFETs) and the fabrication and use of reduced graphene-oxide field-effect transistors (rGO–FETs) as flexible transducers for electronic biosensing. We demonstrate that these platforms allow for the quantitative, *in situ*, and in real time monitoring of bio-affinity reactions between analytes from solution to the surface-immobilized receptors. The examples given include the binding of anti-bovine serum albumin (BSA) antibodies to their antigen, BSA, covalently attached to the channel of an OFET, or the reverse mode of operation, i.e., the binding of BSA from solution to the antibodies immobilized on a rGO transistor. Finally, we will discuss a few results obtained with odorant binding proteins used as receptors on a rGO–FET transducer for the realization of a biomimetic smell sensor.

Introduction

Recently, the field of organic electronics has attracted increasing interest and a consequent growth in scientific research [1, 2]. A particular focus has been on wearable electronics for sensing and monitoring applications [3–5]. Current wearable sensors monitor simple analytes, such as ions, glucose, lactate, etc. In contrast, the human body emits hundreds of volatile organic compounds (VOCs), indicators of a person's health status, their metabolic activity, or their stress situation.

Electronic smell sensors are best suited for such applications as they (i) can be integrated into cell phones for breath analysis [6, 7], (ii) can be embedded into the fabric of clothing to monitor physiological and pathological conditions [8], and (iii) they could also be even implanted into the body for continuous monitoring of specific markers [9].

In addition to the category of flexible organic electrochemical transistors that have gained interest [10], electronic field-effect transistor (FET-) sensing devices can be:

- based on organic semiconducting materials (defined as an organic field-effect transistor (OFET)) [11–13];
- made on flexible and stretchable substrates [14, 15];
- fabricated on graphene [16];
- functionalized by biomimetic molecular modules like antibodies [17, 18], oligonucleotide capture strands [19], aptamers for marker molecules [20] and small VOCs [21], or odorant binding proteins to monitor olfactory cues [22];
- operated in liquids [11] and in air (provided the sensitive biological material is protected by hydrogels) [23].

In this paper, we summarize some of our own research results in this area. The first example that we discuss concerns the design and assembly of a flexible OFET and its characterization as an electronic transducer for the quantitative evaluation of the recognition reaction between a model marker protein, bovine serum albumin (BSA), immobilized on the channel

© 2018 IOP Publishing Ltd

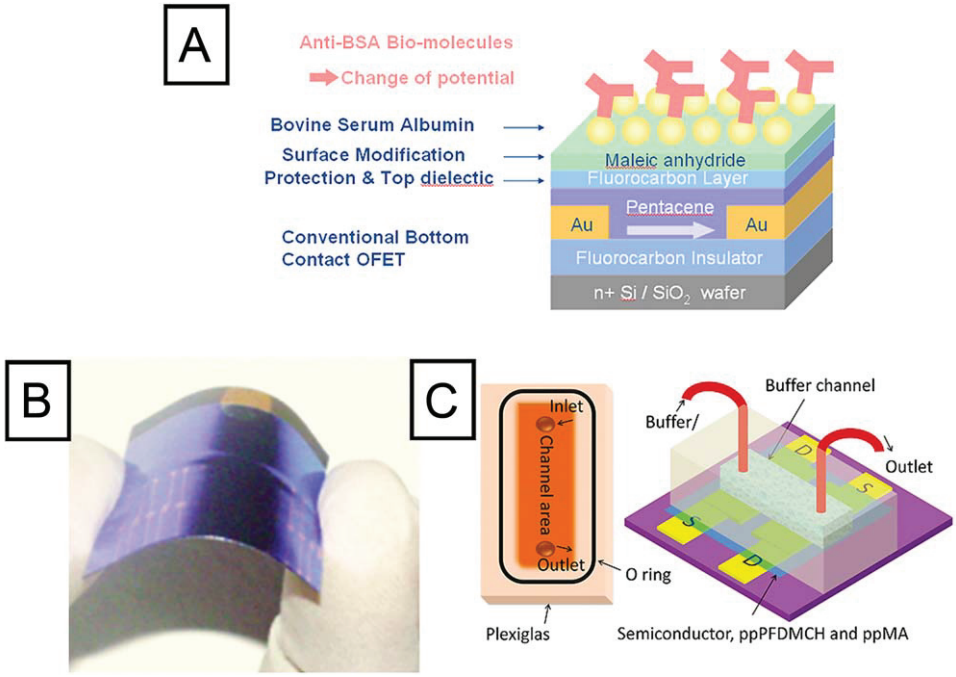

Figure 1. (A) Schematics of the OFET device architecture with surface-immobilized antigens and the corresponding antibodies bound from solution: a thin polymer layer (Cytop) as the dielectric was spin-coated onto a doped Si substrate covered by 200 nm of SiO_2 used as the gate. Onto this the Au source and drain electrodes were evaporated (see also (C)) and it was then covered by pentacene which was used as the polymeric semiconductor. (B) The OFET, prepared on a flexible poly(imide) substrate. (C) Mounting the device onto a flow cell with an inlet and outlet for the analyte solution.

surface of the transistor, and a high affinity antibody binding from solution.

In the next section, we then introduce a novel material, graphene, as the channel material connecting the source and drain electrodes of a transistor. As a test sample, we again use the BSA–anti-BSA antibody system; this time, however, we immobilized the antibody on the gate surface and characterized the performance of the device as an electronic sensor monitoring the binding of the analyte, BSA, from solution.

And finally, we present a few results of a major effort in our group, i.e., the use of graphene-based FET devices as electronic biomimetic smell sensors.

Protein (antibody) sensing by OFET devices

The use of Si-based electronic devices for monitoring biological processes is relatively well established [24, 25]. What has been less demonstrated so far is the use of organic electronic devices, which appear much more recently in the literature, as an option to be applied in combination with physiological buffer solutions for biosensing applications [26].

Our approach was based on a design concept given in figure 1: a very thin layer of a fluoro-polymer, Cytop, as the dielectric, was applied by spin-coating onto a 200 nm thin SiO_2 coating plus the Si substrate, which was highly doped in order to be used as the back-side gate electrode of the transistor. After evaporating the source and the drain Au electrodes (with a width (W) of 500 μm and length (L) of 50 μm), pentacene, as the semiconducting organic material, was deposited by evaporation [14] (figure 1(A)). Alternatively, a flexible poly(imide) substrate could be used for the device fabrication, resulting in a transistor that could be easily bend (figure 1(B)) [14].

An ultrathin (5–10 nm) fluorocarbon layer functioning as a protective barrier that prevents ions from the adjacent analyte buffer solution from diffusing into the organic channel material was deposited onto this OFET device by plasma polymerization. This is also shown schematically in figure 1(A). The further (vacuum) deposition of a maleic anhydride layer then allows for the direct coupling of biological functional units to the device structure via their amine moieties, e.g., the lysine groups of proteins. These then act as receptors for bio-affinity reactions between these surface-immobilized units and their interaction partners, the analytes of interest. This is depicted in figure 1(A) for the immobilization of BSA, with its antibody as the analyte, binding from solution. These transistor devices were then mounted to a flow cell and exposed to analyte solutions of different concentrations for binding studies *in situ* and in real time (figure 1(C)).

An example for a global analysis, i.e., the combination of kinetic and titration measurements for anti-BSA binding to surface-immobilized BSA proteins, is shown in figure 2. Upon injecting analyte solutions of increasing concentrations, c, a decreasing current between the source and the drain is seen, reflecting the

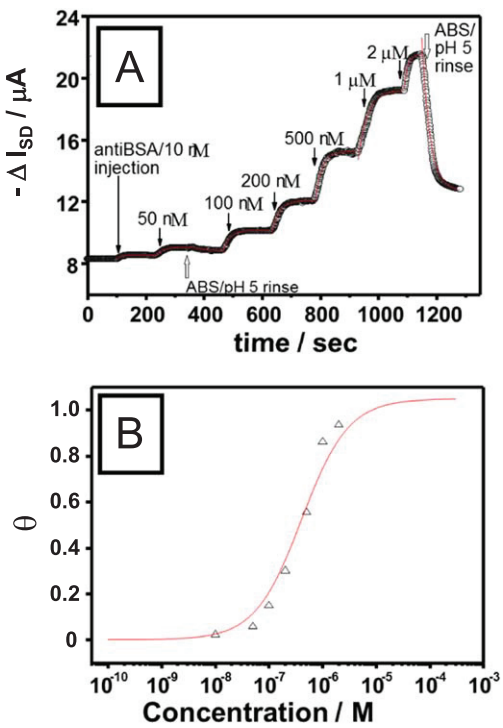

Figure 2. (A) Global analysis of the binding of anti-BSA antibodies from solutions of increasing concentrations to the surface-immobilized antigen molecules, BSA; (B) Langmuir adsorption isotherm from the titration date of (A), plotted as surface coverage, θ, as a function of the concentration of BSA in the bulk solution. The red S-shaped curve is a fit to the data with $K_d = 350$ nM.

increasing occupancy of the originally empty receptor sites on the channel, the immobilized BSA, by the analyte anti-BSA up to a saturation level at full coverage. This is shown in figure 2(A). Upon rinsing the flow cell with pure buffer the full reversibility of the binding reaction (except for a slight drift of the device readout) suggests the applicability of a Langmuir binding model for the quantitative evaluation of both kinetic parameters for the association, k_{on}, and the dissociation constant, k_{off}, (not shown and analyzed here) and for the affinity constant, K_A, or the inverse, i.e., the dissociation constant, $K_d = 1/K_A$, equivalent to the half-saturation concentration, $c_{1/2}$ [17].

According to the Langmuir model the surface coverage, θ, is given by:

$$\theta = K_A c/(1 + K_A c). \quad (1)$$

The stationary current changes, ΔI_{SD}, reached after each change in bulk analyte concentration, c, expressed as surface coverage in percent of the full coverage, i.e.,

$$\theta = \Delta I_{SD}/\Delta I_{SD}{}^{max}, \quad (2)$$

as a function of the corresponding bulk concentration results, when plotted in a lin-log format, in the well-known S-shaped Langmuir isotherm curve. This is shown in figure 2(B). The red curve is the fit to the data with the only fitting parameter being the dissociation constant, $K_d = 350$ nM, a value well in line with reported data from the literature [27].

Immunosensing by reduced graphene oxide (rGO)-FET devices

The next example that we briefly present concerns the use of graphene as the channel material for transistor fabrication [28, 29]. In our case, for simplicity and availability of materials, we start the device fabrication with graphene oxide (GO), which upon reduction (see figure 4(A)) leads to semiconducting rGO [30]. Its excellent conductivity has one important advantage when operating in direct contact with physiological buffer solutions: even in cases where there is no protective coating that shields the electrodes or the channel material from exposure to an electrolyte with a relatively high ionic strength, the operation of the device is straightforward. The low resistance of the channel leads to a situation where 90%–95% of the current between the source and the drain electrodes passes through the rGO, and only a negligible fraction of the current runs through the electrolyte as a shortcut, which can be ignored [18]. This makes the fabrication protocol, compared to the OFET preparation described above, a lot easier as it avoids any processing steps that were essential to protect the sensitive organic/polymeric semiconducting channel material in OFETs.

Figure 3 summarizes the essential steps for the preparation of rGO–FETs, operated in the liquid-gated mode [18]. A very helpful simplification step was achieved with the use of one of the many microchips available in the electrochemical equipment market. We chose one that was only a few mm in size (figure 3(A)), and had an interdigitated Au electrode array of ~3 mm in diameter (figure 3(B)), with a spacing of 10 μm between the source and drain electrodes (figure 3(C)). The preparation of the rGO–FET, which is the conversion of this electrochemical chip into a transistor for biosensing, is given in more detail in figure 4: the electrode area is exposed to an APTES solution, a procedure which leads to the coating of the glass substrate between the Au areas with a monolayer of positive charges (figure 4(A)). These then help to attract and physisorb the GO flakes from a colloidal dispersion. Upon exposure of the deposited GO flakes to hydrazine vapor (figure 4(A)) [31] and a subsequent thermal treatment these flakes are reduced leading to highly conductive rGO flakes (bridging the space between the source and drain electrodes) [32].

The resulting conductive channels between the source and drain electrodes are randomly covered to a high degree with rGO flakes forming a continuous bridge of monomolecular or few-layer graphene sheets as was documented by AFM images (see figure 4(B) and the height scan given in figure 4(C)). The excellent conductivity was demonstrated by

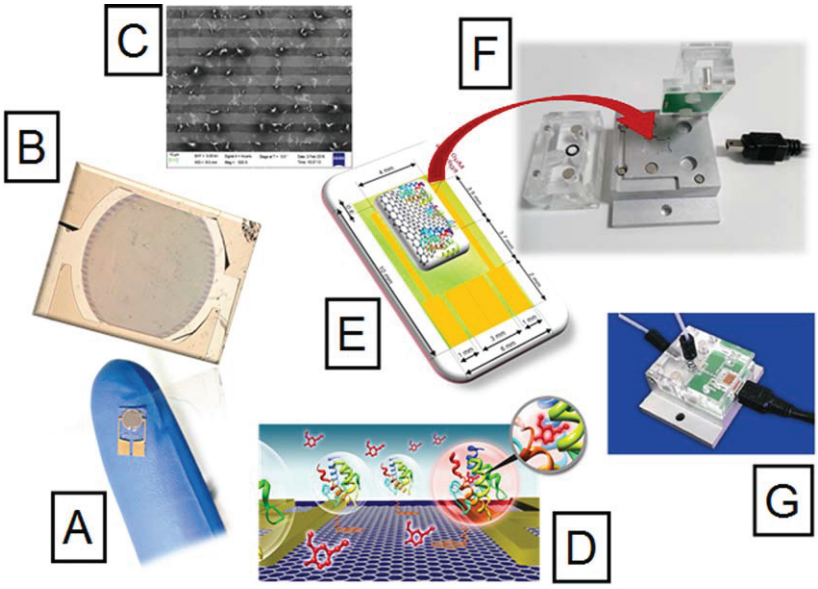

Figure 3. (A) A commercial electrochemical sensing chip on a (rubber glove-covered) fingertip. (B) Optical micrograph of the sensing area which is an interdigitated electrode array used as the source and drain electrodes. (C) A scanning electron microscope (SEM) image of the interdigitated electrode array after immobilization of graphene oxide flakes; the spacing between the electrodes is 10 μm. (D) Schematics of the immobilization of odorant binding proteins as receptors for the smell sensor via pyrene-based coupling strategies; the sensor chip (E) then fits into the commercial flow cell (F), with its analyte solution inlet and outlet and the electrical connector shown (G).

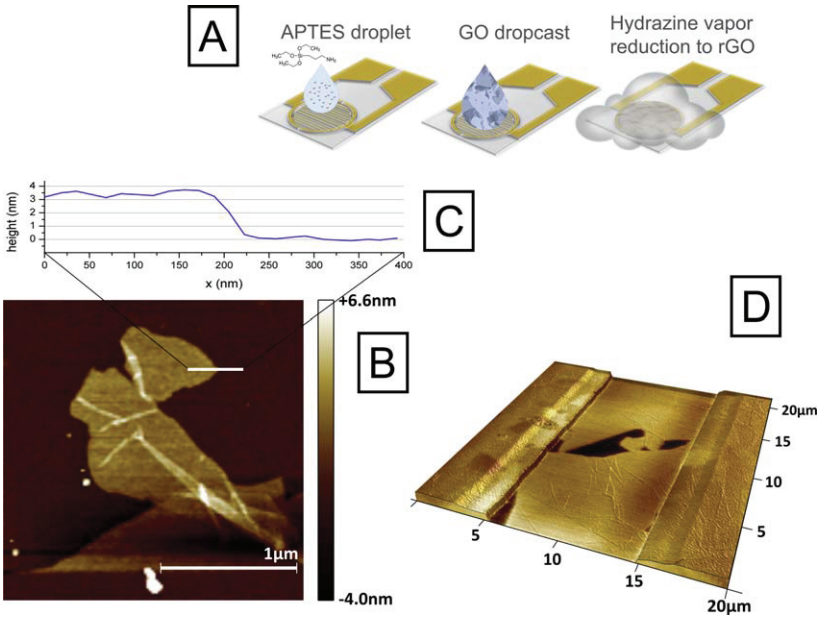

Figure 4. (A) Schematics of the chip functionalization by first covering the substrate between the Au electrodes with a monolayer of amino-propyl-triethoxy-silane (APTES), onto which the graphene oxide flaxes are deposited; after reduction by hydrazine and a thermal treatment the transistor with its semiconducting rGO flakes is ready for bio-functionalization by the receptor molecules (see also figure 3(D)). (B) Atomic force microscope (AFM) image of a single rGO flake. (C) Line scan across the edge of the rGO flake shown in (B). (D) Kelvin probe image of two Au electrodes and the space between them, covered with rGO flakes.

Kelvin probe images that were taken from the electrodes and the space between them, covered with rGO flakes (figure 4(D)). After this preparation step of coating the active area of the chip with rGO flakes (see also the SEM image given in figure 3(C)), their bio-functionalization was then conducted using a protocol borrowed from the literature describing the functionalization of carbon nanotubes [33], using 1-pyrenebutanoic acid succinimidyl ester (PBSE). The linker firmly attaches to the graphene surface through π–π interactions with the pyrene groups, and on the other end it covalently reacts with the amino group of the protein to be coupled to form an amide bond (figure 3(D)). Now the chip with its functionalized

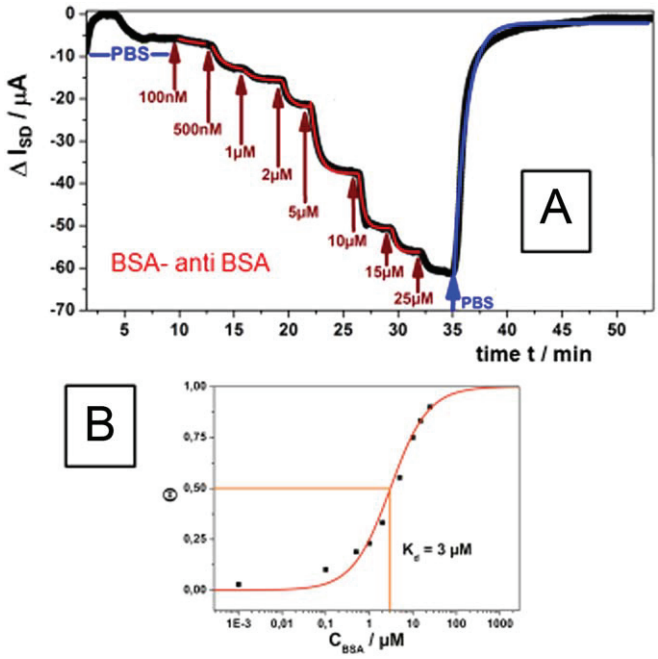

Figure 5. (A) Global analysis of BSA binding from solution to surface-immobilized anti-BSA antibody; solutions with concentrations from 100 nM to (near) saturation at 25 μM were rinsed through the flow cell. (B) Langmuir adsorption isotherm obtained by plotting the (negative) change in the source–drain current, ΔI_{SD}, scaled to its (extrapolated) maximum value, ΔI_{SD}^{max}. The red curve is a fit to the data according to the Langmuir model, resulting in a dissociation constant (half-saturation concentration) of $K_d = 3$ μM.

channel between the source and drain electrodes (figure 3(E)) is ready to be mounted into the commercial chip holder (figure 3(F)) with its convenient fluid inlet and outlet and electrical connections (figure 3(G)).

Similar to the OFET operations described above, the setup can now be used for *in situ* measurements in real time, again giving quantitative data on the reaction rate constants for the association, k_{on}, and the dissociation processes, k_{off}, as well as on the affinity constant, K_A [16].

Figure 5 presents the global analysis of the binding reaction between the surface-immobilized anti-BSA antibodies and BSA, rinsed through the flow cell at different concentrations, as indicated in figure 5(A). The red curves are fits to the association process; the blue curve is a fit to the dissociation.

The change of the source–drain current, ΔI_{SD}, measured after a new equilibrium was established, can be plotted as a function of the bulk analyte concentration to yield an adsorption isotherm, presented in figure 5(B), together with the fit to the Langmuir model with a dissociation constant of $K_d = 3$ μM.

As described by the basic equation for the electrical device performance in the liquid-gated mode of operation, i.e.,

$$I_{SD} = \mu C_{Ox} W/L(V_G - \Psi_S)V_{SD} \quad (3)$$

the source–drain current, I_{SD}, depends on the applied source–drain voltage, V_{SD}, and on the carrier mobility, μ, the gate capacity, C_{Ox}, geometric channel parameters, i.e., the width, W, and the length, L, and the Dirac voltage, V_G, determined by the threshold voltage of the cathodic branch of the hole conductance and the anodic branch of the electron conductance. Of particular importance for the device employed in electronic biosensing is the surface potential, Ψ_S, of the channel–electrolyte interface. Various contributions to the change of the current as a function of a bioaffinity reaction at the gate electrode or directly on the channel have been discussed [18, 34, 35]. The dominant contribution to the change of the surface potential upon binding of a protein to a receptor is believed to be the change in surface charge density (distribution). We demonstrated this experimentally for the electronic recording of the association and dissociation reactions of anti-BSA antibodies binding from solution to their surface-immobilized BSA antigens by changing the bulk solution pH to values below (pH 5) and above (pH 7) the pI of the analyte protein [36] which leads to an increase or a decrease of the current, corresponding to a shift of $(V_G - \Psi_S)$ to more negative or positive values, respectively [17].

Electronic biomimetic smell sensing

The interest in developing smell sensor concepts, sensors for air-born chemical analytes, odorants, pheromones, other VOCs, etc, originates from the many different potential areas where the application of such devices would be extremely relevant.

- More and more research evidence is reported in the literature that quantifies novel types of smell molecules that can be used for diagnostic purposes

[37]. For example, in a recent study the concentration of the molecule isoprene in the exhaled breath of diabetes patients could be linked to their blood glucose level [38].

- European crop losses from plant diseases amount to more than €5 billion per year [39, 40]. Plant pathogens (fungi, viruses, phytoplasma) are typically transmitted by insects using host-derived odors as key foraging cues. Thus, diseased plants draw insect vectors with specific attractant volatiles.
- Our daily protocols for testing grocery quality at home are typically based on optical inspection of the food items; what follows in most cases, however, as the ultimate quality check for edibility is a smell test.
- There is an increasing need for smell detectors in homeland security and the protection of the public and private environment: it is expected that in the future bio-inspired robots will sniff out mines, bombs, and drugs [41].

Given these few examples of the broad range of potential scenarios for the use of smell sensors, it is somewhat surprising that we have essentially no technical device worthy of the term 'artificial nose', that is able to reach the chemical bandwidth, selectivity, and sensitivity of the olfactory sense of mammals and humans or the antennae of insects. For the sensing of light, e.g. in imaging or optical communication, we have extremely powerful devices with the ability to detect even single photons. The monitoring of sound in acoustic communication is also technically unproblematic: microphones are available with an amazing performance profile. However for chemical communication, for smell or taste detection on a technical level, we have (nearly) nothing.

The attempt to detect smells by a specific kind of a chemical sensor or the development of an artificial nose is certainly not new. The general interest in artificial noses, 'electronic noses', or E-noses, originated from the many scenarios outlined above where chemical communication is extremely important in our daily life. There have been several serious attempts described in the literature to develop concepts by which, via more or less unspecific interactions of the molecules of interest (with odorants being typically small, hydrophobic molecules that are difficult to sense by classical techniques, e.g. by surface plasmon sensors with an organic (polymeric) matrix [12]), a measurable and quantifiable signal is generated. All the reported concepts, however, were eventually discarded because of the severe lack of sensitivity compared to natural olfaction.

Our approach tries to realize a biomimetic smell sensor that uses a combination of an electronic transducer, in most of our cases a rGO–FET device, and the biological functional unit used in nature by both insects and mammals, as the first recognition element in the smell sensing cascade, i.e., odorant binding proteins (OBPs) [42].

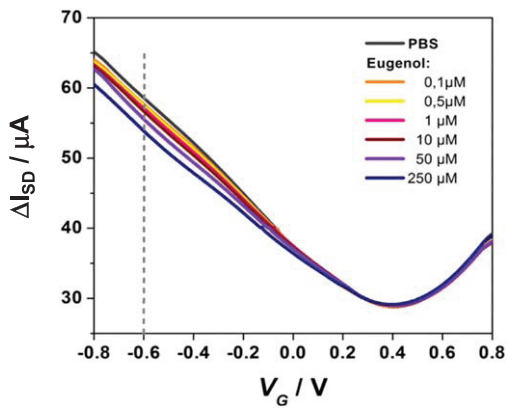

Figure 6. Current–voltage characteristics of the OBP 14 based biosensor device without eugenol, measured just in PBS, and in solutions with increasing eugenol concentrations, ranging from 100 nM to 250 μM. The applied source–drain voltage was $V_{SD} = 50$ mV.

The preparation of the sensors follows the concepts described briefly above for immunosensors: the rGO channel is functionalized by PBSE, to which a variety of OBPs from different insects are coupled covalently by active ester chemistry [22, 43]. The chip is then integrated into the flow cell (see figure 3) and different odorant molecules in aqueous solutions of varying concentrations were then rinsed through the cell for the quantitative recording and evaluation of binding reaction rates and affinity constants for OBPs and their set of ligands.

Examples for electronic smell sensing with such a transducer are given in the following figures for a sensor that was functionalized by OBP 14 from the honey bee, *Apis mellifera*, mounted to the flow cell, and exposed to solutions of a variety of ligands.

Figure 6 gives a series of measurements of the source–drain current–gate voltage characteristics, ΔI_{SD}–V_G, for the sensor in contact with analyte solutions containing the OBP 14 ligand, eugenol, in different concentrations, ranging from pure phosphate-buffered saline solution (PBS), to a 250 μM eugenol solution. As one can see, the device performs as a bipolar FET, with the ΔI_{SD}–V_G curves affected in a quantitative way by the analyte concentration.

For a given gate voltage, in the following experiments fixed at $V_G = -600$ mV (the dashed line in figure 6) one can then use the sensor for the quantitative evaluation of the kinetic parameters of the ligand–OBP association (binding) and dissociation process, as well as, like in the case of the immunosensors described above, the binding strength, i.e. the affinity constant, K_A, of the dissociation constant K_d, respectively.

This is demonstrated in figure 7(A), which shows the global analysis, i.e. the time-dependent recordings of the change of the source–drain current, ΔI_{SD} (with the source–drain voltage set at $V_{SD} = 50$ mV and the

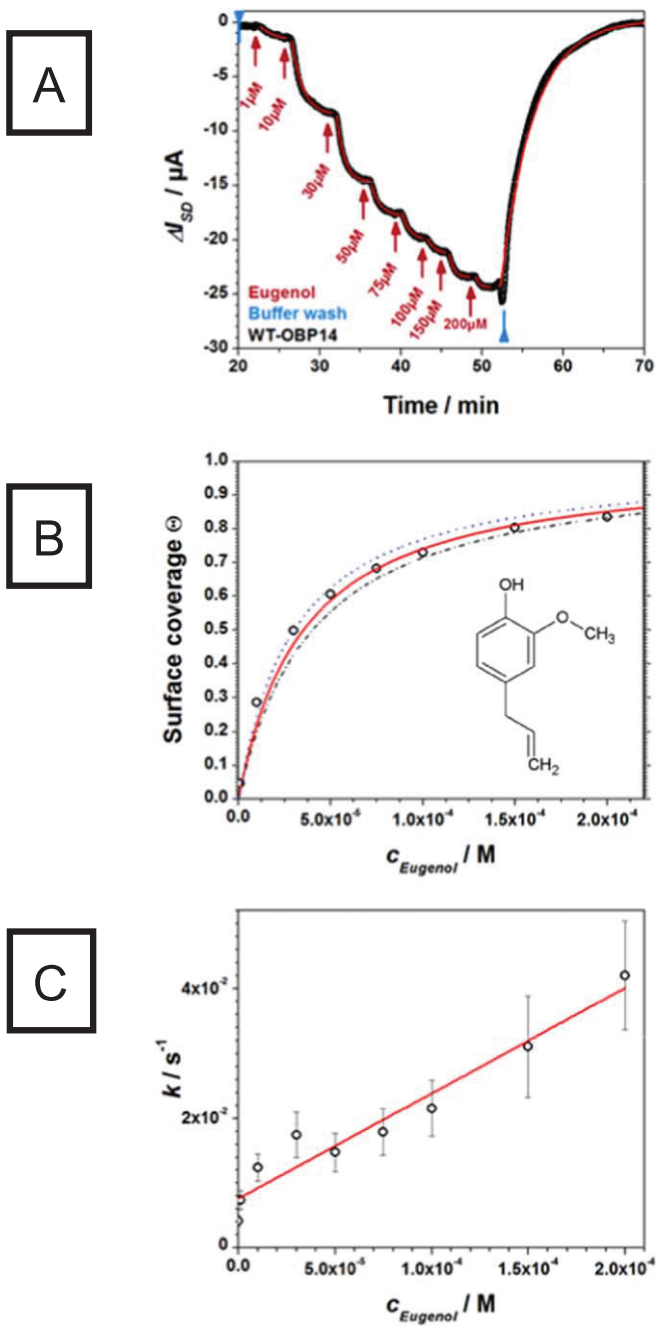

Figure 7. (A) Real time biosensor measurement (global analysis) of the binding of eugenol to OBP 14: the current decreases as the bulk concentration of eugenol increases from 1 μM to 200 μM and then saturates. Blue arrows indicate runs with pure buffer, red arrows indicate experiments with eugenol solutions. The red curves are fits to the raw data by kinetic simulations of the association and dissociation processes based on the Langmuir model. (B) Langmuir adsorption isotherm, obtained from the titration levels of (A). The red fit curve gives $K_d = 35$ μM (also plotted are error limits for K_d of $\pm 20\%$); the inset shows the structural formula of eugenol. (C) Analysis of the reaction rate constants, k, as obtained from the fitted data in (A) as a function of the eugenol concentration; error bars are $\pm 20\%$.

gate voltage at $V_G = -600$ mV, see figure 6), upon a stepwise increase of the eugenol concentration in the bulk solution until saturation of the device response is nearly reached. Upon injecting pure buffer into the flow cell again, the sensor signal returns to its baseline level showing the reversibility of the binding reaction between the ligand and its receptor immobilized on the channel of the transistor.

By plotting the respective surface coverage, θ, obtained from the equilibrium levels reached after each change of the bulk ligand concentration and scaled to the maximum response at high concentrations, see equation (2), one obtains a Langmuir adsorption isotherm from which the dissociation constant K_d can be derived. This is shown in figure 7(B): the full red curve is a fit to the data with equation (1) with $K_d = 35$ μM.

An internal consistency test for the applicability of the Langmuir model is given by the analysis of the measured association and dissociation rate constants

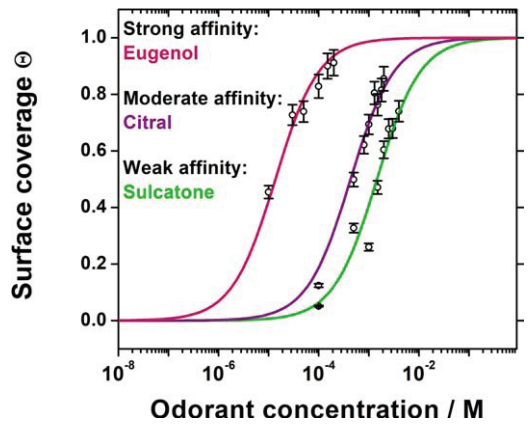

Figure 8. Langmuir adsorption isotherms for three different ligands, as indicated, for OBP 14 from *A. mellifera*.

(see the full red fit curves given in figure 7(A)). According to

$$k = k_{on}c + k_{off}, \quad (4)$$

with k_{on} being the association and k_{off} the dissociation rate constant, respectively, one obtains from the rate constants, k s^{-1}, obtained from the fits in (A) as a function of the bulk concentration, c, a straight line, as shown in figure 7(C). The slope of the fit line yields $k_{on} = 162\ M^{-1}s^{-1}$, and from the intersection of the fit line with the ordinate one obtains $k_{off} = 0.0076\ s^{-1}$. The Langmuir model predicts that the ratio k_{off}/k_{on} equals the dissociation constant, K_d, as obtained from a titration experiment. From the data in figure 7(C) we obtain $K_d = 47\ \mu M$, which agrees very well with the value from figure 7(B), i.e., $K_d = 35\ \mu M$.

Finally, we present some examples for the selective response of such an electronic smell sensor based on OBP functionalized rGO–FETs to different ligands. The sensor used for the experiments given in figure 8 had OBP 14 from *A. mellifera* immobilized on its channel and it was exposed to a variety of different analyte solutions. The odorants bind to the identical receptor with affinity constants that differ by more than two orders of magnitude in their binding strength. The full range that we found for a set of 14 different ligands even covered even three orders of magnitude [43]. Moreover, the sequence of strong and weak affinity ligands qualitatively matches a set of data obtained from a fluorescence assay in solution. A comprehensive comparison of data from receptors immobilised onto a rGO–FET with a fluorescence displacement assay in solution is currently in progress in our laboratory.

Concusions

Electronic biosensing shows great promise for complementing electrochemical detection schemes on the one hand and optical concepts for the quantitative monitoring of bioanalytes on the other. In particular, the use of graphene as the conductive gate material in the preparation of thin film transistors as sensing devices offers a tremendous advantage compared to the use of organic semiconducting materials or compared to Si-based transistors, which both require far more demanding preparation protocols. This has been demonstrated convincingly in many examples reported in the literature. With the introduction of graphene as the semiconducting material used for the fabrication of a channel of a water-stable transistor [10] the electronic read-out concept has become even more attractive.

The use of antibodies as receptors for protein and peptide markers and of odorant binding proteins in smell sensors will be complemented by the development of artificial receptors, e.g. aptamers [44], affimers [45], or seligos [46]. Immunodiagnostics with graphene FETs functionalized by these synthetic immunoreceptors for proteins, but also for the detection of small analytes, are just beginning a very dynamic development in biosensing. All of these electronic biosensing platforms are highly sensitive, label-free, disposable and cheap, with signals that are easy to analyze and interpret, suitable for multiplexed operation and for remote control, compatible with NFC technology, etc, and are in many cases a clear and promising alternative to optical sensors.

Acknowledgments

Partial support for this work was provided by the European Science Foundation (ESF), grant number 10-EuroBioSAS-FP-005, the Austrian Science Fund (FWF) (I681-N24), the Austrian Federal Ministry for Transportation, Innovation and Technology (GZBMVIT-612.166/0001-III/I1/2010), by the FFG within the Comet Program, and from the governments of Lower and Upper Austria.

ORCID iDs

Caroline Kotlowski https://orcid.org/0000-0001-5416-5837
Wolfgang Knoll https://orcid.org/0000-0003-1543-4090

References

[1] Shen G and Fan Z (ed) 2016 *Flexible Electronics, From Materials to Devices* (Singapore: World Scientific)
[2] Lipomi D J and Bao Z 2017 Stretchable and ultraflexible organic electronics *MRS Bull.* **42** 93–7
[3] Myers A, Bowles A, Shahariar H, Bhakta R and Jesse S J 2017 *Wearable Electronics* (Marietta, GA: Textile World)
[4] Han T-H, Kim H, Kwon S-J and Lee T-W 2017 Graphene-based flexible electronic devices *Mater. Sci. Eng.* R **118** 1–43
[5] Lipomi D J, Vosgueritchian M, Tee B C-K, Hellstrom S L, Lee J A, Fox C H and Bao Z 2011 Skin-like pressure and strain

sensors based on transparent elastic films of carbon nanotubes *Nat. Nanotechnol.* **6** 788–92
[6] Frazier K M and Swager T M 2013 Robust cyclohexanone selective chemiresistors based on single-walled carbon nanotubes *Anal. Chem.* **85** 7154–8
[7] Meredith S E, Robinson A, Erb P, Spieler C A, Klugman N, Dutta P and Dallery J 2014 A mobile-phone-based breath carbon monoxide meter to detect cigarette smoking *Nicotine Tob. Res.* **16** 766–73
[8] Stoppa M and Chiolerio A 2014 Wearable electronics and smart textiles: a critical review *Sensors* **14** 11957–92
[9] Bazaka K and Jacob M V 2013 Implantable devices: issues and challenges *Electronics* **2** 1–34
[10] Liao C, Mak C, Zhang M, Chan H L and Yan F 2015 Flexible organic electrochemical transistors for highly selective enzyme biosensors and used for saliva testing *Adv. Mater.* **27** 676–81
[11] Roberts M E, Mannsfeld S C B, Queraltó N, Reese C, Locklin J, Knoll W and Bao Z 2008 Water-stable organic transistors and their application in chemical and biological sensors *Proc. Natl Acad. Sci.* **105** 12134–9
[12] Crone B, Dodabalapur A, Gelperin A, Torsi L, Katz H E, Lovinger A J and Bao Z 2001 Electronic sensing of vapors with organic transistors *Appl. Phys. Lett.* **78** 2229–31
[13] Diacci C, Berto M, Lauro M D, Bianchini E, Pinti M, Simon D T, Biscarini F and Bortolotti C A 2017 Label-free detection of interleukin-6 using electrolyte gated organic field effect transistors *Biointerphases* **12** 05F401
[14] Khan H U, Roberts M E, Knoll W and Bao Z 2011 Pentacene based organic thin film transistors as the transducer for biochemical sensing in aqueous media *Chem. Mat.* **23** 1946–53
[15] Lai S, Viola F A, Cosseddu P and Bonfiglio A 2018 Floating gate, organic field-effect transistor-based sensors towards biomedical applications fabricated with large-area processes over flexible substrates *Sensors* **18** 688
[16] Reiner-Rozman C, Kotlowski C and Knoll W 2015 Electronic biosensing with functionalized rGO FETs *Biosensors* **6** 17
[17] Khan H U, Jang J, Kim J J and Knoll W 2011 *In situ* antibody detection and charge discrimination using aqueous stable pentacene transistor biosensors *J. Am. Chem. Soc.* **133** 2170–6
[18] Reiner-Rozman C, Larisika M, Nowak C and Knoll W 2016 Graphene-based liquid-gated field effect transistor for biosensing: theory and experiments *Biosensors Bioelectron.* **70** 21–7
[19] Khan H U, Roberts M E, Johnson O, Förch R, Knoll W and Bao Z 2010 *In situ*, label-free DNA detection using organic transistor sensors *Adv. Mater.* **22** 4452–6
[20] Berto M *et al* 2018 EGOFET peptide aptasensor for label-free detection of inflammatory cytokines in complex fluids *Adv. Biosyst.* **2** 1700072
[21] Aspermair P, Szunerits S and Knoll W in preparation
[22] Larisika M *et al* 2015 Electronic olfactory sensor based on *A. mellifera* odorant-binding protein 14 on a reduced graphene oxide field-effect transistor *Angewandte Chemie* **127** 13443–6
[23] Gianelli M, Roskamp R F, Jonas U, Loppinet B, Fytas G and Knoll W 2008 Dynamics of swollen gel layers anchorred to solid surfaces *Soft Matter* **4** 1443–7
[24] Fromherz P, Offenhäusser A, Vetter T and Weis J 1991 A neuron-silicon-junction: a Retzius-cell of the leech on an insulated-gate field-effect transistor *Science* **252** 1290–3
[25] Lauer L, Vogt A, Yeung C K, Knoll W and Offenhäusser A 2002 Electrophysiological recordings of patterned rat brain stem slice neurons *Biomaterials* **23** 3123–30
[26] Roberts M E, Queralto N, Mannsfeld S C B, Reinecke B N, Knoll W and Bao Z 2009 Cross-linked polymer gate dielectric films for low-voltage organic transistors *Chem. Mat.* **21** 2292–9
[27] Olson W C, Spitznagel T M and Yarmush M L 1989 Dissociation kinetics of antigen-antibody interactions: studies on a panel of anti-albumin monoclonal antibodies *Mol. Immunol.* **26** 129–36
[28] Schwierz F 2010 Graphene transistors *Nat. Nanotechnol.* **5** 487–96
[29] Lee S-K, Kim B J, Jang H, Yoon S C, Lee C, Hong B H, Rogers J A, Cho J H and Ahn J-H 2011 Stretchable graphene transistors with printed dielectrics and gate electrodes *Nano Lett.* **11** 4642–6
[30] Hummers Jr, William S and Offeman R E 1958 Preparation of graphitic oxide *J. Am. Chem. Soc.* **80** 1339
[31] Larisika M, Huang J F, Tok A, Knoll W and Nowak C 2012 An improved synthesis route to graphene for molecular sensor applications *Mater. Chem. Phys.* **136** 304–8
[32] Bintinger J, Eder D and Knoll W in preparation
[33] Georgakilas V, Kordatos K, Prato M, Guldi D M, Holzinger M and Hirsch A 2002 Organic functionalization of carbon nanotubes *J. Am. Chem. Soc.* **124** 760–1
[34] Melzer K, Brändlein M, Popescu B, Popescu D, Lugli P and Scarpa G 2014 Characterization and simulation of electrolyte-gated organic field-effect transistors *Faraday Discuss.* **174** 399–411
[35] Knopfmacher O, Tarasov A, Fu W, Wipf M, Niesen B, Calame M and Schönenberger C 2010 Nernst limit in dual-gated Si-nanowire FET sensors *Nano Lett.* **10** 2268–74
[36] Chun K-Y and Stroeve P 2002 Protein transport in nanoporous membranes modified with self-assembled monolayers of functionalized thiols *Langmuir* **18** 4653–8
[37] Nakhleh M K *et al* 2017 Diagnosis and classification of 17 diseases from 1404 subjects via pattern analysis of exhaled molecules *ACS Nano* **11** 112–25
[38] Neupane S, Peverall R, Richmond G, Blaikie T P, Taylor D, Hancock G and Evans M L 2016 Exhaled breath isoprene rises during hypoglycemia in type 1 diabetes *Diabetes Care* **39** e97–8
[39] Oerke E-C 2006 Crop losses to pests *J. Agric. Sci.* **144** 31–43
[40] Nelson A D, Savary S, Willocquet L, Esker P, Pethybridge S J and McRoberts N 2018 Assessment of crop health and losses to plant diseases in world agricultural foci *Int. Congress of Plant Pathology 2018: Plant Health in a Global Economy*
[41] Bromenshenk J J, Henderson B B, Seccomb R A, Welch P M, Debnam S E and Firth D R 2015 Bees as biosensors: chemosensory ability, honey bee monitoring systems, and emergent sensor technologies derived from the pollinator syndrome *Biosensors* **5** 678–711
[42] Pelosi P, Mastrogiacomo R, Iovinella I, Tuccori E and Persaud K C 2014 Structure and biotechnological applications of odorant-binding proteins *Appl. Microbiol. Biotechnol.* **98** 61–70
[43] Kotlowski C, Larisika M, Guerin M, Kleber C, Kröber T, Mastrogiacomo R, Nowak C, Pelosi P, Schwaighofer A and Knoll W 2018 Fine discrimination of volatile compounds by graphene-immobilized odorant-binding proteins *Sensors Actuators* B **256** 564–72
[44] Bruno J G 2015 Predicting the uncertain future of aptamer-based diagnostics and therapeutics *Molecules* **20** 6866–87
[45] Tiede C 2017 Affimer proteins are versatile and renewable affinity reagents *eLife* **6** e24903
[46] Jur J, Bowles A, Bhakta R, Mayers A, Shahariar H and Twiddy J 2017 Design and commercialization challenges of garment-based textile electronics *The Electrochemical Society Meeting Abstracts* (vol 50) pp 2121

3. Chapter:

Surface Modifications

Bio-sensing needs capture molecules on the transducer surface to bind an analytes selectively, which can only be guaranteed with a suitable surface modification strategy. In this chapter several of such are compared and discussed to fabricate a bio-sensing platform on graphene, reduced graphene oxide and gold.

Materials and Methods

In this section are all used strategies for the immobilization of capture probes on the bio-sensing surfaces. The herein evaluated and discussed methods are non-covalent as well as covalent surface functionalization of graphene and gold. The methods include the immobilization of capture probes for bio-sensing and blocking agents to avoid non-specific binding.

Graphene modification with pyrene-carboxylic acid

The non-covalent functionalization of graphene was reported in a variety of publications. [100–103] The reports mention different graphene-like structures, like single walled carbon nanotubes (SWCNT), CVD graphene, glassy carbon electrodes and rGO. The latter one is the most ill-defined material in the spectrum of graphene, due to the different fabrication procedures. The here investigated surface modifications are demonstrated on CVD graphene and reduced graphene oxide, which were fabricated as reported in Chapter 2: Fabrication of CVD graphene FET and Chapter 2:Fabrication of reduced graphene oxide FET. The non-covalent functionalization of graphene with pyrene

and its derivates is in literature a standard procedure and is used as the anchor-molecule for further immobilization of capture probes. Figure 33 shows schematically the immobilization of 1-pyrenebutyric acid, which has to be activated for further functionalization of azanide groups, referred also as amide or NH_2 group. Another molecule is 1-pyrenebutyric acid N-hydroxysuccinimid ester, that already contains the ester group and the NH_2-terminated capture probe can be directly immobilized.

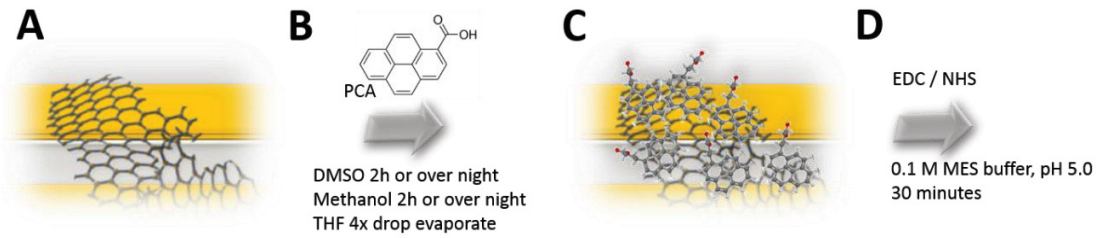

Figure 33: Schematic immobilization of PCA via Pi-Pi stacking on rGO and CVD graphene. A: graphene sheets on interdigitated electrodes. B: PCA solution in different solvents for immobilization. C: Pyrene modified surface with carboxylic acid groups for functionalization. D: The activation duration for EDC and NHS is 30 minutes for all experiments in MES buffer.

The rGO functionalization steps are shown in Figure 33. PCA was prepared in different solvents to determine the best immobilization strategy, always in a concentration of 5 mM. The solvents are DMSO, Methanol and THF. For DMSO and Methanol, the chips were immersed for 2 hours or overnight to determine the best duration. For the THF as solvent a droplet of 20 µL was placed on the sensing area and let it evaporate. This step was repeated four consecutive times. After each deposition method, the chips were thoroughly rinsed with the previously used solvent before the activation.

<u>Activation of carboxylic group:</u>

To activate the COOH group, a mixture of 75 mg/mL (390 mM) N-(3-Dimethylaminopropyl)-N′-ethylcarbodiimide hydrochloride (EDC) and 21 mg/mL (185 mM) N-Hydroxysuccinimide (NHS) in 1 mL of dH_2O was freshly prepared. The activation mixture needs to be prepared right before the gFETs are immersed, because the EDC hydrolysis within 2 hours entirely in water. The chips remain 30 minutes in the solution and are quickly rinsed twice with dH_2O to remove excess of EDC and NHS.

Gold slide DTSP

It is necessary to modify the gold surface for SPR experiments on bare gold slides, therefore the strategy of 3,3′-Dithiodipropionic acid di(N-hydroxysuccinimide ester), short DTSP was used to functionalize Au-surface with bio-recognition elements. The gold slides were immersed in a 4 mM DTSP solution in DMSO in a glass slide holder. The slides remain in the solution for 24 hours under gentle agitation. Subsequently, the slides are stored for another 24 hours at nitrogen atmosphere. Figure 34 depicts the surface functionalization of gold slides with DTSP for SPR experiments.

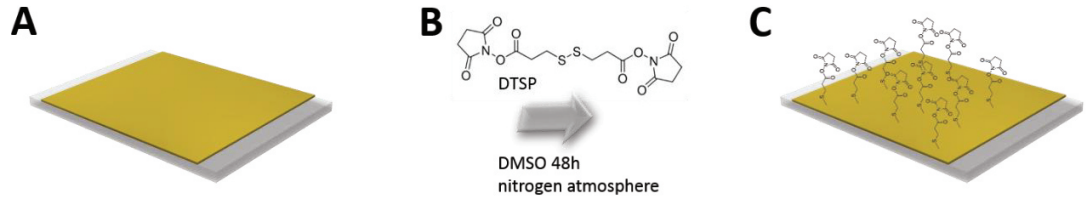

Figure 34: Functionalization of a gold surface with DTSP molecule. The di-sulfide bridge reacts within 48h to form a covalent bond to the Au-surface. The NHS head group remains activated on the surface for the immobilization of NH_2-terminated capture molecules.

This leads to a covalent bond of the thiol to the gold substrate. The active ester on the gold slides is used to immobilize the NH_2-modified capture probe covalently on the surface in an additional step.

Gold slide biotinylation

A reliable binding system is biotin with streptavidin or neutravidin, which shows the highest affinity in nature with a K_D of 10^{-14}. [104] The functionalization of gold slides was performed with a mixture of a biotinylated Alkane-PEG, SPT-0012D (SH-biotin) and dithiolalkanearomatic-PEG3-OH, SPT-0013 (SH-PEG) from Sensopath. Both substrates were prepared in analytical Ethanol at concentrations of 0.1 mM for SH-biotin and 0.9 mM for SH-PEG. Subsequently, both mixtures were added in equal volumes to obtain a 1:10 ratio of biotin/PEG. The gold slides were immersed for 24 hours to the biotin/PEG solution,

were the thiol group covalently binds to the Au-surface. Figure 35 shows schematically the surface modification with the SH-biotin and SH-PEG 1:10 mixture.

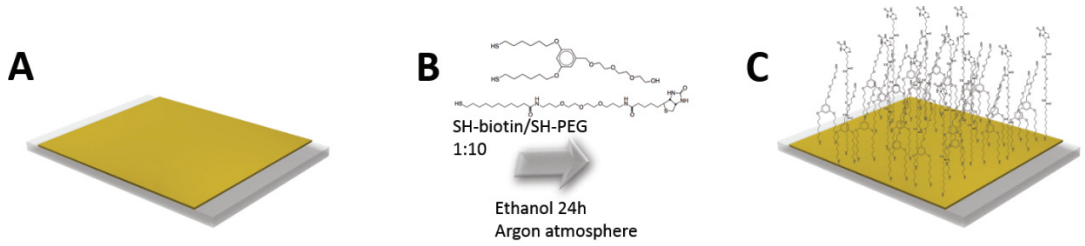

Figure 35: Modification of gold slides with SH-biotin and SH-PEG derivates in a ratio of 1:10 in ethanol for 24 hours. The surface modification enables the immobilization of streptavidin to the biotin. The PEG chain with an OH terminal group avoids non-specific interaction with the gold surface.

Once the surface is modified with biotin, it can used in SPR and gFET/SPR measurements to measure the binding kinetics.

Immobilization of amine-terminated capture probe

Subsequently, after immobilizing the PCA and activation of the surface or immobilization of DTSP with the pre-activated group, any amine-terminated capture probe can be immobilized, forming a covalent amide bond. Therefore, the capture probe was dissolved in carbonate buffer at pH 9.0. The standard immobilization duration was 2 hours, only the PNA, DNA, RNA were immobilized overnight. For ssDNA (Aptamer), ssRNA (Aptamer) and PNA a concentration of 0.5 µM to 10 µM was used in an overnight immobilization step to assure functionalization. Only in real-time experiments, using SPR to observe the binding kinetic, the monitored immobilization was carried out until saturation was achieved.

Immobilization of Streptavidin modified molecules

The immobilization of streptavidin or streptavidin-complexes was performed in a concentration of 1 mg/mL. For binding kinetic studies, the buffer for dilution and immobilization was PBS 1x buffer. For streptavidin-enzyme conjugates, the buffer was Tris buffer with $MgCl_2$, adjusted to pH 8. Therefore, to a final volume of 50 mL dH_2O, 606 mg of Trizma base and 4.76 mg of MgCl2 were added and adjusted to pH8 with HCl.

Blocking agents

Different blocking agents can be used to avoid nonspecific interactions with the sensor surface, the tested strategies were BSA, pyrene-PEG, and just pyrene carboxylic acid.

BSA blocking solution:

Bovine Serum Albumin was prepared in a concentration of 20 mg/mL in PBS (pH 7.4) and deposited on the sensor surface after the capture probe was immobilized to back-fill the remaining non-specific binding sites on the surface. The sticking properties of BSA avoid the binding of other molecules to the surface to a certain extent.

Synthesis of PyPEG

The synthesis of a pyrene anchor molecule with a poly(ethylene glycol) group was carried, because this molecule was not directly available for purchase. The protocol was adapted from [103] and requires three days. Figure 36 shows educts used, resulting in a pyrene with a 34-mer polyethylene glycol chain, later referred as $PyPEG_{34}$ or PyPEG.

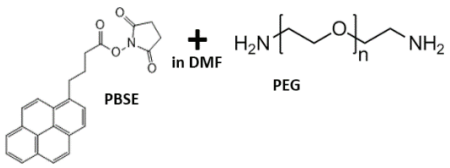

Figure 36: Synthesis of $PyPEG_{34}$: The PBSE linker forms an amide bond with the amine-terminated PEG chain. The pyrene PEG will be used to immobilized it with π-π-stacking on graphene to avoid non-specific binding to the surface.

The following chemicals are required for the synthesis:

- PEG_{34}
- PBSE
- DMF
- DCM
- Diethyl ether

Day 1:

1. Make solutions of PEG and PBSE in separated round-bottom flasks:
   1:1 equivalent solution (2 NH_2 + 1 COOH). PBSE should not exceed amount, otherwise binding to both PEG ends.
   a. PEG 100 mg in 3 mL DMF + steering magnet
   b. PBSE 25.6 mg in 2 mL DMF
2. Fill bottles with inert gas (N or Ar):
   Apply septum on top, insert syringe in solution and fill it for 10 minutes with gas. The reaction has to be performed in inert gas.
3. Extract 2 mL of PBSE solution with Syringe and add to PEG solution:
   Keep in mind to also flush the syringe with inert gas before usage.
4. Steering overnight:
   Fill a balloon with inert gas and apply it via syringe to the overnight reaction to ensure an inert condition.
5. Fill Erlenmeyer flask wit 250 mL diethyl ether:
   Cover it with aluminium foil and parafilm and store it over night at -20 °C.

   Day 2:

6. precipitation of PyPEG in diethyl ether:
   Take off aluminium foil of Erlenmeyer flask.
   Remove balloon and septum from PyPEG-DMF solution.
   Slowly pipetting the 5mL drop by drop into diethyl ether.
7. Storage over night for complete precipitation
   Put aluminium foil on top of Erlenmeyer flask and store it overnight at -20 °C.

   Day 3:

8. Centrifuge the PyPEG diethyl ether solution:
   Divide the 250 mL into 8 Falcon tubes.
   Centrifuge the falcons for 10 min at 4500 rpm.
9. Remove excess of diethyl ether:
   PyPEG is as white solid on the Falcon's bottom.
   Poor waste to non-halogen organic waste.
10. Dissolve solid PyPEG:
    Add 5 mL Dichloromethane (DCM) in each Falcon and poor it into one glass tube (weigh it before to know the yield).
    Add another 1 mL DCM to each Falcon to get remaining PyPEG.

11. Rotary evaporation of DCM from glass tube for 1 hour:
    Put glass tube in rotary evaporator with glassy adapter, septum and syringe.
    Set water temperature to 40 °C and turn on vacuum.
    Rotary speed to 10 (maximum speed).
12. Extract remaining DMC from tube:
    Cover the glass tube with parafilm and make some holes.
    Store it overnight in desiccator at vacuum.

Once the PyPEG is available in a dry state, it can be stored in a glass flask in the fridge.

SPR for blocking performance

To analyze the blocking strategies of BSA, PCA and PEG34, a commercial available SPR device, the Indicator-G from Sensia was used. This device provides a microfluidic system and SPR prisms with CVD graphene coating from Graphenea, which is identical to the CVD graphene for the gFET fabrication, hence the knowledge of the SPR experiments can be transferred to the gFET surface. At first the non-specific response of the SPR with different surface modifications was measured, to see which strategy is suitable. Afterwards, it was necessary to determine the mixture ratio of blocking and binding agent, the Pyrene-PEG/PCA ratio. As a non-specific binding species, the strongly adhering bio-molecule Lysozyme was used in various concentrations. The solutions in different concentrations were always freshly prepared on the day of the experiment in PBS 1x buffer.

Nanobeads immobilization

To determine the best functionalization of reduced graphene oxide and CVD graphene with pyrene-carboxylic acid (PCA), different solvents were investigated. Polystyrene nanobeads with a diameter of 50 to 120 nm were linked to the graphene to visualize the immobilization success with SEM imaging. PCA was dissolved in the different solvents DMSO, methanol and THF, as mentioned in Chapter 3: Graphene modification with pyrene-carboxylic acid, including the EDC/NHS activation. The nanobeads suspension L9904 from Sigma Aldrich with a solid content of 2.3 to 2.7 wt%

was immersed in Milli-Q water to obtain 3.6 x 10^{-19} nanobeads in 1 mL. This concentration represents 60 nM, which is in the same order as for bio-molecule immobilization. Figure 37 represents the immobilization strategy of the amino-modified polystyrene nanobeads on rGO. The diameter of the nanobeads can be also observed in a SEM image. Pyrene-PEG was also immobilized on the surface to observe the blocking properties to avoid non-specific interaction with rGO.

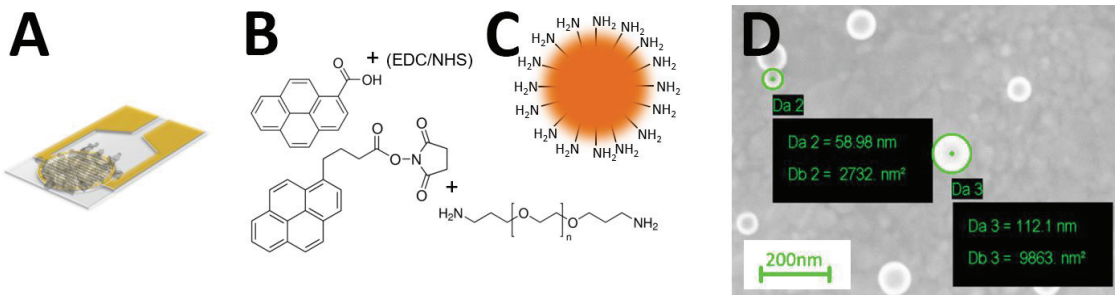

Figure 37: The immobilization strategy of amino-modified polystyrene nanobeads on the rGO of the gFET (A) is shown. The nanobeads (C) are immobilized to observe the surface coverage with different solvents for pyrene carboxylic acid and pyrene-PEG (B). D represents a SEM image of polystyrene nanobeads on rGO. The diameter was measured with 60 nm to 120 nm.

Differential pulse voltammetry for surface investigation

Differential pulse voltammetry was utilized to determine the efficiency of the surface linking strategy. The π-π stacking, as described in Chapter 3: Graphene modification with pyrene-carboxylic acid, is the first building block of a successful bio-functionalization of graphene on the gFET. The linker, pyrene carboxylic-acid (PCA), forms a non-covalent bond with the pyrene anchor to rGO, while the carboxylic-acid can form an amide bond to bio-recognition elements. An artificially synthesized peptide nucleic acid (PNA) was covalently bond to the activated carboxylic-acid with the amine-modified 5'-end. The 3' end of the PNA is biotinylated and can be used for a non-covalent binding of streptavidin, avidin or neutravidin due to the high binding affinities. A streptavidin-alkaline phosphatase complex was immobilized to attach an enzyme on the surface. After assembly of the entire sandwich, the surface was thoroughly rinsed to guarantee only immobilized enzymes remain on the chip. Once attached to the surface,

alkaline phosphatase can enzymatically turn hydroquinone diphosphate into an electrochemical active species, hydroquinone [79,105].

Figure 38 shows the enzyme functionalization of an already carboxylated surface. The experiment was carried out on a commercially available reference chip with carboxylated single-walled carbon nanotubes (COOH-SWCNT) and reduced graphene oxide.

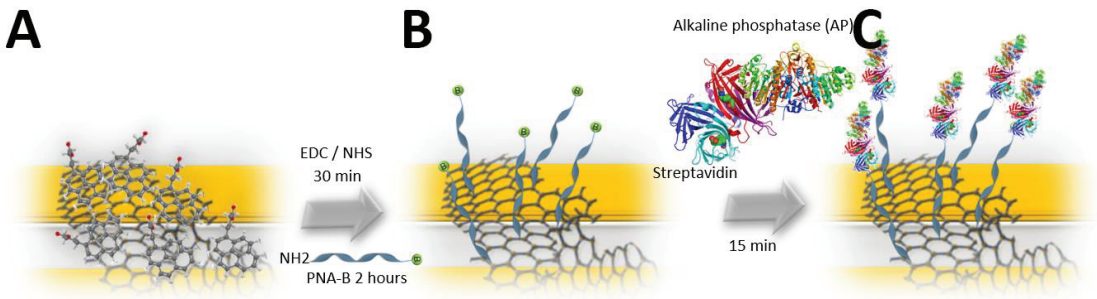

Figure 38: (A) shows a graphene surface with carboxylic-acid functional groups for further immobilization. (B) shows a biotinylated PNA, covalently linked to the carboxy groups. The alkaline phosphatase enzyme is immobilized as a complex with streptavidin to the biotinylated end of the PNA (C).

The PNA was used as spacer between the graphene surface and the enzyme. Two different carboxylated surfaces were used for the DPV readout: single-walled carbon nanotubes on screen-printed electrodes (SPE), purchased from Dropsens, 110SWCNT and on the fabricated rGO gFET. The SWCNT electrodes were used as reference measurement to know if the entire sandwich works. These SPEs are delivered with pre-modified carboxylic-acid groups, so there is no need for a further attachment of COOH on the surface. That is very useful to compare the performance to the π-π stacked PCA on the rGO surface.

The experiments were carried out with a potentiostat µAutolab III from Metrohm in a three-electrode configuration. The working electrode was the SWCNT or the rGO, respectively. A Pt-wire was used as counter electrode and an Ag/AgCl electrode as reference electrode. The differential pulse voltammetry settings are shown in Figure 39.

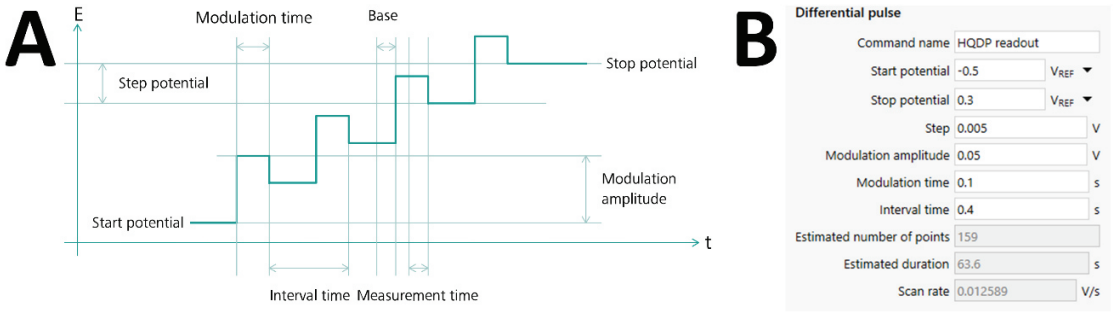

Figure 39: The readout of Hydroquinone (HQ) was carried out with differential pulse voltammetry in a range of -0.5 V to +0.3 V. The pulse sequence is shown in (A), where it is indicated that the "measurement time" is at the end of the modulated amplitude. All settings for the DPV readout are shown in B. Between -0.1 V and 0.0 V the DPV peak for HQ is expected.

Graphene modification with diazonium treatment

The surface modification of the reduced graphene oxide or CVD graphene with biomolecules is a necessary step towards an electrical biosensing platform. The functionalization of graphene can be separated in different groups: direct physisorption of biomolecules[106], non-covalently with π-π-interaction[107–109], covalently to organic functional groups or remaining oxygen groups on graphene oxide [110] or by disrupting the graphene lattice to introduce new functional groups [111,112]. The latter immobilization strategy is the strongest and therefore most reliable surface modification, yielding the highest surface coverage of linker molecules to bind bio-recognition elements.

The covalent functionalization of rGO and CVD graphene was achieved by a diazonium treatment, radically attacking the C-C bonds with aryldiazonium salt, reported by Leroux et al.. [113] This method was carried out for rGO by adopting the protocol for the gFET. The diazonium salt, precisely 4-((triisopropylsilyl)ethylenyl)benzenediazonium tetrafluoroborate, short TIPS-Eth-ArN_2^+, was synthesized by the Leroux et al. and kindly provided for this research purpose. Electrochemical grafting was used to radically attack the C-C bonds of the graphene surface. Five cyclic voltammetry scans from +0.6 V to -0.75 V at a scan rate of 50 mV/s lead to the reduction of TIPS-Eth-ArN_2^+, hence creating the aryl radicals at a reduction peak of -0.2 V. Due to the TIPS protected head group, the formation of a mono layer on graphene is granted, because the newly formed radicals

cannot stack onto the first formed layer. This is an important step towards a biosensing surface to avoid multiple layers and hinder the further bio-functionalization. The potentiostat µAutolab III form Metrohm was used to apply the potential cycles in a three-electrode configuration: Au/graphene as working electrode, a Pt-wire as counter electrode and a Ag/AgCl reference electrode. All electrodes were immersed in a solution of 1 mM 4-((triisopropylsilyl)ethylenyl)benzenediazonium tetrafluoroborate in 0.1 M NBu_4PF_6 in acetonitrile. Subsequently to the deposition, the graphene-based surface was rinsed thoroughly with acetonitrile, acetone and blow dried with inert gas (argon or nitrogen).

Once the deposition of the TIPS protected monolayer is finished, it was deprotected with submerging the chip in a 50 mM tetrabutylammonium fluoride (TBAF) in THF solution for 20 minutes. The so-called "click" chemistry of azide modified compounds is performed under a copper-mediated environment: the chip was submerged in an aqueous solution containing 10 mM $CuSO_4$ and 20 mM L-ascorbic acid in a 0.83 mM azidomethylferrocene, beforehand dissolved in THF under agitation of 300 rpm for one hour, the copper mediated click chemistry of ferrocene was performed. To remove residues of Cu_2^+ from the surface, the graphene surface was submerged in an aqueous solution of 10 mM EDTA for 10 minutes and subsequently rinsed with acetone and dH_2O and blow dried afterwards.

The schematic of the surface modification with diazonium salt, the deprotection of the TIPS group to obtain the acetylene functional group and the cupper mediated "clicking" of azide terminated ferrocene is shown in Figure 40.

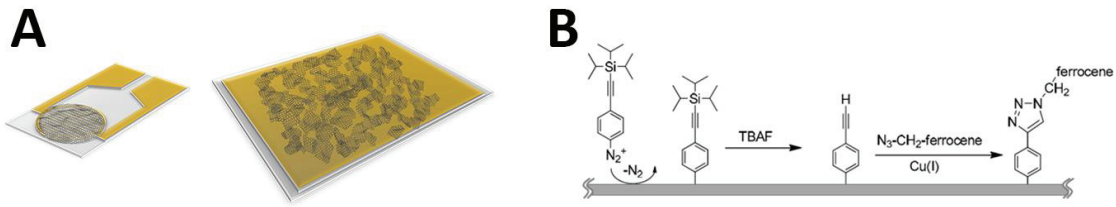

Figure 40: The diazonium modification of reduced graphene oxide and CVD graphene was carried out on the gFET chip to investigate the transfer characteristic after modifications. Au-slides with rGO were functionalized as well. Figure B illustrates the radical diazonium attack of graphene, the deprotection to obtain a triple bond group and the further "click" of ferrocene on the surface.

Results of surface modification

The different surface modifications of graphene and gold are shown in this chapter. Furthermore, the results of non-specific binding interactions with the surface for different blocking strategies and shown and discussed, as well the electrical performance of the gFET after the diazonium treatment.

SPR experiment for blocking agents

Surface plasmon resonance measurements were conducted to determine the best blocking agent for further bio-sensing measurements on the graphene surface. The SPR prisms with 50 nm gold are coated with CVD graphene from Graphenea and the surface was modified with different blocking agents, such as BSA, pyrene carboxylic-acid and the herein synthesized blocking agent PyPEG with a 34-mer polymer chain. The test protein to observe non-specific interaction, was lysozyme, a sticky and rather small (14.4 kDa) analyte. A titration of 1 µM up to 500 µM was carried out to stress the surface for NSB and the adhesions are shown in Figure 41.

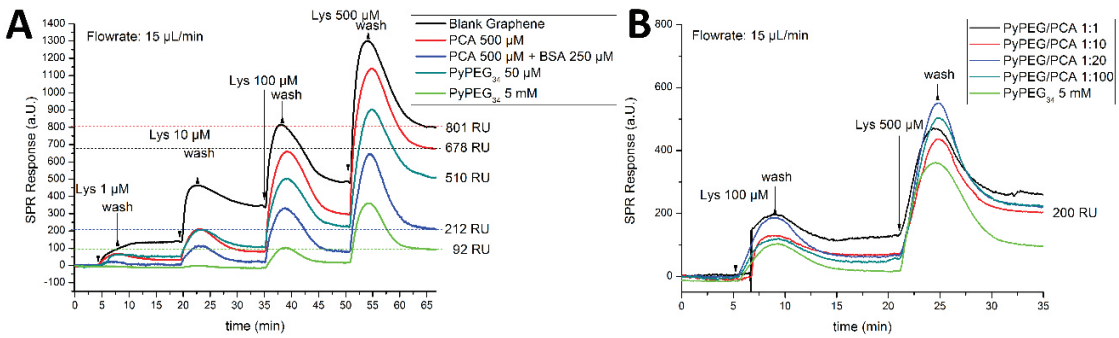

Figure 41: The blocking agents to avoid non-specific interaction where investigated on the commercially available SPR device, Indicator-G from Sensia. The SPR prisms have gold coating with a CVD graphene layer from Graphenea. A: The adhesive molecule lysozyme was exposed to the modified SPR surface. Different blocking agents suppress the binding signal. PyPEG$_{34}$ with a 5 mM concentration avoids a binding of up to 10 µM lysozyme almost to 100%. B: The determination of a balanced ratio of blocking agent and binding molecule is important to be able to immobilize a specific capture probe. The ratio of 1:10 blocks the NSB sufficiently.

The results of the non-specific binding experiments of lysozyme on the CVD graphene surface with SPR indicate good blocking properties of $PyPEG_{34}$. Concentrations of 10 µM are almost completely suppressed with a concentration of 5 µM $PyPEG_{34}$ immobilized on the surface. The ratio of 1:10 PCA/$PyPEG_{34}$ on the surface enable the immobilization of bio-recognition elements on the surface and keeps the unspecific binding at a very low level, even at high lysozyme concentrations of 500 µM and the SPR signal is with 200 RU still smaller than with the BSA blocked surface, shown in the comparison of Figure 41 (A) and (B). Therefore, the surface modification for protein detection experiments will be performed with PCA/$PyPEG_{34}$ in the evaluated ratio of 1:10.

XPS Aptamer surface coverage

The XPS experiments show the quantity of P 2p phosphate on the functionalized rGO surface. Three surfaces were measured in the XPS to determine the aptamer yield of the immobilization of amine-terminated ssDNA. The samples were functionalized with

A: PCA, activation, ssDNA (aptamer) (D)

B: PCA/PyPEG 1:10, activation, ssDNA (aptamer) (E)

C: PCA/PyPEG 1:10, no activation, no DNA. (control experiment) (F)

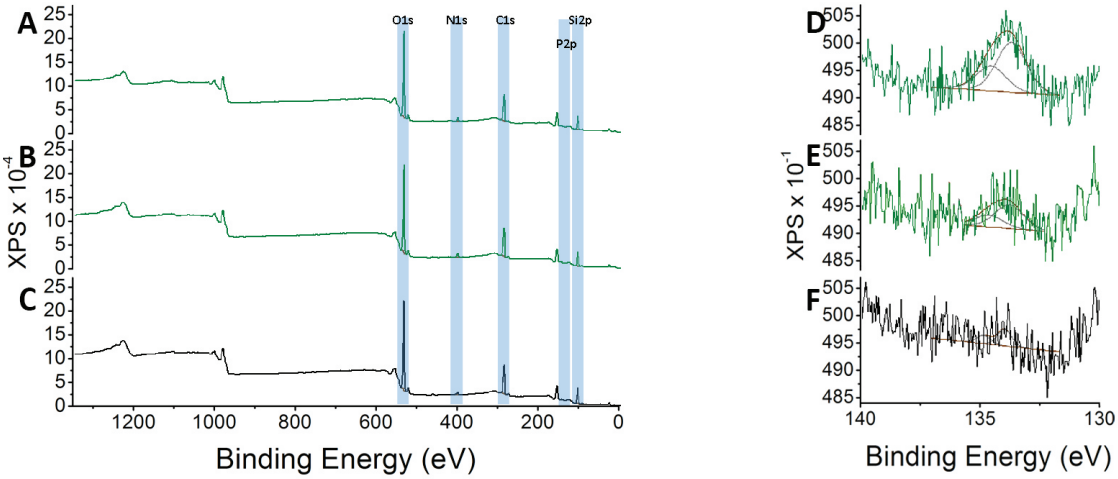

Figure 42: The XPS measurement show the aptamer immobilization on three different surfaces. A: The rGO surface was modified with 1 mM PCA, activated and ssDNA (aptamer) was immobilized. B: The rGO surface was modified with a 1:10 mixture of PCA/PyPEG (0.1 mM, 0.9 mM), activation and subsequently immobilization of the aptamer. C: Control measurement with a 1:10 PCA/PyPEG ratio, but without aptamer. D, E and F show the

corresponding phosphate groups on the surface. D: Quantity of P 2p signal estimated at 0.2 at%. E and F: Quantity of P 2p signal estimated smaller than 0.1 at%.

The result, Figure 42, show only very small P 2p signals with the highest output for probe A with around 0.2 atomic percent. The samples A and B show no significant phosphate increase compared to the control sample C, resulting in a very low surface coverage of aptamer on the surface. The surface modification with PCA and PCA/PyPEG and the given solvents needs to be discussed and maybe improved in additional experiments. The replacement of aptamer with other molecules can lead to better results. The immobilization of amino-modified polystyrene nanobeads is shown in Chapter 3: Nanobeads SEM images.

Nanobeads SEM images

The immobilized polystyrene Nanobeads were investigated with scanning electron microscopy (SEM) to visualize the surface coverage after linking to pyrene carboxylic acid (PCA), immobilized with different solvents Figure 43, Figure 44, Figure 45 und Figure 46 demonstrate the surface coverage of nanobeads on the rGO surface of different gFETs.

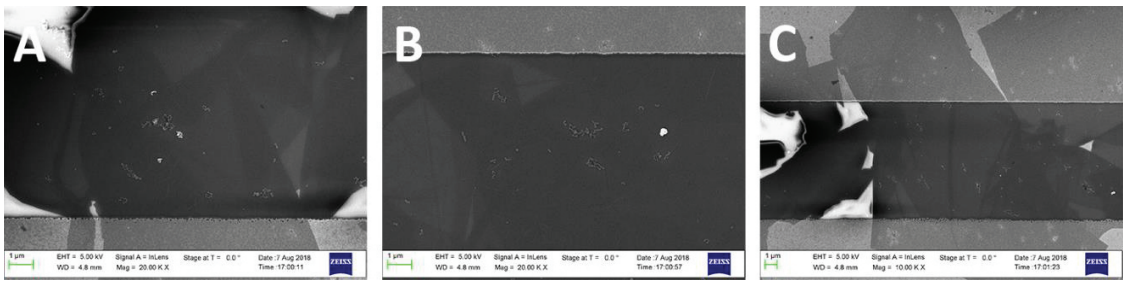

Figure 43: PCA immobilized for 2h in DMSO. Nanobeads linked afterwards with a low surface coverage.

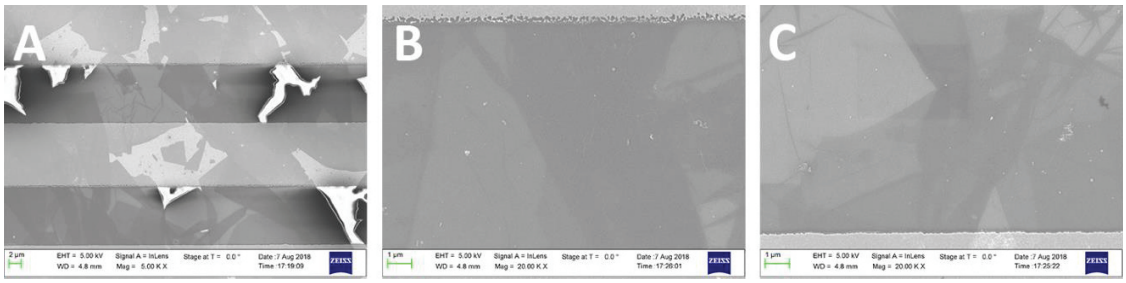

Figure 44: PCA immobilized for 2h in Methanol. Only a few Nanobeads are traceable.

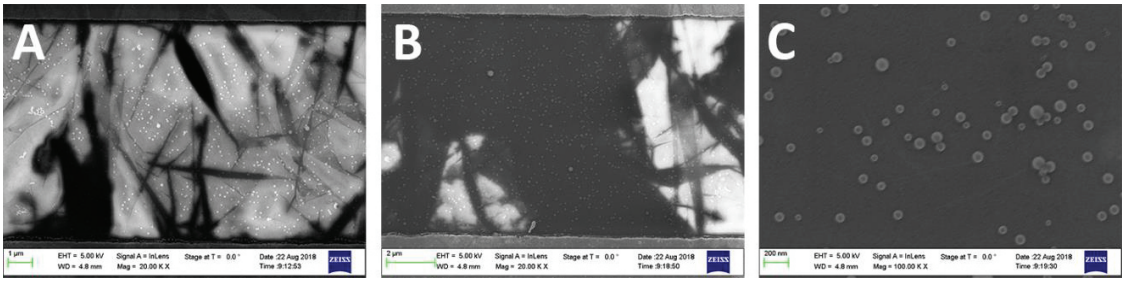

Figure 45: PCA immobilized in THF after 4 times evaporation. Nanobeads concentration with highest surface coverage.

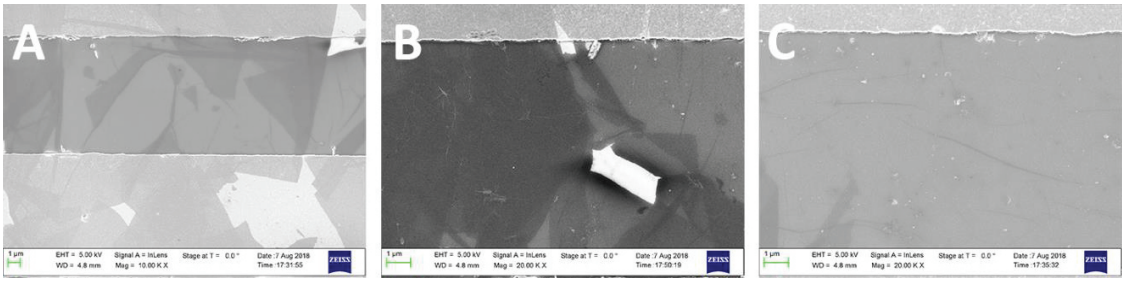

Figure 46: Pyrene-PEG$_{34}$ as a blocking agent. The surface coverage is as expected very low. There was no nanoparticle traceable. The white spots are defects on the graphene.

After the nanobeads were immobilized, the density was evaluated from the SEM images with the graphical picture processing tool ImageJ. The example for the threshold manipulated picture for the PCA in THF is shown in Figure 47 (A). The surface coverage was determined from the pixel count for all 4 surfaces and the percentage values are shown in Figure 47 (B).

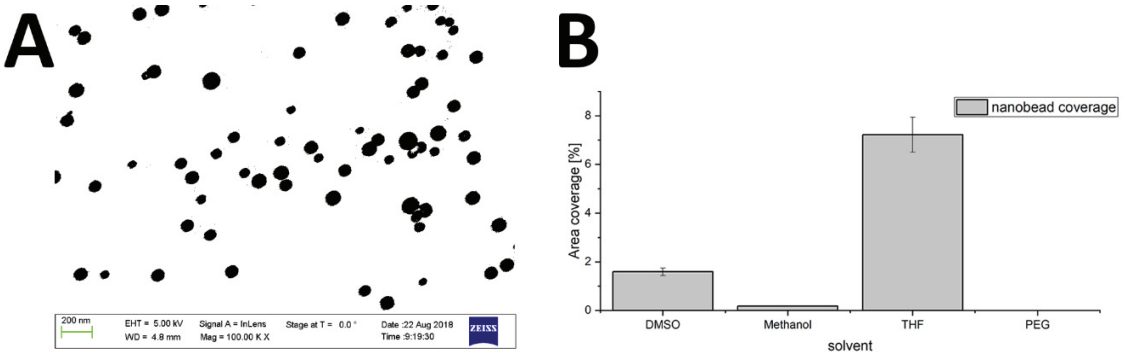

Figure 47: (A) shows the monochromic representation of the nanobead coverage with pyrene carboxylic acid in THF. (B) shows calculated surface coverages of nanobeads after immobilization to pyrene carboxylic acid and pyrene-PEG, dissolved in different solvents. The highest surface coverage was achieved with PCA dissolved in THF. No nanobead could be found on the pyrene-PEG blocked surface.

Differential pulse voltammetry enzyme readout

DPV measurements were performed to compare the surface coverage of bio-recognition elements on rGO chips, Au slides and carbon nanotubes with carboxylated surfaces. The immobilized alkaline phosphatase enzymatically turns hydroquinone diphosphate into the electrochemical active species for readout. [79] The amount of immobilized enzyme on the sensor surface indicates the efficiency of the pyrene carboxylic acid linking strategies in different solvents and is compared to a commercially available carbon-based sensor, the screen-printed electrodes (SPE 110SWCNT, Dropsens) with single walled carbon nanotubes (SWCNT) with carboxylic acid functional groups. In Figure 48 are the DPV experiments shown of the reference system on the SPEs and three different solvents for the PCA immobilization on rGO gFETs. Each DPV measurement was carried out as a specific binding experiment (pos, red curves) and control experiment where the binding sites should not be present (control, black curves), hence exhibit a small signal during the readout. The measurement in Figure 48 (A) demonstrate the DPV peak of the hydroquinone readout. This reference measurement with pre-modified COOH groups yield in a high current peak at about -0.5 V. Both signals, the positive and control measurement, were evaluated with the peak-analyser method in the NOVA software to determine the current peak magnitude. The dashed lines are the baseline for the signal and the Δcurrent in µA represents the electrochemical active species in the measurement setup. All current peaks were evaluated accordingly and for each surface modification the *pos* and *control* were compared in Figure 49. It can be shown, that the modification of SWCNT-COOH on the SPE, the reference measurement, exhibits the highest current for the positive measurement, of more than 25 µA, while the gFET readouts generate a current less than 1 µA. This is due to the different dimensions between the SPE and Micrux sensing area and the fact that SWCNT have an increased surface area, due to their 3D structure. The experiments were also carried out on biotinylated Au-slides to verify the surface modification of the SPR slides, shown in Figure 50 (A). The comparison of all signal-to-noise rations, determined by the ratio of positive to control experiment are shown in Figure 49 and Figure 50 (B). The surface modification with pyrene carboxylic acid, dissolved in THF leads to the highest S/N-ratio

of almost 10, comparable to the modification of the Au slide with a ratio of 8.9, and double the SWNCT S/N.

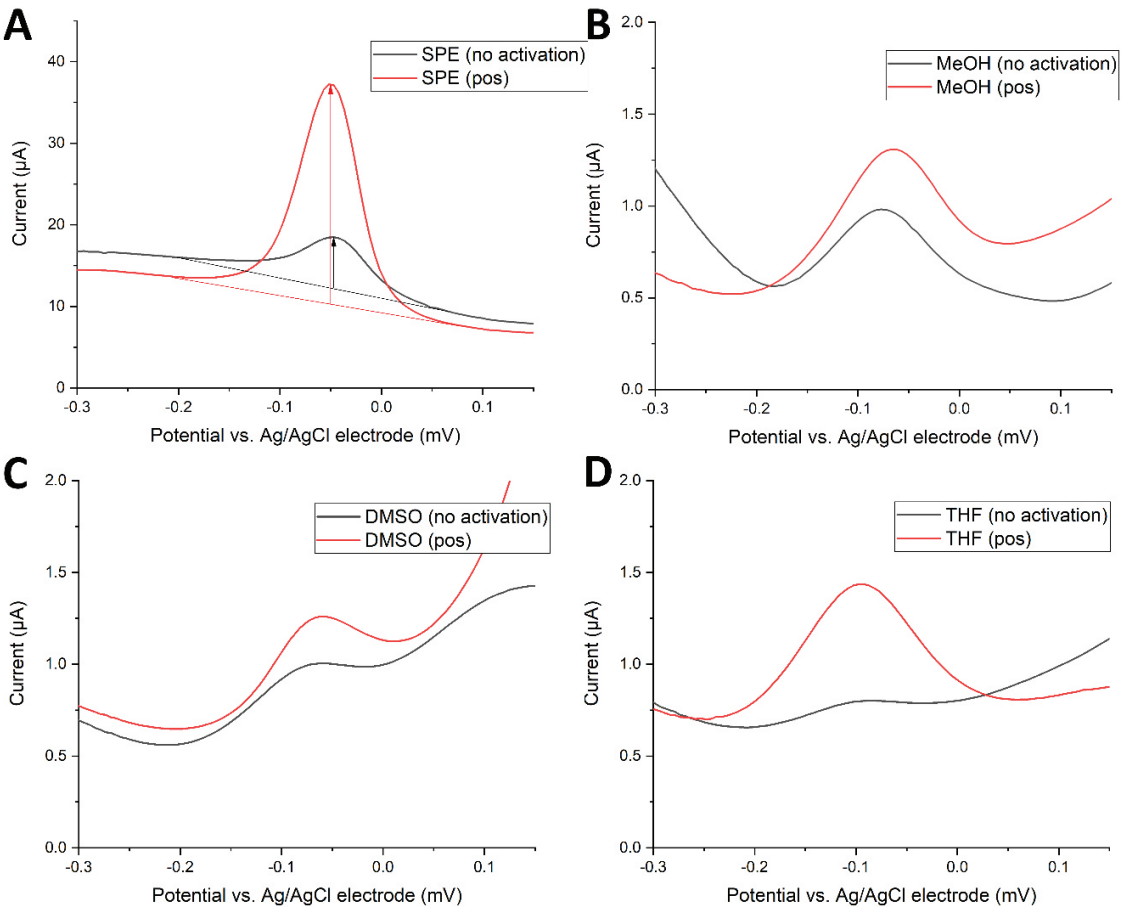

Figure 48: The plots show the differential pulse voltammetry readouts of different surface modifications. A: Screen-printed electrodes with SWCNT-COOH. The heights of the peaks are evaluated as shown with arrows in the plot. B: Reduced graphene oxide with immobilized pyrene carboxylic-acid (PCA) dissolved in methanol, C: PCA dissolved in DMSO and D: PCA dissolved in THF. The red lines are the positive readouts after the immobilization of amine-5'-PNA-3'-biotin and alkaline phosphatase complexation. The black lines are the control experiments, where the activation of the carboxylic-acid was left out. The SPE results are the reference measurements with pre-modified carboxylic-acid groups on the surface, while the rGO surfaces must be modified with a pyrene carboxylic-acid linker to immobilize the bio-recognition element.

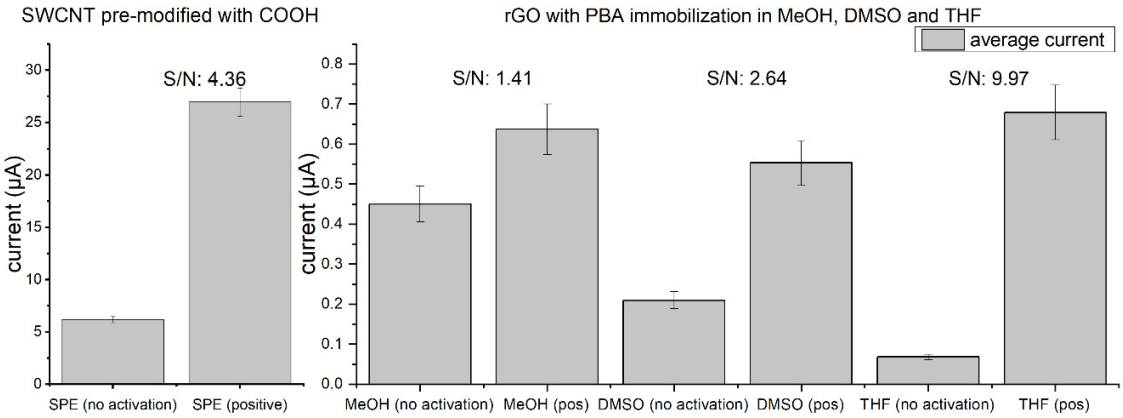

Figure 49: Comparison of SWCNT with COOH-groups and rGO gFETs with different solvents for pyrene carboxylic acid immobilizations. The responses are the peak heights of each surface modification after the enzymatic reaction to convert hydroquinone diphosphate to hydroquinone, an electrochemical active species. It can be observed, that the functionalization of rGO with PCA in THF results in the highest peak and leads to the highest signal-noise ratio (S/N) of 9.97, indicating a successful surface modification with PCA dissolved THF.

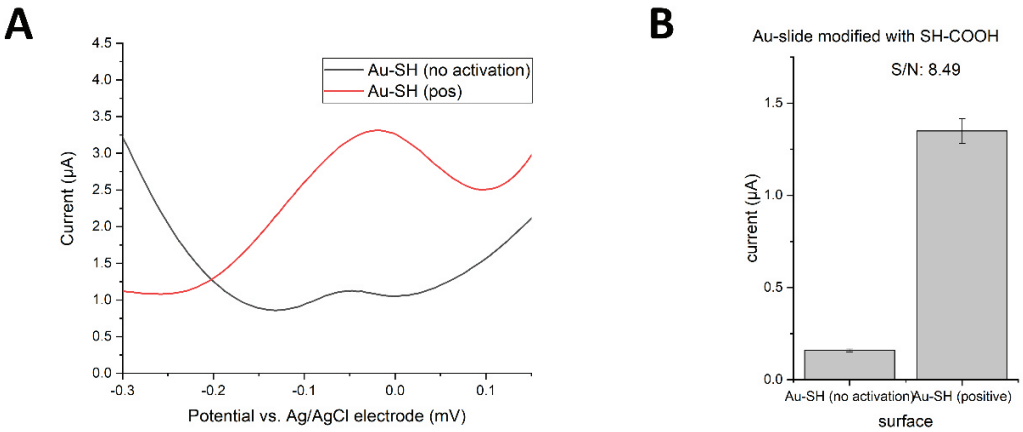

Figure 50: The differential pulse voltammetry readout of the enzyme reaction on Au-slides with 3,3'-Dithiodipropionic acid di(N-hydroxysuccinimide ester), short DTSP, modification is shown in (A). The control experiment was without immobilized biotinylated PNA (COOH not activated), hence there was no biding site for the enzyme to convert HQDP to HQ. The control experiment indicates the non-specific adsorption to the Au-surface. The signal-noise-ratio (S/N) is around 8.5 and indicates a successful surface modification with DTSP (B).

Performance of diazonium treated gFET

The immobilization of TIPS-Eth-ArN_2^+ was carried out with 5 cyclic voltammetry cycles from -0.6 V to +0.6 V. The reduction is most prominent in the first cycle and decreases each cycle due to the fact, that the surface modification is self-inhibiting after the TIPS-protected diazonium is attached to the surface, show in Figure 51 (A). The direct electron transfer from a redox-couple in solution is hindered if the deposition of the TIPS-Eth-ArN_2^+ was successful. The cyclic voltammetry experiment indicating a successful surface coverage is show in Figure 51 (B) on the gFET. The comparison of a gFET before the deposition yields to a prominent oxidation peak at 0.25 V and a reduction peak at 0.2 V (black curve). After deposition of the TIPS-protected diazonium, the current decreases (red curve), indicating a blocked surface. After the TIPS deprotection, the redox current returns to the level of the unmodified gFET due to the successful deprotection. Figure 51 (C) shows the cyclic voltammogram of the "clicked" N3-Ferrocene compound on the surface. The redox reaction of ferrocene covalently immobilized on the gFET surface exhibits peaks at 0.463 V and 0.385 V (ΔE = 78 mV). The integration of the area below the curve indicates a surface coverage of Γ =4.37 10^{-10} mol/cm^2, whereas the maximum surface coverage at a densely packed ferrocene is Γ_{max}: 4.4 10^{-10} mol/cm^2. The calculated coverage of Γ/Γ_{max} is therefore 0.993%. Due to the wrinkled rGO surface and 3D arrangement of the ferrocene molecules it can be discussed the real maximum surface coverage Γ_{max} is higher, but the degree of immobilization still exceeds non-covalent immobilization strategies by far.

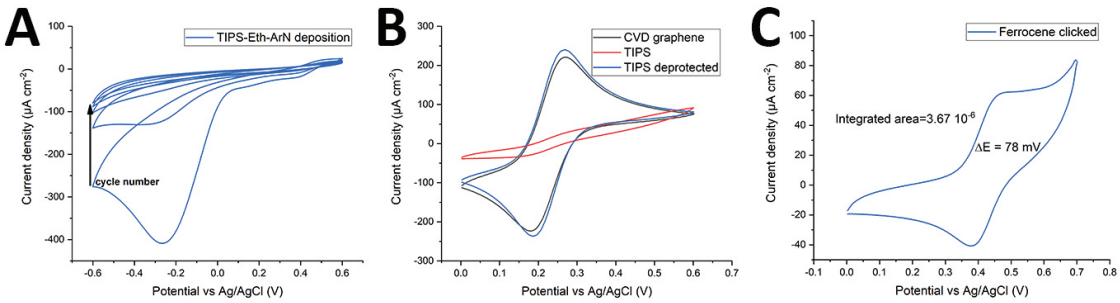

Figure 51: The cyclic voltammograms of click chemistry on graphene. The rapid decrease in (A) indicates a successful deposition of diazonium, forming only a mono layer on the graphene surface. (B) represents the successful TIPS deprotection and in (C) the clicked ferrocene exhibits oxidation and reduction peaks, proving a successful clicking. The calculated surface coverage Γ of ferrocene is approximately greater than 95%.

After the click chemistry was proven to work with electrochemical experiments, the surface morphology of graphene after the harsh treatment with diazonium is shown with SEM images of CVD graphene. Figure 52 shows the results of the surface modification before and after diazonium treatment.

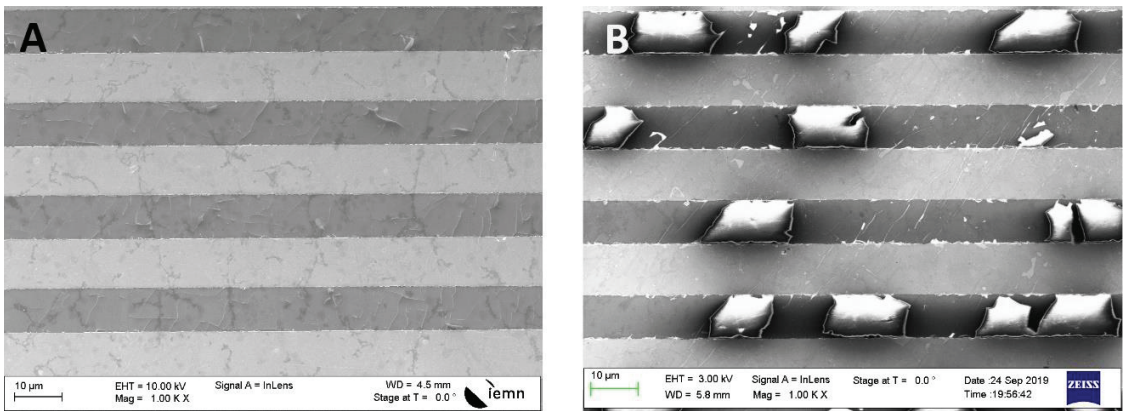

Figure 52: The diazonium treatment of CVD graphene leads to a cleavage of parts of the monolithic graphene layer. While the CVD graphene after deposition shows minor cracks, but a completely coverage of the drain-source channel (A), the CVD graphene after the radical attachment exhibits substantial defects and removed graphene parts in the FET channel (B).

The diazonium treatment for the covalent surface modification leads to a lift-off of CVD graphene from the glass substrate. The adhesion layer of CVD graphene was formed by Triethoxyphenylsilane but forms a non-covalent bond to graphene. The resulting electrical properties of partially removed CVD graphene have to be investigated with I_DV_G curves to investigate if the chip can be used as a bio-sensor. These damages were not observed on reduced graphene oxide.

I_DV_G curves and mobility

Due to the covalent surface modification and the observed damages, visible in SEM images, it is necessary to determine the functionality of the graphene substrate after the harsh treatment with diazonium. Morphological investigations, such as SEM imaging were successful to prove the presence of the substrate, but the electrical properties need to be investigated for further sensing properties. The transfer characteristic of the graphene FET is a parameter to observe the semiconducting properties of the channel material and to

compare the before and after state. In Figure 53, the I_DV_G curves of rGO FET (A) and CVD graphene FET (B) before and after diazonium treatment are shown. The slope of the p-type curve (left of the Dirac point) was evaluated using a linear fitting to obtain the value for m_{lin} and calculate the mobility.

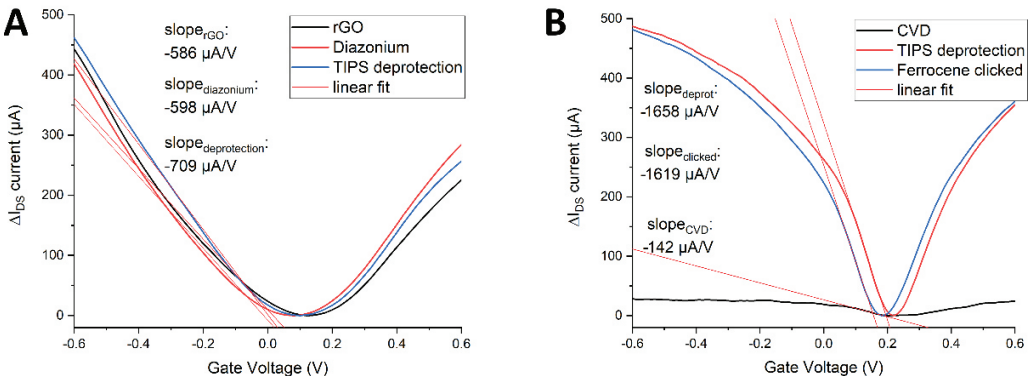

Figure 53: The I_DV_G curves before and after the diazonium treatment lead to only minor changes of the transfer slope for reduced graphene oxide (A), while the CVD graphene exhibits a significant increase of more than a ten-fold for m_{lin} (slope). The diazonium attack of the graphene lattice improves the semiconducting properties for CVD graphene.

The mobility of the gFET can be calculated from the slope of the linear fit, as previously reported in Chapter 2: Mobility calculation with eq 7. The results of the mobility µ for rGO and CVD graphene FETs are:

$\mu_{rGO} = 725\ {}^{cm^2}/_{Vs}$ $\mu_{diazonium} = 740\ {}^{cm^2}/_{Vs}$ $\mu_{deprotected} = 877\ {}^{cm^2}/_{Vs}$

$\mu_{CVDg} = 142\ {}^{cm^2}/_{Vs}$ $\mu_{deprotected} = 1658\ {}^{cm^2}/_{Vs}$ $\mu_{clicked} = 1619\ {}^{cm^2}/_{Vs}$

After verifying the existence of rGO and CVD graphene on the surface with SEM imaging, it can be also observed, that the semiconducting properties of both graphene substrates are still present. Interestingly, the mobility μ_{rOG} increases with the diazonium treatment on rGO by about a 1.2-fold, while the mobility μ_{CVDg} of the deposited CVD graphene and the herein fabricated FET increases by more than a ten-fold, precisely by an 11-fold. This behaviour was observed for an entire batch of diazonium treated FETs and makes the CVD graphene FET suitable for sensing.

Discussion

This chapter about different surface modifications of CVD graphene, reduced graphene oxide and gold shows several different approaches to visualize weather an immobilization strategy works or cannot be used for further bio-sensing. The discussed methods cover the non-covalent immobilization with pyrene derivates on graphene and the covalent immobilization strategy of diazonium treatment. Furthermore, covalent functionalization of gold slides is shown and the successful immobilization of bio-molecules was shown.

The reported blocking strategies to avoid non-specific binding (NSB) to the sensor surface were proven to work up concentrations of 10 µM of the sticky protein lysozyme. The synthesized pyrene-polyethylene glycol molecule with 34 repetition units is best suited for the deposition and blocking of NSB. It outperformed the standard blocking strategy used in ELISA, the BSA blocking. Furthermore, the $PyPEG_{34}$ allows the mixing with pyrene-carboxylic acid to specifically immobilize a capture probe on the surface, leading to the conclusion that this is a practical way to modify the gFET surface. Experiment to determine the ratio of blocking agent $PyPEG_{34}$ and PCA for functionalization show, that a ratio of 1:10 is best suited to have a sensor surface that is selective and specific at the same time. The strategy of a 1:10 ratio was also adapted for the functionalization of Au slides, while here the immobilization was with the well-established covalent thiol chemistry.

Unfortunately, XPS measurements on immobilized aptamer on the gFET surface exhibit minute signals of less than 0.2 at% and cannot prove the successful aptamer linking to the graphene surface. The investigation of the best solvent for PCA was carried out with amino-modified polystyrene nanobeads and amino-terminated PNA strains. The nanobeads could be depicted with SEM imaging after immobilization to the graphene surface. The quantification with a graphical image processing tool lead to a maximum surface coverage of 7%. Differential pulse voltammetry of enzymatic reactions was exploited to determine the best solvent for the non-covalent immobilization of pyrene-carboxylic acid. The nanobead immobilization and enzymatic DPV readout indicated both the best immobilization strategy for PCA: dissolve 1 mM of PCA in THF and apply 4 times a droplet on the surface until evaporation.

The covalent functionalization of graphene leads to promising results for surface chemistry. The immobilization of azide-terminated “click”-molecules was extensively proven and results in outstanding surface coverage rates of approximately 95%. The extremely high packing density of immobilized molecules and the controlled formation of monolayer formation on the surface make this linking strategy to one of the most promising tools for graphene bio-sensors. A positive side-effect of the diazonium treatment could be observed: the huge increase of charge mobility within the CVD graphene after the diazonium deposition makes this material probably most useful for bio-sensing applications. The transfer characteristic of the chips indicate a comparable stable and reproducible gFET architecture with high surface functionalization rates.

Due to the establishment of the covalent diazonium deposition method at the end of this project, it was not possible to perform bio-sensing experiments with “clicked” bio-recognition elements. The detailed results of the diazonium treatment on graphene can be found in the publication Mishyn *et al.* 2019. [114]

Manuscript #2:

Before proceeding, the publication proving the working principles and covalent surface modification of reduced graphene oxide by diazonium salt and the further usage of “click” chemistry is attached, herein referred as Mishyn *et al.* 2019. [114]

Mishyn, V., Aspermair, P., Leroux, Y., Happy, H., Knoll, W., Boukherroub, R. and Szunerits, S., 2019. **“Click” Chemistry on Gold Electrodes Modified with Reduced Graphene Oxide by Electrophoretic Deposition.** *Surfaces, 2(1),* pp.193-204. doi: 10.3390/surfaces2010015

surfaces

MDPI

Article

"Click" Chemistry on Gold Electrodes Modified with Reduced Graphene Oxide by Electrophoretic Deposition

Vladyslav Mishyn [1], Patrik Aspermair [1,2], Yann Leroux [3], Henri Happy [1], Wolfgang Knoll [2,4], Rabah Boukherroub [1] and Sabine Szunerits [1,*]

1 Univ. Lille, CNRS, Centrale Lille, ISEN, Univ. Valenciennes, UMR 8520—IEMN, F-59000 Lille, France; vladyslav.mishyn@univ-lille.fr (V.M.); patrik.aspermair@univ-lille.fr or patrik.aspermair@cest.at (P.A.); henri.happy@iemn.univ-lille.fr (H.H.); rabah.boukherrroub@univ-lille.fr (R.B.)
2 CEST Competence Center for Electrochemical Surface Technology, 3430 Tulln, Austria; wolfgang.knoll@cest.at
3 Univ. Rennes, CNRS, ISCR—UMR 6226, Campus de Beaulieu, F-35000 Rennes, France; yann.leroux@univ-rennes1.fr
4 AIT Austrian Institute of Technology, 3430 Tulln, Austria
* Correspondence: sabine.szunerits@unvi-lille.fr; Tel.: +33-3-62-53-17-25

Received: 22 January 2019; Accepted: 8 March 2019; Published: 18 March 2019

Abstract: The coating of electrical interfaces with reduced graphene oxide (rGO) films and their subsequent chemical modification are essential steps in the fabrication of graphene-based sensing platforms. In this work, electrophoretic deposition (EPD) of graphene oxide at 2.5 V for 300 s followed by vapor treatment were employed to coat gold electrodes uniformly with rGO. These interfaces showed excellent electron transfer characteristics for redox mediators such as ferrocene methanol and potassium ferrocyanide. Functional groups were integrated onto the Au/rGO electrodes by the electro-reduction of an aryldiazonium salt, 4-((triisopropylsilyl)ethylenyl)benzenediazonium tetrafluoroborate (TIPS-Eth-ArN) in our case. Chemical deprotection of the triisopropylsilyl function resulted in propargyl-terminated Au/rGO electrodes to which azidomethylferrocene was chemically linked using the Cu(I) catalyzed "click" chemistry.

Keywords: reduced graphene oxide; electrophoretic deposition; surface chemistry; click chemistry

1. Introduction

Accurate analysis of the presence of disease-specific biomarkers in biological fluids remains of great importance in clinical settings [1] and electrochemical sensors can reach that goal by converting a chemical or a biological response into a processable and quantifiable electrochemical signal [2]. Graphene and its related derivatives have generated great expectations as a transducing platform in biosensing, due to their good mechanical properties accompanied by biocompatibility, electrical conductivity and fast charge transfer kinetics [3–6]. A mandatory step in the production of biosensors is the modification of graphene-based materials with recognition elements. Covalent and non-covalent strategies have been employed, including amide bond formation and π–π interactions, among others [7–9], to integrate surface functionalities and ligands onto graphene-based transducers. The development of these approaches depends on having robust graphene-coated interfaces at hand. Next to drop-casting and spin-coating of reduced graphene oxide (rGO) suspensions onto electrical interfaces, electrophoretic deposition (EPD) has been shown to be an effective technique for manipulating graphene oxide (GO) suspensions with the aim of producing graphene-related films [9–13]. The ability of EPD to be applied to different materials and to control the thickness of

the deposits has been well known for a decade [14,15]. EPD has gained increased interest as an alternative processing technique for the deposition of various nanomaterials ranging from metal oxide particles [16] to carbon nanotubes [17]. EPD is also relevant to the development of graphene-based coatings in a cost-effective manner [13,18]. Its capacity to be used in more complex, integrated electrode systems is an advantage over drop-casting and other less defined deposition techniques [10,11,19–24]. The group of Boccaccini added intensively to this field by deepening our understanding of EPD through the investigation of GO-EPD kinetics as a function of deposition time and potential [12].

To design a powerful electrochemical sensor, working with highly reduced graphene oxide nanosheets formed by EPD is required. Cathodic EPD would be the preferential approach, as it allows the simultaneous deposition and reduction of GO to rGO [9]. The presence of carboxyl and hydroxyl functions on GO results in an overall negatively charged material of about -41.3 ± 0.8 mV for aqueous GO suspensions. Migration to the anode rather to the cathode occurs upon applying a DC voltage [13]. The anodic EPD of GO results in GO with a low degree of reduction during the deposition process. Thermal or chemical reductions [25] are necessary to restore the aromatic network in order to obtain a material with good electron transfer properties. This is one of the reasons why GO is often charged with a cationic polymer (e.g., polyethyleneimine) [8] or metallic cations (Ni^{2+}, Cu^{2+}, etc.) [21–23] to achieve a positively charged GO nanomaterial, which can be deposited by cathodic EPD. The presence of polyethyleneimine (PEI) has been shown to be advantageous for the integration of surface ligands and the formation of an immunosensor for the selective and sensitive electrochemical detection of uropathogenic *Escherichia coli* [8], the detection of dopamine in meat [20] and Ni^{2+} for the construction of non-enzymatic glucose sensors operating in a basic medium. However, the formation of well-reduced rGO by EPD free of metal ions and other surface ligands remains a challenge.

In this study, we evaluate the effect of applied electrical current and applied voltage on the electrochemical behavior of electrophoretically deposited rGO on gold thin film electrodes. It is shown that the use of a voltage bias of 2.5 V for 5 min results in rGO thin films of good electrochemical behavior. These films can also be submitted to further surface modification using diazonium electrochemistry without altering their adhesion characteristics.

2. Materials and Methods

2.1. Materials

Potassium hexacyanoferrate(II) ($[K_4Fe(CN)_6]$), hydrazine hydrate, phosphate buffer tablets (PBS, 0.1 M), tetrabutylammonium fluoride (TBAF), ferrocenemethanol, copper(II) sulfate ($CuSO_4$), L-ascorbic acid, EDTA and N-butylhexafluorophosphate (NBu_4PF_6) were purchased from Sigma-Aldrich and used as received. Graphene oxide (GO) powder was purchased from Graphenea, Spain. 4-((triisopropylsilyl)ethylenyl)benzenediazonium tetrafluoroborate (TIPS-Eth-ArN_2^+) was synthesized as reported previously [26].

Azidomethylferrocene was synthesized according to Reference [27].

Au thin film electrodes were prepared by thermal evaporation of 5 nm of titanium and 40 nm of gold onto cleaned glass slides.

2.2. Electrophoretic Deposition

Before electrophoretic deposition, the gold electrode was cleaned by UV/ozone for 5 min, rinsed with acetone and water and dried under a nitrogen flow. The deposition took place in a two-electrode system with a platinum foil (1 cm^2) as the cathode and the cleaned gold surface as the anode (0.5 cm^2). The electrodes were placed in parallel to each other at a fixed distance of 1.5 cm. An aqueous GO solution of 1 mg mL^{-1} was used for the EPD. Voltage biases of 1.25 V, 2.5 V, 5 V or 10 V were applied using a potentiostat/galvanostat (Metrohm Autolab, Utrecht, The Netherlands) for 5 min. The modified gold electrodes were slowly withdrawn manually from the solution and dried in a horizontal position under ambient conditions for 1 h. After the deposition was complete, the modified electrodes were

placed into a Teflon autoclave (45 mL) and sealed with 1 mL of hydrazine hydrochloride. The autoclave was heated to 80 °C and kept under a constant temperature for 4 h. The interfaces were then removed and gently washed with water.

2.3. Surface Modification

2.3.1. Diazonium Chemistry

The electrografting of 4-((triisopropylsilyl)ethylenyl)benzenediazonium tetrafluoroborate (TIPS-Eth-ArN_2^+) (1 mM) in 0.1 M NBu_4PF_6 in acetonitrile was performed using cyclic voltammetry with a scan rate of 50 mV s^{-1} for five cycles between +0.60 V and −0.75 V vs. Ag/AgCl. The electrodes were rinsed with copious amounts of acetonitrile and acetone and dried under a stream of argon.

2.3.2. "Click" Chemistry

Before "click" chemistry, the TIPS protection group was removed by the immersion of the Au/rGO-TIPS surface into tetrabutylammonium fluoride (TBAF, 0.05 M in THF) for 20 min. The Au/rGO interface was then immersed into an aqueous solution of $CuSO_4$ (10 mM) and L-ascorbic acid (20 mM) in the presence of azidomethylferrocene (0.83 mM in THF) and left for 1 h under an argon atmosphere. The interface was then treated with an aqueous solution of EDTA for 10 min to chelate any remaining Cu^{2+} residues and finally washed copiously with acetone and water and left to dry.

2.4. Surface Characterization Techniques

2.4.1. Scanning Electron Microscopy (SEM)

SEM images were obtained using an electron microscope ULTRA 55 (Zeiss, Paris, France) equipped with a thermal field emission emitter and three different detectors (EsB detector with filter grid, high efficiency in-lens SE detector and Everhart–Thornley Secondary Electron Detector).

2.4.2. X-Ray Photoelectron Spectroscopy (XPS)

X-ray photoelectron spectroscopy (XPS) was performed in a PHI 5000 VersaProbe-Scanning ESCA Microprobe (ULVAC-PHI, Osaka, Japan) instrument at a base pressure below 5×10^{-9} mbar. Core-level spectra were acquired at a pass energy of 23.5 eV with a 0.1 eV energy step. All spectra were acquired with 90° between the X-ray source the and analyzer. After the subtraction of the linear background, the core-level spectra were decomposed into their components with mixed Gaussian−Lorentzian (30:70) shape lines using CasaXPS software. Quantification calculations were conducted using sensitivity factors supplied by PHI.

2.4.3. Electrochemical Measurements

Electrochemical measurements were performed with a potentiostat/galvanostat (Metrohm Autolab, Utrecht, The Netherlands). A conventional three-electrode configuration was employed using a silver wire and a platinum mesh as the reference and auxiliary electrodes, respectively.

2.4.4. Micro-Raman Analysis

Micro-Raman spectroscopy measurements were performed on a LabRam HR Micro-Raman system (Horiba Jobin Yvon, Palaiseau, France) combined with a 473 nm laser diode as the excitation source. Visible light was focused by a 100× objective. The scattered light was collected by the same objective in backscattering configuration, dispersed by a 1800 mm focal length monochromator and detected by a CCD.

2.4.5. Atomic Force Microcopy (AFM)

Tapping mode AFM images in air and ambient temperature were recorded using a Bruker Dimension 3100 AFM (Bruker, Champs-sur-Marne, France). The surfaces were imaged with a silicon cantilever (AppNano TM300, typical spring constant: 50 N/m) working at a frequency of 369 kHz. Image treatment and root mean square (RMS) roughness R_a were obtained with WSXM software (Bruker, Champs-sur-Marne, France). Surface roughness of the samples was measured by scanning over a 5 × 5 μm area.

2.4.6. Profilometry

The thickness of the deposited films was determined by using an optical profilometer (Zygo NewView 6000 Optical Profilometer with MetroPro software). This equipment uses non-contact, three-dimensional scanning white light and optical phase-shifting interferometry, has vertical *z*-scan measurements ranging from 0.1 nm to 15,000 μm and has capabilities of 1 nm height resolution with step accuracies better than 0.75%. Images were taken with a 10× lens with a 14 mm field of view.

3. Results

3.1. Electrophoretic Deposition

The process for the formation of stable electrochemically active reduced graphene oxide (rGO) thin films on gold thin film electrodes is schematically depicted in Figure 1A. It is based on a two-step process in which, after EPD at 2.5 V for 5 min, the full reduction of GO to rGO is obtained by immersion into hydrazine vapor for 4 h. The use of a potential of 2.5 V proved to be of high importance in the process. Initial investigation revealed that the electrical current signature changes significantly at voltages greater than 2.5 V (Figure 1B), where the electrical current passing through the interface increases during the first 25 s before stabilizing. In contrast, at potential biases of 2.5 V and lower, a decrease of the electrical current is first observed before its stabilization. Indeed, due to the insulating character of GO, the electrical current should decrease during the deposition process as observed for a low voltage bias. The current drop at 2.5 V is slower than that at 1.25 V. The reason for this is not well understood, but could be due to a partial electrochemical reduction of GO under these conditions. A similar behavior was observed by Diba et al. following the deposition of GO at 3 and 5 V [12].

The increase in current at elevated voltages indicates that next to the material deposition an electrochemical reaction occurs, delaying surface passivation [12]. Visual inspection of the interfaces (Figure 1C) shows clearly that the deposition occurred. However, a closer visual inspection of the electrical interfaces (Figure 1D) reveals that the gold thin films were partially destroyed, most likely by the gas evolution during water hydrolysis occurring in parallel at these voltage biases. This results in the swelling of the GO deposit and eventual gold film rupture with poor film attachment.

Figure 2A shows SEM images of the different interfaces. While the films formed at 1.25 V display granular like structures, the films deposited at 2.5 V exhibit the typical rGO-like wrinkle structures with no evident local surface inhomogeneities and a complete and even coating of the gold thin film interface. From the cross-section image (Figure 1A), no protrusions and hollow internal structures are visible, indicating that at a lower potential local inhomogeneities associated with rGO formation are avoided. The average surface roughness (R_a), as determined by tapping-mode atomic force microscopy (AFM) measurements, changed from R_a = 4.1 nm (Au) to R_a = 3.5 nm for Au/rGO (2.5 V deposition potential).

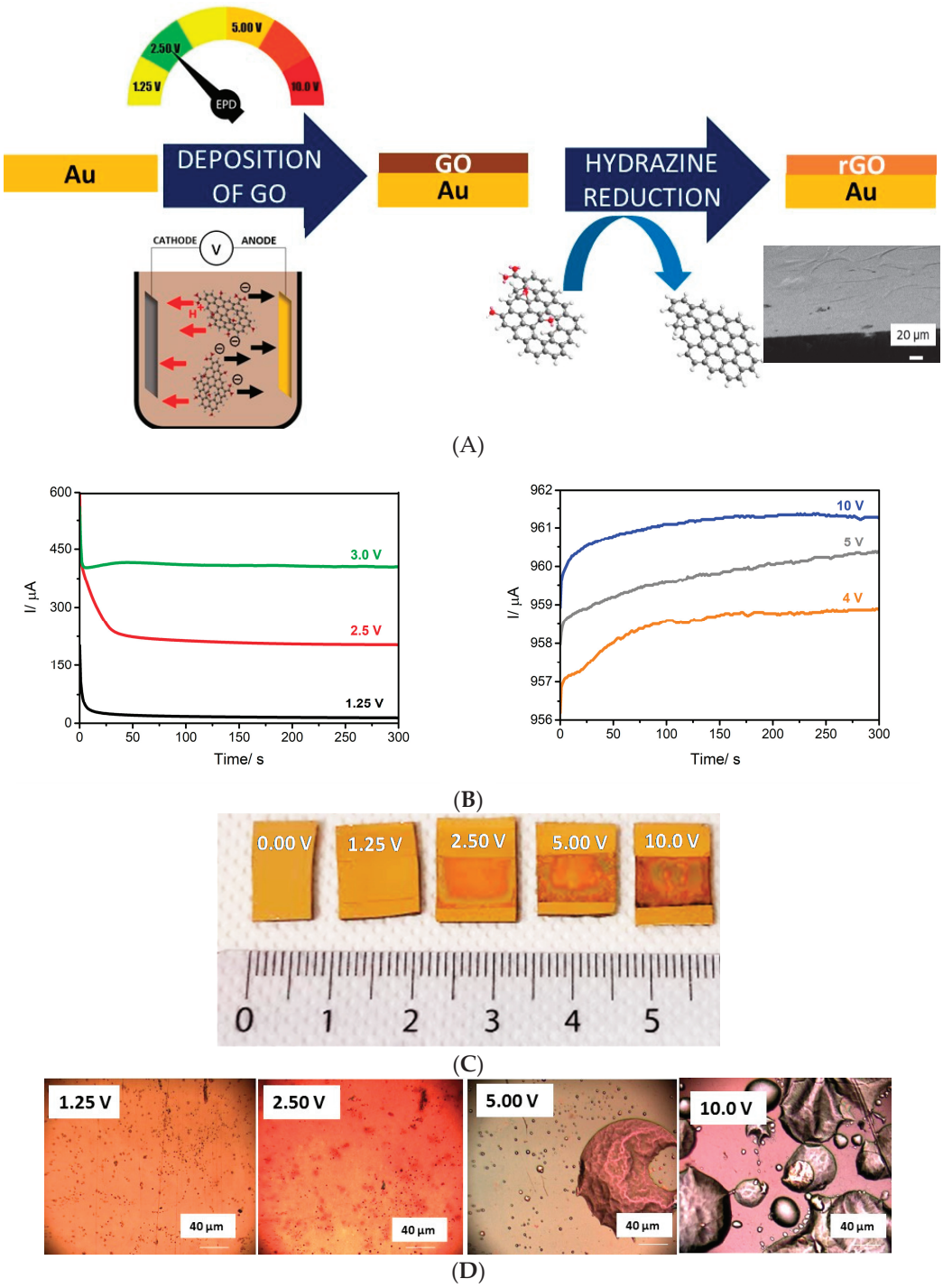

Figure 1. (**A**) Schematic illustration of the formation of an electrochemically active reduced graphene oxide (rGO) thin film by anodic electrophoretic deposition (EPD) from an aqueous graphene oxide suspensions (GO, 1 mg/mL) at a potential bias of 2.5 V for 5 min, followed by chemical treatment in hydrazine vapor; cross-sectional SEM image of a gold interface coated with rGO using EPD at 2.5 V for 5 min. (**B**) Change of current as a function of deposition time using different applied potentials: concentration of GO (1 mg/mL) in water (pH 7.5), deposition interface: gold thin film electrode. (**C**) Photographic images of gold thin film electrodes before (0.00 V) and after anodic EPD of an aqueous solution of GO (1 mg/mL, pH 7.5) for 5 min at 1.25, 2.50, 5.00 and 10.00 V. (**D**) Photographs of the different interfaces obtained (objective: 10×, numerical aperture: 0.9).

To estimate the anodic efficiency of the EPD process, the gold interface was weighed before and after rGO deposition and reduction. To convert the deposited weight ($m_{rGO,}$ 10 µg for 2.5 V for 5 min) into a film thickness (d_{rGO}), Equation (1) was used:

$$d_{rGO}\ (nm) = \frac{m_{rGO\times}}{A \times \rho} \tag{1}$$

where A is the surface area (0.8 cm^2 in our case) and ρ is the density of rGO (2.09 g cm^{-3}) [28]. A film thickness of 59 nm was determined. This is in agreement with profilometry measurements where a film thickness of about 55 nm was determined (Figure 2B). Samples prepared at 1.25 V for 5 min had a deposited mass of 3 µg and an estimated rGO film thickness of 20 nm, below the acceptable accuracy limit of profilometry to be validated. Increasing the potential to 5 V resulted in 120 nm thick films. The Hamakar model [29] correlates the time-dependent (t = 300 s) amount of deposited materials (m_{rGO} in g) with the electrical field strength (E, 1.6 V m^{-1} in our case), the surface area of the electrode (0.8 cm^2), the electrophoretic mobility of GO (1.97×10^{-4} $cm^2/(Vs)^{-1}$), the concentration of the particle suspension (1 mg mL^{-1}, 0.001 g cm^{-3}) and the anodic efficiency factor f (Equation (2)) [29].

$$m_{rGO} = c_{rGO} \times A \times \mu \times E \times t \times f \tag{2}$$

In the case of f = 1, the amount of deposited rGO should be equal to m_{rGO} = 47 µg. The determined rGO amount, however, was only 10 µg, which implies an efficiency factor of f = 0.2.

As a voltage bias of 2.5 V seems to be the best condition for the EDP of rGO films onto the gold electrodes, these interfaces were investigated in greater detail. The electrochemical behavior of this interface using ferrocene-methanol redox couple in an aqueous solution is depicted in Figure 2C. Whereas on a bare gold surface a fully reversible voltammogram was observed, an irreversible voltammogram with a very small oxidation peak was observed on GO-coated gold surfaces. To improve the electrochemical behavior of such coated gold surfaces, the interfaces were further treated with hydrazine vapor, known for its strong reducing power. The cyclic voltammograms of hydrazine treated surfaces were largely improved, showing a well-defined redox couple with increased capacitance behavior as expected for rGO materials (Figure 2B, blue curve).

The chemical composition of the deposited graphene matrix was further evaluated using XPS (Figure 2D). The high resolution C1s core level spectrum of the initial GO suspensions showed contributions at 284.2 (C=C sp^2), 285.0 (C–H/C–Csp^3), 286.7 (C–O) 288.7 (C=O) and a small contribution at 291.0 (O–C=O). The C1s XPS core spectra of GO-coated gold surfaces revealed similar contributions with different intensities. In particular, the band at 284.2 eV due to C=C sp^2 increased compared to the GO solution, indicating the partial restoration of the sp^2 network of the deposited graphene material. The XPS of GO-coated gold showed additional bands at 285.0 and 286.7 eV with a large band at 288.0 eV due to C=O. The hydrazine reduction of the GO–gold interfaces resulted in a decrease of the epoxy/ether functions at 286.7 eV, in accordance with a partial reduction of GO mostly likely due to the elimination of CO by a Kolb-like mechanism [12,13]. The ketone groups remained preserved.

The Raman spectrum of GO-coated gold surfaces before and after hydrazine reduction (4 h) is presented in Figure 2E. The increase of the D/G ratio from 0.86 to 0.97 after hydrazine chemical reduction was observed.

Figure 3A summarizes the electrochemical behavior of a neutral redox species, ferrocene methanol, on bare and GO-coated gold surfaces after the hydrazine chemical reduction. The electrochemically active surface area of the different electrodes was determined by plotting the peak current as a function of the square root of the scan rate (Figure 3B), according to Equation (3) [30]:

$$A = \text{slope}/(268600 \times n^{3/2} \times D^{1/2} \times c) \tag{3}$$

where n is the number of electrons transferred in the redox event (n = 1), D is the diffusion coefficient of ferrocene methanol (7.5×10^{-6} cm^2 s^{-1}) and c is the concentration of ferrocene methanol (1 10^{-6} mol cm^{-3}). Taking into account the experimentally determined slopes (9.265×10^{-5} $AV^{1/2}$ $s^{-1/2}$ for Au and 9.980×10^{-5} $AV^{1/2}s^{-1/2}$ for Au/rGO), the active surfaces of 0.126 cm^2 (naked gold) and 0.136 cm^2 (Au/rGO) were determined. By plotting the current density vs. potential (Figure 3B), a larger current density was detected on the EPD coated gold interface due to the excellent electrochemical behavior of the interface. This is in agreement with the deposition of an electrochemically active 3D rGO material.

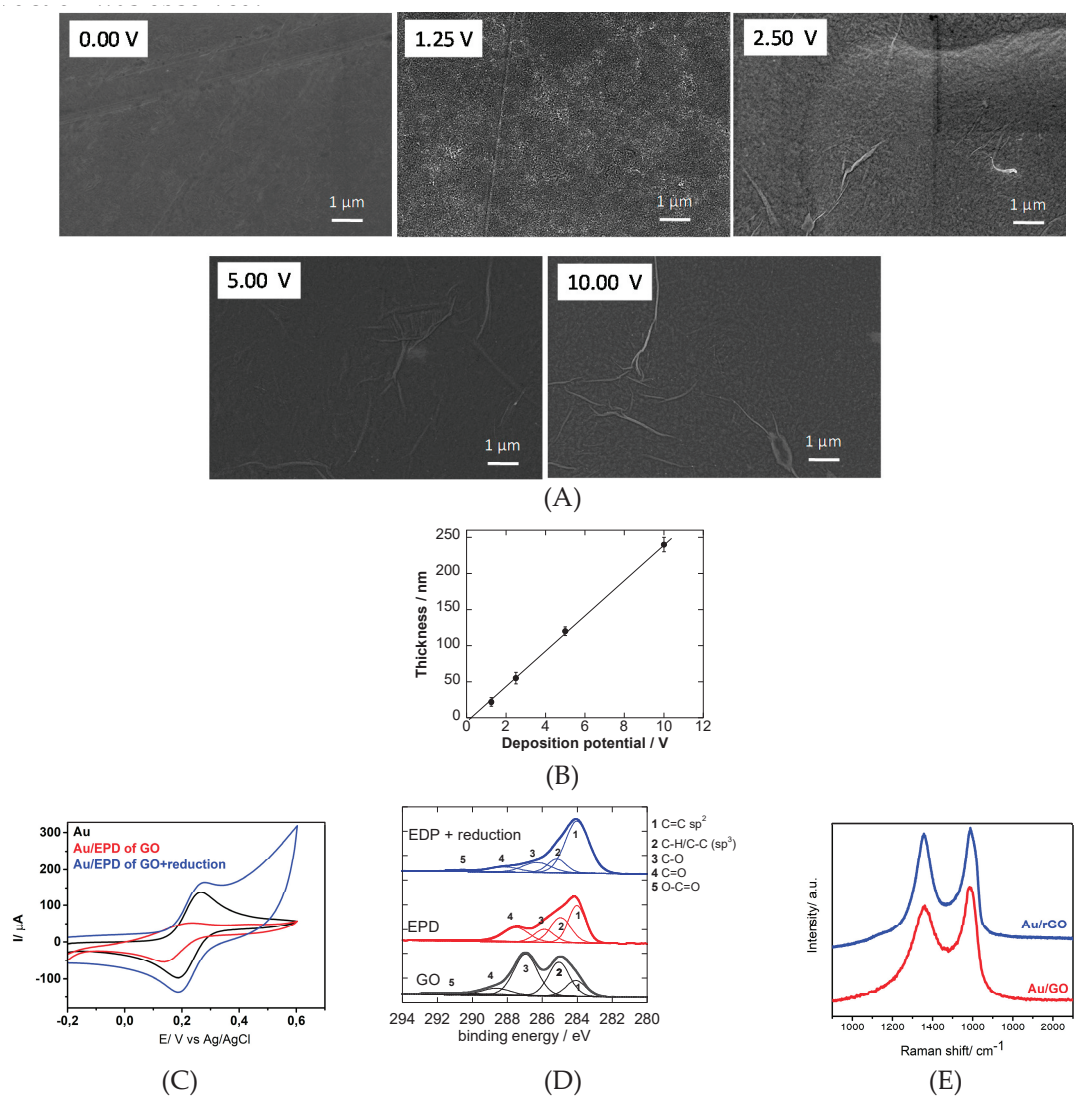

Figure 2. (**A**) SEM image of gold thin films before and after EPD from an aqueous graphene oxide suspension (GO, 1 mg/mL) at different potential biases for 5 min. (**B**) Thickness of reduced graphene oxide as a function of applied potential (t = 5 min). (**C**) Cyclic voltammograms recorded on gold thin film electrodes (black), after EPD from an aqueous graphene oxide suspension (GO, 1 mg/mL) at a potential bias of 2.5 V for 5 min (red); after further reduction with hydrazine (blue) using ferrocenemethanol (1 mM)/PBS (0.1 M), scan rate = 100 mV s^{-1}. (**D**) C1s high-resolution spectra of GO (black), EPD GO (red) and further reduced GO (blue). (**E**) Raman spectra of the EPD film formed at 2.5 V before (red) and after hydrazine reduction (blue).

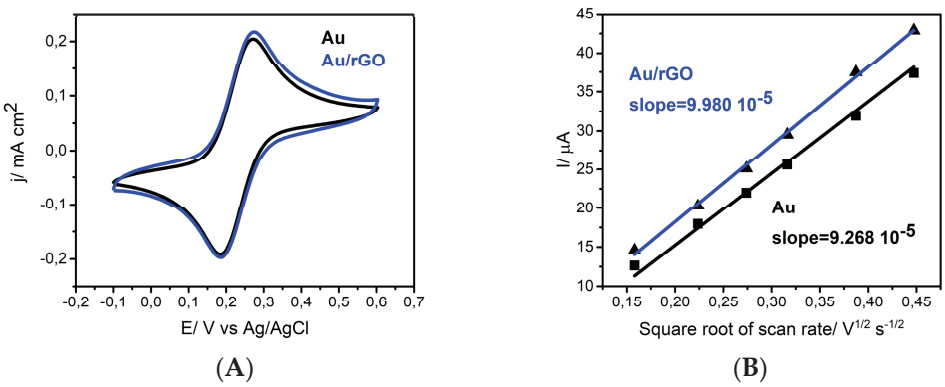

Figure 3. (**A**) Cyclic voltammograms recorded on gold thin film electrodes (black) and after EPD and further reduction with hydrazine using ferrocene methanol (1 mM)/PBS (0.1 M), scan rate = 100 mV s^{-1}. (**B**) Cyclic voltammograms recorded on gold thin film electrodes (black) and after EPD and further reduction with hydrazine using ferrocene methanol (1 mM)/PBS (0.1 M), scan rate = 100 mV s^{-1}.

3.2. Surface Modification Using Diazonium Electrografting

To validate the stability of the formed interface, efficient covalent modification based on the electroreduction of a triisopropylsilyl-protected ethynyl diazonium salt was performed (Figure 4A). Covalent surface modification of graphene-based materials using the electroreduction of aryldiazonium salts is a popular approach as it allows the introduction of different chemical groups. The major drawback of this approach is the difficulty to control the extent of the reaction—notably, to limit the reaction to the formation of a functional monolayer. The highly reactive nature of the formed aryl radical results in the formation of disordered polyaryl multilayers, which in the case of a sensor might limit the dynamic range of sensing. The introduction of bulky substitutions on the ArN_2^+ moieties limits radical addition reactions and allows the formation of ultrathin functional layers [26,31,32]. On the basis of this concept, the precursor 4-((triisopropylsilyl)ethylenyl)benzenediazonium tetrafluoroborate (TIPS-Eth-ArN_2^+) was used for the formation of an organic thin film on Au/rGO. The layer was obtained by potential cycling in a solution containing TIPS-Eth-ArN_2^+ (Figure 4B). As observed by cyclic voltammetry, the reduction peak of TIPS-Eth-ArN_2^+ at −0.2 V decreased rapidly after five cycles, indicating the blocking of the Au/rGO electrode. Compared to glassy carbon electrodes, the reduction peak shifted to more negative potentials [26]. The blocking properties of the layer was further investigated by recording the cyclic voltammogram of the oxidation of ferrocene methanol in water before and after the electrografting process (Figure 4C) and was found to be typical of a totally blocked electrode.

To have access to the acetylene function, the modified Au/rGO-TIP surface was immersed into tetrabutylammonium fluoride (TBAF, 0.05 M in THF) at room temperature. The success of the deprotection step was evidenced by the recovery of the ferrocene oxidation signal, being almost identical to that obtained on Au/rGO (not shown). The deprotected substrate was further treated by "click" chemistry (Huisgen 1,3-dipolar cyclization) using azidomethylferrocene, as first reported by Gooding et al. [33]. The success of the integration of ferrocene units onto the Au/rGO electrodes was seen from the presence of the Fe2p component in the XPS survey spectrum (Figure 5A). In the absence of copper catalyst, no click reaction took place and no Fe2p component could be recorded. Figure 5B shows the cyclic voltammogram of the ferrocene-modified electrode examined in electrolytic ethanol solution. A surface concentration of $\Gamma = 2.5\times 10^{-10}$ mol cm^{-2} of bound ferrocene groups was derived from these measurements using Equation (4):

$$\Gamma = Q/nFA \tag{4}$$

where Q is the passed charge, n is the number of exchanged electrons (n = 1), F is the Faraday constant and A is the electroactive surface of the electrode determined as 0.136 cm^2. Considering the ferrocene

molecules as spheres with a diameter of 6.6 Å, the theoretical maximum coverage for an idealized ferrocene monolayer can be estimated as $\Gamma = 4.8 \times 10^{-10}$ mol cm^{-2} [34]. In our case, about half of the full coverage was achieved.

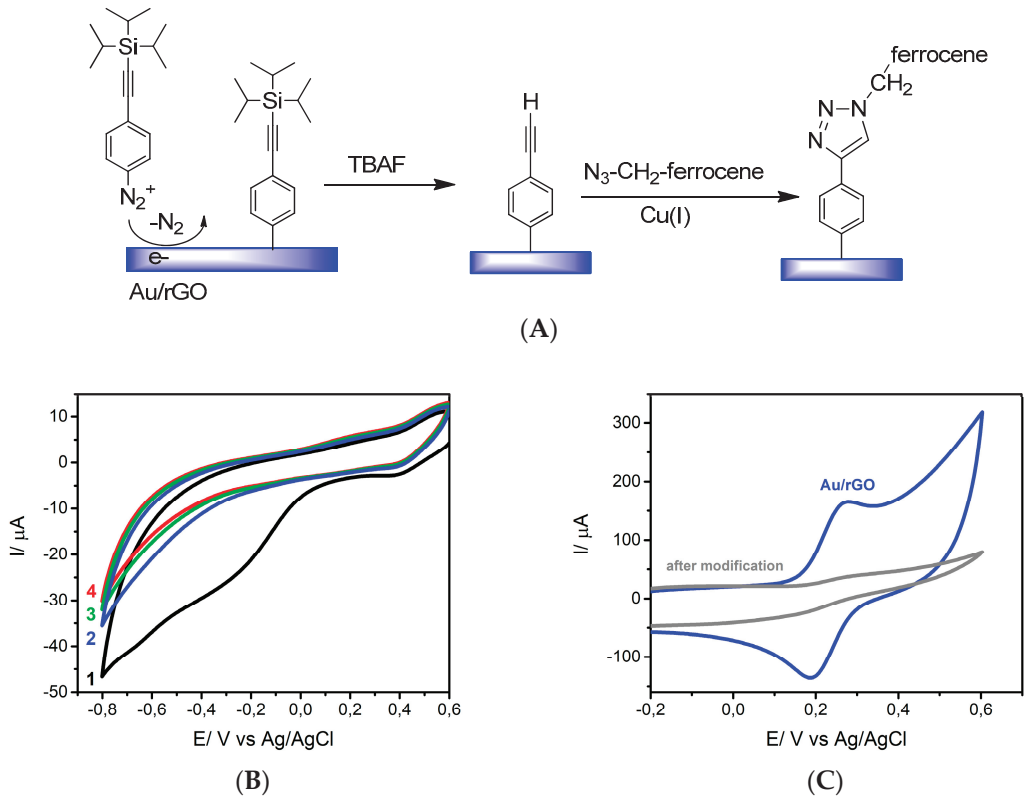

Figure 4. (**A**) Covalent modification of Au/rGO electrodes using a silyl-protected diazonium salt followed by tetrabutylammonium fluoride (TBAF)-based deprotection and "click" reaction using azidomethylferrocene as a model compound. (**B**) Electroreduction of 4-((triisopropylsilyl) ethylenyl)benzenediazonium tetrafluoroborate (TIPS-Eth-ArN_2^+) on Au/rGO, scan rate 50 mV s^{-1}. (**C**) Cyclic voltammograms of ferrocene methanol (1 mM)/0.1 M PBS of rGO/Au before (blue) and after modification with TIPS-Eth-ArN_2^+.

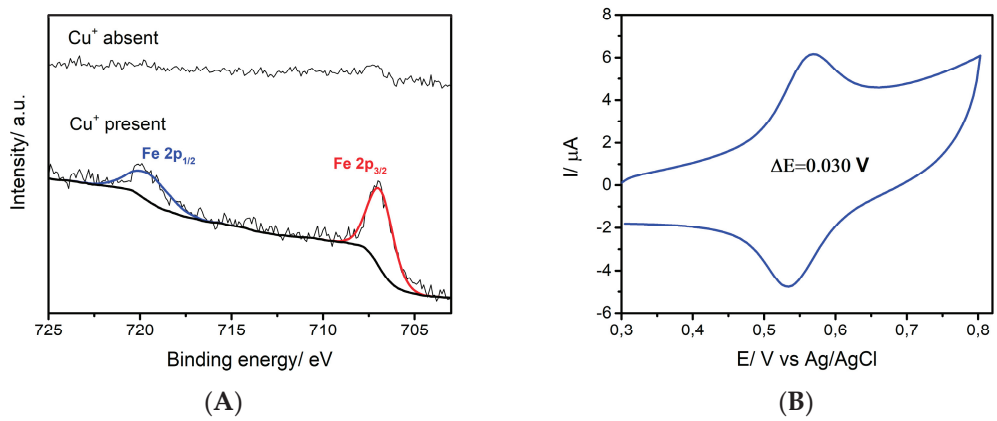

Figure 5. (**A**) High-resolution Fe2p X-ray photoelectron spectroscopy (XPS) core-level spectrum of ferrocene modified Au/rGO interfaces. (**B**) Cyclic voltammograms in acetonitrile/ NBu_4PF_6 0.1 M), scan rate 100 mV s^{-1}.

4. Conclusions

In conclusion, by applying a low EPD voltage of 2.5 V, the deposition of partially reduced graphene oxide film can be formed on gold thin film electrodes in a homogenous, and mechanically and chemically stable manner. Further reduction of the films in hydrazine vapor results in reduced graphene oxide-coated substrates showing excellent electron transfer characteristics. The films proved to be of high robustness and could be further modified via the electroreduction of aryldiazonium salts. Using a protection–deprotection approach allows the immobilization of a functional monolayer which can be further functionalized by Cu(I)-catalyzed "click" chemistry. We have demonstrated that a densely packed ferrocenenyl monolayer can be efficiently integrated on these rGO-modified surfaces. Due to the versatility and mild conditions of the "click" chemistry reaction, a wide range of functional groups can be immobilized on such surfaces. These results pave the way for the use of this technology for the modification of more complex electrode configuration such as screen-printed or flexible integrated electrode arrays and the integration of surface ligands for sensing-related applications.

Author Contributions: V.M.: electrophoretic deposition and electrochemistry; P.A.: click chemistry; Y.L.: surface chemistry; H.H.: characterization; W.K.: editing of the draft; R.B.: characterization, editing of the draft; S.S.; original draft preparation, supervision of work.

Acknowledgments: General financial support from the Centre National de la Recherche Scientifique (CNRS), the University of Lille, the Hauts-de-France region and the EU through FLAG-ERA JTC2015 "Graphtivity" is acknowledged.

Conflicts of Interest: The authors declare no conflict of interest.

References

1. Reina, G.; González-Domínguez, J.M.; Criado, A.; Vázquez, E.; Bianco, A.; Prato, M. Promises, facts and challenges for graphene in biomedical applications. *Chem. Soc. Rev.* **2017**, *46*, 4400–4416. [CrossRef]
2. Szunerits, S.; Boukherroub, R. Graphene-based bioelectrochemistry and bioelectronics: A concept for the future? *Curr. Opin. Electrochem.* **2018**, *12*, 141–147. [CrossRef]
3. Ambrosi, A.; Chua, C.K.; Latiff, N.M.; Loo, A.H.; Wong, C.H.; Eng, A.Y.; Bonanni, A.; Pumera, M. Graphene and its electrochemistry—An update. *Chem. Soc. Rev.* **2016**, *45*, 2458–2493. [CrossRef] [PubMed]
4. Peña-Bahamonde, J.; Nguyen, H.N.; Sofia, K.; Rodrigues, D.F. Recent advances in graphene-based biosensor technology with applications in life sciences. *J. Nanobiotechnol.* **2018**, *16*, 75. [CrossRef] [PubMed]
5. Szunerits, S.; Boukherroub, R. Electrochemistry of graphene: The current state of the art. *Electrochemistry* **2013**, *12*, 211–242.
6. Szunerits, S.; Boukherroub, R. Graphene-based nanomaterials in innovative electrochemistry. *Curr. Opin. Electrochem.* **2018**, *10*, 24–30. [CrossRef]
7. Chekin, F.; Vasilescu, A.; Jijie, R.; Singh, S.K.; Kurungot, S.; Iancu, M.; Badea, G.; Boukherroub, R.; Szunerits, S. Sensitive electrochemical detection of cardiac troponin I in serum and saliva by nitrogen-doped porous reduced graphene oxide electrode. *Sens. Actuators B Chem.* **2018**, *262*, 180–187. [CrossRef]
8. Jijie, R.; Kahlouche, K.; Barras, A.; Yamakawa, N.; Bouckaert, J.; Gharbi, T.; Szunerits, S.; Boukherroub, R. Reduced graphene oxide/polyethylenimine based immunosensor for the selective and sensitive electrochemical detection of uropathogenic Escherichia coli. *Sens. Actuators B.* **2018**, *260*, 255–263. [CrossRef]
9. Wang, Q.; Vasilescu, A.; Wang, Q.; Coffinier, Y.; Li, M.; Boukherroub, R.; Szunerits, S. Electrophoretic Approach for the Simultaneous Deposition and Functionalization of Reduced Graphene Oxide Nanosheets with Diazonium Compounds: Application for Lysozyme Sensing in Serum. *ACS Appl. Mater. Interfaces* **2017**, *9*, 12823–12831. [CrossRef] [PubMed]
10. Subramanian, P.; Lesniewski, A.; Kaminska, I.; Vlandas, A.; Vasilescu, A.; Niedziolka-Jonsson, J.; Pichonat, E.; Happy, H.; Boukherroub, R.; Szunerits, S. Lysozyme detection on aptamers functionalized graphene-coated SPR interfaces. *Biosens. Bioelectron.* **2013**, *50*, 239–243. [CrossRef]
11. Subramanian, P.; Barka-Bouaifel, F.; Bouckaert, J.; Yamakawa, N.; Boukherroub, R.; Szunerits, S. Graphene-coated surface plasmon resonance interfaces for studing the interactions between cells and surfaces. *ACS Appl. Mater. Interfaces* **2014**, *6*, 5422–5431. [CrossRef] [PubMed]

12. Diba, M.; Garcia-Callastegui, A.; Klupp Taylor, R.N.; Pishbin, F.; Ryan, M.P.; Shaffer, M.S.P.; Boccaccini, A.R. Quantitative evaluation of electrophoretic deposition kinetics of graphene oxide. *Carbon* **2014**, *67*, 656–661. [CrossRef]
13. An, S.J.; Zhu, Y.; Lee, S.H.; Stoller, M.D.; Emilsson, T.; Park, S.; Velamakanni, A.; An, J.; Ruoff, R.S. Thin Film Fabrication and Simultaneous Anodic Reduction of Deposited Graphene Oxide Platelets by Electrophoretic Deposition. *J. Phys. Chem. Lett.* **2010**, *1*, 1259–1263. [CrossRef]
14. Besra, L.; Liu, M. A review on fundamentals and applications of electophoretic depositon (EDP). *Prog. Mater. Sci.* **2007**, *52*, 1–61. [CrossRef]
15. Ammam, M. Electrophoretic deposition under modulated electric fields: A review. *RSC Adv.* **2012**, *2*, 7633–7646. [CrossRef]
16. Ata, M.S.; Liu, Y.; Zhitomirsky, I. A review of new methods of surface chemical modification, dispersion and electrophoretic deposition of metal oxide particles. *RSC Adv.* **2014**, *4*, 22716–22732. [CrossRef]
17. Boccaccini, A.R.; Cho, H.; Roether, J.A.; Thoimasz, B.J.C.; Minay, E.J.; Shaffer, M.S.P. Electrophoretic deposition of carbon nanotubes. *Carbon* **2006**, *44*, 3149–3160. [CrossRef]
18. Chavez-Valdez, A.; Shaffer, M.S.P.; Boccaccini, A.R. Applications of Graphene Electrophoretic Deposition. A Review. *J. Phys. Chem. B* **2013**, *117*, 1502–1515. [CrossRef]
19. He, L.; Sarkar, S.; Barras, A.; Boukherroub, R.; Szunerits, S.; Mandler, D. Electrochemically stimulated drug release from flexible electrodes coated electrophoretically with doxorubicin loaded reduced graphene oxide. *Chem. Commun.* **2017**, *53*, 4022–4025. [CrossRef]
20. Kahlouche, K.; Jijie, R.; Hosu, I.; Barras, A.; Gharbi, T.; Yahiaoui, R.; Herlem, G.; Ferhat, M.; Szunerits, S.; Boukherroub, R. Controlled modification of electrochemical microsystems with polyethylenimine/reduced graphene oxide using electrophoretic deposition: Sensing of dopamine levels in meat samples. *Talanta* **2018**, *178*, 32–440. [CrossRef]
21. Maaoui, H.; Singh, S.K.; Teodorescu, F.; Coffinier, Y.; Barras, A.; Chtourou, R.; Kurungot, S.; Szunerits, S.; Boukherroub, R. Copper oxide supported on three-dimensional ammonia-doped porous reduced graphene oxide prepared through electrophoretic deposition for non-enzymatic glucose sensing. *Electrochim. Acta* **2017**, *224*, 346–354. [CrossRef]
22. Wang, Q.; Li, M.; Szunerits, S.; Boukherroub, R. Preparation of reduced graphene oxide-Cu composites through electrophoretic deposition: Application for nonenzyamtic glucose sensing. *RSC Adv.* **2015**, *5*, 15861–15869. [CrossRef]
23. Subramanian, P.; Niedziolka-Jonsson, J.; Lesniewski, A.; Wang, Q.; Li, M.; Boukherroub, R.; Szunerits, S. Preparation of reduced graphene oxide-Ni$(OH)_2$ composites by electrophoretic deposition: Application for non-enzymatic glucose sensing. *J. Mater. Chem. A* **2014**, *2*, 5525–5533. [CrossRef]
24. Wang, Q.; Vasilescu, A.; Wang, Q.; Li, M.; Boukherroub, R.; Szunerits, S. Electrophoretic approach for the modification of reduced graphene oxide nanosheets with diazonium compounds: Application for electrochemical lysozyme sensing. *ACS Appl. Mater. Interfaces* **2017**, *9*, 12823–12831. [CrossRef]
25. Pei, S.; Cheng, H.-M. The reduction of graphene oxide. *Carbon* **2012**, *50*, 3210–3228. [CrossRef]
26. Leroux, Y.R.; Fei, H.; Noel, J.-M.; Roux, C.; Hapiot, P. Efficient Covalent Modification of a carbon surface: Use of a silyl protecting group to form an active monolayer. *J. Am. Chem. Soc.* **2010**, *132*, 14039–14041. [CrossRef] [PubMed]
27. Casas-Solva, J.M.; Vargas-Berenguel, A.; Captian-Vallvey, L.F.; Santoyo-Gonzalez, F. Convenient Methods for the Synthesis of Ferrocene−Carbohydrate Conjugates. *Org. Lett.* **2004**, *6*, 3687–3690. [CrossRef]
28. Park, S.; An, J.; Jung, I.; Piner, R.D.; An, S.J.; Li, X.; Velamakanni, A.; Ruoff, R.S. Colloidal suspensions of highly reduced graphene oxide in a wide variety of organic solvents. *Nano Lett.* **2009**, *9*, 1593–1597. [CrossRef]
29. Hamaker, H.C. Formation of a deposite by electrophoresis. *Trans. Farady Soc.* **1940**, *35*, 279–287. [CrossRef]
30. Ngamchuea, K.; Eloul, S.; Tschulik, K.; Compton, R.G. Planar diffusion to macro disc electrodes—What electrode size is required for the Cottrell and Randles-Sevcik equations to apply quantitatively? *J. Sol. State Electrochem.* **2014**, *18*, 3251–3257. [CrossRef]
31. Nielsen, L.T.; Vase, K.H.; Dong, M.; Besenbacher, F.; Pedersen, S.U.; Daasbjerg, K. Electrochemical Approach for Constructing a Monolayer of Thiophenolates from Grafted Multilayers of Diaryl Disulfides. *J. Am. Chem. Soc.* **2007**, *129*, 1888–1889. [CrossRef]

32. Combellas, C.; Jiang, D.-E.; Kanoufi, F.; Pinson, J.; Podvorica, F.I. Steric Effects in the Reaction of Aryl Radicals on Surfaces. *Langmuir* **2009**, *25*, 286–293. [CrossRef] [PubMed]
33. Ciampi, S.; Le Saux, G.; Harper, J.B.; Gooding, J.J. Optimization of Click Chemistry of Ferrocene Derivatives on Acetylene-Functionalized Silicon(100) Surfaces. *Elecroanalysis* **2008**. [CrossRef]
34. Chidsey, C.E.D.; Bertozzi, C.R.; Putvinski, T.M.; Mujsce, A.M. Coadsorption of ferrocene-terminated and unsubstituted alkanethiols on gold: Electroactive self-assembled monolayers. *J. Am. Chem. Soc.* **1990**, *112*, 4301–4306. [CrossRef]

© 2019 by the authors. Licensee MDPI, Basel, Switzerland. This article is an open access article distributed under the terms and conditions of the Creative Commons Attribution (CC BY) license (http://creativecommons.org/licenses/by/4.0/).

4. Chapter:

gFET/SPR measurement tool

To guarantee stable and reproducible measurement conditions over a long period of time it is important to have a measurement tool for the produced gFET with defined specifications and settings. Beside characterization of the devices, it is important to continuously measure the modulated current between drain and source, I_{DS} during binding events, store the data and process it, if necessary. Therefore, a data logger with visualization of the ongoing measurement is required and shown in this chapter.

Materials and Methods

This section shows all used materials and software tools to measure the graphene FET in the laboratory environment. The tools apply for the experiments in the static and flow cell of Micrux, as well as the created gFET/SPR flow cell.

Source measure unit

A standard device to characterize semiconductors like field-effect transistors is a source meter unit, SMU, that has the capability to measure the current while applying a voltage. The most important parameters for such a device are the resolution (typical fA), low current measurement capability (typical pA) and a long-time stability with low drift over hours and days. The initial experiments on the produced gFET devices where performed on two-channel source measure units from Keithley Instruments: the SMU 2612B and the SMU 4200, depicted in the Figure 54 A and B. These high-end measurement devices provide versatile units to specify newly developed semiconductors but are overpowered for bio-sensing applications. It is only possible to measure one device

a at a time, because both channels are utilized for the field-effect transistor. The measurement circuit is depicted in Figure 54 C, where two channels are connected to one FET. The parameters for each channel can be adjusted individually to completely characterize the device.

Figure 54: Source measure units to characterize semiconductors with high accuracy and high resolution down to the fA range. Both channels of the source measure units are required to measure one field effect transistor.

As an alternative, a common gate electrode could be used to modulate two or more FETs at the same time. That is only allowed, if the leakage current I_{Gate} of the Gate electrode is less than 1% of the drain source current I_{DS}. Under the assumption, that the drain-source conductivity of a graphene FET is at any time high enough, such a configuration can be used to measure two gFETs with a common gate electrode. The expected ohmic resistance of each sensor chip can be expected to be below 300 Ω due to a stable manufacturing practice and a sufficient rGO surface coverage on the drain-source sensor array. Hence, when applying a voltage of 50 mV to the drain and source terminal the current will be in the range on hundreds of µA to mA. The need for a high accuracy SMU isn't given for the present measurement specifications. Commercial alternatives to a high priced and bulky SMU are available, like the measurement device U2722A from Keysight Technologies, shown in Figure 55 (A). The advantage of this device is the presence of three independent controllable channels, where two can be used to measure simultaneously two gFETs, while the third channel controls the gate. The circuit diagram for the I_D/V_G characterization of two gFETs parallel is shown in Figure 55 (B).

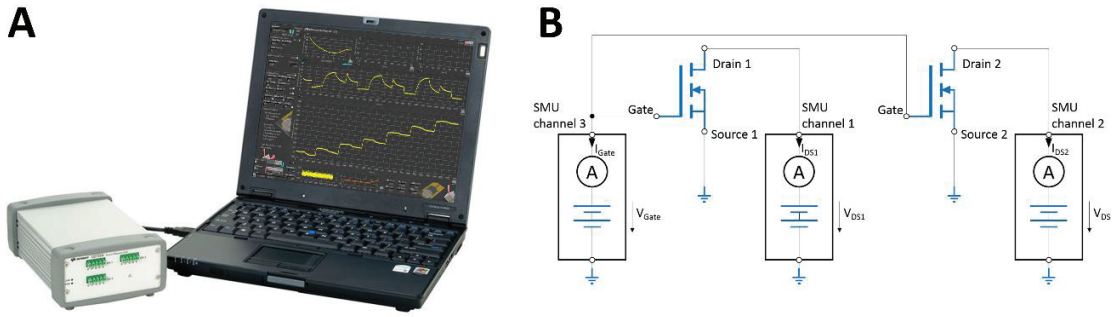

Figure 55: A: Three channel Keysight U2722A alternative to expensive and bulky source meter units for the simultaneous measurement of two gFETs. B: electrical circuit diagram to measure two gFETs with a common gate electrode.

Software: gFET measurement utility

A software module controls the SMU U2722A to achieve reproducible results during all experiments. The gFET measurement utility takes over all task of setting the parameters for the measurement, running the experiment and logging the measured data. The customized requirements for the software tool contain the following requirements:

- Adjust parameters for the measurement:
  - V_{DS}, V_{Gate}, current ranges, Start and Stop potentials, repetitions
- Read and save configuration files for measurements
- Measure the I_{DS} current once a second and plot it vs. time
- Measure the transfer characteristic I_DV_G
- Evaluate the Dirac point shift and slope change
- Export all measurements in an excel table at the end of the experiment
- Control two gFETs simultaneously

The programming environment Labview™ 2016 from National Instruments offers all driver components to connect the hardware Keysight U2722A via USB and provides a graphical user interface (GUI) for a good working platform on the computer.

Flow cell 1: micro fluidic design

The commercially available flow cell from the company Micrux Technologies provides a micro fluidic device for electrochemical experiments, where all electrodes are planar on a glass substrate with dimensions of 6 x 10 mm. Typically, such sensors chips consist of two or three electrodes, working electrode (WE), counter electrode (CE) and optional the reference electrode (RE) to measure electrochemical properties on the surface or in solution. Figure 56 shows the flow cell base (ED-AIO-CELL), the lid (FC-PMMA-3,5) and the sensor chip with two interdigitated electrodes (ED-IDE1-Au), available at Micrux Technologies. These components are commercially available from Micrux Technologies and can be connected via standard USB-mini cable to a potentiostat to perform measurements.

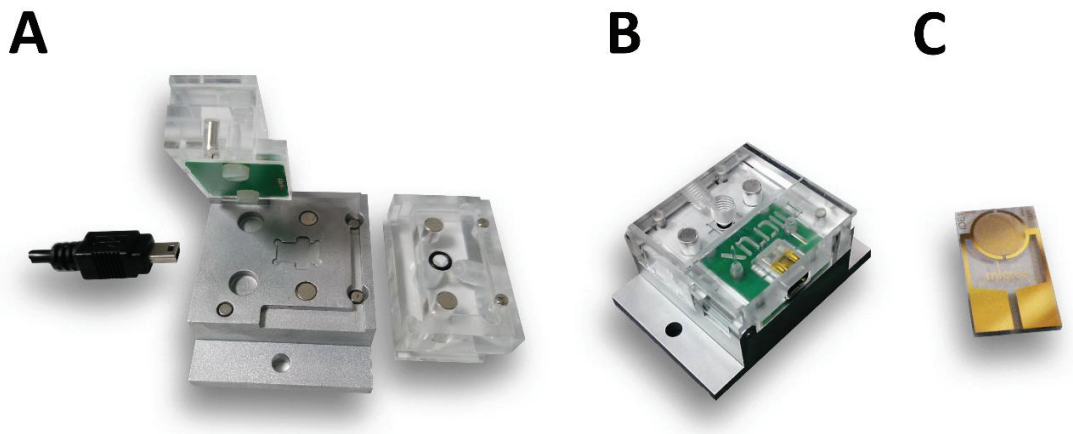

Figure 56: A: Flow cell for electrochemical experiments with a microfluidic lid to inject analytes in a precise volume. B: assembled flow cell. C: Sensor chip with two interdigitated Au electrodes with a size of 6 x 10 mm. The sensor chip can be inserted in the flow cell and is connected to a USB plug, accessible at the back of the cell. All parts are available at Micrux Technologies.

The commercially available lid is not suited for a liquid gated FET experiment. The interdigitated electrodes of the standard Micrux chip (ED-IDE1-Au) can be used as drain and source electrodes, while an additional AgCl wire is necessary in the lid as a gate electrode on top of the sensor chip. Micrux Technologies produced the adapted lid according to 3D design, shown in Figure 57. The 3D parts were all designed with Autodesk Inventor and the lid was produced of Poly(methyl methacrylate) PMMA.

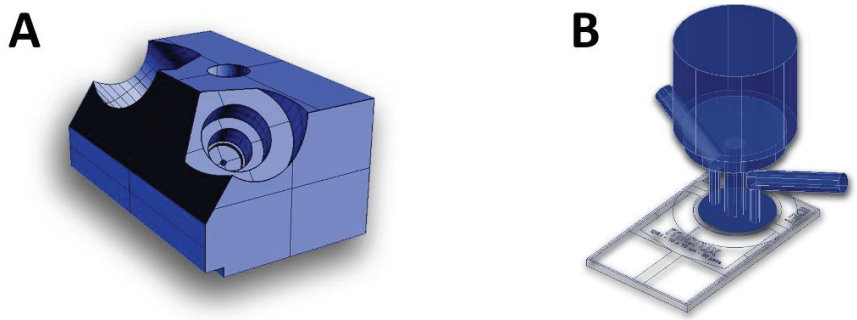

Figure 57: The flow cell was re-designed to implement a gate electrode inside the measurement chamber. A: Customized microfluidic flow cell lid, produced by Micrux Technologies according to 3D drawing for the integration of a AgCl wire on top of the sensor chip. B: detailed view to in- and outlet of the microfluidic system. The cylindrical center was implemented to insert the gate electrode.

Flow cell 2: gFET/SPR

The aim of this work is to create a research platform to compare the performance of electrical field-effect transistors with optical surface plasmon resonance for bio-sensing experiments. When the results of two independent techniques are compared, it underlies mismatches between the two systems. Variations in the flow rate and temperatures due to different set-ups yield errors in binding kinetics measurements. To sort that out, a novel approach for simultaneous measurements of optical and electrical sensor signals within one flow cell is shown in this work. SPR bio-sensors are commonly composed of a planar thin gold film coated glass slide that is adjusted for plasmon excitation. In the event of an incident light from the backside through a glass prism, the Kretschmann configuration, plasmons are excited and can be observed as the missing component of the reflected light in the resonance angle. The gold slide is modified with capture molecules, which, in case of binding events change the resonance angle of the plasmons. Typically, the gold slide is assembled in a flow cell to wash a buffer solution containing the analytes over the sensing area. Liquid gated field-effect transistors for bio-sensing comprise of a similar flow cell architecture. The gold slide of the SPR set-up can be used as gate electrode instead of a AgCl wire. It is necessary to assemble a sandwich of the drain-source electrodes on one side with the gate electrode on the other side of a liquid channel. The gold slide has now two functions: for the electrical FET it is the gate electrode and for the SPR configuration,

it exhibits the surface plasmons. The essential components for the gFET/SPR set-up are the gold slide, the drain-source electrodes and a gasket, shown in Figure 58.

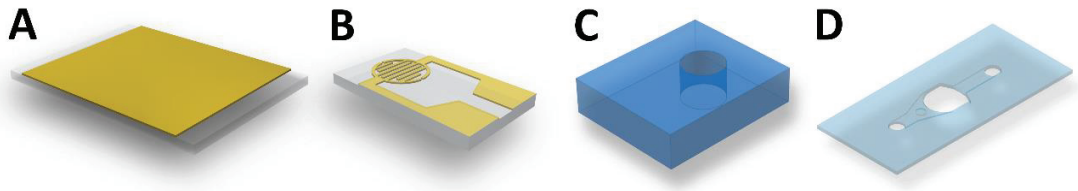

Figure 58: A: Planar SPR slide with 2 nm chromium and 50 nm gold on a microscope glass slide, working also as gate electrode. B: FET sensor chip with interdigitated electrodes as drain and source terminal. C: first approach of gasket in the gFET/SPR assembly with a channel height of 3 mm. D: second iteration microfluidic gasket with a channel height of 400 µm.

Figure 59 shows the approaches of combining the SPR in a Kretschmann configuration with a gFET in one flow cell, fabricated in a fused deposition modeling (FDM) process, a specific method of 3D printing. All FDM parts were fabricated with the Ultimaker S5 and two different filaments: polylactic acid (PLA) as building material and polyvinyl alcohol as water soluble support material.

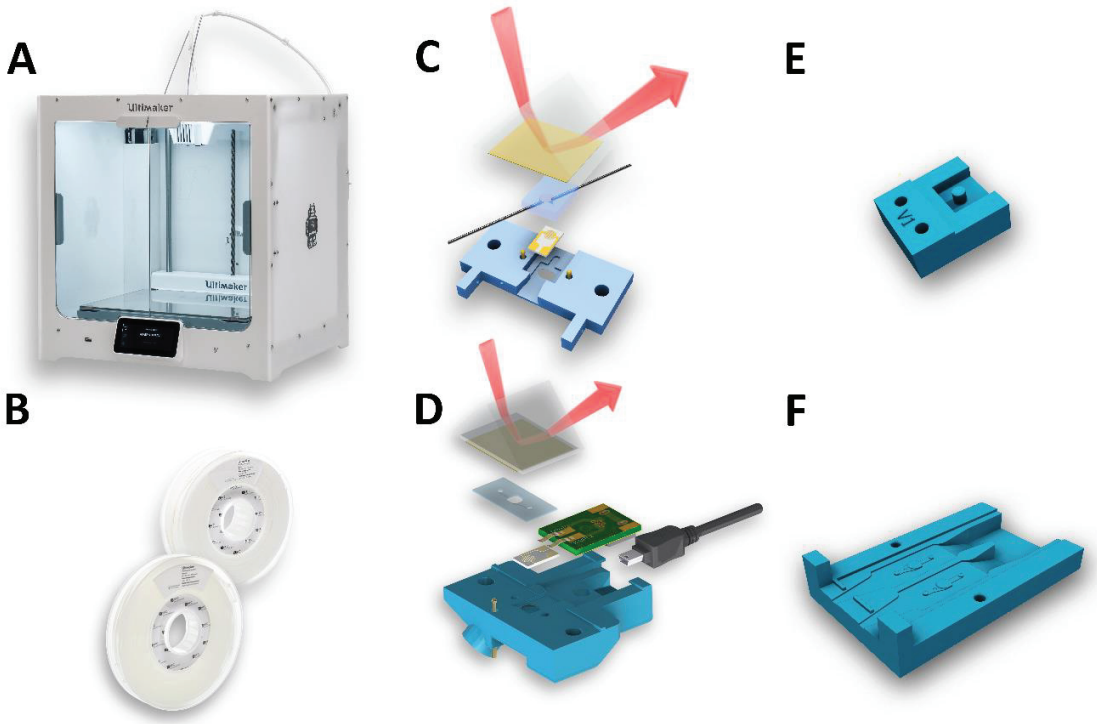

Figure 59: A: Ultimaker S5 for fused deposition modeling (FDM) of the necessary parts for the gFET/SPR flow cell. B: PLA filament as molding material, PVA as supporting material C and D: both designed 3D models of the gFET/SPR flow cells (blue) in combination with all required parts to assemble the sandwich for the measurement. E and F: molding forms for the PDMS gaskets. Figure D and F show the second iteration step towards the gFET/SPR system.

The gasket between the gold slide and the field-effect transistor was designed according to the requirements of the created flow cell. The in- and outlet of the molded cell are perfectly aligned with the gasket's openings in the 3D design file. With an FDM process the flow cells and molds for the PDMS gaskets were fabricated. The first approach of combing the electrical chip with the SPR slide contained a 3 mm thick PDMS gasket, connected to tubing with syringe needles. The first gFET holder and the 3 mm gasket are later referred as 3 mm flow cell. This first gFET/SPR flow cell was the proof of principle and lead to the second iteration of the flow cell, later called µCell with a microfluidic gasket of only 400 µm liquid channel height.

Gasket for µCell

It was necessary to create a molding form to produce the 400 µm high gasket for the µCell with its unique properties. The special feature about this gasket is the 3D channel architecture. Commonly, a sealing gasket has only two-dimensional features which are cut out of a Polydimethylsiloxane, called PDMS, foil or produced in a lithography step. The required gasket needs to seal the channel between the in-/out-let and the sensing are on the gFET side, because of a gap between the molded part and the sensor chip, shown in Figure 60.

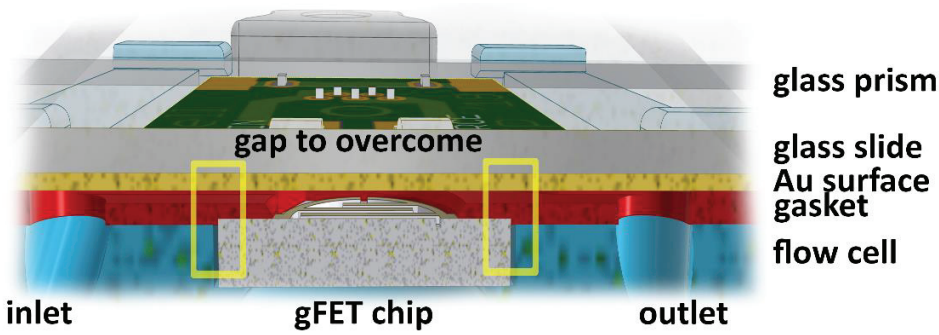

Figure 60 The sketch illustrates the important detail of the µCell: the microfluidic combination of the gFET (bottom) and the gold slide (Au surface). On the left and right side are the in- and outlet for injecting solutions containing the analytes. The gasket, in red, seals the channel between gFET and SPR surface. The yellow squares mark the gap between the gFET holder (blue) and the gFET chip, sealed by the unique gasket design.

The gasket is asymmetrically designed between inlet and outlet. The inlet side opens like a funnel towards the measurement spot, in the center of the gasket. A spacer dot between top and bottom part is implemented inside the funnel to avoid a lift off from the gFET surface. The outlet side reduces the cross section rapidly to avoid trapping air bubbles.

PDMS gasket fabrication

Once the molds for the 3 mm and µCell gaskets were fabricated, the PDMS gasket can be produced. Standard microscope slides (25 x 75 mm) cover the molding forms to make a sealed chamber for casting the liquid PDMS. The polydimethylsiloxane solution is prepared right before the casting for good pouring properties. The source of the PDMS is

the Slygard 184 kit from Sigma Aldrich. The monomer and the curing agent are mixed in a ratio of 10:1 and stirred with a glass spatula for 10 minutes to assure a homogenous mixture. Air bubbles immerse in the solution during this process, which are removed in a desiccator for 15 minutes under vacuum. The liquid siloxane solution is carefully poured into the top of the molding forms in an upright position. The molds are put inside a vacuum oven at 35 °C over night for the curing the PDMS. The final silicone elastomer shows all features of the designed molding form and can be used in the gFET/SPR flow cells after removing under isopropanol alcohol rinsing with a tweezer.

Tube connection to the gFET/SPR flow cells

The first model of the gFET/SPR flow cell with the 3 mm gasket is connected with two syringe needles of diameter 0.75 mm with a length of 35 mm. One side of the needle is connected to silicone tubes SC0002 from Ismatec, with an inner diameter of 0.25 µm. The tip of the syringe is inserted through a guidance hole in the gFET holder to plunge inside the 3 mm gasket. This step is repeated for inlet and outlet.

To connect the in- and outlet tubes to the µCell it was necessary to tap 1/16” screw threads for standard HPLC tube end fittings, like Bola F 702-38. PTFE tubes with an outer diameter of 1/16”, like Sigma Aldrich 58702 are inserted. The PTFE tubes are attached to the terminal pieces Kinesis 002310 for a good sealing in the final mounting position. This allows a rapid disassembly of the flow cell.

Fabrication of printed circuit boards

A copper etching technique was used for rapid prototyping of printed circuit boards, to create the required connections between the measurement equipment and the gFET. The base material for the PCB boards are 1.6 mm thick copper laminated (60 µm) fiberglass plates. The raw copper sheet is polished with a fine sandpaper of grit size P1200 to remove the copper oxide layer. Subsequently, the sheet is washed briefly with water and remaining grease residues are rinsed off with acetone. All PCB boards are designed using the layout software Eagle V7.6.0., laser printed on transparent overhead foil (Avery, A4) and

transferred to the copper board using and heat plate. A heat plate is preheated to 140 °C and the copper plate placed on it with the copper upside. The printed circuit on the overhead foil is placed on the board, with the laser printer toner facing to the copper. A cork matt covers the PCB and for 5 minutes a constant pressure is applied to transfer the toner onto the copper. After the 5 minutes, the PCB is immersed in cold tapped water to cool it down rapidly and remove the foil. The copper layer of typically 60 µm is etched in a sodium persulfate solution (Sigma Aldrich, CAS Number: 7775-27-1) with a concentration of 20 g/100 mL in the 50 °C bath under constant stirring. Only copper exposed to the etching solution is removed. Figure 61 shows the designed PCB boards for Keysight/gFET connections, using standard USB connections.

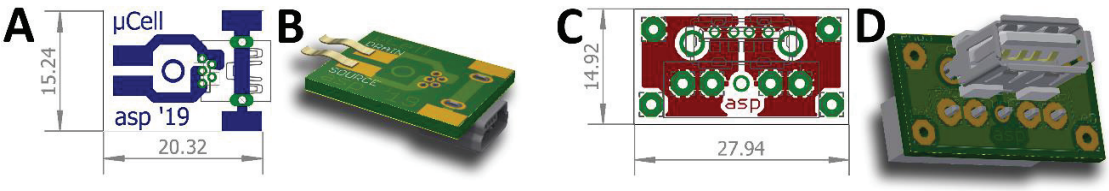

Figure 61: Illustration of the designed printed circuit boards for the connection of the gFET/SPR cell to the source measure unit. A and B: Eagle layout file and 3D visualization of the gFET/SPR connector board. C and D: Eagle layout file and 3D visualization of the Keysight U2722A USB connector board. A standard USB-A to mini cable connects the measurement set-up.

Results of gFET/SPR design

All results from the creation of the measurement system, the developed software tool and the novel gFET/SPR flow cells are listed. The realization of all these tools were a corner stone of the present work, without the project would have been possible.

Measurement set-up for the gFET and gFET/SPR

The combination of the new source measure unit Keysight U2722A, the designed liquid gated Micrux or SPR flow cells and the developed software tool "gFET measurement utility 4.4" guarantee a reproducible way to perform all gFET and gFET/SPR experiments throughout this project under stable conditions. To connect the SMU with the gFET measurement flow cells it was necessary to create an adapter to a standard USB cable. Beside the availability of such standard USB-A to USB mini cables, it is impossible for the user to connect the devices wrong. The mechanical stability was achieved with an in house produced connector board, shown in Figure 62.

Figure 62: A: Connector board to a standard USB-A plug for both drain-source channels. B: Connected USB cables to the SMU. The gate electrode is connected to the shield of the USB cable for the gFET/SPR flow cell and to a wire for the Micrux flow cell, shown in C. D: The connection of the Keysight U2722A source meter unit to the Micrux flow cell with a USB cable and a wire for the liquid gate electrode. The gFET/SPR flow cell and Micrux gFET flow cell are connected for parallel measurements.

The USB housing connects the gate electrode to the shielding of the cable for a gate connection in the gFET/SPR flow cell, while a wire connects the gate electrode of the new Micrux flow cell, re-designed to include a gate electrode. The developed software fulfills

all requirements stated in Chapter 4: Software: gFET measurement utility and Figure 63 shows the final version of the gFET measurement utility.

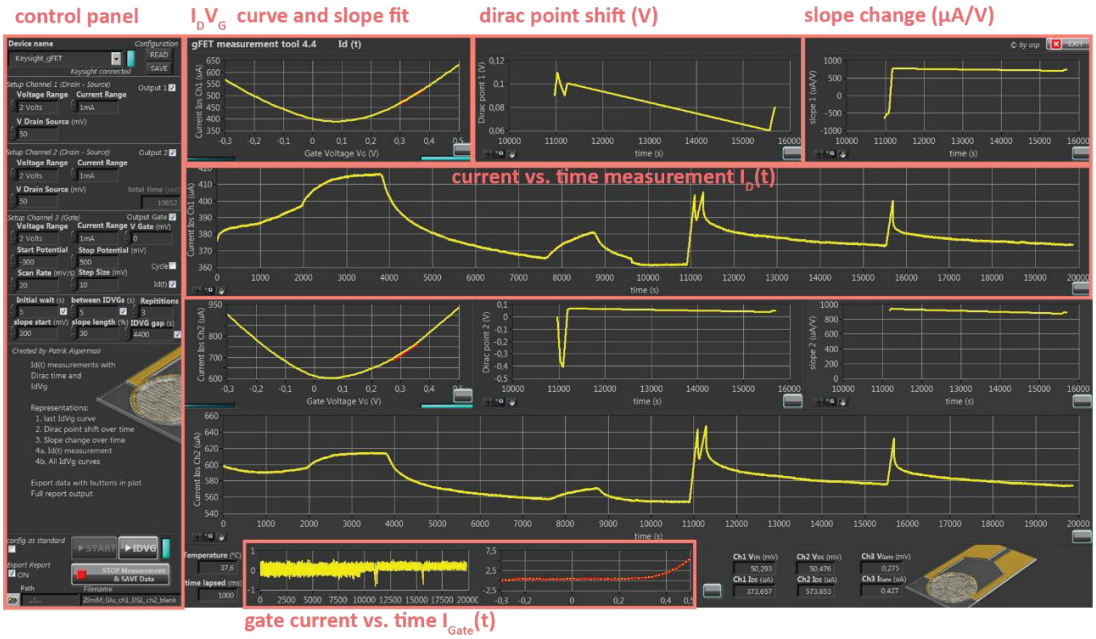

Figure 63: The software "gFET measurement utility V4.4" is controlling the Keysight U2722A, logging the measured data and plots the data of the running experiment. Further features are the automated evaluation of the Dirac point and the slope of the transfer characteristic of each gFET (I_DV_G curve).

The gFET measurement utility V4.4 allows the adjustment of all parameters, required to start the measurement with the Keysight U2722A.

Graphical user interface (GUI)

In the control panel sets the gate and drain-source voltages, current ranges and time values for a voltage sweep. Furthermore

Transfer characteristic I_DV_G

The recording of the Drain-Source current I_{DS} or short I_D during the V_G sweep yields a so-called I_DV_G curve. All I_DV_G curves represent the interfacial properties of the gFET at the moment of measurement. It is a sweep of the gate voltage V_G from the start to the stop potential in discrete voltage steps per time units, adjusted in the GUI by the user.

Dirac point and slope evaluation

Surface charges, ionic double layer and molecule adhesion on the surface influence the parameters of eq 2, causing a shift in the Dirac point and the slope of the transfer

characteristic. The automated evaluation of the Dirac point shift, in V, and slope change, in µA/V, were implemented in the software and the results are plotted in real time during the experiment, shown in Figure 63. The Dirac point is the minimum of each I_DV_G curve, plotted as the voltage value vs. time, while the slope is evaluated either from the n-type or p-type branch of the curve. The user chooses the evaluated direction and length of the slope, according to the Dirac point. The settings "slope start" in mV and "slope length" in percentage define the considered data points for linear regression. It is not advisable to choose 100 % because the center of the Dirac point has a slope of 0 µA/V, therefore the linear regression would yield a high error.

Repetitions, automation and Dirac time

Automation in measurements makes the experiment easier and leads to reproducible data. The user adjusts the time delays and number of repetitions for the I_DV_G curves. In case of holistic studies for the changes of surface properties, a continuous I_DV_G measurement is necessary. The novel technique called "Dirac time" records transfer characteristics during the entire experiment and plots the shift of the Dirac point and slope variations as a function of time. The logged data contains kinetic in case of binding events on the gFET architecture.

As an additional interface, it was adapted to measure the electrical gFET and optical SPR signal at the same time, where the input signal for the channel two is provided by the locked-in amplifier of the SPR measurement set-up. Figure 64 shows the simultaneous readout of the gFET (upper graph) and the SPR signal (lower graph). The signal shows the simultaneous read-out of a layer-by-layer assembly, further discussed in Chapter 5: Layer by layer measurements.

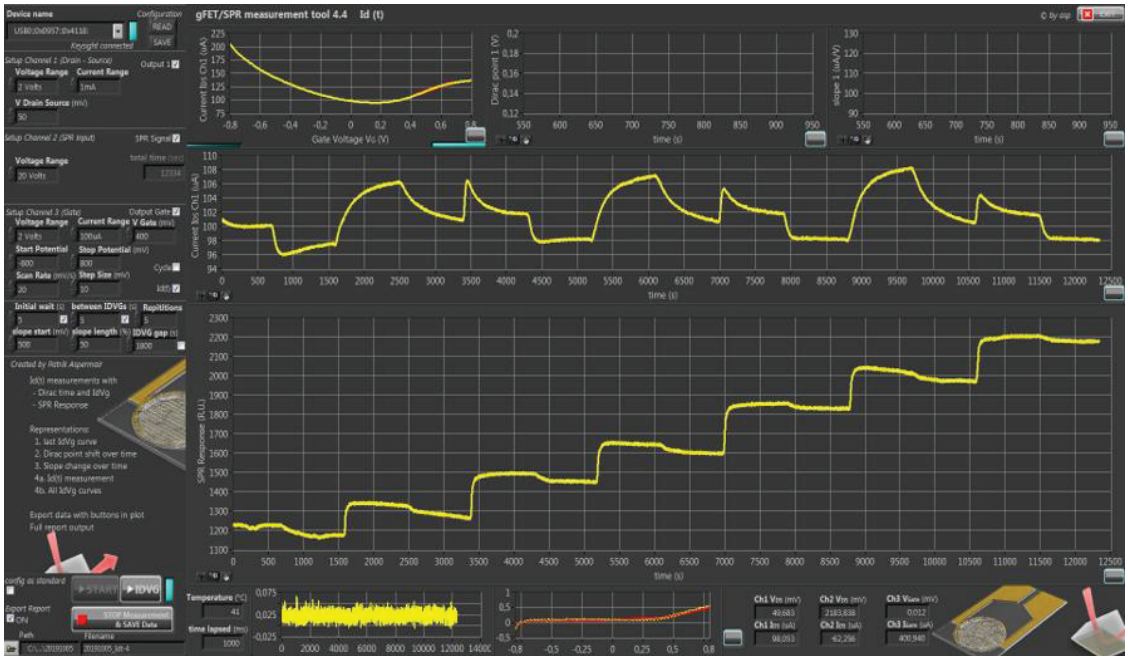

Figure 64: Demonstration of electrical and optical readout in the combined gFET/SPR measurement tool 4.4. The upper halve plots the transfer characteristic and the real-time $I_D(t)$ readout, while the lower graph is the recording from the optical SPR machine, at a certain adjusted angle.

Exported Data

Once the measurement is finished, the gFET measurement utility exports a Windows Excel spreadsheet with all logged and processed data. The output file is shown in Figure 65 and Figure 66. The entire data set for both channels during the experiment is automatically saved on the hard drive for further data processing and documentation.

	A	B	C	D	E	F	G	H	I	J
1	time	I\-(DS) 1		time	Dirac Point 1		time	Slope 1	V\-(Threshold) 1	
2	sec	µA		sec	V		sec	µA/mV	V	
3	0	376,027425		10965	0,09		10965	-639,65	0,611	
4	1	376,46993		11025	0,11		11025	-539,79	0,740	
5	2	376,719157		11086	0,1		11086	-504,29	0,795	
6	3	376,861572		11177	0,09		11177	762,57	-0,308	
7	4	376,907348		11227	0,1		11227	776,72	-0,295	
8	5	377,003987		11278	0,1		11278	773,45	-0,297	
9	6	377,17692		15577	0,06		15577	712,43	-0,365	
10	7	377,288818		15627	0,07		15627	731,78	-0,342	
11	8	377,390543		15678	0,08		15678	746,15	-0,326	
12	9	377,400716								
13	10	377,548218								
14	11	377,461751								
15	12	377,792358								

Time 1 | IDVG 1 | Time 2 | IDVG 2 | gate

Figure 65: The gFET measurement utility 4.4 creates an Excel spreadsheet with the measured and calculated values during the experiment. Separated sheets store the data for both gFETs measured simultaneously, including the Dirac point shift, the slope and the threshold voltage V_T.

	A	B	C	D	E	F	G	H	I	J
1	V\-(Gate)	I\-(DS) 1								
2	V	µA								
3	number	1	2	3	0	1	2	3	0	
4	time	10965,13867	11025,42676	11085,71582	0	11177,17285	11227,46289	11277,75195	0	15577,18
5	-0,5	761,138916	739,013672	729,125977	-0,3	563,812256	560,882568	562,225342	-0,3	580,108
6	-0,49	749,908447	727,152507	717,753092	-0,29	557,383219	554,64681	555,124918	-0,29	572,814
7	-0,48	738,382976	715,667725	705,759684	-0,28	550,526937	547,241211	547,8007	-0,28	564,992
8	-0,47	727,193197	704,376221	694,3868	-0,27	543,416341	540,395101	540,781657	-0,27	557,647
9	-0,46	717,010498	694,091797	683,492025	-0,26	536,539713	533,589681	533,894857	-0,26	550,109
10	-0,45	706,634521	683,746338	673,034668	-0,25	530,049642	527,1403	526,855469	-0,25	542,653
11	-0,44	696,573893	673,878988	663,543701	-0,24	523,376465	520,253499	520,273845	-0,24	535,135
12	-0,43	687,266032	664,296468	653,727214	-0,23	516,916911	514,200846	513,783772	-0,23	527,923
13	-0,42	678,029378	655,222575	644,582113	-0,22	510,945638	507,832845	507,588705	-0,22	520,833
14	-0,41	668,93514	646,433512	636,189779	-0,21	504,811605	501,89209	501,790365	-0,21	513,671
15	-0,4	660,583496	638,559977	627,614339	-0,2	498,860677	495,859782	495,788574	-0,2	506,947

Time 1 | IDVG 1 | Time 2 | IDVG 2 | gate

Figure 66: The Excel spreadsheet contains all measured I_DV_G curves including the time stamp to associate the transfer characteristic to a specific binding event on the gFET substrate.

Assembly of gFET/SPR cells:

After all parts were fabricated with the Ultimaker S5, they were cleaned and assembled as shown in Figure 59. The 3 mm flow cell requires a soldering step to connect the gFET chip with the Keysight U2722A, while the µCell is attached with a USB mini

cable. A connector board for the µCell was designed and fabricated in house. Figure 67 shows the assembled components in the gFET/SPR configuration.

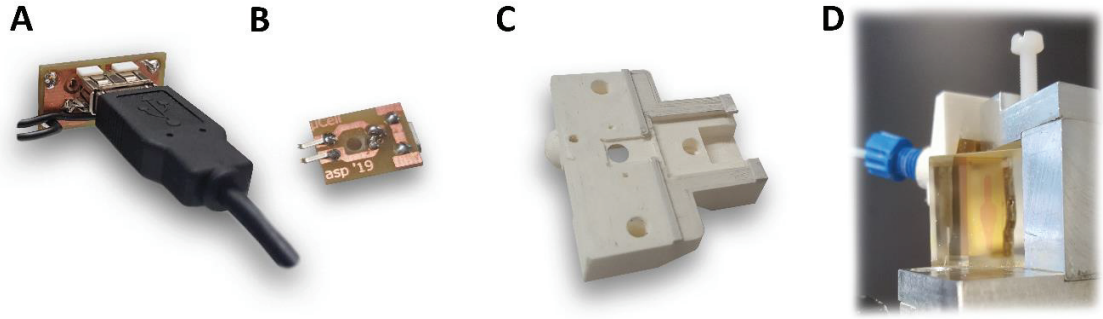

Figure 67: The pictures show the designed and produced connectors and flow cells for the gFET/SPR architecture. A: USB connector board for Keysight U2722A. B: gFET connector board for µCell adapter with USB mini plug. C: Fused deposition modeled µCell adapter for the gFET/SPR configuration. D: Assembly of µCell with the glass prism. The 400 µm gasket can be seen inside the prism, where it is pressed against the SPR gold substrate.

Discussion

This chapter shows the development of a completely new measurement set-up, using a commercially available source meter unit with three channels to measure two gFETs and apply on the third terminal a gate voltage. The new developed software package for the user to control all channels of the SMU, start measurements in different modes and store the data in an Excel spreadsheet is in its final version suitable to measure any gFET bio-sensing event. The gFET measurement utility 4.4 contains a novel measurement technique to observe the Dirac point shift and slope change during the real time measurement. This new feature in FET bio-sensing aims a comprehensive way to study the kinetic of binding events, not only by a fixed gate voltage or a transfer characteristic after the binding event is finish, but a real time monitoring of the influence of ligands to its binding partner, immobilized on the sensing surface.

In combination with a FET micro fluidic flow cell, such as the new fabricated Micrux cell and the novel development of the gFET/SPR cell, this tool can be used as a research platform to investigate binding phenomena. The Micrux cell has the advantages of fast assembly and commercial availability. The disadvantage is caused by the architecture: the modification of the gate electrode is not possible with the AgCl wire, therefore all experiments have to be carried out on the rGO surface, at the drain-source channel substrate. The surface chemistry for bio-functionalization can be a difficult task and needs to be adapted for each substrate. The gFET/SPR micro fluidic device enables the use of a standard Au slide with established thiol-chemistry and can benefit from a dual measurement system with optical and electrical readout. The first approach with the 3 mm flow cell was the first attempt of combining the gFET with the SPR device. Once the working principle was tested, the system could be improved with a microfluidic gasket and a better way for assembly. The here shown improvements from a 3 mm high measurement chamber towards 400 µm was a big leap for the rapid solvent change inside the cell. The required volume is drastically decreased, and a laminar flow is available inside the chamber. The gFET connector board makes the system compatible with a daily lab practice and the USB connection to the source measure unit decreased connection problems. The herein developed gFET/SPR setup, combined with the electronic measurement tool and

facile usability of the software package provides a platform for bio-sensing applications for future researcher.

5. Chapter:

Measurements with gFET and SPR

This chapter applies the knowledge gained throughout the Chapters Introduction, Fabrication of graphene FETs and gold slides, Surface Modifications and gFET/SPR measurement tool, to perform electrical gFET and optical SPR measurements on the sensor surfaces.

Materials and Methods

At the beginning of this work, electrical measurements on the gFET were carried out independently from the optical surface plasmon resonance measurements. The surfaces, such as graphene FETs, gold slides and graphene/gold slides were fabricated according to the protocols of Chapter 2: Fabrication of graphene FETs and gold slides.

Initially, optical SPR experiments on CVD graphene were carried out on a commercial SPR system from Sensia, the Indicator-G. The prisms for this device were purchased directly from Sensia, already coated by Graphenea with a CVD graphene layer.

Human Papilloma Virus protein

The first aptamer experiments were carried out on CVD graphene coated gold surfaces in an SPR system Indicator-G (Sensia). The functionalization of graphene was demonstrated and discussed in Chapter 3: Surface Modifications and consists of the surface architecture for specific binding of the analyte and blocking of non-specific bio-molecules. A self-assembly layer of pyrene-carboxylic acid and pyrene-PEG mixture was applied before the bio-recognition element was immobilized. An amine-terminated Aptamer was immobilized on the EDC/NHS activated surface. The sequence for the best suitable ssRNA

aptamer originates from a SELEX process and was determined among six candidates with the highest affinity to the human papilloma virus protein [115]

Layer by Layer assembly

The combination of the optical SPR and electrical gFET measurement creates the possibility of simultaneously recording the refractive index change and the influence on surface charges on the bio-sensor surface. To observe and understand the difference between positively and negatively charged species on the surface, a layer by layer assembly of alternating charged species was carried out. The optical signal represents the change of refractive index upon mass deposition on the surface. These adsorbed molecules on the surface lead to a collective new order of charges on the gate electrode, modulating the drain-source current of the graphene FET. The electrical readout is based on sensing of continuous deposition of different charges, redefining the electric double layer or the electrostatic field[i]. The formation of PDADMAC/PSS polyelectrolyte multilayer films, so called PEM, was used to obtain differently charged surfaces in a controlled experiment. The electrostatic interaction supports the alternating adsorption of PDADMAC poly(diallyldimethylammonium chloride) and PSS poly(sodium 4-styrenesulfonate) on the Au-surface .

The experiment was carried out with the novel gFET/SPR measurement setup and the polyelectrolytes with different charges were injected to the surface using a peristaltic pump at a flow rate of 50 µL/min, while the optical and electrical responses were monitored. The details are show in publication Aspermair *et al.* [116]

Biotinylated gold surface

The surface of the SPR slide was modified with biotin, following the procedure reported in Chapter 3: Gold slide biotinylation. The experiment was carried out in the gFET/SPR setup, were only the golds slide was functionalized. The specific binding events of avidin, neutravidin or streptavidin to the biotin leads to an increase in surface mass and

therefore change of the resonance angel, which can be observed in a real-time SPR measurement. The adherence of any avidin complex leads also to a charge re-distribution on the gold slide, which works as gate electrode for the gFET at the same time. The gFET readout signal is therefore modulated upon binding events. The binding experiments were always observed with continuous SPR readout at a fixed angle to trace the change of reflectance during the binding events. The gFET experiment was carried out in two different modes: $I_D(t)$ and I_DV_G.

$I_D(t)$ mode: continuous current I_{DS} measurement with a fixed gate voltage V_G

I_DV_G mode: measurement of the transfer characteristic after the binding

The two methods have both advantages: the $I_D(t)$ can be used to evaluate the binding kinetic for each concentration because a data point is acquired every second, while the I_DV_G curve measurements cover the entire transfer spectrum of the gFET after each binding event. This is in particular interesting, if it is not known, at what gate voltage the binding event will be most prominent.

Results of gFET/SPR measurements

Human papilloma virus protein detection

The detection of the human papilloma virus was carried out on the commercial SPR Indicator-G from Sensia and on the stand-alone gFET measurement flow cell. The results for the human papilloma virus protein titration from 7.5 nM to 1000 nM are shown in Figure 68. The titration of insulin was performed at the end of the HPV protein titration to observe the non-specific interaction on the rGO surface. Since the protein has a similar molecular weight of around 60 kDa, it would lead to a similar non-specific interaction on the surface. The response to an insulin concentration of 1000 nM is around 4 µA, comparable to the specific signal at 7.5 nM HPV-protein concentration. A concentration of three orders of magnitude higher to this, 1 mM, was injected to exhibit a response of insulin on the gFET. This demonstrates that the anti-fouling surface modification suppresses the non-specific interaction, while specific interaction occurs at 7.5 nM.

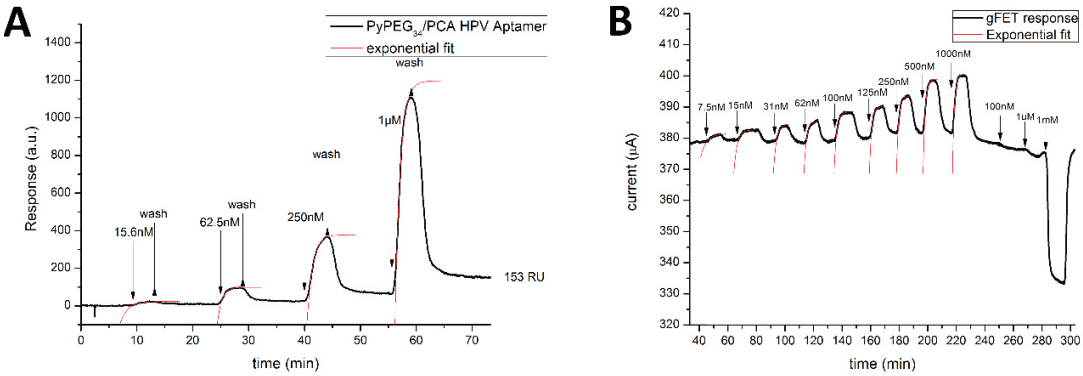

Figure 68: The graphs show the titration of the human papilloma virus protein to an HPV-aptamer modified surface. A: sensorgram illustrates the change of the SPR signal on binding events. The right sensorgram (B) shows the electrical rGO gFET readout upon specific binding. Both experiments were carried out on the same day with the same surface modification on graphene. Both sensor responses contain the exponential fit upon binding events for further investigation of the binding kinetics involved at different concentrations.

The exponential fits upon binding events were evaluated and are plotted in the Figure 68. The time constant of the exponential equation represents the affinity of the ligand to the capture probe at different concentrations. If this value is inserted in the

Langmuir equation, the half-saturation value can be determined, which represents the dissociation constant K_D. Figure 69 illustrates the different Langmuir curves for the optical SPR and electrical gFET sensor responses.

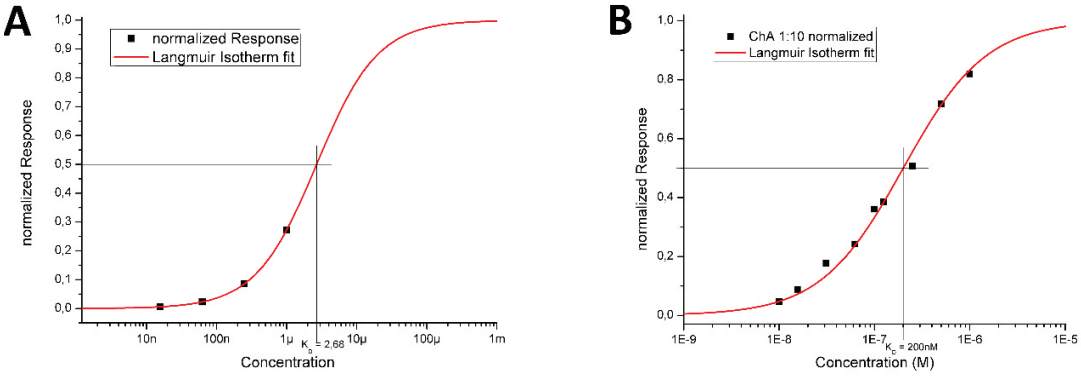

Figure 69: The evaluation of the exponetial binding kinetic at different concentrations from the sensorgrams results in the Langmuir plot. The dissociation constant K_D can be determined at half-saturation of this representation. The values of the optical (A) and electrical readout (B) differ, while the surface functionalization is the same. The electrical gFET response represents a K_D of 10 times lower than the optical SPR experiment.

The binding of the HPV-protein to a densly packed surface, a more losely packed surface and to a scrambled, but anti-fouling surface are shown in Figure 70. The SPR sensor exhibits the highest magnitude of around 200 response units at a loosely packed surface coverage. The CVD graphene surface was modified with a 1:10 ratio of aptamer linker and anti-fouling agent. A high packing density of the HPV-aptamer without any anti-fouling agent leads to a reduced sensor response. The non-specific surpression with the pyrene-PEG anti-fouling agent is shown with the sensor response at 1 µM HPV-protein injection. The latter surface was modified with a scrambled DNA sequence that has no affinity to the protein.

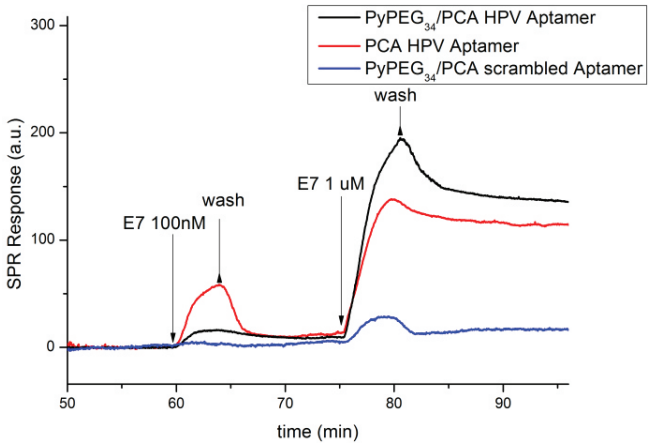

Figure 70: A comparison of different surface modifications of CVD graphene/Au-SPR prisms is shown. The injection of 1 µM HPV-protein results in the highest magnitude for spacially modified surfaces, while the densly packed HPV-aptamer has a lower signal magnitude upon bining. The control experiment with an immobilized scrambled aptamer exhibits a relatively small response, due to the pyrene-PEG anti-fouling surface modification.

The increased binding signal at 1 µM for a diluted aptamer surface coverage can be explained with possibility for the protein to access the binding site of the aptamer easier. A more loosely packed arrangement of aptamers increases the amount of binding proteins to the capture probe, hence increasing the signal amplitude, as shown in **Error! Reference source not found.**.

Titration of different pH solutions in gFET/SPR setup

The comparison of the graphene FET inside the Micrux flow cell with the novel gFET/SPR flow cell is shown in Figure 71. The two systems consist of different gate electrodes. The Micrux cell has a chloride coated silver wire, while the gFET/SPR uses the gold coated optical SPR slide as gate electrode. Therefore, the influence of different cell arrangements, is investigated with the titration of ionic solutions with increasing pH values. The ionic solution consists of standard PBS buffer (pH 7.4), adjusted with 0.1 M and 0.01 M HCl solutions to the values of pH 4 up to pH 7 in 0.5 increments.

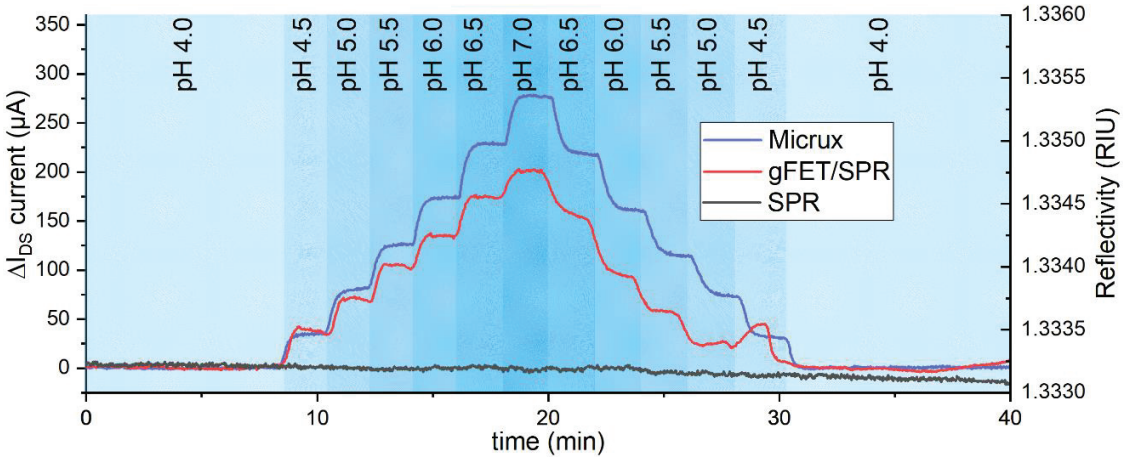

Figure 71: The response of the graphene FET to changing pH values of an ionic solution in two different flow cells is shown. The gate electrode of the Micrux flow cell consist of an Ag/Cl electrode (blue), while in the gFET/SPR cell uses a gold slide opposite to the drain-source-channel (red). While the I_{DS} current of the gFET measurement with V_{DS} = 50 mV and V_G = -400mV is modulated upon changing pH values, the SPR signal remains constant. The simultaneous optical readout is only modulated by refractive index changes, not occurring at different pH values, shown in black.

The response of the gFET in the Micrux cell differs from the gFET/SPR cell in a minimalistic manner. The magnitude of the signal differs according to the device-to-device variation, which can't be controlled better in this stage research. The SPR response remains constant upon pH value changes, due to the constant refractive index between the pH 4.0 and pH 7.0. The measurement proves the dependency of the gFET to pH concentrations, related to the variations of the electrical double layer formation on the two interfaces in the liquid channel between the gate electrode and the drain-source-channel.

Layer by layer measurements

The deposition of polyelectrolytes onto the SPR surface with simultaneous optical SPR and electrical gFET readout is shown in Figure 72. While figure (A) represents recorded SPR signal for two different experiments, (B) shows the gFET readout $I_D(t)$ upon layerdeposition. The blue curve represents the experiment carried out at a fixed gate voltage V_G = -400 mV, while the red curve is the result of a positive gate voltage V_G = +400 mV applied to the gFET.

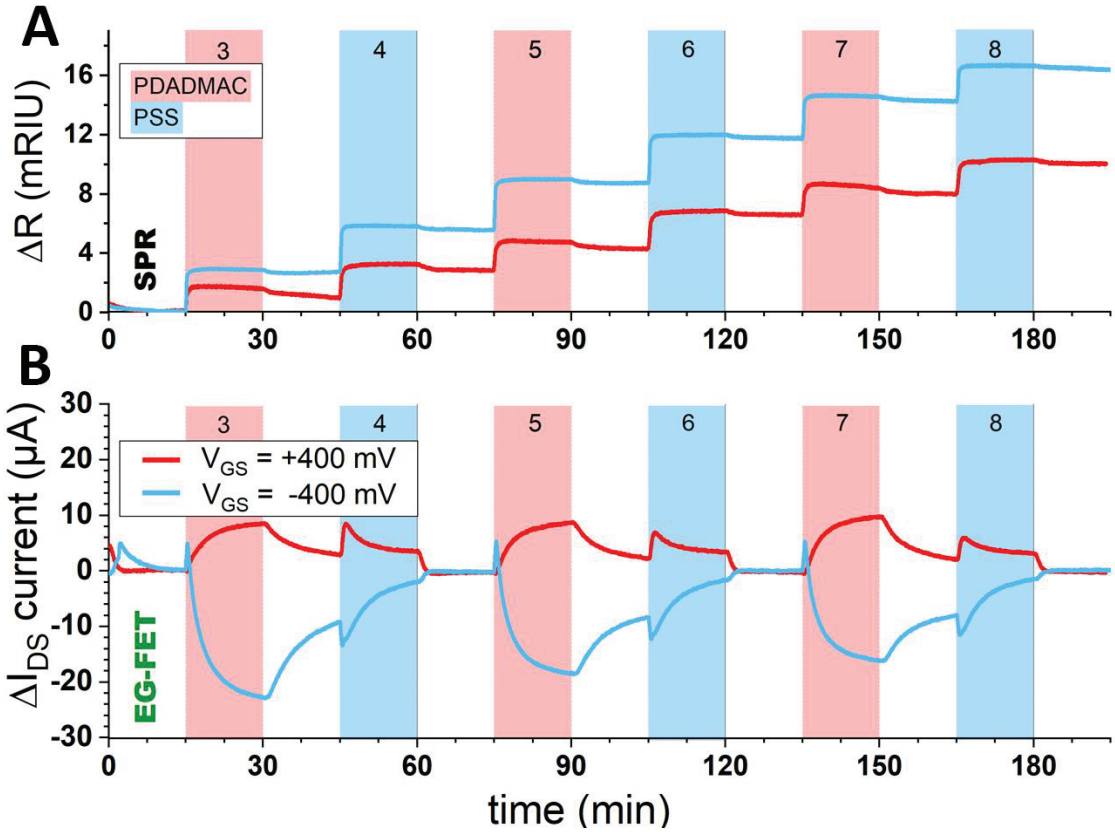

Figure 72: The in-situ readout of the gFET/SPR during the growth of a layer-by-layer assembly. The red bars represent the injection of PDADMAC (layer 3, 5, 7) and the blue bars represent the time of injected PSS (layer 4, 6, 8). The experiments were performed with two different gate voltages for the gFET: V_G = +400 mV (red) and -400 mV (blue). The signals in (A) are the mass uptake upon layer deposition, monitored by SPR and (B) are the charge displacements on the surface for different polyelectrolytes and their charges.

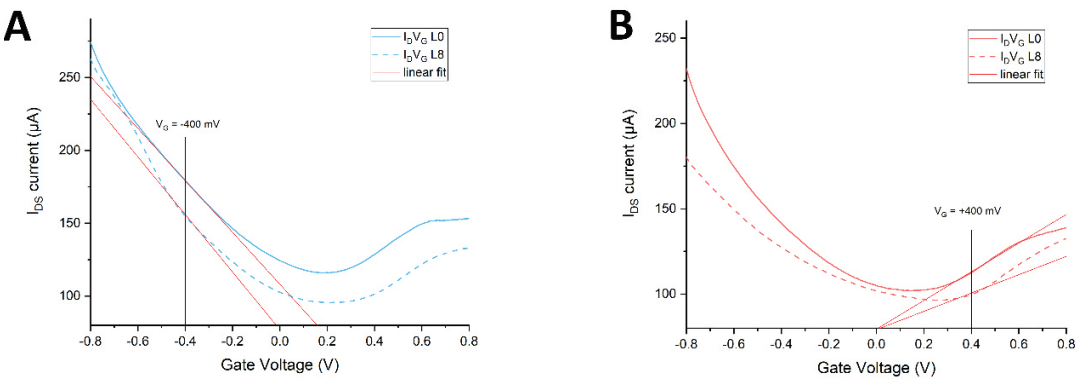

Figure 73: The comparison of the two gFETs before and after the polyelectrolyte depositions are shown. The transfer characteristics of V_G = -400 mV (blue) and +400 mV (red) gFETs experience both a change in their magnitude after the deposition. It can be noted, that the slope in the p-type regime (-400 mV) is steeper than the n-type (+400 mV). It correlates with a more prominent response for chip (A) during the $I_D(t)$ measurement.

The SPR signal shows expected behavior upon deposition of each polyelectrolyte layer. The rinsing after each layer with KCl stabilizes rapidly and proves that the layer remain on the surface. Each Layer was deposited and rinsed long for exactly 15 minutes to establish a static condition for the SPR readout. The gFET on the other hand was even after 15 minutes prone re-arrangement processes, visible at every deposition step in Figure 72 (B). The explanation for this behavior can be found in the re-orientation of charges on the surface of the polyelectrolyte, as well as within the layer. The diffusion of ions into the layer causes as slow process of surface charge fluctuation. This can be attributed to the alternatingly charged polyelectrolytes: depositing the positively charged PDADMAC results in an increase of the signal for a gFET with the gate voltage of +400 mV applied. The deposition of the negative PSS layer decreases the current I_{DS}. For a gate potential of -400 mV the response is exactly mirrored, although with different magnitudes.

The combined system of gFET and SPR in one flow cell enables the simultaneous observation of mass deposition and surface charge re-orientation. Due to the fact, that the gFET detection principle is based on the modulation of surface charges, this system can used to study the electrical properties of the system and maybe derive an equation for each binding couple.

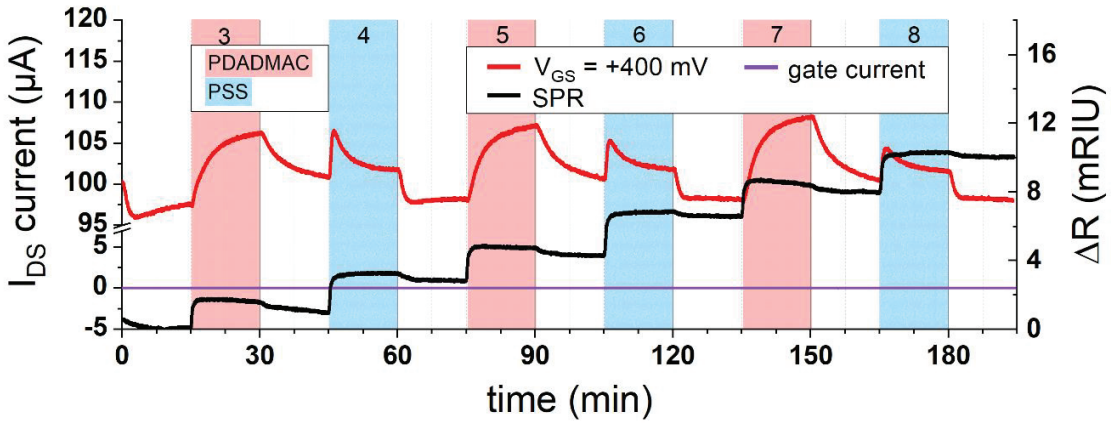

Figure 74:The raw signals of the measured gFET and the SPR signal are shown in one graph with an exact time stamp overlay of the layer-by-layer deposition. Beside the measured deposition of polymers on the surface, also the gate-source leakage current is shown in the graph as a purple line at 0 µA. The gate leakage current is a parasitic phenomenon and should be small. The here observed signal has approximately 200 nA, without any variations above the noise level and therefore can be neglected.

An outstanding property of graphene can be observed in Figure 74: the gate current I_G remains at any time during the entire measurement constant and below 200 nA. This proves the ability graphene to work in aqueous solutions without the coating of the drain and source electrodes to avoid a high leakage current. The ratio of leakage current to drain-source current I_{DS}, is below 1% of, for this experiment at about 0.2%, therefore negligible.

Biotin – Streptavidin interaction

The results of the biotin streptavidin binding upon a biotinylated gold slide for the plasmon surface and at the same time acting as gate electrode are shown in Figure 75. The SPR signal with the binding of different concentrations of streptavidin from 1 nM to 1 µM are shown in (A), while in (B) the SPS angular scan for the gold slide is shown before and after the streptavidin depositon. The angular scan was used to determine the surface mass density of streptavidn bound to the surface throughout the experiment. It was calculated to be 194.22 ng/cm^2 of streptavidn. The artefacts in the SPR signal, looking like a sawtooth signal originate from the I_DV_G curves measured after the sensor was exposed to each streptavidin concentration.

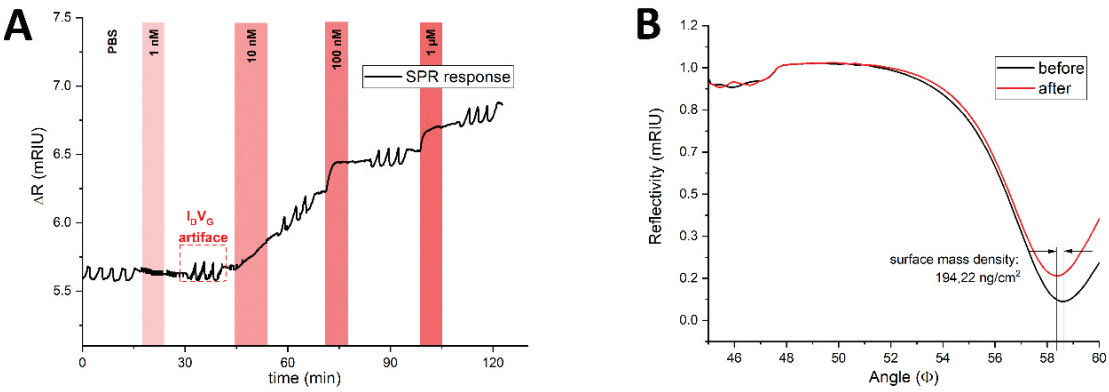

Figure 75: The titration of streptavidin and the specific binding to the biotinylated Au-slide is shown in (A). The SPR signal increases upon mass uptake at different streptavidin concentrations. The sawtooth artefacts are induced by the I_DV_G curve measurements of the gFET, because the Au slide is as well the gate electrode of the gFET. (B) shows the angular scan before and after the streptavidin binding. A surface mass density of 194.22 ng/cm^2 were calculated afterwards.

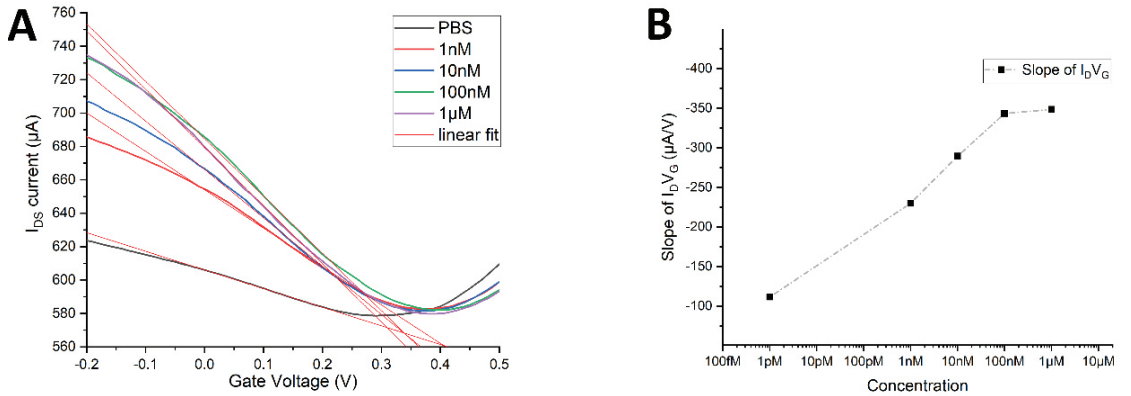

Figure 76: Binding of streptavidin to the immobilized biotin changes the I_DV_G curve of the gFET (A). The transfer characteristic was measured after each streptavidin concentration and the slope on the left side of the Dirac point is plotted versus the concentration (B).

The recorded I_DV_G curves after each streptavidin concentration are plotted in Figure 76 (A). Upon binding events, the slope of the I_DV_G curve changes and the slope increase can be used plotted versus the concentration, shown in Figure 76 (B). The herein demonstrated readout is modulated by the attachment of streptavidin to the biotinylated surface and can be read simultaneously in the electrical and optical system. The change in slope can now be attributed to a surface mass increase of 194.22 ng/cm^2 and further attributed to the surface charges incorporated by the amount of proteins.

Biotin – Neutravidin interaction

A protein with a similar binding kinetic as streptavidin to biotin, but differently charged is neutravidin. The gold surface, used as SPR slide and gate electrode for the gFET, was modified with biotin and different concentrations of neutravidin were injected to the sensor (0.2 nM to 25 nM). The sensor response of the gFET and of the SPR were recorded simultaneously and are shown in Figure 77. It can be observed, that the binding of 0.78 nM neutravidin generates a response of the gFET, while the sensitivity of the SPR is too low to induce a response. It can be noted, that after each neutravidin titration, the signal increases in the PBS buffer, which is a similar behavior as observed in the LBL assembly.

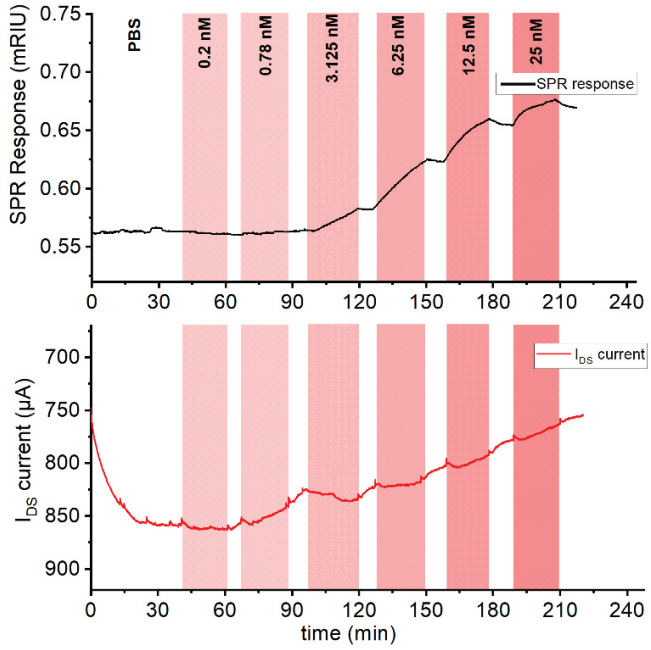

Figure 77: The optical (top) and electrical (bottom) measurements of neutravidin binding to a biotinilated gold-surface are shown in these figures. The measurements were performed simultanously in an assempled gFET/SPR flow cell, where the titration of Neutravidin started at 0.2 nM up to 25 nM. Both, the SPR and the gFET exhibit binding readouts upon neutravidin binding. Interestingly, the gFET signal exhibits an increase of the signal already at 0.78 nM, while the SPR signal remains in a steady equilibrium.

The gFET signal always increases upon neutravidin injection and starts to stabilize in the buffer solution. As well as in the layer-by-layer experiment, it can be noted that during buffer rinsing the sensor response indicates charge re-distribution. This phenomenon can be studied to investigate binding activity of bio-molecules.

Human Papilloma Virus I_DV_G analysis

The binding of the human papilloma virus protein E7 (HPV-E7) to the specific aptamer was beforehand shown in an SPR experiment on the commercially available "Indicator-G" (Sensia) and on the gFET in the Micrux flow cell. The assembly of the gFET/SPR setup leads to changes in the assembly and surface architecture. Whereas in the previous experiment, the aptamer was immobilized on graphene, for the gFET/SPR combination it was immobilized on the gold surface, which is the gate electrode for the gFET and the optical resonance substrate for the SPR.

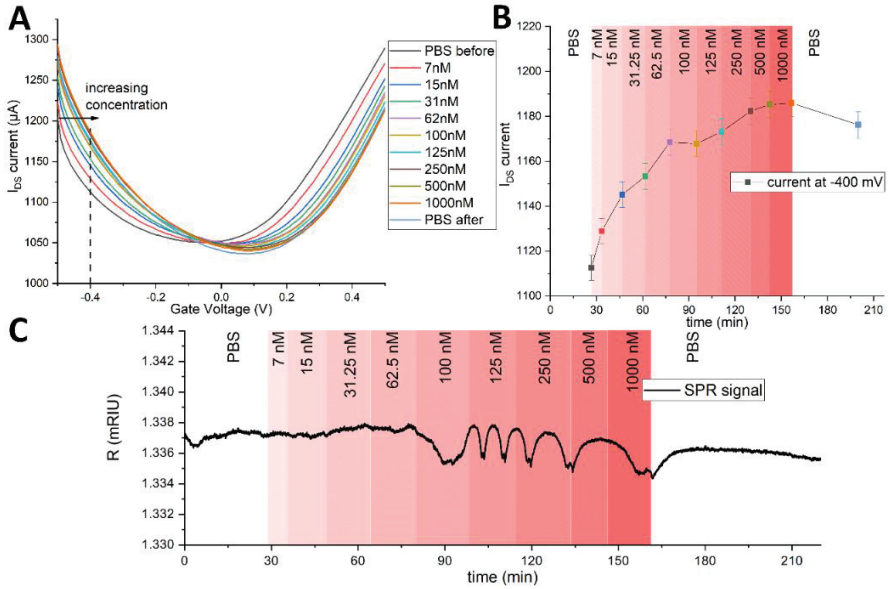

Figure 78: The binding of the HPV-E7 protein to the specific binding aptamer in the gFET/SPR setup, immobilized on the gold slide, working as SPR and GFET signal. The electrical signals were measured as I_DV_G curves after each concentration was injected to the surface. It can be observed, that the Dirac point of the I_DV_G curves shifts to a more positive voltage upon binding events, even at low concentrations as 7 nM, whereas the SPR signal is does not exhibit changes.

Figure 78 shows the measurements of the I_DV_G curves after each injected concentration (A). This leads to discrete time intervals for the acquired signals. A virtual $I_D(t)$ can be generated afterwards by selecting all currents at a certain voltage, here -400 mV. The datapoints plotted verses the recorded time stamps are shown in (B). It can be observed, that the concentration of 7 nM exhibits a significant signal of a 9 µA, caused by the specific binding of the protein to the aptamer on the gate electrode. Simultaneously, the SPR signal remains constant until the concentration of 31.25 nM, where the signal is still not very prominent in terms of optical readout.

Discussion

The initial experiments on separated graphene surfaces for SPR and graphene FETs indicated that the two systems behave different, due to the two entirely separated transducer principles. SPR measurements change the optical reflectivity upon binding events on a bio-sensor arrangement, caused by the increasing mass on the bio-interface. The drain-source current I_{DS} through a field-effect transistor, such as the here presented gFET, is modulated by the charge re-distribution on the surface of the semiconductor. But although those two sensor platforms have very different transducing principles to convert molecule attachment to the surface, both share a similar architecture: a functionalized surface inside a flow cell, connected to a pump to inject the analyte and the response to the change in concentration is recorded over time. The herein presented gFET/SPR device consists of the gFET and SPR surface within one flow cell, reading the same binding events at the same interface, just with different transducing principles. The results in this chapter show, that the combination of the two sensing principles lead to a versatile tool where the effects of mass uptake and charge re-orientation on one surface can be observed simultaneously and in real-time, as shown in the layer-by-layer deposition. [116] The measurements of biotin-neutravidin and biotin-streptavidin experiments show the detection of protein binding in both devices, while the gFET has a lower limit of detection: the neutravidin binding to the surface can be observed already at 0.78 nM, whereas the SPR response remains constant. This leads to the conclusion, that the deposition of small quantities of charges lead to a modulation of the sensor response and can be exploited for sensors with lower limits of detections. The advantage of the combination with the SPR is also the real-time measurement of deposited molecules. The immobilized proteins or other binding sites can be quantified with the SPR readout and the gFET can be calibrated with this value. This is a first step towards quantification of electrical readout signals in-situ. The immobilized ssDNA aptamer strain used for the detection of the human papilloma virus protein E7, a biomarker for the presence of the HPV, indicates once more, that the binding signal, in the $I_D(t)$ as well as I_DV_G signal generation show low limits of detections at already 7 nM. Further quantitative studies should be carried out to support this hypothesis.

Manuscript #3:

Before proceeding, the publication proving the working principles of the gFET and SPR combination and decoupling effects of surface charges from mass deposition is attached, herein referred as Aspermair *et al.* 2019. [116]

Aspermair, P., Ramach, U., Lechner, B., Fossati, S., Azzaroni, O., Dostalek, J., Szunerits, S., Knoll, W., Bintinger, J., 2019. **Dual Monitoring of Surface Reactions in Real-time by Combined Surface- Plasmon Resonance and Field-Effect Transistor Interrogation.** *manuscript submitted*

This is an open access article published under an ACS AuthorChoice License, which permits copying and redistribution of the article or any adaptations for non-commercial purposes.

ACS AUTHORCHOICE

JACS
JOURNAL OF THE AMERICAN CHEMICAL SOCIETY

pubs.acs.org/JACS

Article

Dual Monitoring of Surface Reactions in Real Time by Combined Surface-Plasmon Resonance and Field-Effect Transistor Interrogation

Patrik Aspermair,[⊥] Ulrich Ramach,[⊥] Ciril Reiner-Rozman, Stefan Fossati, Bernadette Lechner, Sergio E. Moya, Omar Azzaroni, Jakub Dostalek, Sabine Szunerits, Wolfgang Knoll, and Johannes Bintinger*

Cite This: *J. Am. Chem. Soc.* 2020, 142, 11709−11716

Read Online

ACCESS | Metrics & More | Article Recommendations | Supporting Information

ABSTRACT: By combining surface plasmon resonance (SPR) and electrolyte gated field-effect transistor (EG-FET) methods in a single analytical device we introduce a novel tool for surface investigations, enabling simultaneous measurements of the surface mass and charge density changes in real time. This is realized using a gold sensor surface that simultaneously serves as a gate electrode of the EG-FET and as the SPR active interface. This novel platform has the potential to provide new insights into (bio)adsorption processes on planar solid surfaces by directly relating complementary measurement principles based on (i) detuning of SPR as a result of the modification of the interfacial refractive index profile by surface adsorption processes and (ii) change of output current as a result of the emanating effective gate voltage modulations. Furthermore, combination of the two complementary sensing concepts allows for the comparison and respective validation of both analytical techniques. A theoretical model is derived describing the mass uptake and evolution of surface charge density during polyelectrolyte multilayer formation. We demonstrate the potential of this combined platform through the observation of layer-by-layer assembly of PDADMAC and PSS. These simultaneous label-free and real-time measurements allow new insights into complex processes at the solid−liquid interface (like non-Fickian ion diffusion), which are beyond the scope of each individual tool.

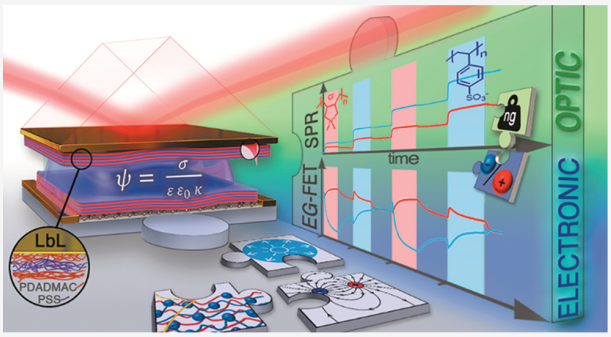

INTRODUCTION

Electronic sensing devices including those based on electrolyte gated field-effect transistors (EG-FETs) have attracted increasing attention in recent years due to their potential for the use in compact and cost-efficient analytical devices.[1−7] Despite the progress in understanding the underlying principles and even demonstrating label-free single-molecule detection,[8] no commercial EG-FET biosensor has yet entered the market. Specifically, low reproducibility, unspecific binding, sensor drift, and batch to batch variations have hindered large-scale deployment of this emerging class of biosensors.[9] In the early 1980s and 1990s, comparable challenges were addressed in the field of surface plasmon resonance (SPR) biosensor systems.[10,11] Research carried out over the last decades has paved the way for establishing this method in the market of biomolecular interaction analysis,[12] and we have witnessed the gradual advancement of this technology for rapid detection of chemical and biological species.[10,13] SPR biosensors allow direct label-free monitoring of molecular affinity binding events on the sensor surface associated with changes in surface mass density.[14,15] They are probed by the confined optical field of surface plasmons and monitored through variations in the local refractive index. Over the last years, progress in the instrumentation of SPR biosensor technology has allowed for detection of minute changes in surface mass density, enabling analysis of molecules with low molecular weight and species that are present in trace amounts in analyzed liquid samples. However, they typically rely on complex optical systems that are deployed in specialized laboratories, particularly when combined with other techniques for measurement of additional parameters beyond the affinity binding rates. These parameters include identification of biomolecular interactions by coupling SPR biosensors with mass spectrometry,[16] surface-enhanced Raman spectrometry,[17] fluorescence spectroscopy,[18] or monitoring of conformational changes of biomolecules with

Received: November 11, 2019
Published: May 14, 2020

Downloaded via 62.218.164.126 on February 21, 2022 at 17:49:15 (UTC).
See https://pubs.acs.org/sharingguidelines for options on how to legitimately share published articles.

© 2020 American Chemical Society

https://dx.doi.org/10.1021/jacs.9b11835
J. Am. Chem. Soc. 2020, 142, 11709−11716

plasmonically enhanced IR spectroscopy.[19] In comparison with these methods, EG-FET systems offer the advantage of simpler device architecture combined with an electronic readout principle, scalable cost-efficient production, low power consumption, and facile integration into point-of-care platforms that do not require specialists for operation.[7] The measurement principle is based on sensing of complementary changes caused by electric field effects[2,20−25] associated with changes in charge distribution upon capture of a target species. This approach allows probing at closer proximity to the sensor surface[26] than SPR and has the potential to monitor effects that are beyond the scope of the optical SPR technique, for instance, conformational changes of biomolecule surface reactions.[27] As many biologically relevant processes are inherently linked to mass and charge variations, fusing different sensing techniques into one multifunctional instrument could offer intriguing possibilities to investigate phenomena from different perspectives. Only a few reports in this context attempt to separate mass and charge effects,[28−30] and neither offered temporal resolution, performed proper spatial coupling of the system, nor provided a satisfying theoretical framework.

Here, we report an approach to combine SPR (optical) and EG-FET (electronic) readouts for simultaneous and real-time observation of optical and electronic aspects of molecular interactions. It is realized that using a gold sensor surface simultaneously serves as the gate electrode of the EG-FET and as the SPR-active interface (Figure 1). We demonstrate the capabilities of the developed SPR/EG-FET platform through the real-time observation of layer-by-layer (LbL) assembly of charged polyelectrolytes. We elucidate surface effects including intralayer ion diffusion processes from complementary techniques. This surface architecture represents a well-established system that offers a simple bottom-up modification strategy on different substrates.[31−35] LbL multilayers are sequentially assembled using the attractive forces between oppositely charged polyelectrolytes and typically characterized after each layer deposition step. Moreover, this technology shows great potential in multiple, diverse fields such as fuel cells,[36] batteries,[37] drug delivery,[38] and water desalination,[39] but a better understanding of the intrinsic processes and the resulting film properties is essential for guiding the development of new films and specific applications.[40,41]

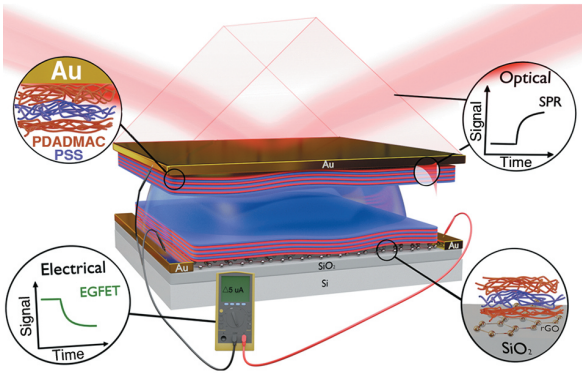

Figure 1. Schematic illustration of the combined SPR/EG-FET setup. Top Au electrode plays the dual role of SPR sensing surface and EG-FET gate electrode.

Real-time measurement using the SPR/EG-FET approach offer a means to observe typically inaccessible effects associated with the kinetics of binding and redistribution of mass and charge density during the growth of individual layers. In addition, the reported approach of the bifunctional sensor can be extended in a straightforward manner for measurement of other (bio)molecular interactions and serve to further develop these platforms and to elucidate surface effects that neither SPR nor EG-FET can address individually. Due to their relatively large mass and high charge density, LbL architectures are well-suited model systems to demonstrate the capability of the novel platform for monitoring mass deposition and charge distribution.

RESULTS

SPR chemo-optical signal transduction relies on the detuning of the resonant optical excitation of surface plasmons on a metallic surface. It occurs due to the increase of refractive index upon growth of a (bio)molecular assembly on the sensor surface.[11] The observed detuning of SPR can be converted into changes in the surface mass density Γ of the (bio)molecular layer using effective medium theory.[42,43] In contrast, the chemo-electrical signal transduction in EG-FETs is based on the locally induced electric field variations induced by surface charge density changes on the sensor modulating the Fermi level,[44] observed as a shift of the Dirac point V_i, the voltage of lowest conductance (Figure 2). We observed LbL assembly of polyelectrolyte multilayers (PEM) using SPR with Kretschmann configuration of the attenuated total internal reflection method.

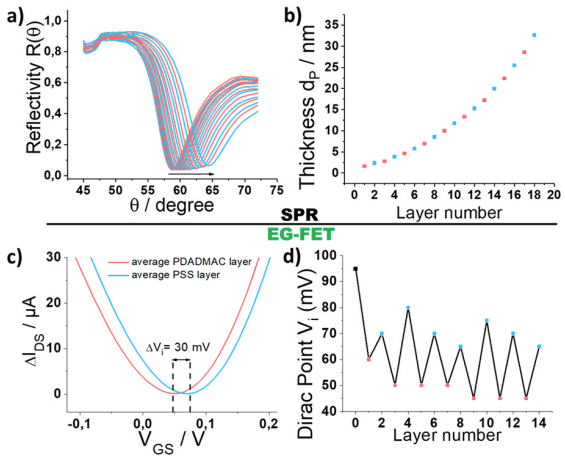

Figure 2. (Top) Sequential LbL assembly monitored by a SPR system using a planar gold surface. (a) Shift of the resonance angle as result of layer deposition, and (b) total thickness of the adsorbed films as a function of deposited layers. (Bottom) LbL assembly monitored in situ by an EG-FET system based on rGO. (c) Transfer curves of EG-FET for PDADMAC/PSS assemblies, and (d) change of the Dirac points V_i as a function of the number of adsorbed layers and their respective charges.

The resonant excitation of surface plasmons manifests itself as a dip in the angular reflectivity $R(\theta)$ (Figure 2a). At the resonant angle, the excited surface plasmons probe the gold sensor surface with a PEM that was sequentially grown from positively charged poly(diallyldimethylammonium chloride) (PDADMAC; average molecular weight < 100 kDa) and negatively charged poly(sodium 4-styrenesulfonate) (PSS; average molecular weight approximately 70 kDa) during

https://dx.doi.org/10.1021/jacs.9b11835
J. Am. Chem. Soc. 2020, 142, 11709−11716

continuous flow (100 μL/min,). Polymer solutions (1 mg/mL in 0.1 M KCl aqueous solution) with refractive index n_s = 1.333 were sequentially pumped over the UV−ozone activated gold sensor surface with intermediate rinsing steps (see Supporting Information for details). After growth of each layer, angular reflectivity scans $R(\theta)$ were recorded and the thickness d_p and refractive index n_p of the assembled PEM were obtained by fitting the spectra using the Fresnel reflectivity model. Analysis was described in detail in previous work,[35] and the refractive index of PDADMAC/PSS layers was measured as n_p = 1.577 when dried in contact with air. After swelling of the PEM in 0.1 M aqueous KCl solution, its refractive decreases to n_p = 1.476. Fitting $R(\theta)$ for swollen PEMs allows determining the dependence of layer thickness d_p on the number of growth steps, which can be seen in Figure 2b (corresponding kinetic measurements as well as angular scans are shown in Figure S1). In accordance with previous reports,[45] this dependence exhibits a parabolic trend, and the average increase of Δd_p = 0.95 nm was determined for the first eight layers. The average surface mass density increase $\Delta\Gamma$ per layer associated with LbL deposition of the PEM was determined by[46,47]

$$\Delta\Gamma = \Delta d_p \cdot (n_p - n_s) \cdot \left(\frac{\partial n}{\partial c}\right)^{-1} \quad (1)$$

resulting in $\Delta\Gamma$ = 69 ng/cm^2. In this equation the coefficient $\partial n/\partial c$ = 0.2 mm^3 mg^{-1} relates the changes in refractive index with the concentration of (bio)polymers bound to the surface.[48]

We further investigated the PEM assembly using reduced-graphene oxide-based field-effect transistors (rGO-FET) by monitoring the resulting Dirac point shifts ΔV_i (Figure 2c and 2d).[34,35] rGO-FETs were fabricated by previously reported procedures (see Supporting Information).[35] All measurements were performed in a dedicated flow cell (Figures S19 and S20). Electrical measurements were performed by applying a 50 mV source−drain bias and sweeping the gate potential V_{GS} while monitoring the current between the drain and the source I_{DS} using a Keysight U2722A instrument with custom-made LabVIEW software (Figure S21). An Ag/AgCl reference electrode was used as a gate electrode. As shown in Figure 2c, positively charged PDADMAC layers shift the transfer curve ($I_{DS}V_{GS}$) to more negative voltage values compared to a positive Dirac shift ΔV_i introduced by negatively charged PSS layers, which is in agreement with previous publications.[49] The observed ΔV_i between alternating layers are on the order of 25−40 mV. Furthermore, the dependence on the ionic strength of the KCl solutions was also evaluated (Figure S11).

Interestingly, these shifts obtained from dynamic LbL-processes are smaller than values obtained from static assembly processes, as recently shown by our group,[35] and can be explained by the absent drying step after each layer deposition. The drying step causes a collapse of the polymer layer and thus increases the surface charge density σ.

After determining the viability of in situ monitoring LbL assembly using individual SPR and EG-FET measurements, each in a separate flow cell configuration, the concept of the dual-electro/plasmonic signal transduction was demonstrated with the combined SPR/EG-FET tool. A 50 nm thin gold layer used in SPR measurements with Kretschmann configuration was simultaneously employed as the gate electrode of the EG-FET. A custom-made polydimethylsiloxane gasket defining the flow cell volume (5 μL, 400 μm flow channel thickness) attached the EG-FET to the SPR substrate. The flow cell was sealed using a 3D-printed holder with a commercially available interdigitated electrode chip (Micrux IDE1) using rGO as channel material (Figures 1, S17, and S19).

Sequential LbL growth of PEM, composed of PDADMAC and PSS, was monitored in parallel using the optical (SPR) and electronic (EG-FET) readout channels. The acquired sensor response kinetics are presented in Figure 3 for the growth of layers 3−8, revealing a stepwise increase in the SPR response and an alternating, more complex, electrical EG-FET signal.

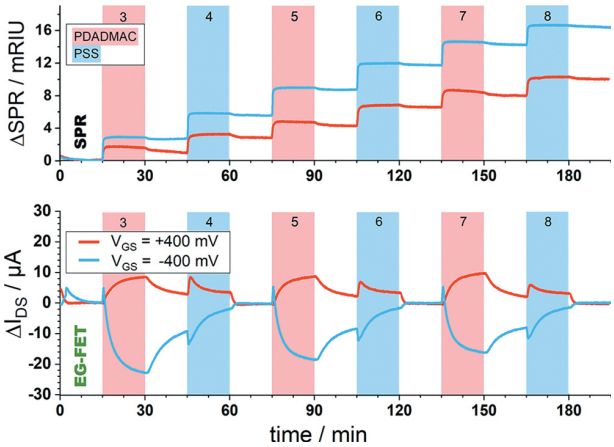

Figure 3. In situ readout of the sequential growth of alternating PDADMAC (red bars, N = 3, 5, 7) and PSS (blue bars, N = 4, 6, 8) layers by the use of SPR (upper graph) and EG-FET (bottom graph). Device was operated with applied negative (blue curve) and positive (red curve) V_{GS} voltages. Baseline correction was applied to level post-PSS I_{DS} current values to zero. See Figures S1 and S13 for raw data and gate leakage current values.

The first two layers (see Figure S1 for raw data) act as precursor and ensure sufficient PEM coverage for the subsequent layers.[50] The SPR sensor response was measured in refractive index unit (RIU) by calibrating the sensor to bulk refractive index changes n_s (Figure S1). Prior to growth of the second pair of PDADMAC/PSS layers (layers 3 and 4), a baseline was established (KCl, 100 mM, 0−15 min). Then the solution with positively charged PDADMAC was injected (15 min), and a rapid increase in SPR response was observed as a result of surface mass deposition. The system was rinsed with KCl for 15 min, and a rapid small decrease in the SPR signal was observed due to the bulk refractive index change n_s and the desorption of loosely bound polymer chains.[51] Next, the solution with negatively charged PSS was injected for 15 min followed again by a 15 min rinsing step, leading to a similar increase in SPR signal. The growth of the first 8 layers was linearly approximated (Figure S12) and shows a gate-voltage dependency.

The equilibrium ΔSPR signal of 10−16 mRIU (and respective surface mass density $\Delta\Gamma$ and PEM thickness d_p) are in accordance with those measured in static mode and presented in Figure 2. Interestingly, the overall surface mass density Γ of the grown PEM was about 60% higher for the negative V_{GS} applied to the gold surface compared to the positive one due to the respective changes in the surface mass density of the initial positively charged PDADMAC layer. Due

https://dx.doi.org/10.1021/jacs.9b11835
J. Am. Chem. Soc. 2020, 142, 11709−11716

to the polarizability of charged polymers, the polymer chains exhibit instantaneous response to the electrostatic attraction by V_{GS}.[52] Hence, electrophoretic deposition occurs and the electrostatic compensation process between cationic and anionic polyelectrolytes is stronger, resulting in thicker films as seen by the SPR signals (Figure S12). This corresponds to a mean layer growth of d_p = 2.82 ± 0.06 nm with $\Delta\Gamma$ = 202 ± 4 ng/cm^2 for V_{GS} = −400 mV and d_p = 1.69 ± 0.06 nm with $\Delta\Gamma$ = 121 ± 4 ng/cm^2 for V_{GS} = +400 mV, as extracted from the coupled SPR/EG-FET system according to eq 1. As the same PEM is formed on both interfaces of the flow cell, we further assume that both SPR and EG-FET channels respond to the same supramolecular architecture. While the SPR is sensitive to the binding of higher molecular weight PDADMAC and PSS polymers, it will not respond to the presence of low molecular weight K^+ and Cl^- ions. In contrast, the EG-FET responds to charge density variations independent of the molecular weight.

In comparison to the SPR, the response observed with the EG-FET channel (ΔI_{DS}), shown in Figure 3, shows different behavior. In this experiment changes in ΔI_{DS} were measured in time for a fixed applied gate-potential (V_{GS}), which defines the working point of the EG-FET system. The measured current changes are proportional to the slope of the $I_{DS}V_{GS}$ curve, which is opposite for the set V_{GS} = ±400 mV (Figure S14). The binding of positively charged PDADMAC polymer and negatively charged PSS polymer is accompanied by opposite changes in I_{DS} current as the binding of these polymers shifts the Dirac point V_i to more negative or positive voltages, respectively (Figure 2c). Only the ambipolar properties of certain semiconducting materials (such as rGO) allow for using both positive and negative gate voltages (V_{GS}) and thus investigating the electric field dependence of the LbL adsorption.

Strikingly, trends in the EG-FET signal due to growth of PEMs are inherently different from those observed with SPR, in terms of both magnitude and kinetics. For example, deposition of positively charged PDADMAC gradually increases the I_{DS} current (in the case of V_{GS} = +400 mV) until equilibrium is reached in about 15 min, thus taking 30 times longer than the SPR signal. At the beginning of PSS injection, a rapid increase in I_{DS} (in the case of V_{GS} = +400 mV) occurs in about 1 min and overlays with a slow competing decrease that reaches equilibrium in about 15 min. As expected, the current output sign is reversed when applying a negative gate potential (V_{GS} = −400 mV).

A detailed investigation of the EG-FET signal reveals two contributions, both exhibiting exponential behavior with different time constants (Figure S2). The two processes can be attributed to the accumulated charge density σ (EG-FET), which is composed of (i) σ_a, originating from adsorbed charged mass density (SPR), and (ii) σ_i, induced by capacitive effects, according to $\sigma = \sigma_a + \sigma_i$.

Changes of the surface charge density correspond to variations of the surface potential ψ (Debye−Hückel, eq 2), thus modifying I_{DS}

$$\psi = \frac{\sigma}{\varepsilon\varepsilon_0\kappa} \tag{2}$$

where $\kappa = 1/\lambda_D = [(2\, z^2e^2n_0)/(\varepsilon k_B T)]^{-1/2}$, with Debye length λ_D, ion valency z, electron charge e, ion concentration of the bulk n_0, Boltzmann constant k_B, temperature T, permittivity constant ε_0, and relative permittivity ε of the solution.

Experimental confirmation was obtained by eliminating any capacitive contributions (σ_i = 0), which was realized by replacing the gate electrode with a nonconductive substrate (Figure S4), thus leading to $\sigma = \sigma_a$. Such two-terminal devices have been demonstrated for sensing applications.[53] As shown in Figure 4, the time constants t_0 for noncapacitive experiments

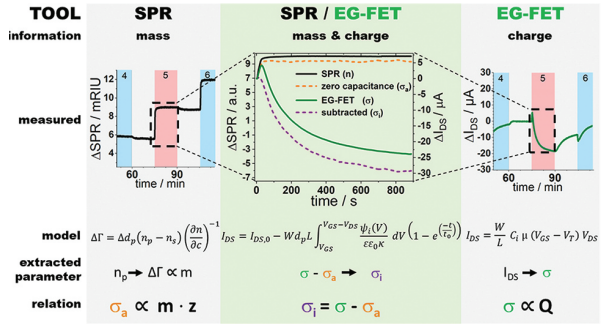

Figure 4. (Left and right) Detailed signal response of layer 5 from Figure 3. (Middle) Obtained capacitance contribution by subtracting the zero-capacitance measurement from the EG-FET response upon layer formation.

(orange dashed line) are nearly identical to the SPR response (black solid line), which is attributed to the adsorbed surface charge density σ_a. Hence, we demonstrated that the SPR mass uptake is proportional to σ_a, which is deduced from the adsorbed mass using the molar weight and valency of the monomers (Figure S12). Calculating the surface charge density for formation of the PDADMAC/PSS multilayers, we obtain σ_a = 120.2 ± 2.5 μC/cm^2 for PDADMAC for V_{GS} = −400 mV and σ_a = 72.0 ± 2.6 μC/cm^2 for V_{GS} = +400 mV and for PSS σ_a = 104.9 ± 2.5 μC/cm^2 for V_{GS} = −400 mV and σ_a = 62.9 ± 2.6 μC/cm^2 for V_{GS} = +400 mV. Subtracting the zero-capacitance data from the EG-FET response (green solid line) reveals the contribution of the induced surface charge density σ_i (purple dashed line).

■ DISCUSSION

The different nature of the SPR and EG-FET originates from the capacitive contributions (σ_i), yielding additional information about the charge distribution processes in PEMs. The SPR signal corresponds to mass uptake, attesting to the adsorption of long polymer chains in a fast process. Counterions surrounding the charged polymer backbone in the bulk solution are introduced into the PEM structure during surface adsorption. Oppositely charged PEMs achieve their electroneutrality by intrinsic charge compensation, resulting in expulsion of previously trapped counterions. This Donnan exclusion originates from the electroosmotic pressure of trapped counterions[54] and from screening between charge-like polymers due to layer to layer charge neutralization.[55,56] The resulting intralayer K^+ or Cl^- flux can be described as slow non-Fickian diffusion[50,57] to the solid−liquid interface, modifying the surface charge density σ_i.[54] Hence, the potential in the PEM layer changes over time, and a corresponding electrical double layer forms at the polyelectrolyte interface, extending approximately 100 nm into the ion solution (Figure S16),[35,58] leading to a modulation in the local electric field. The changes in charge distribution and ion concentration can also be described by the chemical potential by a thermodynamic approach (eq S19, Chapter S1C). Since our

https://dx.doi.org/10.1021/jacs.9b11835
J. Am. Chem. Soc. 2020, 142, 11709−11716

setup allows a direct measurement of mass and charge, we describe the equivalent by the more direct approach using a theoretical model for determination of the surface charge density utilizing a diffusion model[58]

$$\sigma_i(t) = \sigma_{EDL}(1 - e^{(-t/t_0)}) + I_f t \quad (3)$$

where I_f is the Faraday current density at the gate. We measured a constant gate current I_{GS} (leakage current, 21 nA) during all experiments and deposition steps, thus indicating a negligible redox potential at the electrode (Figure S13). Therefore, we assume I_f to be close to zero. The standard FET equation for I_{DS} is

$$I_{DS} = \frac{W}{L} C_i \mu (V_{GS} - V_T) V_{DS} \quad (4)$$

where W is the channel width, L the channel length, C_i the insulating layer capacitance, μ the charge mobility in the rGO, and V_T the threshold voltage. Rewriting eq 4 as a function of the surface charge density[59] and expressing the surface potential ψ via the Debye−Hückel model (see eq 2), we obtain eq 5, which describes the modulation of the observed I_{DS} as a consequence of ψ from σ_i due to ion diffusion and the depletion layer in the EDL

$$I_{DS} = I_{DS,0} - W d_p L \int_{V_{GS}}^{V_{GS}-V_{DS}} \frac{\psi_i(V)}{\varepsilon \varepsilon_0 \kappa} \, dV \cdot (1 - e^{(-t/t_0)}) \quad (5)$$

where d_p is the polyelectrolyte layer thickness. Equation 5 describes the modulation of the observed I_{DS} resulting from changes in the Fermi level of the rGO from the surface potential $\psi(V_{GS})$, which is determined by the voltage drop in the PEMs and the potential drop at the solid−electrolyte interface in proximity of the depletion layer (Figure 5). From eqs 2 and 5 it becomes clear that the corresponding potential drop ψ_i results in a change of the observed EG-FET signal.

The EG-FET signal after PDADMAC deposition gradually decreased throughout rinsing with KCl solution and equilibrated over about 15 min, while ΔSPR stabilized rapidly. This observation hints at the loss of approximately 5% of the loosely bound surface layer[60] into which the majority of the ions previously diffused. The desorption results in a surface charge density alteration and triggers the corresponding EDL formation, leading to a minute SPR response but a distinct EG-FET response. Our observations originate from inherent material properties and corresponding ion interactions, leading to different charge densities at the surface. Therefore, rinsing with KCl after PSS deposition exhibits a less prominent but faster change to a stable current.

The applied electric field (from V_{GS}) effects the diffusion, depending on the charge polarity of ions by either slowing or accelerating the diffusion flux. To evaluate the characteristics of the observed behavior, kinetics obtained from the EG-FET regarding σ_i were used for assessment of an arbitrary time ratio ξ, which is obtained from the time constant ratio of layer deposition and rinsing ($\xi = t_{on}/t_{off}$) (Chapter S1c). Therefore, we assume that the obtained time ratio ξ reflects a measure for ion affinity during diffusion, similar to diffusion-influenced transport in transmembrane channels.[61] $\xi = 1.7 \pm 0.2$ for PDADMAC at $V_{GS} = -400$ mV and 1.3 ± 0.1 for +400 mV, while obtained ξ values for PSS are 0.22 ± 0.02 at −400 mV and 0.32 ± 0.04 at +400 mV. This is intuitive because negatively charged PEMs layers have stronger affinities toward positively charged ions in the Helmholtz layer at positive applied V_{GS}. The values of ξ for PDADMAC and PSS PEMs are different as measured with the EG-FET. Most likely the differences of ξ are related to the polarity of V_{GS}, the corresponding Helmholtz double layer ion type, and the intrinsic charge of the PEMs. Furthermore, we speculate that the trapping of counterions is more pronounced in PSS layers due to ionic π-interactions,[62] leading to slower ion diffusion in comparison to PDADMAC. Additionally, the $\pi-\pi$ interactions of the PSS layer itself could lead to a difference in interlayer ion diffusion flux.

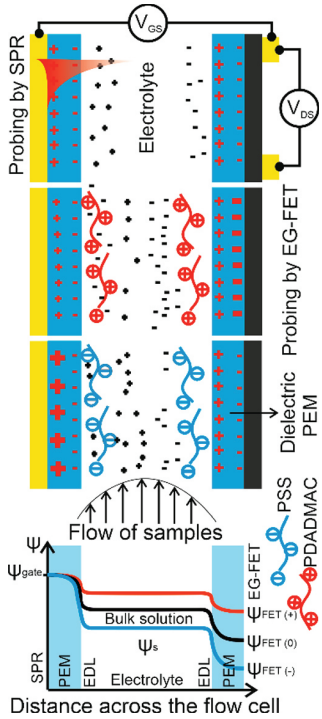

Figure 5. Schematics of the simultaneous readout of surface mass and charge density at the two interfaces of the combined SPR/EG-FET platform. Upper graph demonstrates initial conditions, followed by subsequent PDADMAC and PSS depositions under constant flow of polyelectrolyte solutions. Left side illustrates the SPR-Au-PEM surface, and right side represents the PEM-rGO-EG-FET. Surface charge density variations upon layer formation lead to the gate potential (Ψ) drop across the fluidic channel that is shown below.

■ SUMMARY

In summary, we herein present a powerful novel combinatorial sensing platform which provides new insights into real-time surface processes and enables direct measurement of surface charge density and mass obtained from electro/plasmonic signal transductions. We applied this platform to investigate PEM formation using a PDADMAC/PSS system. Due to the complementary sensing principles, the solid−liquid interface can be investigated from different perspectives, which is crucial as certain processes are beyond the scope of each individual tool. For instance, sole observation of the layer formation via SPR would suggest a completed material deposition within 60 s, whereas the subsequent slower charge diffusion takes more than 15 min as observed by EG-FET. To the best of our knowledge, this is the first report of a SPR/EG-FET platform for simultaneous real-time monitoring under dynamic flow

https://dx.doi.org/10.1021/jacs.9b11835
J. Am. Chem. Soc. 2020, 142, 11709−11716

conditions, deconvoluting mass and charge contributions. On the basis of experimental observations, we derived a theoretical model to account for the evolution of surface charge density due to PEM adsorption and intralayer ion diffusion. The theory describes the time dependence of both mass uptake and charge distribution, elucidated from changes of the refractive index and surface potential at the solid–liquid interface. To this end, we combined the Debye–Hückel model and non-Fickian diffusion theory to unravel intrinsic material processes. Correlation of optical and electronic read-outs allows for the discrimination of superimposed signals which originate from charged mass uptake and subsequent surface charge redistribution. We attribute each contribution to adsorbed and induced components by deconvoluting the superimposed yet time-correlated, EG-FET signal from the SPR data. By doing so, we can interpret an optical signal such that a direct comparison to an electronic signal is possible. Thus, our bifunctional sensor platform is a new tool to monitor surface events by simultaneously analyzing both the adsorbed mass and the intrinsic molecular charges at the same surface and under dynamic conditions. We hope these new insights can lead to a better understanding of intrinsic processes, aid in predicting material properties, and thus guide material and application development.

■ ASSOCIATED CONTENT

Supporting Information

The Supporting Information is available free of charge at https://pubs.acs.org/doi/10.1021/jacs.9b11835.

Experimental details and fabrication procedures, additional EG-FET and SPR measurements, detailed theoretical framework, SPR/EG-FET setup, software, materials (PDF)

■ AUTHOR INFORMATION

Corresponding Author

Johannes Bintinger – *Biosensor Technologies, Austrian Institute of Technology, 3430 Tulln, Austria;* orcid.org/0000-0002-6397-4254; Email: johannes.bintinger@ait.ac.at

Authors

Patrik Aspermair – *Biosensor Technologies, Austrian Institute of Technology, 3430 Tulln, Austria; CEST Competence Center for Electrochemical Surface Technologies, 3430 Tulln, Austria; CNRS, Centrale Lille, ISEN, Universite Valenciennes, UMR 8520-IEMN, Universite de Lille, 59000 Lille, France;* orcid.org/0000-0003-1671-1328

Ulrich Ramach – *CEST Competence Center for Electrochemical Surface Technologies, 3430 Tulln, Austria;* orcid.org/0000-0002-1111-2994

Ciril Reiner-Rozman – *Biosensor Technologies, Austrian Institute of Technology, 3430 Tulln, Austria;* orcid.org/0000-0002-6476-2413

Stefan Fossati – *Biosensor Technologies, Austrian Institute of Technology, 3430 Tulln, Austria;* orcid.org/0000-0002-1109-0035

Bernadette Lechner – *Biosensor Technologies, Austrian Institute of Technology, 3430 Tulln, Austria;* orcid.org/0000-0002-4949-5118

Sergio E. Moya – *CIC biomaGUNE, 20014 San Sebastian, Spain;* orcid.org/0000-0002-7174-1960

Omar Azzaroni – *Instituto de Investigaciones Fisicoquímicas Teóricas y Aplicadas (INIFTA), Departamento de Química, Facultad de Ciencias Exactas, Universidad Nacional de La Plata–CONICET, 1900 La Plata, Argentina;* orcid.org/0000-0002-5098-0612

Jakub Dostalek – *Biosensor Technologies, Austrian Institute of Technology, 3430 Tulln, Austria;* orcid.org/0000-0002-0431-2170

Sabine Szunerits – *CNRS, Centrale Lille, ISEN, Universite Valenciennes, UMR 8520-IEMN, Universite de Lille, 59000 Lille, France;* orcid.org/0000-0002-1567-4943

Wolfgang Knoll – *Biosensor Technologies, Austrian Institute of Technology, 3430 Tulln, Austria; CEST Competence Center for Electrochemical Surface Technologies, 3430 Tulln, Austria;* orcid.org/0000-0003-1543-4090

Complete contact information is available at: https://pubs.acs.org/10.1021/jacs.9b11835

Author Contributions

[⊥]P.A. and U.R. contributed equally.

Author Contributions

This manuscript was written through contributions of all authors. All authors have given approval to the final version of the manuscript.

Funding

We gratefully acknowledge the financial support from the Austrian Research Promotion Agency (FFG; 870025) for this research. SF and JD are grateful for the support from the Austrian Research Promotion Agency (FFG; 861578, ERANET project PLABAN). This work was financially supported by the European Union's Horizon 2020 research and innovation program under grant agreement No 690836. General financial supports from the Centre National de la Recherche Scientifique (CNRS), the University of Lille, and the Hauts-de-France region are acknowledged.

Notes

The authors declare no competing financial interest.

■ ACKNOWLEDGMENTS

We thank Esteban Piccinini for valuable input and discussions and David Ebner for initial design input. Cover art by Ella Maru Studio.

■ REFERENCES

(1) Das, A.; Pisana, S.; Chakraborty, B.; Piscanec, S.; Saha, S. K.; Waghmare, U. V.; Novoselov, K. S.; Krishnamurthy, H. R.; Geim, A. K.; Ferrari, A. C.; Sood, A. K. Monitoring Dopants by Raman Scattering in an Electrochemically Top-Gated Graphene Transistor. *Nat. Nanotechnol.* **2008**, *3* (4), 210–215.

(2) Kergoat, L.; Herlogsson, L.; Braga, D.; Piro, B.; Pham, M.-C.; Crispin, X.; Berggren, M.; Horowitz, G. A Water-Gate Organic Field-Effect Transistor. *Adv. Mater.* **2010**, *22* (23), 2565–2569.

(3) Palazzo, G.; De Tullio, D.; Magliulo, M.; Mallardi, A.; Intranuovo, F.; Mulla, M. Y.; Favia, P.; Vikholm-Lundin, I.; Torsi, L. Detection Beyond Debye's Length with an Electrolyte-Gated Organic Field-Effect Transistor. *Adv. Mater.* **2015**, *27* (5), 911–916.

(4) Casalini, S.; Leonardi, F.; Cramer, T.; Biscarini, F. Organic Field-Effect Transistor for Label-Free Dopamine Sensing. *Org. Electron.* **2013**, *14* (1), 156–163.

(5) Ang, P. K.; Chen, W.; Wee, A. T. S.; Loh, K. P. Solution-Gated Epitaxial Graphene as PH Sensor. *J. Am. Chem. Soc.* **2008**, *130* (44), 14392–14393.

(6) Sailapu, S. K.; Macchia, E.; Merino-Jimenez, I.; Esquivel, J. P.; Sarcina, L.; Scamarcio, G.; Minteer, S. D.; Torsi, L.; Sabaté, N. Standalone Operation of an EGOFET for Ultra-Sensitive Detection of HIV. *Biosens. Bioelectron.* **2020**, *156*, 112103.
(7) Berto, M.; Diacci, C.; D'Agata, R.; Pinti, M.; Bianchini, E.; Lauro, M. D.; Casalini, S.; Cossarizza, A.; Berggren, M.; Simon, D.; Spoto, G.; Biscarini, F.; Bortolotti, C. A. EGOFET Peptide Aptasensor for Label-Free Detection of Inflammatory Cytokines in Complex Fluids. *Adv. Biosyst.* **2018**, *2* (2), 1700072.
(8) Macchia, E.; Manoli, K.; Holzer, B.; Di Franco, C.; Ghittorelli, M.; Torricelli, F.; Alberga, D.; Mangiatordi, G. F.; Palazzo, G.; Scamarcio, G.; Torsi, L. Single-Molecule Detection with a Millimetre-Sized Transistor. *Nat. Commun.* **2018**, *9* (1), 3223.
(9) Pappa, A.-M.; Parlak, O.; Scheiblin, G.; Mailley, P.; Salleo, A.; Owens, R. M. Organic Electronics for Point-of-Care Metabolite Monitoring. *Trends Biotechnol.* **2018**, *36* (1), 45−59.
(10) Homola, J. Surface Plasmon Resonance Sensors for Detection of Chemical and Biological Species. *Chem. Rev.* **2008**, *108* (2), 462−493.
(11) Liedberg, B.; Nylander, C.; Lunström, I. Surface Plasmon Resonance for Gas Detection and Biosensing. *Sens. Actuators* **1983**, *4*, 299−304.
(12) Olaru, A.; Bala, C.; Jaffrezic-Renault, N.; Aboul-Enein, H. Y. Surface Plasmon Resonance (SPR) Biosensors in Pharmaceutical Analysis. *Crit. Rev. Anal. Chem.* **2015**, *45* (2), 97−105.
(13) Homola, J. Present and Future of Surface Plasmon Resonance Biosensors. *Anal. Bioanal. Chem.* **2003**, *377* (3), 528−539.
(14) Englebienne, P.; Hoonacker, A. V.; Verhas, M. Surface Plasmon Resonance: Principles, Methods and Applications in Biomedical Sciences. *Spectroscopy* **2003**, *17* (2−3), 255−273.
(15) Piliarik, M.; Vaisocherová, H.; Homola, J. Surface Plasmon Resonance Biosensing. In *Biosensors and Biodetection*; Rasooly, A., Herold, K. E., Eds.; Methods in Molecular BiologyTM; Humana Press: Totowa, NJ, 2009; pp 65−88. DOI: 10.1007/978-1-60327-567-5_5.
(16) Bouffartigues, E.; Leh, H.; Anger-Leroy, M.; Rimsky, S.; Buckle, M. Rapid Coupling of Surface Plasmon Resonance (SPR and SPRi) and ProteinChipTM Based Mass Spectrometry for the Identification of Proteins in Nucleoprotein Interactions. *Nucleic Acids Res.* **2007**, *35* (6), e39−e39.
(17) Zhang, X.; Young, M. A.; Lyandres, O.; Van Duyne, R. P. Rapid Detection of an Anthrax Biomarker by Surface-Enhanced Raman Spectroscopy. *J. Am. Chem. Soc.* **2005**, *127* (12), 4484−4489.
(18) Sergelen, K.; Fossati, S.; Turupcu, A.; Oostenbrink, C.; Liedberg, B.; Knoll, W.; Dostálek, J. Plasmon Field-Enhanced Fluorescence Energy Transfer for Hairpin Aptamer Assay Readout. *ACS Sens.* **2017**, *2* (7), 916−923.
(19) Rodrigo, D.; Tittl, A.; Ait-Bouziad, N.; John-Herpin, A.; Limaj, O.; Kelly, C.; Yoo, D.; Wittenberg, N. J.; Oh, S.-H.; Lashuel, H. A.; Altug, H. Resolving Molecule-Specific Information in Dynamic Lipid Membrane Processes with Multi-Resonant Infrared Metasurfaces. *Nat. Commun.* **2018**, *9* (1), 1−9.
(20) Mulla, M. Y.; Tuccori, E.; Magliulo, M.; Lattanzi, G.; Palazzo, G.; Persaud, K.; Torsi, L. Capacitance-Modulated Transistor Detects Odorant Binding Protein Chiral Interactions. *Nat. Commun.* **2015**, *6*, 6010.
(21) Panzer, M. J.; Frisbie, C. D. Exploiting Ionic Coupling in Electronic Devices: Electrolyte-Gated Organic Field-Effect Transistors. *Adv. Mater.* **2008**, *20* (16), 3177−3180.
(22) Barbaro, M.; Bonfiglio, A.; Raffo, L. A Charge-Modulated FET for Detection of Biomolecular Processes: Conception, Modeling, and Simulation. *IEEE Trans. Electron Devices* **2006**, *53* (1), 158−166.
(23) Cramer, T.; Kyndiah, A.; Murgia, M.; Leonardi, F.; Casalini, S.; Biscarini, F. Double Layer Capacitance Measured by Organic Field Effect Transistor Operated in Water. *Appl. Phys. Lett.* **2012**, *100* (14), 143302.
(24) Ohno, Y.; Maehashi, K.; Yamashiro, Y.; Matsumoto, K. Electrolyte-Gated Graphene Field-Effect Transistors for Detecting PH and Protein Adsorption. *Nano Lett.* **2009**, *9* (9), 3318−3322.
(25) Torsi, L.; Magliulo, M.; Manoli, K.; Palazzo, G. Organic Field-Effect Transistor Sensors: A Tutorial Review. *Chem. Soc. Rev.* **2013**, *42* (22), 8612−8628.
(26) Tibaldi, A.; Fillaud, L.; Anquetin, G.; Woytasik, M.; Zrig, S.; Piro, B.; Mattana, G.; Noël, V. Electrolyte-Gated Organic Field-Effect Transistors (EGOFETs) as Complementary Tools to Electrochemistry for the Study of Surface Processes. *Electrochem. Commun.* **2019**, *98*, 43−46.
(27) Nakatsuka, N.; Yang, K.-A.; Abendroth, J. M.; Cheung, K. M.; Xu, X.; Yang, H.; Zhao, C.; Zhu, B.; Rim, Y. S.; Yang, Y.; Weiss, P. S.; Stojanović, M. N.; Andrews, A. M. Aptamer−Field-Effect Transistors Overcome Debye Length Limitations for Small-Molecule Sensing. *Science* **2018**, *362* (6412), 319−324.
(28) Goda, T.; Maeda, Y.; Miyahara, Y. Simultaneous Monitoring of Protein Adsorption Kinetics Using a Quartz Crystal Microbalance and Field-Effect Transistor Integrated Device. *Anal. Chem.* **2012**, *84* (17), 7308−7314.
(29) Okuda, S.; Ono, T.; Kanai, Y.; Ikuta, T.; Shimatani, M.; Ogawa, S.; Maehashi, K.; Inoue, K.; Matsumoto, K. Graphene Surface Acoustic Wave Sensor for Simultaneous Detection of Charge and Mass. *ACS Sens.* **2018**, *3* (1), 200−204.
(30) Kojori, H. S.; Ji, Y.; Paik, Y.; Braunschweig, A. B.; Kim, S. J. Monitoring Interfacial Lectin Binding with Nanomolar Sensitivity Using a Plasmon Field Effect Transistor. *Nanoscale* **2016**, *8* (39), 17357−17364.
(31) Decher, G.; Eckle, M.; Schmitt, J.; Struth, B. Layer-by-Layer Assembled Multicomposite Films. *Curr. Opin. Colloid Interface Sci.* **1998**, *3* (1), 32−39.
(32) Dubas, S. T.; Schlenoff, J. B. Factors Controlling the Growth of Polyelectrolyte Multilayers. *Macromolecules* **1999**, *32* (24), 8153−8160.
(33) Ai, H.; Jones, S. A.; Lvov, Y. M. Biomedical Applications of Electrostatic Layer-by-Layer Nano-Assembly of Polymers, Enzymes, and Nanoparticles. *Cell Biochem. Biophys.* **2003**, *39* (1), 23.
(34) Piccinini, E.; Bliem, C.; Reiner-Rozman, C.; Battaglini, F.; Azzaroni, O.; Knoll, W. Enzyme-Polyelectrolyte Multilayer Assemblies on Reduced Graphene Oxide Field-Effect Transistors for Biosensing Applications. *Biosens. Bioelectron.* **2017**, *92*, 661−667.
(35) Piccinini, E.; Alberti, S.; Longo, G. S.; Berninger, T.; Breu, J.; Dostalek, J.; Azzaroni, O.; Knoll, W. Pushing the Boundaries of Interfacial Sensitivity in Graphene FET Sensors: Polyelectrolyte Multilayers Strongly Increase the Debye Screening Length. *J. Phys. Chem. C* **2018**, *122* (18), 10181−10188.
(36) Michel, M.; Taylor, A.; Sekol, R.; Podsiadlo, P.; Ho, P.; Kotov, N.; Thompson, L. High-Performance Nanostructured Membrane Electrode Assemblies for Fuel Cells Made by Layer-By-Layer Assembly of Carbon Nanocolloids. *Adv. Mater.* **2007**, *19* (22), 3859−3864.
(37) Wu, F.; Li, J.; Su, Y.; Wang, J.; Yang, W.; Li, N.; Chen, L.; Chen, S.; Chen, R.; Bao, L. Layer-by-Layer Assembled Architecture of Polyelectrolyte Multilayers and Graphene Sheets on Hollow Carbon Spheres/Sulfur Composite for High-Performance Lithium−Sulfur Batteries. *Nano Lett.* **2016**, *16* (9), 5488−5494.
(38) Ariga, K.; Lvov, Y. M.; Kawakami, K.; Ji, Q.; Hill, J. P. Layer-by-Layer Self-Assembled Shells for Drug Delivery. *Adv. Drug Delivery Rev.* **2011**, *63* (9), 762−771.
(39) Gu, J.-E.; Lee, S.; Stafford, C. M.; Lee, J. S.; Choi, W.; Kim, B.-Y.; Baek, K.-Y.; Chan, E. P.; Chung, J. Y.; Bang, J.; Lee, J.-H. Molecular Layer-by-Layer Assembled Thin-Film Composite Membranes for Water Desalination. *Adv. Mater.* **2013**, *25* (34), 4778−4782.
(40) Richardson, J. J.; Cui, J.; Björnmalm, M.; Braunger, J. A.; Ejima, H.; Caruso, F. Innovation in Layer-by-Layer Assembly. *Chem. Rev.* **2016**, *116* (23), 14828−14867.
(41) Richardson, J. J.; Bjornmalm, M.; Caruso, F. Technology-Driven Layer-by-Layer Assembly of Nanofilms. *Science* **2015**, *348* (6233), aaa2491−aaa2491.
(42) Aspnes, D. E. Local-field Effects and Effective-medium Theory: A Microscopic Perspective. *Am. J. Phys.* **1982**, *50* (8), 704−709.

https://dx.doi.org/10.1021/jacs.9b11835
J. Am. Chem. Soc. 2020, 142, 11709−11716

(43) Ogieglo, W.; Wormeester, H.; Eichhorn, K.-J.; Wessling, M.; Benes, N. E. In Situ Ellipsometry Studies on Swelling of Thin Polymer Films: A Review. *Prog. Polym. Sci.* **2015**, *42*, 42−78.
(44) Piccinini, E.; Bliem, C.; Giussi, J. M.; Knoll, W.; Azzaroni, O. Reversible Switching of the Dirac Point in Graphene Field-Effect Transistors Functionalized with Responsive Polymer Brushes. *Langmuir* **2019**, *35*, 8038.
(45) Tang, K.; Besseling, N. A. M. Formation of Polyelectrolyte Multilayers: Ionic Strengths and Growth Regimes. *Soft Matter* **2016**, *12* (4), 1032−1040.
(46) De Feijter, J. A.; Benjamins, J.; Veer, F. A. Ellipsometry as a Tool to Study the Adsorption Behavior of Synthetic and Biopolymers at the Air−Water Interface. *Biopolymers* **1978**, *17* (7), 1759−1772.
(47) Stenberg, E.; Persson, B.; Roos, H.; Urbaniczky, C. Quantitative Determination of Surface Concentration of Protein with Surface Plasmon Resonance Using Radiolabeled Proteins. *J. Colloid Interface Sci.* **1991**, *143* (2), 513−526.
(48) Perlmann, G. E.; Longsworth, L. G. The Specific Refractive Increment of Some Purified Proteins. *J. Am. Chem. Soc.* **1948**, *70* (8), 2719−2724.
(49) Wang, Y. Y.; Burke, P. J. Polyelectrolyte Multilayer Electrostatic Gating of Graphene Field-Effect Transistors. *Nano Res.* **2014**, *7* (11), 1650−1658.
(50) Donath, E.; Vardanyan, I.; Meyer, S.; Murray, R. A.; Moya, S. E.; Navoyan, Z.; Arakelyan, V. A Typical Diffusion Monitored by Flow Cytometry: Slow Diffusion of Small Molecules in Polyelectrolyte Multilayers. *Nanoscale* **2018**, *10* (2), 765−772.
(51) Wong, J. E.; Zastrow, H.; Jaeger, W.; von Klitzing, R. Specific Ion versus Electrostatic Effects on the Construction of Polyelectrolyte Multilayers †. *Langmuir* **2009**, *25* (24), 14061−14070.
(52) Ko, Y. H.; Kim, Y. H.; Park, J.; Nam, K. T.; Park, J. H.; Yoo, P. J. Electric-Field-Assisted Layer-by-Layer Assembly of Weakly Charged Polyelectrolyte Multilayers. *Macromolecules* **2011**, *44* (8), 2866−2872.
(53) Kim, Y.-T.; Lee, S.; Park, S.; Lee, C. Y. Graphene Chemiresistors Modified with Functionalized Triphenylene for Highly Sensitive and Selective Detection of Dimethyl Methylphosphonate. *RSC Adv.* **2019**, *9* (58), 33976−33980.
(54) Sui, Z.; Schlenoff, J. B. Phase Separations in PH-Responsive Polyelectrolyte Multilayers: Charge Extrusion versus Charge Expulsion. *Langmuir* **2004**, *20* (14), 6026−6031.
(55) Klos, J. S. Dendritic Polyelectrolytes Revisited through the Poisson−Boltzmann−Flory Theory and the Debye−Hückel Approximation. *Phys. Chem. Chem. Phys.* **2018**, *20* (4), 2693−2703.
(56) Dai, J.; Balachandra, A. M.; Lee, J. I.; Bruening, M. L. Controlling Ion Transport through Multilayer Polyelectrolyte Membranes by Derivatization with Photolabile Functional Groups. *Macromolecules* **2002**, *35* (8), 3164−3170.
(57) Song, L.; Sun, W.; Gao, J. Time Dependent Chloride Diffusion Coefficient in Concrete. *J. Wuhan Univ. Technol., Mater. Sci. Ed.* **2013**, *28* (2), 314−319.
(58) Tybrandt, K.; Zozoulenko, I. V.; Berggren, M. Chemical Potential−Electric Double Layer Coupling in Conjugated Polymer−Polyelectrolyte Blends. *Sci. Adv.* **2017**, *3* (12), eaao3659.
(59) Shirinskaya, A.; Horowitz, G.; Rivnay, J.; Malliaras, G.; Bonnassieux, Y. Numerical Modeling of an Organic Electrochemical Transistor. *Biosensors* **2018**, *8* (4), 103.
(60) Iturri Ramos, J. J.; Stahl, S.; Richter, R. P.; Moya, S. E. Water Content and Buildup of Poly(Diallyldimethylammonium Chloride)/Poly(Sodium 4-Styrenesulfonate) and Poly(Allylamine Hydrochloride)/Poly(Sodium 4-Styrenesulfonate) Polyelectrolyte Multilayers Studied by an in Situ Combination of a Quartz Crystal Microbalance with Dissipation Monitoring and Spectroscopic Ellipsometry. *Macromolecules* **2010**, *43* (21), 9063−9070.
(61) Zhou, H.-X. Diffusion-Influenced Transport of Ions across a Transmembrane Channel with an Internal Binding Site. *J. Phys. Chem. Lett.* **2010**, *1* (13), 1973−1976.
(62) Schottel, B. L.; Chifotides, H. T.; Dunbar, K. R. Anion-π Interactions. *Chem. Soc. Rev.* **2008**, *37* (1), 68−83.

https://dx.doi.org/10.1021/jacs.9b11835
J. Am. Chem. Soc. 2020, 142, 11709−11716

6. Chapter:

Conclusion

In an effort to unravel more fundamental details about the underlying bio-sensing principles of label-free, bio-adsorption based sensors, a novel dynamic sensor platform was developed with this work. Combining SPR (optical-) and EG-FET (electronic-) sensors in a single analytical device, simultaneous measurements of the surface mass and charge density variations on the same chip were realized. The sum of little steps led to the achievements of several goals throughout this project. The cornerstone of the sensor platform was the fabrication, characterization and optimization of the graphene FET. Different graphene sources were investigated to fabricate a reliable FET for bio-sensing.

The functionalization of the sensor surface is equally important to detect specifically biomolecules and to be able to avoid non-specific interactions. Many different methods were used to evaluate qualitatively the surface functionalization with bio-recognition elements: XPS analysis, differential pulse voltammetry, cyclic voltammetry, SPR and SEM imaging. A sufficient non-specific blocking strategy was synthesized and established and the combination with a specific surface functionalization could be shown.

To combine the gFET and SPR measurement to one device, it was necessary to develop a novel flow cell with optical and electrical coupling to the analyte solution for label-free detection in-situ, in real-time and simultaneously. Therefore, a special design of a microfluidic gasket was developed to seal both transducer surfaces including an in- and outlet to inject the carrier solutions.

A unique software package was developed, the gFET/SPR measurement utility, to control the measurement setup, represent the acquired data in real-time and export the output in a processable format for data processing. A graphical user interface enables an

easy-to-use software for future researcher to operate the tool and generate data with this novel platform.

The hardware development focused on the future usage for a broad community of researchers with plug-and-play features, such as standard USB cables because of the interdisciplinary research field, who might work on this platform.

The measurements to evaluate the performance of the gFET show already, how versatile the platform is:

- polyelectrolyte layer-by-layer deposition
- Biotin (Vitamin B) – Protein interactions
- Aptamer – ligand interactions.

Outlook

The development of the gFET/SPR platform is finished and ready to use, but constant improvements should be considered to obtain more reliability and more sensitivity. The semiconductor rGO used within this project is just one example and can be replaced by other materials, such as P3HT, TIPS-pentacene, graphene composite materials, carbon nanotubes, etc.

The biggest improvement is probably possible with a covalent surface modification. It was shown, that the diazonium chemistry on rGO is very promising, but was not realized in the timeframe of this project.

Moreover, with this platform one can now directly correlate the sensor's electronic response to the number of adsorbed biorecognition units, thus allowing to measure in-situ on one chip the contribution of a single binding event under dynamic flow conditions.

Bibliography

(1) Sergelen, K.; Liedberg, B.; Knoll, W.; Dostálek, J. A Surface Plasmon Field-Enhanced Fluorescence Reversible Split Aptamer Biosensor. *Analyst* **2017**, *142* (16), 2995–3001. https://doi.org/10.1039/C7AN00970D.

(2) Stojanovic, M. N.; de Prada, P.; Landry, D. W. Aptamer-Based Folding Fluorescent Sensor for Cocaine. *J. Am. Chem. Soc.* **2001**, *123* (21), 4928–4931. https://doi.org/10.1021/ja0038171.

(3) Wang, Y.; Dostálek, J.; Knoll, W. Long Range Surface Plasmon-Enhanced Fluorescence Spectroscopy for the Detection of Aflatoxin M1 in Milk. *Biosensors and Bioelectronics* **2009**, *24* (7), 2264–2267. https://doi.org/10.1016/j.bios.2008.10.029.

(4) Rich, R. L.; Myszka, D. G. Survey of the Year 2007 Commercial Optical Biosensor Literature. *Journal of Molecular Recognition* **2008**, *21* (6), 355–400. https://doi.org/10.1002/jmr.928.

(5) Reiner-Rozman, C.; Kotlowski, C.; Knoll, W. Electronic Biosensing with Functionalized RGO FETs. *Biosensors* **2016**, *6* (2), 17. https://doi.org/10.3390/bios6020017.

(6) Mulla, M. Y.; Tuccori, E.; Magliulo, M.; Lattanzi, G.; Palazzo, G.; Persaud, K.; Torsi, L. Capacitance-Modulated Transistor Detects Odorant Binding Protein Chiral Interactions. *Nature Communications* **2015**, *6*, 6010. https://doi.org/10.1038/ncomms7010.

(7) Piccinini, E.; Bliem, C.; Reiner-Rozman, C.; Battaglini, F.; Azzaroni, O.; Knoll, W. Enzyme-Polyelectrolyte Multilayer Assemblies on Reduced Graphene Oxide Field-Effect Transistors for Biosensing Applications. *Biosensors and Bioelectronics* **2017**, *92*, 661–667. https://doi.org/10.1016/j.bios.2016.10.035.

(8) Berto, M.; Vecchi, E.; Baiamonte, L.; Condò, C.; Sensi, M.; Di Lauro, M.; Sola, M.; De Stradis, A.; Biscarini, F.; Minafra, A.; et al. Label Free Detection of Plant Viruses with Organic Transistor Biosensors. *Sensors and Actuators B: Chemical* **2019**, *281*, 150–156. https://doi.org/10.1016/j.snb.2018.10.080.

(9) Biosensing with Electrolyte Gated Organic Field Effect Transistors. In *Materials Research Foundations*; Materials Research Forum LLC, 2019; Vol. 56, pp 71–96. https://doi.org/10.21741/9781644900376-2.

(10) Briscoe, S. E.; McWhinney, B. C.; Lipman, J.; Roberts, J. A.; Ungerer, J. P. J. A Method for Determining the Free (Unbound) Concentration of Ten Beta-Lactam Antibiotics in Human Plasma Using High Performance Liquid Chromatography with Ultraviolet Detection. *Journal of Chromatography B* **2012**, *907*, 178–184. https://doi.org/10.1016/j.jchromb.2012.09.016.

(11) Van den Meersche, T.; Pamel, E. V.; Poucke, C. V.; Herman, L.; Heyndrickx, M.; Rasschaert, G.; Daeseleire, E. Development, Validation and Application of an Ultra High Performance Liquid Chromatographic-Tandem Mass Spectrometric Method for the Simultaneous Detection and Quantification of Five Different Classes of Veterinary Antibiotics in Swine Manure. *Journal of Chromatography A* **2016**, *1429*, 248–257. https://doi.org/10.1016/j.chroma.2015.12.046.

(12) Yang, S.; Zhu, X.; Wang, J.; Jin, X.; Liu, Y.; Qian, F.; Zhang, S.; Chen, J. Combustion of Hazardous Biological Waste Derived from the Fermentation of Antibiotics Using TG–FTIR and Py–GC/MS Techniques. *Bioresource Technology* **2015**, *193*, 156–163. https://doi.org/10.1016/j.biortech.2015.06.083.
(13) Gbylik-Sikorska, M.; Posyniak, A.; Sniegocki, T.; Zmudzki, J. Liquid Chromatography–Tandem Mass Spectrometry Multiclass Method for the Determination of Antibiotics Residues in Water Samples from Water Supply Systems in Food-Producing Animal Farms. *Chemosphere* **2015**, *119*, 8–15. https://doi.org/10.1016/j.chemosphere.2014.04.105.
(14) Mehlhorn, A.; Rahimi, P.; Joseph, Y. Aptamer-Based Biosensors for Antibiotic Detection: A Review. *Biosensors* **2018**, *8* (2), 54. https://doi.org/10.3390/bios8020054.
(15) Macchia, E.; Manoli, K.; Holzer, B.; Franco, C. D.; Ghittorelli, M.; Torricelli, F.; Alberga, D.; Mangiatordi, G. F.; Palazzo, G.; Scamarcio, G.; et al. Single-Molecule Detection with a Millimetre-Sized Transistor. *Nature Communications* **2018**, *9* (1), 3223. https://doi.org/10.1038/s41467-018-05235-z.
(16) Korotkaya, E. V. Biosensors: Design, Classification, and Applications in the Food Industry. *Foods and Raw materials* **2014**, *2* (2).
(17) Torsi, L.; Magliulo, M.; Manoli, K.; Palazzo, G. Organic Field-Effect Transistor Sensors: A Tutorial Review. *Chem. Soc. Rev.* **2013**, *42* (22), 8612–8628. https://doi.org/10.1039/C3CS60127G.
(18) Kergoat, L.; Herlogsson, L.; Braga, D.; Piro, B.; Pham, M.-C.; Crispin, X.; Berggren, M.; Horowitz, G. A Water-Gate Organic Field-Effect Transistor. *Advanced Materials* **2010**, *22* (23), 2565–2569. https://doi.org/10.1002/adma.200904163.
(19) Kergoat, L.; Piro, B.; Berggren, M.; Horowitz, G.; Pham, M.-C. Advances in Organic Transistor-Based Biosensors: From Organic Electrochemical Transistors to Electrolyte-Gated Organic Field-Effect Transistors. *Anal Bioanal Chem* **2012**, *402* (5), 1813–1826. https://doi.org/10.1007/s00216-011-5363-y.
(20) Barbaro, M.; Bonfiglio, A.; Raffo, L. A Charge-Modulated FET for Detection of Biomolecular Processes: Conception, Modeling, and Simulation. *IEEE Transactions on Electron Devices* **2006**, *53* (1), 158–166. https://doi.org/10.1109/TED.2005.860659.
(21) Piccinini, E.; Bliem, C.; Giussi, J. M.; Knoll, W.; Azzaroni, O. Reversible Switching of the Dirac Point in Graphene Field-Effect Transistors Functionalized with Responsive Polymer Brushes. *Langmuir* **2019**. https://doi.org/10.1021/acs.langmuir.9b00910.
(22) Nakatsuka, N.; Yang, K.-A.; Abendroth, J. M.; Cheung, K. M.; Xu, X.; Yang, H.; Zhao, C.; Zhu, B.; Rim, Y. S.; Yang, Y.; et al. Aptamer–Field-Effect Transistors Overcome Debye Length Limitations for Small-Molecule Sensing. *Science* **2018**, *362* (6412), 319–324. https://doi.org/10.1126/science.aao6750.
(23) Förster, U.; Weigand, J. E.; Trojanowski, P.; Suess, B.; Wachtveitl, J. Conformational Dynamics of the Tetracycline-Binding Aptamer. *Nucleic Acids Research* **2012**, *40* (4), 1807–1817. https://doi.org/10.1093/nar/gkr835.
(24) Nakatsuka, N.; Yang, K.-A.; Abendroth, J. M.; Cheung, K. M.; Xu, X.; Yang, H.; Zhao, C.; Zhu, B.; Rim, Y. S.; Yang, Y.; et al. Aptamer–Field-Effect Transistors

Overcome Debye Length Limitations for Small-Molecule Sensing. *Science* **2018**, *362* (6412), 319–324. https://doi.org/10.1126/science.aao6750.
(25) Berto, M.; Casalini, S.; Di Lauro, M.; Marasso, S. L.; Cocuzza, M.; Perrone, D.; Pinti, M.; Cossarizza, A.; Pirri, C. F.; Simon, D. T.; et al. Biorecognition in Organic Field Effect Transistors Biosensors: The Role of the Density of States of the Organic Semiconductor. *Anal. Chem.* **2016**, *88* (24), 12330–12338. https://doi.org/10.1021/acs.analchem.6b03522.
(26) Berto, M.; Diacci, C.; D'Agata, R.; Pinti, M.; Bianchini, E.; Lauro, M. D.; Casalini, S.; Cossarizza, A.; Berggren, M.; Simon, D.; et al. EGOFET Peptide Aptasensor for Label-Free Detection of Inflammatory Cytokines in Complex Fluids. *Advanced Biosystems* **2018**, *2* (2), 1700072. https://doi.org/10.1002/adbi.201700072.
(27) Tibaldi, A.; Fillaud, L.; Anquetin, G.; Woytasik, M.; Zrig, S.; Piro, B.; Mattana, G.; Noël, V. Electrolyte-Gated Organic Field-Effect Transistors (EGOFETs) as Complementary Tools to Electrochemistry for the Study of Surface Processes. *Electrochemistry Communications* **2019**, *98*, 43–46. https://doi.org/10.1016/j.elecom.2018.10.022.
(28) Reiner-Rozman, C.; Kotlowski, C.; Knoll, W. Electronic Biosensing with Functionalized RGO FETs. *Biosensors* **2016**, *6* (2), 17. https://doi.org/10.3390/bios6020017.
(29) Trilling, A. K.; Beekwilder, J.; Zuilhof, H. Antibody Orientation on Biosensor Surfaces: A Minireview. *Analyst* **2013**, *138* (6), 1619–1627. https://doi.org/10.1039/C2AN36787D.
(30) Nakatsuka, N.; Cao, H. H.; Deshayes, S.; Melkonian, A. L.; Kasko, A. M.; Weiss, P. S.; Andrews, A. M. Aptamer Recognition of Multiplexed Small-Molecule-Functionalized Substrates. *ACS Appl. Mater. Interfaces* **2018**, *10* (28), 23490–23500. https://doi.org/10.1021/acsami.8b02837.
(31) Davis, J. J.; Tkac, J.; Laurenson, S.; Ferrigno, P. K. Peptide Aptamers in Label-Free Protein Detection: 1. Characterization of the Immobilized Scaffold. *Anal. Chem.* **2007**, *79* (3), 1089–1096. https://doi.org/10.1021/ac061863z.
(32) Castro, M. A. G. de; Höbartner, C.; Opazo, F. Aptamers Provide Superior Stainings of Cellular Receptors Studied under Super-Resolution Microscopy. *PLOS ONE* **2017**, *12* (2), e0173050. https://doi.org/10.1371/journal.pone.0173050.
(33) Tuerk, C.; Gold, L. Systematic Evolution of Ligands by Exponential Enrichment: RNA Ligands to Bacteriophage T4 DNA Polymerase. *Science* **1990**, *249* (4968), 505–510. https://doi.org/10.1126/science.2200121.
(34) Ellington, A. D.; Szostak, J. W. In Vitro Selection of RNA Molecules That Bind Specific Ligands. *Nature* **1990**, *346* (6287), 818–822. https://doi.org/10.1038/346818a0.
(35) Escorihuela, J.; Bañuls, M.-J.; Puchades, R.; Maquieira, Á. Site-Specific Immobilization of DNA on Silicon Surfaces by Using the Thiol–Yne Reaction. *J. Mater. Chem. B* **2014**, *2* (48), 8510–8517. https://doi.org/10.1039/C4TB01108B.
(36) *Water Quality: Guidelines, Standards, and Health: Assessment of Risk and Risk Management for Water-Related Infectious Disease*; Fewtrell, L., Bartram, J., Eds.; World Health Organization water series; World Health Organization: Geneva, 2001.

(37) Ventola, C. L. The Antibiotic Resistance Crisis. *P T* **2015**, *40* (4), 277–283.
(38) Rose, J. B.; Jiménez-Cisneros, B. Global Water Pathogen Project https://www.waterpathogens.org/ (accessed Sep 28, 2019).
(39) 14:00-17:00. ISO 9308-1:2014 http://www.iso.org/cms/render/live/en/sites/isoorg/contents/data/standard/05/58/55832.html (accessed Sep 28, 2019).
(40) Farnleitner, B. Microbial Indicators - "Workhorses" in the Field of Health-related Water Quality Testing https://www.waterpathogens.org/book/editorial (accessed Sep 28, 2019).
(41) Marton, S.; Cleto, F.; Krieger, M. A.; Cardoso, J. Isolation of an Aptamer That Binds Specifically to E. Coli. *PLOS ONE* **2016**, *11* (4), e0153637. https://doi.org/10.1371/journal.pone.0153637.
(42) Cao, X.; Li, S.; Chen, L.; Ding, H.; Xu, H.; Huang, Y.; Li, J.; Liu, N.; Cao, W.; Zhu, Y.; et al. Combining Use of a Panel of SsDNA Aptamers in the Detection of Staphylococcus Aureus. *Nucleic Acids Res* **2009**, *37* (14), 4621–4628. https://doi.org/10.1093/nar/gkp489.
(43) Park, H.-C.; Baig, I. A.; Lee, S.-C.; Moon, J.-Y.; Yoon, M.-Y. Development of SsDNA Aptamers for the Sensitive Detection of Salmonella Typhimurium and Salmonella Enteritidis. *Appl Biochem Biotechnol* **2014**, *174* (2), 793–802. https://doi.org/10.1007/s12010-014-1103-z.
(44) Dunn, M. R.; Jimenez, R. M.; Chaput, J. C. Analysis of Aptamer Discovery and Technology. *Nat Rev Chem* **2017**, *1* (10), 1–16. https://doi.org/10.1038/s41570-017-0076.
(45) Famulok, M.; Mayer, G. Aptamers and SELEX in Chemistry & Biology. *Chemistry & Biology* **2014**, *21* (9), 1055–1058. https://doi.org/10.1016/j.chembiol.2014.08.003.
(46) Baird, G. S. Where Are All the Aptamers? *Am J Clin Pathol* **2010**, *134* (4), 529–531. https://doi.org/10.1309/AJCPFU4CG2WGJJKS.
(47) Zenneck, J. Über Die Fortpflanzung Ebener Elektromagnetischer Wellen Längs Einer Ebenen Leiterfläche Und Ihre Beziehung Zur Drahtlosen Telegraphie. *Annalen der Physik* **1907**, *328* (10), 846–866. https://doi.org/10.1002/andp.19073281003.
(48) Ritchie, R. H. Plasma Losses by Fast Electrons in Thin Films. *Phys. Rev.* **1957**, *106* (5), 874–881. https://doi.org/10.1103/PhysRev.106.874.
(49) Raether, H. Surface Plasmons on Smooth Surfaces. In *Surface Plasmons on Smooth and Rough Surfaces and on Gratings*; Raether, H., Ed.; Springer Tracts in Modern Physics; Springer: Berlin, Heidelberg, 1988; pp 4–39. https://doi.org/10.1007/BFb0048319.
(50) Kretschmann, E.; Raether, H. Notizen: Radiative Decay of Non Radiative Surface Plasmons Excited by Light. *Zeitschrift für Naturforschung A* **2014**, *23* (12), 2135–2136. https://doi.org/10.1515/zna-1968-1247.
(51) Huang, D.-W.; Ma, Y.-F.; Sung, M.-J.; Huang, C.-P. Approach the Angular Sensitivity Limit in Surface Plasmon Resonance Sensors with Low Index Prism and Large Resonant Angle. *OE* **2010**, *49* (5), 054403. https://doi.org/10.1117/1.3431662.

(52) Surface Plasmon Resonance (SPR) Biosensors in Pharmaceutical Analysis: Critical Reviews in Analytical Chemistry: Vol 45, No 2 https://www.tandfonline.com/doi/full/10.1080/10408347.2014.881250?casa_token=Vfxx8B9SHrMAAAAA%3AfINAl9xIyzy5DIN_F_pAS6swlyr0qm_q2qbs8QS_vwWI0K2-ZkKsM-hWw6mi7df8_DyElqxSlNNPjA (accessed Nov 3, 2019).
(53) Surface Plasmon Resonance Sensors for Detection of Chemical and Biological Species | Chemical Reviews https://pubs.acs.org/doi/10.1021/cr068107d (accessed Nov 3, 2019).
(54) MacKenzie, C. R.; Hirama, T. [18] - Quantitative Analyses of Binding Affinity and Specificity for Glycolipid Receptors by Surface Plasmon Resonance. In *Methods in Enzymology*; Merrill, A. H., Hannun, Y. A., Eds.; Sphingolipid Metabolism and Cell Signaling, Part B; Academic Press, 2000; Vol. 312, pp 205–216. https://doi.org/10.1016/S0076-6879(00)12911-8.
(55) Schasfoort, R. B. M.; Tudos, A. J. *Handbook of Surface Plasmon Resonance*; Royal Society of Chemistry, 2008.
(56) Morales, M. D.; Serra, B.; Prada, A. G.-V. de; Reviejo, Á. J.; Pingarrón, J. M. An Electrochemical Method for Simultaneous Detection and Identification of Escherichia Coli, Staphylococcus Aureus and Salmonella Choleraesuis Using a Glucose Oxidase-Peroxidase Composite Biosensor. *Analyst* **2007**, *132* (6), 572–578. https://doi.org/10.1039/B618159G.
(57) Estrela, P.; Pachauri, V.; Ingebrandt, S. Biologically Sensitive Field-Effect Transistors: From ISFETs to NanoFETs. *Essays Biochem* **2016**, *60* (1), 81–90. https://doi.org/10.1042/EBC20150009.
(58) Berto, M.; Diacci, C.; D'Agata, R.; Pinti, M.; Bianchini, E.; Lauro, M. D.; Casalini, S.; Cossarizza, A.; Berggren, M.; Simon, D.; et al. EGOFET Peptide Aptasensor for Label-Free Detection of Inflammatory Cytokines in Complex Fluids. *Adv. Biosys.* **2018**, *2* (2), 1700072. https://doi.org/10.1002/adbi.201700072.
(59) Tibaldi, A.; Fillaud, L.; Anquetin, G.; Woytasik, M.; Zrig, S.; Piro, B.; Mattana, G.; Noël, V. Electrolyte-Gated Organic Field-Effect Transistors (EGOFETs) as Complementary Tools to Electrochemistry for the Study of Surface Processes. *Electrochemistry Communications* **2019**, *98*, 43–46. https://doi.org/10.1016/j.elecom.2018.10.022.
(60) Biosensing with Electrolyte Gated Organic Field Effect Transistors. *Materials Research Forum*.
(61) Water-stable organic transistors and their application in chemical and biological sensors | PNAS https://www.pnas.org/content/105/34/12134.short (accessed Nov 2, 2019).
(62) Wan, X.; Huang, Y.; Chen, Y. Focusing on Energy and Optoelectronic Applications: A Journey for Graphene and Graphene Oxide at Large Scale. *Acc. Chem. Res.* **2012**, *45* (4), 598–607. https://doi.org/10.1021/ar200229q.
(63) Zhan, B.; Li, C.; Yang, J.; Jenkins, G.; Huang, W.; Dong, X. Graphene Field-Effect Transistor and Its Application for Electronic Sensing. *Small* **2014**, *10* (20), 4042–4065. https://doi.org/10.1002/smll.201400463.
(64) Reiner-Rozman, C.; Larisika, M.; Nowak, C.; Knoll, W. Graphene-Based Liquid-Gated Field Effect Transistor for Biosensing: Theory and Experiments. *Biosensors and Bioelectronics* **2015**, *70*, 21–27. https://doi.org/10.1016/j.bios.2015.03.013.

(65) Green, N. S.; Norton, M. L. Interactions of DNA with Graphene and Sensing Applications of Graphene Field-Effect Transistor Devices: A Review. *Analytica Chimica Acta* **2015**, *853*, 127–142. https://doi.org/10.1016/j.aca.2014.10.023.
(66) Van Zeghbroeck, B. V. *Principles of Semiconductor Devices and Heterojunctions*; Prentice Hall, 2010.
(67) Pope, M. A. *Electrochemical Double-Layer Capacitors Based on Functionalized Graphene*; 2013.
(68) Larisika, M.; Kotlowski, C.; Steininger, C.; Mastrogiacomo, R.; Pelosi, P.; Schütz, S.; Peteu, S. F.; Kleber, C.; Reiner-Rozman, C.; Nowak, C.; et al. Electronic Olfactory Sensor Based on A. Mellifera Odorant-Binding Protein 14 on a Reduced Graphene Oxide Field-Effect Transistor. *Angew. Chem.* **2015**, *127* (45), 13443–13446. https://doi.org/10.1002/ange.201505712.
(69) Huang, E.; Zhou, F.; Deng, L. Studies of Surface Coverage and Orientation of DNA Molecules Immobilized onto Preformed Alkanethiol Self-Assembled Monolayers. *Langmuir* **2000**, *16* (7), 3272–3280. https://doi.org/10.1021/la9910834.
(70) Knoll, W. *Handbook of Biofunctional Surfaces*; Pan Stanford, 2013.
(71) Xiao, Y.; Isaacs, S. N. Enzyme-Linked Immunosorbent Assay (ELISA) and Blocking with Bovine Serum Albumin (BSA)—Not All BSAs Are Alike. *Journal of Immunological Methods* **2012**, *384* (1), 148–151. https://doi.org/10.1016/j.jim.2012.06.009.
(72) Siegers, C.; Biesalski, M.; Haag, R. Self-Assembled Monolayers of Dendritic Polyglycerol Derivatives on Gold That Resist the Adsorption of Proteins. *Chemistry – A European Journal* **2004**, *10* (11), 2831–2838. https://doi.org/10.1002/chem.200306073.
(73) Rühe, J.; Knoll, W. Functional Polymer Brushes*. *Journal of Macromolecular Science, Part C* **2002**, *42* (1), 91–138. https://doi.org/10.1081/MC-120003096.
(74) Dai, H.; Meyer, M.; Stepaniants, S.; Ziman, M.; Stoughton, R. Use of Hybridization Kinetics for Differentiating Specific from Non-specific Binding to Oligonucleotide Microarrays. *Nucleic Acids Res* **2002**, *30* (16), e86–e86. https://doi.org/10.1093/nar/gnf085.
(75) Khan, H. U.; Roberts, M. E.; Johnson, O.; Knoll, W.; Bao, Z. The Effect of PH and DNA Concentration on Organic Thin-Film Transistor Biosensors. *Organic Electronics* **2012**, *13* (3), 519–524. https://doi.org/10.1016/j.orgel.2011.12.013.
(76) Yu, F.; Tian, S.; Yao, D.; Knoll, W. Surface Plasmon Enhanced Diffraction for Label-Free Biosensing. *Anal. Chem.* **2004**, *76* (13), 3530–3535. https://doi.org/10.1021/ac049964p.
(77) Liu, J.; Tian, S.; Nielsen, P. E.; Knoll, W. In Situ Hybridization of PNA/DNA Studied Label-Free by Electrochemical Impedance Spectroscopy. *Chem. Commun.* **2005**, No. 23, 2969–2971. https://doi.org/10.1039/B419425J.
(78) Park, H.; Germini, A.; Sforza, S.; Corradini, R.; Marchelli, R.; Knoll, W. Kinetic and Affinity Analyses of Hybridization Reactions between Peptide Nucleic Acid Probes and DNA Targets Using Surface Plasmon Field-Enhanced Fluorescence Spectroscopy. *Biointerphases* **2006**, *1* (4), 113–122. https://doi.org/10.1116/1.2365386.

(79) Fortunati, S.; Rozzi, A.; Curti, F.; Giannetto, M.; Corradini, R.; Careri, M. Single-Walled Carbon Nanotubes as Enhancing Substrates for PNA-Based Amperometric Genosensors. *Sensors* **2019**, *19* (3), 588. https://doi.org/10.3390/s19030588.
(80) Larisika, M.; Huang, J.; Tok, A.; Knoll, W.; Nowak, C. An Improved Synthesis Route to Graphene for Molecular Sensor Applications. *Materials Chemistry and Physics* **2012**, *136* (2), 304–308. https://doi.org/10.1016/j.matchemphys.2012.08.003.
(81) Stannowski, B.; Schropp, R. E. I.; Wehrspohn, R. B.; Powell, M. J. Amorphous-Silicon Thin-Film Transistors Deposited by VHF-PECVD and Hot-Wire CVD. *Journal of Non-Crystalline Solids* **2002**, *299–302*, 1340–1344. https://doi.org/10.1016/S0022-3093(01)01098-5.
(82) MacKay, S.; Wishart, D.; Xing, J. Z.; Chen, J. Developing Trends in Aptamer-Based Biosensor Devices and Their Applications. *IEEE Transactions on Biomedical Circuits and Systems* **2014**, *8* (1), 4–14. https://doi.org/10.1109/TBCAS.2014.2304718.
(83) Virolainen, N.; Karp, M. Biosensors, Antibiotics and Food. In *Bioluminescence: Fundamentals and Applications in Biotechnology - Volume 2*; Thouand, G., Marks, R., Eds.; Advances in Biochemical Engineering/Biotechnology; Springer: Berlin, Heidelberg, 2014; pp 153–185. https://doi.org/10.1007/978-3-662-43619-6_5.
(84) Walter, J.-G.; Heilkenbrinker, A.; Austerjost, J.; Timur, S.; Stahl, F.; Schepe, T. Aptasensors for Small Molecule Detection. *Zeitschrift für Naturforschung B* **2014**, *67* (10), 976–986. https://doi.org/10.5560/znb.2012-0147.
(85) Niazi, J. H.; Lee, S. J.; Kim, Y. S.; Gu, M. B. SsDNA Aptamers That Selectively Bind Oxytetracycline. *Bioorganic & Medicinal Chemistry* **2008**, *16* (3), 1254–1261. https://doi.org/10.1016/j.bmc.2007.10.073.
(86) Lysozyme Detection on Aptamer Functionalized Graphene-Coated SPR Interfacesm Lysozyme.Pdf.
(87) HPV Aptamer Application of Nucleic Acid Aptamers to Viral Detection and Inhibition.Pdf.
(88) Alsager, O. A.; Kumar, S.; Willmott, G. R.; McNatty, K. P.; Hodgkiss, J. M. Small Molecule Detection in Solution via the Size Contraction Response of Aptamer Functionalized Nanoparticles. *Biosensors and Bioelectronics* **2014**, *57*, 262–268. https://doi.org/10.1016/j.bios.2014.02.004.
(89) Feicht, P.; Siegel, R.; Thurn, H.; Neubauer, J. W.; Seuss, M.; Szabó, T.; Talyzin, A. V.; Halbig, C. E.; Eigler, S.; Kunz, D. A.; et al. Systematic Evaluation of Different Types of Graphene Oxide in Respect to Variations in Their In-Plane Modulus. *Carbon* **2017**, *114*, 700–705. https://doi.org/10.1016/j.carbon.2016.12.065.
(90) Chen, W.; Yan, L.; Bangal, P. R. Preparation of Graphene by the Rapid and Mild Thermal Reduction of Graphene Oxide Induced by Microwaves. *Carbon* **2010**, *48* (4), 1146–1152. https://doi.org/10.1016/j.carbon.2009.11.037.
(91) Fu, W.; Feng, L.; Mayer, D.; Panaitov, G.; Kireev, D.; Offenhäusser, A.; Krause, H.-J. Electrolyte-Gated Graphene Ambipolar Frequency Multipliers for Biochemical Sensing. *Nano Lett.* **2016**, *16* (4), 2295–2300. https://doi.org/10.1021/acs.nanolett.5b04729.

(92) Tanaka, S.; Goto, H.; Tomori, H.; Ootuka, Y.; Tsukagoshi, K.; Kanda, A. Effect of Current Annealing on Electronic Properties of Multilayer Graphene. *J. Phys.: Conf. Ser.* **2010**, *232*, 012015. https://doi.org/10.1088/1742-6596/232/1/012015.
(93) Grande, M.; D'Orazio, A.; Bianco, G. V.; Bruno, G.; Vincenti, M. A.; de Ceglia, D.; Scalora, M. Optically Transparent Graphene-Based Salisbury Screen Microwave Absorber. In *2015 IEEE 15th Mediterranean Microwave Symposium (MMS)*; 2015; pp 1–3. https://doi.org/10.1109/MMS.2015.7375386.
(94) Liu, J.; Notarianni, M.; Will, G.; Tiong, V. T.; Wang, H.; Motta, N. Electrochemically Exfoliated Graphene for Electrode Films: Effect of Graphene Flake Thickness on the Sheet Resistance and Capacitive Properties. *Langmuir : the ACS journal of surfaces and colloids* **2013**, *29* (43), 13307–13314. https://doi.org/10.1021/la403159n.
(95) Randin, J.-P.; Yeager, E. Differential Capacitance Study on the Basal Plane of Stress-Annealed Pyrolytic Graphite. *Journal of Electroanalytical Chemistry and Interfacial Electrochemistry* **1972**, *36* (2), 257–276. https://doi.org/10.1016/S0022-0728(72)80249-3.
(96) Lemme, M. C.; Echtermeyer, T. J.; Baus, M.; Szafranek, B. N.; Bolten, J.; Schmidt, M.; Wahlbrink, T.; Kurz, H. Mobility in Graphene Double Gate Field Effect Transistors. *Solid-State Electronics* **2008**, *52* (4), 514–518.
(97) Bolotin, K. I.; Sikes, K. J.; Jiang, Z.; Klima, M.; Fudenberg, G.; Hone, J.; Kim, P.; Stormer, H. L. Ultrahigh Electron Mobility in Suspended Graphene. *Solid State Communications* **2008**, *146* (9), 351–355. https://doi.org/10.1016/j.ssc.2008.02.024.
(98) Castro, E. V.; Ochoa, H.; Katsnelson, M. I.; Gorbachev, R. V.; Elias, D. C.; Novoselov, K. S.; Geim, A. K.; Guinea, F. Limits on Charge Carrier Mobility in Suspended Graphene Due to Flexural Phonons. *Phys. Rev. Lett.* **2010**, *105* (26), 266601. https://doi.org/10.1103/PhysRevLett.105.266601.
(99) Electronic Biosensing with Flexible Organic Transistor Devices, Kotlowski.Pdf.
(100) Effect of 1- Pyrene Carboxylic-Acid Functionalization of Graphene on Its Capacitive Energy Storage, Kar.Pdf.
(101) Liu, J.; Yang, W.; Tao, L.; Li, D.; Boyer, C.; Davis, T. P. Thermosensitive Graphene Nanocomposites Formed Using Pyrene-Terminal Polymers Made by RAFT Polymerization. *Journal of Polymer Science Part A: Polymer Chemistry* **2010**, *48* (2), 425–433. https://doi.org/10.1002/pola.23802.
(102) Noncovalent Interaction of Single-Walled Carbon Nanotubes with 1-Pyrenebutanoic Acid Succinimide Ester and Glucoseoxidase, Karachevtsev2011.Pdf.
(103) Liu, J.; Bibari, O.; Mailley, P.; Dijon, J.; Rouvière, E.; Sauter-Starace, F.; Caillat, P.; Vinet, F.; Marchand, G. Stable Non-Covalent Functionalisation of Multi-Walled Carbon Nanotubes by Pyrene–Polyethylene Glycol through π–π Stacking. *New J. Chem.* **2009**, *33* (5), 1017–1024. https://doi.org/10.1039/B813085J.
(104) Green, N. M. Avidin. In *Advances in Protein Chemistry*; Anfinsen, C. B., Edsall, J. T., Richards, F. M., Eds.; Academic Press, 1975; Vol. 29, pp 85–133. https://doi.org/10.1016/S0065-3233(08)60411-8.
(105) da Silva Neves, M. M. P.; García, M. B. G.; Santos, D. H.; Fanjul-Bolado, P. Hydroquinone Diphosphate/Ag+ as an Enzymatic Substrate for Alkaline

Phosphatase Catalyzed Silver Deposition. *Electrochemistry Communications* **2015**, *60*, 1–4. https://doi.org/10.1016/j.elecom.2015.07.015.
(106) Kang, X.; Wang, J.; Wu, H.; Aksay, I. A.; Liu, J.; Lin, Y. Glucose Oxidase–Graphene–Chitosan Modified Electrode for Direct Electrochemistry and Glucose Sensing. *Biosensors and Bioelectronics* **2009**, *25* (4), 901–905. https://doi.org/10.1016/j.bios.2009.09.004.
(107) Chakarova-Käck, S. D.; Schröder, E.; Lundqvist, B. I.; Langreth, D. C. Application of van Der Waals Density Functional to an Extended System: Adsorption of Benzene and Naphthalene on Graphite. *Phys. Rev. Lett.* **2006**, *96* (14), 146107. https://doi.org/10.1103/PhysRevLett.96.146107.
(108) Stable Non-Covalent Functionalisation of Multi-Walled Carbon Nanotubes by Pyrene–Polyethylene Glycol through π–π Stacking, Jie Liu.Pdf.
(109) The Nature of the Binding of Au, Ag, and Pd to Benzene, Coronene, and Graphene: From Benchmark CCSD(T) Calculations to Plane-Wave DFT Calculations | Journal of Chemical Theory and Computation https://pubs.acs.org/doi/abs/10.1021/ct200625h (accessed Oct 23, 2019).
(110) Yu, D.; Yang, Y.; Durstock, M.; Baek, J.-B.; Dai, L. Soluble P3HT-Grafted Graphene for Efficient Bilayer−Heterojunction Photovoltaic Devices. *ACS Nano* **2010**, *4* (10), 5633–5640. https://doi.org/10.1021/nn101671t.
(111) Kosynkin, D. V.; Higginbotham, A. L.; Sinitskii, A.; Lomeda, J. R.; Dimiev, A.; Price, B. K.; Tour, J. M. Longitudinal Unzipping of Carbon Nanotubes to Form Graphene Nanoribbons. *Nature* **2009**, *458* (7240), 872–876. https://doi.org/10.1038/nature07872.
(112) Kinetics of Diazonium Functionalization of Chemically Converted Graphene Nanoribbons | ACS Nano https://pubs.acs.org/doi/abs/10.1021/nn901899j (accessed Oct 22, 2019).
(113) Leroux, Y. R.; Fei, H.; Noël, J.-M.; Roux, C.; Hapiot, P. Efficient Covalent Modification of a Carbon Surface: Use of a Silyl Protecting Group To Form an Active Monolayer. *J. Am. Chem. Soc.* **2010**, *132* (40), 14039–14041. https://doi.org/10.1021/ja106971x.
(114) Mishyn, V.; Aspermair, P.; Leroux, Y.; Happy, H.; Knoll, W.; Boukherroub, R.; Szunerits, S. "Click" Chemistry on Gold Electrodes Modified with Reduced Graphene Oxide by Electrophoretic Deposition. *Surfaces* **2019**, *2* (1), 193–204. https://doi.org/10.3390/surfaces2010015.
(115) Gourronc, F. A.; Rockey, W. M.; Thiel, W. H.; Giangrande, P. H.; Klingelhutz, A. J. Identification of RNA Aptamers That Internalize into HPV-16 E6/E7 Transformed Tonsillar Epithelial Cells. *Virology* **2013**, *446* (1), 325–333. https://doi.org/10.1016/j.virol.2013.08.015.
(116) Aspermair, P.; Ramach, U.; Lechner, B.; Fossati, S.; Azzaroni, O.; Dostalek, J.; Szunerits, S.; Knoll, W.; Bintinger, J. Dual Monitoring of Surface Reactions in Real-Time by Combined Surface-Plasmon Resonance and Field-Effect Transistor Interrogation. 5.

List of Figures

Figure 1: Schematic principle of a biosensor, converting a biological binding event to a physically measurable dimension 2

Figure 2: The schematic illustrations of an aptamer with its ligand is shown in (A). [23] Figure (B) shows the target-binding induced changes of the transfer characteristic on the electrical sensor readout. [24] The aptamer selection, purification and amplification process are schematically shown in (C). (from igem.org). 3

Figure 3: The schematic Kretschmann configuration is shown in (A) with the incident light, illustrated as input signal and the reflected light beam at an angle Θ. The decay of the electromagnetic field is indicated on top of the thin metallic film with the thickness t_M. The reflected angle Θ dependent magnitudes at different refractive indices n are shown in (B). [51] 7

Figure 4: The two common architectures of graphene field-effect transistors for bio-sensing are shown. (A) represents the liquid-gated graphene FET and (B) the back-gated graphene FET. Only the channel architecture (A) is exposed to the ionic liquid, hence the analyte in solution. Therefore, the solution itself experiences the applied voltage and field-effect and electrical double layer form on both sides, the gate electrode and the drain-source channel. 9

Figure 5: Immobilization strategy used to covalently couple proteins to graphene via a pyrene derivative with an NHS activated ester group that couples spontaneously to the lysine groups of the odorant binding protein. [68] 10

Figure 6: At sub-monolayer coverage (A) free transducer surface invites (bio-) molecules to adsorb. Upon forming a closed monolayer (right panel), the entropic penalty for an additional molecule trying to adsorb leads to the anti-fouling property of the coating. A balance of bio-recognition elements and blocking molecules is required for a selective bio-sensor. [73] 12

Figure 7: Global analysis of the binding of BSA from solution to an antiBSA-AB functionalized gFET sensor; (a) shows the original data measured after injecting BSA solutions of different concentrations, as indicated by the red arrows, and after rinsing pure PBS buffer though the flow cell (blue arrow); the inset shows the current race after injecting an analyte solution of only 100 nM concentration; (b) Analysis of the rate constants, resulting in kon and koff values for the binding process; (c) Langmuir isotherm of the equilibrium coverage currents, ΔI_{DS}, as a function of the bulk concentration. The figure was taken from Reiner-Rozman et al. 2015. [64] 13

Figure 8: Structural changes for a surface-immobilized DNA double strand upon changing the ionic strength of the surrounding buffer solution. The collapsing DNA strand results in a quenched optical signal, while the electrochemical active species ferrocene is not influenced, resulting in a constant readout. [77] 14

Figure 9: The readout of differential pulse voltammetry (DPV) on two different surfaces is shown in (A). Once the capture probe PNA was immobilized on SWCNT (higher signal) and on glassy carbon electrodes. (B) illustrates the different sensitivities of the surface architecture. The limit of detection (LOT) as well as the dynamic range vary between the two different, but yet carbon based systems. [79] 15

Figure 10: The different measurement systems of SPR and gFET comprise of a similar surface architecture: both have graphene, or rGO as surface layer for bio-functionalization (A). The well understood SPR system can be used compare to the novel architecture of the graphene FET. (B) illustrates one approach to combine the two devices within one flow cell. 19

Figure 11: Graphene can be used on the gFET and SPR interfaces. The drain-source current of the FET is modulated upon the specific binding of analytes, inducing changes in the electrical double layer of the sensing area. Using the same sensor substrate graphene both devices yields in an observation tool to verify the electrical with the optical read-out. 20

Figure 12: The concept of the combined FET/SPR is schematically illustrated here, where the gate electrode and SPR interface can be functionalized with bio-recognition elements (A), leading to a modulation of both, the SPR and FET signal. In contrary, if functionalizing only the drain-source channel, the read-out of the SPR signal remains constant, while the FET signal represents the specific binding of analytes 20

Figure 13: (A) CVD graphene from Graphenea Inc. on copper discs with 12 mm diameter. (B) Synthesized graphene oxide from the University of Bayreuth, Germany. The GO solution was produced from graphite flakes with the modified Hummers [89] method. 27
Figure 14: The process of deposition of CVD graphene on a glass substrate with interdigitated electrodes. First the backside of the copper disc is plasma etched to remove residual graphene, then the copper foil is etched in a diluted hydrochloride solution. The remaining graphene, supported by a PMMA layer is transferred to the chip and annealed for 30 min at 90 °C. The PMMA is removed in the final step. 29
Figure 15: Annealing step after the deposition of the CVD graphene. 29
Figure 16: The deposition of graphene oxide starts with a self-assembly monolayer of APTES. Subsequently, the graphene oxide in a diluted dH_2O is drop casted onto the substrate. After a rinsing and baking step for one hour at 120 °C, the GO is reduced to rGO in hydrazine vapor for 4 hours. A thermal reduction afterwards increases the stability of the rGO gFET. 30
Figure 17: SEM images of CVD graphene on interdigitated electrodes. (A): full coverage of drain-source channel at magnification of 1,000x. (B): crack in CVD graphene at edge of electrode array, magnification 500x 38
Figure 18: SEM images of reduced graphene oxide after 4 hours of reduction. (A): spread coverage of interdigitated electrodes, magnification 400x. (B): visible double layers of rGO flakes when they overlap, magnification 1,000x 38
Figure 19: SEM images of defects in reduced graphene oxide after reduction for more than 12 hours. Defect size approximately 100 nm to 200 nm. A: rGO flakes covering the interdigitated electrodes, magnification 2,000x. B: defect holes in rGO flakes, magnification 10,000x 39
Figure 20: The reduction of graphene oxide measured in real time. The conductance increases during the reduction process, indicating the successful reduction to rGO. First, the graphene oxide on the interdigitated electrodes was reduced for 8 hours in hydrazine vapor at 80 °C, subsequently the same chip was thermally reduced at 200 °C under vacuum for 3 hours to obtain the minimum reduction time. 40
Figure 21: The Raman spectra of CVD graphene and reduced graphene oxide, recorded with a Raman spectrometer and a laser wavelength of 515 nm. A: The CVD graphene after deposition on the electrode surface shows a strong 2D band, representing a monolayer graphene. B: The reduction of graphene leads to a decrease of the G band, observable in the comparison with the graphene oxide. 41
Figure 22: Topographical images of the reduced graphene oxide surface. A: KFM image of the interdigitated electrodes covered with rGO. The KFM image is a representation of the work function of the surface and shows that the rGO flakes are homogeneously reduced. The black spot in the middle is the uncovered glass slide. B: precise AFM images show the height of the graphene sheets and the recorded profile of one flake leads to the assumption, that the flakes consist of about two to three layers of graphene. [94] 42
Figure 23: The NanoDrop 2000 measures the absorbance of solutions. It is used to determine the graphene oxide concentration in dH_2O. A: Spectra of four different GO concentrations with a maximum absorbance peak at 298 nm. B: Linear fit of measured GO absorbance. The linear equation can be used to determine the GO concentration of any given dilution. 43
Figure 24: The SEM images of the interdigitated electrodes with different surface coverages at four different concentrations of GO solutions. All SEM images have a magnification of 400x and show the density of rGO flakes. A and B: densely packed rGO flakes. C: rGO flakes connect the drain and source electrodes, but minor overlap of different GO sheets. D: The rGO concentration is very low and connects the electrodes partially. 44
Figure 25: The images represent the graphical analysis to determine the coverage of rGO on the gFET surface with a drop casted GO concentration of 50 µg/mL. (A): section of SEM image with grayscale histogram below, 400x magnification. (B): The grayscale was adjusted to determine the uncovered glass slide. (C): Single layer graphene sheets. (D): represents the double layered graphene sheets. 45
Figure 26: The channel between drain and source electrode was evaluated with the graphical software tool Image J to determine the rGO coverage. Different GO concentrations were deposited on the gFET to determine the best properties for bio-sensing. It can be seen, that the concentration of 50 µg/mL and 25 µg/mL cover more than 90% of the channel surface, but this leads to more than 50% of double layered graphene sheets. At 25 µg/mL, around 50% of the channel are covered and the single layer

GRAPHENE SHEETS EXCEED THE DOUBLE LAYERED. AT A LOW GO CONCENTRATION OF 6.25 μG/ML, ONLY 40% OF THE CHANNEL ARE COVERED BY GRAPHENE SHEETS. 45
FIGURE 27: THE FIGURE REPRESENTS THE I_DV_G CURVES OF DIFFERENT DEPOSITED GRAPHENE OXIDE CONCENTRATIONS. THE BLACK CURVES WERE MEASURED AFTER THE REDUCTION IN HYDRAZINE VAPOR AT 80 °C AT AMBIENT PRESSURE. THE BLUE CURVES WERE MEASURED ON THE SAME GFET AFTER AN ADDITIONAL THERMAL REDUCTION AT 200 °C IN A VACUUM OVEN. THE RED LINES ARE LINEAR FITS IN THE P-DOPED BRANCH OF THE GFET. THERE IS A SIGNIFICANT INCREASE FOR ALL SLOPES AFTER THERMAL REDUCTION. THE GFET WITH A DEPOSITED GO CONCENTRATION OF 12.5 μG/ML SHOWS THE HIGHEST MOBILITY. 46
FIGURE 28: EVALUATION OF THE SLOPE OF EACH GFET AFTER HYDRAZINE VAPOR AND AFTER SUBSEQUENT THERMAL REDUCTION. THE STEEPEST SLOPE WITH AROUND 750 μA/V WAS OBTAINED FOR A GO CONCENTRATION OF 12.54 μG/ML AFTER THERMAL REDUCTION, WHILE THE 6.25 μG/ML CHIPS EXHIBIT THE HIGHEST INCREASE AFTER THERMAL REDUCTION, BY A FACTOR OF 2.83. 47
FIGURE 29: THE FOUR I_DV_G CURVE PLOTS SHOW THE PH DEPENDENCIES OF FOUR GFETS WITH DIFFERENT GO CONCENTRATIONS. BLACK LINES ARE GFETS AFTER THE HYDRAZINE VAPOR REDUCTION. BLUE LINES SHOW THE TRANSFER CHARACTERISTICS AFTER AN ADDITIONAL THERMAL REDUCTION. WITH INCREASING PH VALUES OF THE IONIC SOLUTIONS, THE CURVES SHIFT TO THE RIGHT. IT CAN BE OBSERVED, THAT THE CHIP C WITH 12.5 μG/ML HAS THE STEEPEST SLOPE THROUGHOUT THE ENTIRE PH RANGE. ALL CHIPS HAVE AN INCREASED SLOPE AFTER THE THERMAL REDUCTION. 48
FIGURE 30: PLOT A SHOWS THE DIRAC POINT AT DIFFERENT PH VALUES OF ALL FOUR CHIPS BEFORE AND AFTER THERMAL REDUCTION. THE DIRAC POINT SHIFT IS SLIGHTLY SHIFTED TOWARDS A POSITIVE VOLTAGE AFTER THERMAL REDUCTION. PLOT B SHOWS THE BASELINE DRIFT OF THE GFETS WITH DIFFERENT GRAPHENE SURFACE COVERAGES. IT OCCURS THAT A HIGHER RGO COVERAGE LEADS TO A STRONGER BASELINE DRIFT. THE 50 μG/ML CHIP DRIFTS WITHIN 30 MIN ABOUT 120 μA, WHILE THE CHIP WITH 6.25 μG/ML CHANGES ONLY FOR 40 μA. 49
FIGURE 31: PLOT A SHOWS THE COMPARISON OF THE TRANSFER CHARACTERISTIC OF TO DIFFERENT FABRICATED GFETS. BLUE IS RGO AND BLACK CVD GRAPHENE AS DRAIN-SOURCE CHANNEL SUBSTRATE. THE INSERT IS A CLOSE-UP TO THE CVD GRAPHENE I_DV_G CURVE. PLOT B ILLUSTRATES THE BASELINE DRIFT OF THE RGO FET (BLUE) AND THE CVD GRAPHENE FET (BLACK) AT AN APPLIED GATE VOLTAGE OF -600 MV. THE CVD GRAPHENE FET HAS ONLY 30% RESPONSIVENESS COMPARED TO THE RGO FET, BUT A VERY STABLE BASELINE. 50
FIGURE 32: CYCLIC VOLTAMMETRY MEASUREMENTS AT DIFFERENT SCAN RATES ARE SHOWN TO OBTAIN THE CAPACITANCE OF THE MICRUX CELL WITH AN AGCL WIRE GATE ELECTRODE (A). THE CURRENT AT 230 MV IS PLOTTED VERSUS THE SCAN RATE IN (B) AND A LINEAR FIT RESULTS IN THE CAPACITANCE OF THE SYSTEM: 3.3 μF. 50
FIGURE 33: SCHEMATIC IMMOBILIZATION OF PCA VIA PI-PI STACKING ON RGO AND CVD GRAPHENE. A: GRAPHENE SHEETS ON INTERDIGITATED ELECTRODES. B: PCA SOLUTION IN DIFFERENT SOLVENTS FOR IMMOBILIZATION. C: PYRENE MODIFIED SURFACE WITH CARBOXYLIC ACID GROUPS FOR FUNCTIONALIZATION. D: THE ACTIVATION DURATION FOR EDC AND NHS IS 30 MINUTES FOR ALL EXPERIMENTS IN MES BUFFER. 66
FIGURE 34: FUNCTIONALIZATION OF A GOLD SURFACE WITH DTSP MOLECULE. THE DI-SULFIDE BRIDGE REACTS WITHIN 48H TO FORM A COVALENT BOND TO THE AU-SURFACE. THE NHS HEAD GROUP REMAINS ACTIVATED ON THE SURFACE FOR THE IMMOBILIZATION OF NH_2-TERMINATED CAPTURE MOLECULES. 67
FIGURE 35: MODIFICATION OF GOLD SLIDES WITH SH-BIOTIN AND SH-PEG DERIVATES IN A RATIO OF 1:10 IN ETHANOL FOR 24 HOURS. THE SURFACE MODIFICATION ENABLES THE IMMOBILIZATION OF STREPTAVIDIN TO THE BIOTIN. THE PEG CHAIN WITH AN OH TERMINAL GROUP AVOIDS NON-SPECIFIC INTERACTION WITH THE GOLD SURFACE. 68
FIGURE 36: SYNTHESIS OF $PYPEG_{34}$: THE PBSE LINKER FORMS AN AMIDE BOND WITH THE AMINE-TERMINATED PEG CHAIN. THE PYRENE PEG WILL BE USED TO IMMOBILIZED IT WITH Π-Π-STACKING ON GRAPHENE TO AVOID NON-SPECIFIC BINDING TO THE SURFACE. 69
FIGURE 37: THE IMMOBILIZATION STRATEGY OF AMINO-MODIFIED POLYSTYRENE NANOBEADS ON THE RGO OF THE GFET (A) IS SHOWN. THE NANOBEADS (C) ARE IMMOBILIZED TO OBSERVE THE SURFACE COVERAGE WITH DIFFERENT SOLVENTS FOR PYRENE CARBOXYLIC ACID AND PYRENE-PEG (B). D REPRESENTS A SEM IMAGE OF POLYSTYRENE NANOBEADS ON RGO. THE DIAMETER WAS MEASURED WITH 60 NM TO 120 NM. 72
FIGURE 38: (A) SHOWS A GRAPHENE SURFACE WITH CARBOXYLIC-ACID FUNCTIONAL GROUPS FOR FURTHER IMMOBILIZATION. (B) SHOWS A BIOTINYLATED PNA, COVALENTLY LINKED TO THE CARBOXY GROUPS. THE ALKALINE PHOSPHATASE ENZYME IS IMMOBILIZED AS A COMPLEX WITH STREPTAVIDIN TO THE BIOTINYLATED END OF THE PNA (C). 73
FIGURE 39: THE READOUT OF HYDROQUINONE (HQ) WAS CARRIED OUT WITH DIFFERENTIAL PULSE VOLTAMMETRY IN A RANGE OF -0.5 V TO +0.3 V. THE PULSE SEQUENCE IS SHOWN IN (A), WHERE IT IS INDICATED THAT THE "MEASUREMENT TIME"

is at the end of the modulated amplitude. All settings for the DPV readout are shown in B. Between -0.1 V and 0.0 V the DPV peak for HQ is expected. 74
Figure 40: The diazonium modification of reduced graphene oxide and CVD graphene was carried out on the gFET chip to investigate the transfer characteristic after modifications. Au-slides with rGO were functionalized as well. Figure B illustrates the radical diazonium attack of graphene, the deprotection to obtain a triple bond group and the further "click" of ferrocene on the surface. 75
Figure 41: The blocking agents to avoid non-specific interaction where investigated on the commercially available SPR device, Indicator-G from Sensia. The SPR prisms have gold coating with a CVD graphene layer from Graphenea. A: The adhesive molecule lysozyme was exposed to the modified SPR surface. Different blocking agents suppress the binding signal. $PyPEG_{34}$ with a 5 mM concentration avoids a binding of up to 10 µM lysozyme almost to 100%. B: The determination of a balanced ratio of blocking agent and binding molecule is important to be able to immobilize a specific capture probe. The ratio of 1:10 blocks the NSB sufficiently. 77
Figure 42: The XPS measurement show the aptamer immobilization on three different surfaces. A: The rGO surface was modified with 1 mM PCA, activated and ssDNA (aptamer) was immobilized. B: The rGO surface was modified with a 1:10 mixture of PCA/PyPEG (0.1 mM, 0.9 mM), activation and subsequently immobilization of the aptamer. C: Control measurement with a 1:10 PCA/PyPEG ratio, but without aptamer. D, E and F show the corresponding phosphate groups on the surface. D: Quantity of P 2p signal estimated at 0.2 at%. E and F: Quantity of P 2p signal estimated smaller than 0.1 at%. 78
Figure 43: PCA immobilized for 2h in DMSO. Nanobeads linked afterwards with a low surface coverage. 79
Figure 44: PCA immobilized for 2h in Methanol. Only a few Nanobeads are traceable. 79
Figure 45: PCA immobilized in THF after 4 times evaporation. Nanobeads concentration with highest surface coverage. 80
Figure 46: Pyrene-PEG_{34} as a blocking agent. The surface coverage is as expected very low. There was no nanoparticle traceable. The white spots are defects on the graphene. 80
Figure 47: (A) shows the monochromic representation of the nanobead coverage with pyrene carboxylic acid in THF. (B) shows calculated surface coverages of nanobeads after immobilization to pyrene carboxylic acid and pyrene-PEG, dissolved in different solvents. The highest surface coverage was achieved with PCA dissolved in THF. No nanobead could be found on the pyrene-PEG blocked surface. 80
Figure 48: The plots show the differential pulse voltammetry readouts of different surface modifications. A: Screen-printed electrodes with SWCNT-COOH. The heights of the peaks are evaluated as shown with arrows in the plot. B: Reduced graphene oxide with immobilized pyrene carboxylic-acid (PCA) dissolved in methanol, C: PCA dissolved in DMSO and D: PCA dissolved in THF. The red lines are the positive readouts after the immobilization of amine-5'-PNA-3'-biotin and alkaline phosphatase complexation. The black lines are the control experiments, where the activation of the carboxylic-acid was left out. The SPE results are the reference measurements with pre-modified carboxylic-acid groups on the surface, while the rGO surfaces must be modified with a pyrene carboxylic-acid linker to immobilize the bio-recognition element. 82
Figure 49: Comparison of SWCNT with COOH-groups and rGO gFETs with different solvents for pyrene carboxylic acid immobilizations. The responses are the peak heights of each surface modification after the enzymatic reaction to convert hydroquinone diphosphate to hydroquinone, an electrochemical active species. It can be observed, that the functionalization of rGO with PCA in THF results in the highest peak and leads to the highest signal-noise ratio (S/N) of 9.97, indicating a successful surface modification with PCA dissolved THF. 83
Figure 50: The differential pulse voltammetry readout of the enzyme reaction on Au-slides with 3,3'-Dithiodipropionic acid di(N-hydroxysuccinimide ester), short DTSP, modification is shown in (A). The control experiment was without immobilized biotinylated PNA (COOH not activated), hence there was no biding site for the enzyme to convert HQDP to HQ. The control experiment indicates the non-specific adsorption to the Au-surface. The signal-noise-ratio (S/N) is around 8.5 and indicates a successful surface modification with DTSP (B). 83
Figure 51: The cyclic voltammograms of click chemistry on graphene. The rapid decrease in (A) indicates a successful deposition of diazonium, forming only a mono layer on the graphene surface. (B) represents the successful TIPS deprotection and in (C) the clicked ferrocene exhibits oxidation and reduction peaks,

PROVING A SUCCESSFUL CLICKING. THE CALCULATED SURFACE COVERAGE Γ OF FERROCENE IS APPROXIMATELY GREATER THAN 95%. 84
FIGURE 52: THE DIAZONIUM TREATMENT OF CVD GRAPHENE LEADS TO A CLEAVAGE OF PARTS OF THE MONOLITHIC GRAPHENE LAYER. WHILE THE CVD GRAPHENE AFTER DEPOSITION SHOWS MINOR CRACKS, BUT A COMPLETELY COVERAGE OF THE DRAIN-SOURCE CHANNEL (A), THE CVD GRAPHENE AFTER THE RADICAL ATTACHMENT EXHIBITS SUBSTANTIAL DEFECTS AND REMOVED GRAPHENE PARTS IN THE FET CHANNEL (B). 85
FIGURE 53: THE I_DV_G CURVES BEFORE AND AFTER THE DIAZONIUM TREATMENT LEAD TO ONLY MINOR CHANGES OF THE TRANSFER SLOPE FOR REDUCED GRAPHENE OXIDE (A), WHILE THE CVD GRAPHENE EXHIBITS A SIGNIFICANT INCREASE OF MORE THAN A TEN-FOLD FOR M_{LIN} (SLOPE). THE DIAZONIUM ATTACK OF THE GRAPHENE LATTICE IMPROVES THE SEMICONDUCTING PROPERTIES FOR CVD GRAPHENE. 86
FIGURE 54: SOURCE MEASURE UNITS TO CHARACTERIZE SEMICONDUCTORS WITH HIGH ACCURACY AND HIGH RESOLUTION DOWN TO THE FA RANGE. BOTH CHANNELS OF THE SOURCE MEASURE UNITS ARE REQUIRED TO MEASURE ONE FIELD EFFECT TRANSISTOR. 102
FIGURE 55: A: THREE CHANNEL KEYSIGHT U2722A ALTERNATIVE TO EXPENSIVE AND BULKY SOURCE METER UNITS FOR THE SIMULTANEOUS MEASUREMENT OF TWO GFETS. B: ELECTRICAL CIRCUIT DIAGRAM TO MEASURE TWO GFETS WITH A COMMON GATE ELECTRODE. 103
FIGURE 56: A: FLOW CELL FOR ELECTROCHEMICAL EXPERIMENTS WITH A MICROFLUIDIC LID TO INJECT ANALYTES IN A PRECISE VOLUME. B: ASSEMBLED FLOW CELL. C: SENSOR CHIP WITH TWO INTERDIGITATED AU ELECTRODES WITH A SIZE OF 6 X 10 MM. THE SENSOR CHIP CAN BE INSERTED IN THE FLOW CELL AND IS CONNECTED TO A USB PLUG, ACCESSIBLE AT THE BACK OF THE CELL. ALL PARTS ARE AVAILABLE AT MICRUX TECHNOLOGIES. 104
FIGURE 57: THE FLOW CELL WAS RE-DESIGNED TO IMPLEMENT A GATE ELECTRODE INSIDE THE MEASUREMENT CHAMBER. A: CUSTOMIZED MICROFLUIDIC FLOW CELL LID, PRODUCED BY MICRUX TECHNOLOGIES ACCORDING TO 3D DRAWING FOR THE INTEGRATION OF A AGCL WIRE ON TOP OF THE SENSOR CHIP. B: DETAILED VIEW TO IN- AND OUTLET OF THE MICROFLUIDIC SYSTEM. THE CYLINDRICAL CENTER WAS IMPLEMENTED TO INSERT THE GATE ELECTRODE. 105
FIGURE 58: A: PLANAR SPR SLIDE WITH 2 NM CHROMIUM AND 50 NM GOLD ON A MICROSCOPE GLASS SLIDE, WORKING ALSO AS GATE ELECTRODE. B: FET SENSOR CHIP WITH INTERDIGITATED ELECTRODES AS DRAIN AND SOURCE TERMINAL. C: FIRST APPROACH OF GASKET IN THE GFET/SPR ASSEMBLY WITH A CHANNEL HEIGHT OF 3 MM. D: SECOND ITERATION MICROFLUIDIC GASKET WITH A CHANNEL HEIGHT OF 400 μM. 106
FIGURE 59: A: ULTIMAKER S5 FOR FUSED DEPOSITION MODELING (FDM) OF THE NECESSARY PARTS FOR THE GFET/SPR FLOW CELL. B: PLA FILAMENT AS MOLDING MATERIAL, PVA AS SUPPORTING MATERIAL C AND D: BOTH DESIGNED 3D MODELS OF THE GFET/SPR FLOW CELLS (BLUE) IN COMBINATION WITH ALL REQUIRED PARTS TO ASSEMBLE THE SANDWICH FOR THE MEASUREMENT. E AND F: MOLDING FORMS FOR THE PDMS GASKETS. FIGURE D AND F SHOW THE SECOND ITERATION STEP TOWARDS THE GFET/SPR SYSTEM. 107
FIGURE 60 THE SKETCH ILLUSTRATES THE IMPORTANT DETAIL OF THE μCELL: THE MICROFLUIDIC COMBINATION OF THE GFET (BOTTOM) AND THE GOLD SLIDE (AU SURFACE). ON THE LEFT AND RIGHT SIDE ARE THE IN- AND OUTLET FOR INJECTING SOLUTIONS CONTAINING THE ANALYTES. THE GASKET, IN RED, SEALS THE CHANNEL BETWEEN GFET AND SPR SURFACE. THE YELLOW SQUARES MARK THE GAP BETWEEN THE GFET HOLDER (BLUE) AND THE GFET CHIP, SEALED BY THE UNIQUE GASKET DESIGN. 108
FIGURE 61: ILLUSTRATION OF THE DESIGNED PRINTED CIRCUIT BOARDS FOR THE CONNECTION OF THE GFET/SPR CELL TO THE SOURCE MEASURE UNIT. A AND B: EAGLE LAYOUT FILE AND 3D VISUALIZATION OF THE GFET/SPR CONNECTOR BOARD. C AND D: EAGLE LAYOUT FILE AND 3D VISUALIZATION OF THE KEYSIGHT U2722A USB CONNECTOR BOARD. A STANDARD USB-A TO MINI CABLE CONNECTS THE MEASUREMENT SET-UP. 110
FIGURE 62: A: CONNECTOR BOARD TO A STANDARD USB-A PLUG FOR BOTH DRAIN-SOURCE CHANNELS. B: CONNECTED USB CABLES TO THE SMU. THE GATE ELECTRODE IS CONNECTED TO THE SHIELD OF THE USB CABLE FOR THE GFET/SPR FLOW CELL AND TO A WIRE FOR THE MICRUX FLOW CELL, SHOWN IN C. D: THE CONNECTION OF THE KEYSIGHT U2722A SOURCE METER UNIT TO THE MICRUX FLOW CELL WITH A USB CABLE AND A WIRE FOR THE LIQUID GATE ELECTRODE. THE GFET/SPR FLOW CELL AND MICRUX GFET FLOW CELL ARE CONNECTED FOR PARALLEL MEASUREMENTS. 111
FIGURE 63: THE SOFTWARE "GFET MEASUREMENT UTILITY V4.4" IS CONTROLLING THE KEYSIGHT U2722A, LOGGING THE MEASURED DATA AND PLOTS THE DATA OF THE RUNNING EXPERIMENT. FURTHER FEATURES ARE THE AUTOMATED EVALUATION OF THE DIRAC POINT AND THE SLOPE OF THE TRANSFER CHARACTERISTIC OF EACH GFET (I_DV_G CURVE). 112
FIGURE 64: DEMONSTRATION OF ELECTRICAL AND OPTICAL READOUT IN THE COMBINED GFET/SPR MEASUREMENT TOOL 4.4. THE UPPER HALVE PLOTS THE TRANSFER CHARACTERISTIC AND THE REAL-TIME $I_D(T)$ READOUT, WHILE THE LOWER GRAPH IS THE RECORDING FROM THE OPTICAL SPR MACHINE, AT A CERTAIN ADJUSTED ANGLE. 114

Figure 65: The gFET measurement utility 4.4 creates an Excel spreadsheet with the measured and calculated values during the experiment. Separated sheets store the data for both gFETs measured simultaneously, including the Dirac point shift, the slope and the threshold voltage V_T. 115
Figure 66: The Excel spreadsheet contains all measured I_DV_G curves including the time stamp to associate the transfer characteristic to a specific binding event on the gFET substrate. 115
Figure 67: The pictures show the designed and produced connectors and flow cells for the gFET/SPR architecture. A: USB connector board for Keysight U2722A. B: gFET connector board for µCell adapter with USB mini plug. C: Fused deposition modeled µCell adapter for the gFET/SPR configuration. D: Assembly of µCell with the glass prism. The 400 µM gasket can be seen inside the prism, where it is pressed against the SPR gold substrate. 116
Figure 68: The graphs show the titration of the human papilloma virus protein to an HPV-aptamer modified surface. A: sensorgram illustrates the change of the SPR signal on binding events. The right sensorgram (B) shows the electrical rGO gFET readout upon specific binding. Both experiments were carried out on the same day with the same surface modification on graphene. Both sensor responses contain the exponential fit upon binding events for further investigation of the binding kinetics involved at different concentrations. 123
Figure 69: The evaluation of the exponetial binding kinetic at different concentrations from the sensorgrams results in the Langmuir plot. The dissociation constant K_D can be determined at half-saturation of this representation. The values of the optical (A) and electrical readout (B) differ, while the surface functionalization is the same. The electrical gFET response represents a K_D of 10 times lower than the optical SPR experiment. 124
Figure 70: A comparison of different surface modifications of CVD graphene/Au-SPR prisms is shown. The injection of 1 µM HPV-protein results in the highest magnitude for spacially modified surfaces, while the densly packed HPV-aptamer has a lower signal magnitude upon bining. The control experiment with an immobilized scrambled aptamer exhibits a relatively small response, due to the pyrene-PEG anti-fouling surface modification. 125
Figure 71: The response of the graphene FET to changing pH values of an ionic solution in two different flow cells is shown. The gate electrode of the Micrux flow cell consist of an Ag/Cl electrode (blue), while in the gFET/SPR cell uses a gold slide opposite to the drain-source-channel (red). While the I_{DS} current of the gFET measurement with V_{DS} = 50 mV and V_G = -400mV is modulated upon changing pH values, the SPR signal remains constant. The simultaneous optical readout is only modulated by refractive index changes, not occurring at different pH values, shown in black. 126
Figure 72: The in-situ readout of the gFET/SPR during the growth of a layer-by-layer assembly. The red bars represent the injection of PDADMAC (layer 3, 5, 7) and the blue bars represent the time of injected PSS (layer 4, 6, 8). The experiments were performed with two different gate voltages for the gFET: V_G = +400 mV (red) and -400 mV (blue). The signals in (A) are the mass uptake upon layer deposition, monitored by SPR and (B) are the charge displacements on the surface for different polyelectrolytes and their charges. 127
Figure 73: The comparison of the two gFETs before and after the polyelectrolyte depositions are shown. The transfer characteristics of V_G = -400 mV (blue) and +400 mV (red) gFETs experience both a change in their magnitude after the deposition. It can be noted, that the slope in the p-type regime (-400 mV) is steeper than the n-type (+400 mV). It correlates with a more prominent response for chip (A) during the $I_D(t)$ measurement. 127
Figure 74:The raw signals of the measured gFET and the SPR signal are shown in one graph with an exact time stamp overlay of the layer-by-layer deposition. Beside the measured deposition of polymers on the surface, also the gate-source leakage current is shown in the graph as a purple line at 0 µA. The gate leakage current is a parasitic phenomenon and should be small. The here observed signal has approximately 200 nA, without any variations above the noise level and therefore can be neglected. 128
Figure 75: The titration of streptavidin and the specific binding to the biotinylated Au-slide is shown in (A). The SPR signal increases upon mass uptake at different streptavidin concentrations. The sawtooth artefacts are induced by the I_DV_G curve measurements of the gFET, because the Au slide is as well the gate electrode of the gFET. (B) shows the angular scan before and after the streptavidin binding. A surface mass density of 194.22 ng/cm^2 were calculated afterwards. 129

FIGURE 76: BINDING OF STREPTAVIDIN TO THE IMMOBILIZED BIOTIN CHANGES THE I_DV_G CURVE OF THE GFET (A). THE TRANSFER CHARACTERISTIC WAS MEASURED AFTER EACH STREPTAVIDIN CONCENTRATION AND THE SLOPE ON THE LEFT SIDE OF THE DIRAC POINT IS PLOTTED VERSUS THE CONCENTRATION (B). _____ 130
FIGURE 77: THE OPTICAL (TOP) AND ELECTRICAL (BOTTOM) MEASUREMENTS OF NEUTRAVIDIN BINDING TO A BIOTINILATED GOLD-SURFACE ARE SHOWN IN THESE FIGURES. THE MEASUREMENTS WERE PERFORMED SIMULTANOUSLY IN AN ASSEMPLED GFET/SPR FLOW CELL, WHERE THE TITRATION OF NEUTRAVIDIN STARTED AT 0.2 NM UP TO 25 NM. BOTH, THE SPR AND THE GFET EXHIBIT BINDING READOUTS UPON NEUTRAVIDIN BINDING. INTERESTINGLY, THE GFET SIGNAL EXHIBITS AN INCREASE OF THE SIGNAL ALREADY AT 0.78 NM, WHILE THE SPR SIGNAL REMAINS IN A STEADY EQUILIBRIUM. _____ 131
FIGURE 78: THE BINDING OF THE HPV-E7 PROTEIN TO THE SPECIFIC BINDING APTAMER IN THE GFET/SPR SETUP, IMMOBILIZED ON THE GOLD SLIDE, WORKING AS SPR AND GFET SIGNAL. THE ELECTRICAL SIGNALS WERE MEASURED AS I_DV_G CURVES AFTER EACH CONCENTRATION WAS INJECTED TO THE SURFACE. IT CAN BE OBSERVED, THAT THE DIRAC POINT OF THE I_DV_G CURVES SHIFTS TO A MORE POSITIVE VOLTAGE UPON BINDING EVENTS, EVEN AT LOW CONCENTRATIONS AS 7 NM, WHEREAS THE SPR SIGNAL IS DOES NOT EXHIBIT CHANGES. _____ 132

Abstract

The race in biomedical diagnostics between optical detection principles and electrical concepts is not decided yet. Both approaches continue to offer solutions for fast, multiplexed, simple and cheap detection of biological relevant molecules. However, if it comes to the detection of small analytes and/or if the achievable analyte binding density at the transducer surface is low, label-free optical detection schemes have a problem because the change in the optical interfacial architecture induced by the mere binding of the analyte may be simply too minute to be detected. In this work, an innovative and versatile sensing platform, combining an electrical and optical read-out device to compare the different signal behaviors during a biological binding event in real time was developed. It is based in coupling the read out of a graphene-based field-effect transistor (gFET) with that of surface plasmon resonance (SPR). Various binding events including biotin/neutravidin, PNA/DNA and ssRNA/ssDNA aptamers for protein detection were investigated and the results discussed.

Résumé

Le choix entre les principes de détection optique et les concepts électriques pour un diagnostic biomédical n'a pas encore été décidée. Ces deux approches continuent à offrir des solutions pour une détection rapide, multiplexée, simple et peu coûteuse de molécules biologiques pertinentes. Toutefois, s'il s'agit de détecter de petits analytes et/ou si la densité de liaison d'analyte à la surface du transducteur est faible, les détections optiques sans marquages posent des problèmes. Dans ce travail, une plate-forme de détection innovante et polyvalente, combinant un dispositif de lecture électrique et optique pour comparer les signaux lors d'une reconnaissance biologique en temps réel, a été développée. Elle est basée sur le couplage de la lecture d'un transistor à effet de champ (gFET) à base de graphène avec celle de la résonance plasmonique de surface (SPR). Divers types de liaison dont la biotine/neutravidine, l'ANP/ADN et l'aptamère ssARN/ssADN pour la détection de protéines ont été étudiés et les résultats discutés.

Kurzfassung

Der Wettlauf in der biomedizinischen Diagnostik zwischen optischen Detektionsprinzipien und elektrischen Konzepten ist noch nicht entschieden. Beide Ansätze bieten weiterhin Lösungen für den schnellen, gebündelten, einfachen und kostengünstigen Nachweis biologisch relevanter Moleküle. Wenn es jedoch um den Nachweis kleiner Analyten geht und/oder wenn die erreichbare Analytbindungsdichte an der Sensoroberfläche gering ist, haben markierungsfreie optische Nachweismethoden ein Problem, weil die Änderung der optischen Grenzflächenarchitektur durch die bloße Bindung der Analyten einfach zu klein sein, um nachgewiesen zu werden. In dieser Arbeit wurde eine innovative und vielseitige Erfassungsplattform entwickelt, die ein elektrisches und ein optisches Auslesegerät kombiniert, um die verschiedenen Signalverläufe während eines biologischen Bindungsvorgangs in Echtzeit zu vergleichen. Es basiert auf der Kopplung des Auslesens eines Graphen-basierten Feldeffekttransistors (gFET) mit dem der Oberflächenplasmonresonanz (SPR). Verschiedene Bindungsereignisse einschließlich Biotin/Neutravidin-, PNA/DNA- und ssRNA/ssDNA-Aptameren für den Proteinnachweis wurden untersucht und die Ergebnisse diskutiert.

Patrik Aspermair, 2019